FACULTY
OF MATHEMATICS
AND PHYSICS
Charles University

DOCTORAL THESIS

Libor Šachl

Modelling of global ocean circulation and ocean-induced magnetic field

Department of geophysics

Supervisor of the doctoral thesis: prof. RNDr. Zdeněk Martinec, DrSc.
Study programme: Physics
Study branch: Geophysics

Prague 2020

I declare that I carried out this doctoral thesis independently, and only with the cited sources, literature and other professional sources. It has not been used to obtain another or the same degree.

I understand that my work relates to the rights and obligations under the Act No. 121/2000 Sb., the Copyright Act, as amended, in particular the fact that the Charles University has the right to conclude a license agreement on the use of this work as a school work pursuant to Section 60 subsection 1 of the Copyright Act.

In .... date ....

Author's signature

This thesis would never be written without my supervisor Prof. Zdeněk Martinec and my family. I have to mention them at the first place.

I am grateful to Prof. Martinec for his guidance through the field of oceanography which was a new world for both of us. I would like to thank him for the opportunity to spend three years at the Dublin Institute for Advanced Studies (DIAS). It was a valuable experience. I have seen what the scientific work involves. I have learned that the nicely written concise papers are results of many hours of hard work, dead ends and planning the next steps. I have also learned to drink coffee because “no coffee, no science”. I enjoyed our discussions about science but also about everyday life. And I met many interesting persons. I think that the stay in Dublin enriched me as a scientist but also as a human being.

I would like to thank my family for two reasons. First, they supported me in my decision to study physics and do this PhD. Second, they never let me down and always tried to cheer me up when everything seemed to be lost. Especially my mother has always done her best to help me whenever I needed help. I regret that my father and grandmother have seen my progress but they both passed away and can not read this thesis. For all these reasons, I would like to dedicate this thesis to my family.

I am grateful to my colleague Dr. Jakub Velímský especially for his help during the preparation of the manuscript about the modelling of ocean-induced magnetic field. He “mercilessly” shortened my draft and forced me to rewrite it several times which was driving me crazy but it also greatly improved the manuscript.

Let me thank my colleagues at the Department of Geophysics in Prague as well as my colleagues at DIAS for pleasant atmosphere and nice coffee breaks. My special thanks to Filip, Franta, Míra and Honza who shared our office with me. I really enjoyed our discussions about so many various topics that only life can bring.

There are many people who gave me a piece of advice when I was preparing a presentation, listened to my problems and gave me suggestions or simply inspired me by their own work and attitude to science. I can not list them all but let me thank all these anonymous souls for their kindness.

Last but not least, I acknowledge the support by the Grant Agency of the Czech Republic, project No. P210/17-03689S, by the European Space Agency Contract No. 4000109562/14/NL/CBi “Swarm+Oceans” under the STSE Programme, by the Science Foundation Ireland grant 11/RFP.1/GEO/3309, by The Ministry of Education, Youth and Sports from the Large Infrastructures for Research, Experimental Development and Innovations project “IT4Innovations National Supercomputing Center – LM2015070”, and by the Charles University grant SVV 260447.

Title: Modelling of global ocean circulation and ocean-induced magnetic field

Author: Libor Šachl

Department: Department of geophysics

Supervisor: prof. RNDr. Zdeněk Martinec, DrSc., Department of geophysics

Abstract: The ocean modelling community commonly use several renown ocean general circulation models (OGCMs) such as NEMO, MOM and FESOM. These models have been developed by research groups for many years, which resulted in complex mathematical and numerical algorithms. There are geophysically relevant problems, such as the glacial isostatic adjustment, in which the global ocean plays an important role. Ocean circulation does not need to be modeled extremely complex, but other phenomena such as time changing geometry of ocean domain needs to be considered. Geophysical applications motivated us to develop a new OGCM called LSOMG. The LSOMG model is not meant to substitute the existing OGCMs but to provide a modelling framework for geophysical rather than purely oceanographic applications. LSOMG is a 3-D baroclinic ocean model fully parallelized using the MPI standard. It is forced by atmospheric fluxes (wind stresses, heat fluxes, etc.) but also by tides. The model can be run in a simplified 2-D barotropic version if 3-D effects can be neglected. LSOMG was tested in a series of simplified barotropic numerical tests: the tsunami and tidal numerical tests and the Munk problem. In the full baroclinic version, we tested the generation of the Ekman layer and the advection of tracers. Finally, we present realistic wind and tidally driven ocean circulations computed by the LSOMG model.

The second part of the thesis is devoted to the study of ocean-induced magnetic field (OIMF). The ultimate goal is to extract information about the ocean circulation from the observed OIMF, e.g., by Swarm satellites, and assimilate it into an OGCM. However, it is a challenging task since the OIMF has small amplitudes of about 2 nT maximum at Swarm altitudes. It is overlaid by the main, ionospheric and magnetospheric magnetic fields that are several orders of magnitude larger. We thus focus on the precision of forward modelling and study the impact of physical and numerical approximations. Namely, we inspected the impact of galvanic coupling, vertical stratification of ocean flow and electrical conductivity, self-induction and horizontal resolution on the numerically predicted OIMF. Another possibility is to use localized magnetic measurements at the sea bottom instead of satellite data. Consequently, we studied the toroidal magnetic field inside the ocean using fully 3-D versions of both LSOMG and the magnetic-induction solver Elmgiv. The toroidal magnetic field is zero at the surface but it is significant inside the ocean. According to our computations, its magnitude can reach 15 nT, i.e., it is about one order of magnitude larger than the OIMF at satellite altitudes.

Keywords: ocean modelling, global circulation, ocean-induced magnetic field

Název práce: Modelování globální oceánské cirkulace a oceánem indukovaného magnetického pole

Autor: Libor Šachl

Katedra: Katedra geofyziky

Vedoucí disertační práce: prof. RNDr. Zdeněk Martinec, DrSc., Katedra geofyziky

Abstrakt: Komunita věnující se modelování oceánů používá několik renomovaných modelů (OGCM) jako jsou NEMO, MOM a FESOM. Tyto modely jsou vyvíjeny vědeckými týmy po mnoho let a využívají složité matematické a numerické algoritmy. Existují geofyzikálně relevantní problémy, jako například post-glaciální výzdvih, ve kterých globální oceán hraje významnou roli. Oceánská cirkulace zde nemusí být namodelována extrémně přesně, ale naopak je třeba uvážit ostatní jevy jako např. v čase proměnnou geometrii oceánského dna a pobřeží. Geofyzikální aplikace byly naší motivací pro vývoj nového OGCM pojmenovaného LSOMG. Model LSOMG nemá nahradit stávající OGCM. Měl by poskytnout nástroj pro geofyzikální spíše než čistě oceánografické aplikace. LSOMG je 3-D baroklinní oceánský model plně paralelizovaný pomocí MPI standardu. Model je buzen atmosférickými toky (tření větru, tepelné toky, atd.) ale také slapy. Model lze spustit ve zjednodušené 2-D barotropní verzi, pokud je možné zanedbat 3-D efekty. LSOMG byl testován v řadě zjednodušených barotropních numerických testů: tsunami a slapových numerických testech a v Munkově úloze. V kompletní baroklinní verzi jsme otestovali tvorbu Ekmanovy vrstvy a advekci tracerů. Na závěr prezentujeme realistická proudění buzená větrem a slapy napočtená pomocí LSOMG modelu.

Druhá část této práce je věnována studii oceánem indukovaného magnetického pole (OIMF). Cílem je získat informace o oceánské cirkulaci z pozorovaného OIMF, např. ze satelitů Swarm, a asimilovat je do OGCM. Jedná se o složitou úlohu, protože amplitudy OIMF nabývají maximálně 2 nT ve výškách, kde operuje Swarm. OIMF je překryto hlavním, ionosferickým a magnetosférickým pole, jež jsou o několik řádu větší. Proto se soustředíme na přímé modelování a studujeme dopad fyzikálních a numerických aproximací na jeho přesnost. Prozkoumali jsme dopad galvanického couplingu, vertikálního zvrstvení oceánského proudění a elektrické vodivosti, self-indukce a horizontálního rozlišení na numericky predikované OIMF. Další možností je místo satelitních dat použít lokalizovaná měření magnetického pole na oceánském dně. Proto jsme studovali toroidální magnetické pole uvnitř oceánu pomocí plně 3-D verzí LSOMG a magnetického indukčního řešiče Elmgiv. Toroidalní magnetické pole je nulové na hladině oceánu, ale je významné uvnitř oceánu. Podle našich výpočtů může jeho amplituda dosáhnout až 15 nT, takže je asi o řád větší než OIMF ve výškách, kde měří satelity.

Klíčová slova: modelování oceánů, globalní cirkulace, oceánem indukované magnetické pole

Contents

II Ocean model LSOMG 44

Introduction

0.1 Basic facts about ocean

The global ocean covers around three quarters of the Earth surface and it accumulates 97% of the total volume of water on the planet Earth. Human mankind is affected by the ocean in many ways. The ocean currents are important for the fisheries and ship transport. The ocean interacts with the atmosphere and it plays a key role in the Earth's climate. The ocean water has high thermal capacity which allows global ocean to store a significant amount of heat. If the atmospheric temperature suddenly drops, the heat stored in the ocean is released and vice versa. Consequently, the ocean mitigates temperature fluctuations in the atmosphere. The ocean also accumulates dissolved gasses. Some of them are greenhouse gasses such as water vapour or carbon dioxide. If they were released, it would influence climate. The presence of oceans brings benefits but it may also be dangerous. The tsunami waves can hit the coastal areas with incredible destructive power. Some endangered countries have developped systems of early warning which have already saved human lives. To sum it up, it is important to understand ocean dynamics and be able to predict the ocean circulation.

The global ocean circulation is mainly driven by the surface fluxes of momentum, heat and fresh water as well as the pressure gradients due to density variations. People sometimes refer to the wind- and buoyancy-driven circulation rather than the global circulation. Another commonly used term is the meridional overturning circulation (MOC) since the zonally integrated flow "overturns" from surface to the abyss and vice versa. The older term is the thermohaline circulation since the density variations are caused by the variations of temperature and salinity. The global ocean circulation can be divided to the surface and deep circulations [Siedler et al., 2013].

The surface surface circulation is dominated by six large-scale ocean gyres, out of which five are located in the ocean basins. The western boundary currents in these gyres are typically warm, fast (up to 2 m/s), narrow but strong (around 50 Sv; 1 Sv=10^3 m^3/s) currents such as the Gulf Stream or the Kuroshio current. The eastern boundary currents are typically cold, slower, wider but weaker currents such as the Peru (also Humboldt) Current or the Benguela Current. Both western and eastern boundary currents affect the climate. For example, the Gulf Stream makes the climate of east coast of North America and west coast of Europe warmer. The Peru Current takes part in the climate disruption called El-Nino. During this event, Peru Current weakens, surface waters in the eastern tropical Pacific gets warmer which is accompanied by heavy rainfalls. The sixth gyre does not sit in an ocean basin but it rather circumvents the Antarctica due to the absence of continental barriers. It is called the Antarctic Circumpolar Current (ACC) and it is the strongest ocean current with the average transport of 130 Sv [Cunningham et al., 2003].

If the ocean waters are very cold or salty, they become dense enough to sink into the abyss and form deep waters. There are a few locations of deep-water formation in the global ocean. For example, deep waters form in the North Atlantic (salty waters) and around Antarctica (cold waters) in Wedell and Ross seas Stewart [2008]. The deep waters are transported for long distances (several thousands of kilometers) and then uplifted back to the surface. Broecker et al. [1991] used a simple ribbon model to depict the deep circulation. The ribbon model has become popular and it has been adopted by many other authors. Its detailed version is depicted in Fig. II-8 in Schmitz Jr [1996] but the structure of the real circulation is even more complicated [Bower et al., 2009].

0.2 History of oceanography

The oceanography has a long history. According to Stewart [2008], the Polynesian navigators used their experience and knowledge about ocean during their sails as early as in 4000 BC. Pytheas, Arabs, Romans or Vikings also proved to be great sailors which would not be possible without certain oceagraphic knowledge. The Indian Vedic scripts from 2000 to 1400 BC mention the connection between tides and the Moon and Sun. The Europeans started to study oceans in the 15th and 16th centuries AD, during the exploratory voyages of Bartholomew Dias, Christopher Columbus, Vasco da Gama and Ferdinand Magellan. They were followed by scientific voyages of James Cook, Charles Darwin, Sir James Clark Ross, Sir John Ross and Edward Forbes. Noticably, Edmond Halley descibed the system of trade winds in the 17th century, Benjamin Franklin created the first map of Gulf stream in the 18th century and Matthew Fontaine Maury published the first thorough oceanographic book Physical Geography of the Sea [Maury, 1874].

The pioneering works focused on the ocean surface and its shallow parts. In the 19th century, the Challenger, Gazelle and Fram expeditions initiated the studies of deeper parts of the ocean. However, a real breakthrough in the ocean exploration came in the 20th century due to the progress in instrumental science. In the 1920s, the expedition Meteor studied the South Atlantic using an early version of sonar and it brought the first bathymetry maps of the South Atlantic. After the Second World War, a number of international projects have been organized. The NORPAC expedition which studied the Pacific Ocean was one of them. Various studies were conducted during the International Geophysical Year (July 1957 - December 1958) as summarized in Gordon and Baker [2013], and during the International Decade of Ocean Exploration (1971-1980) [Intergovernmental Oceanographic Commission, 1974]. For example, Mid-Ocean Dynamics Experiment (MODE) studied the mid-ocean mesoscale eddies [Mode Group and others, 1978], the POLYMODE project [Collins and Heinmiller, 1989] was its US-Soviet successor and Climate: Long Range Mapping and Prediction (CLIMAP) was a paleoclimate project which studied the global climate during the last interglacial [CLIMAP Project, 1981].

Finally, the satellite era started with the SeaSat mission. It was launched in 1978 and it was the first oceanographic satellite mission. SeaSat collected more data than all ship measurements during the past 100 years despite its short operational time of 110 days. SeaSat was followed by many oceanographic satellite missions such as GEOSAT, Topex/Poseidon, Jason missions (1-3), OceanSat missions (1-2) or SMOS. At about the same time, ocean researchers have started to install large arrays of floats and buoys to acquire data from the ocean interior. It is worth to mention World Ocean Circulation Experiment (WOCE) and the

Tropical Ocean Global Atmosphere program (TOGA) which led to the construction of the TAO/TRITON array of moored buoys in the Pacific Ocean, PIRATA array in the Atlantic Ocean and RAMA array in the Indian Ocean. Besides that, a global array of free-drifting profiling floats called ARGO has been built.

Of course, data science goes hand in hand with computer science. The computer processing power has increased dramatically during the last three decades. It has made the calculations of ocean circulation feasible which stimulated the development of various numerical models. The ocean modelling is also the key subject of this thesis.

0.3 Modelling of oceans and the ocean-induced magnetic field

The global ocean circulation includes physical processes on many different spatial and temporal scales. Fig. 1 in Ruhl et al. [2011] shows that spatial scales are ranging from centimeters (molecular processes such as molecular diffusion) and meters (surface gravity waves) over kilometers (internal tides) up to thousands of kilometers (ocean gyres). Temporal scales are ranging from seconds (molecular processes) and days (internal waves and internal motions) over months (seasonal cycle) up to thousands of years (climate change). In this thesis, we use one of the so-called ocean general circulation models (OGCMs) which are designed to simulate the circulation in the global ocean, a single ocean basin or sea. However, as the spectrum of processes in the ocean is broad, there also exist models which are dedicated to a particular oceanic process such as tsunami or wave models. These dedicated models are based on the similar principles as the OGCMs and it may seem that they are only a subset of OGCMs which is used for certain special cases. This is not true. For example, the tsunami models solve the so-called shallow-water equations for the tsunami propagation. These equations are also contained in the OGCMs, see Sec. 4, but tsunami models resolve not only the tsunami propagation on the open ocean but also the innundation process. These two processes represent two rather different flow regimes which complicates the choice of suitable numerical methods George [2006]. The modern tsunami models are also able to simulate the debris transport during the inundation process. These processes are not considered in the OGCMs.

An OGCM is a complex system; a mixture of primitive equations, physically motivated parameterizations and numerical schemes. It is not surprising that there are many options for the individual parts of the model which creates many possibilities how to put the model together. OGCMs can be divided into categories based on the selection criteria as follows.

Coupling with other environmental models. The global ocean is not an isolated system. It exchanges fluxes of heat, momentum and mass with the other parts of the global ecosystem such as the atmosphere, ice-sheets or rivers. An OGCM can read these fluxes from the input data file. These are ocean-only simulations. A more complex approach is to run two or more environmental models simultaneously and exchange the fluxes between them on the fly. The ocean-only simulations are faster but they are missing feedback, which can be both positive and negative, between the interacting systems. It depends on the particular application whether the feedbacks play a key role and coupled model is needed. For example, the climate predictions require coupled models but the modelling of Gulf stream can be done in ocean-only simulations.

Modelling era. We distinguish two large groups: The models of the present-day ocean circulation and the models of paleocean circulation. A typical OGCM is a representant of the first group. These models are used for sensitivity experiments, hindcast simulations, short-term or climate predictions. Both ocean-only and coupled models are used, typically in eddy-permiting or eddy-resolving configurations (see Sec. 1 for definitions). After the spin up, the model is usually run for a few months or years and the output sampling period varies from days to months. The paleocean models contribute to the understanding of ocean dynamics by studying the past events. Paleoceanographers typically perform scenario testing to inspect model sensitivity on forcing, input parameters and subgrid scale parameterizations. The paleocean models are commonly run for hundreds or even thousands of years which significantly increases computational demands. Additionally, the coupled models are preferred over the ocean-only models since data which can be used to prescribe forcing are not available in the sufficient spatial and temporal resolutions. Consequently, certain modelling compromises are inevitable. The most common are eddy-parameterized configurations, the eddy-resolving configurations are far beyond the computational limits. It is also common to use light-weight models, sometimes older versions of the renowned OGCMs, which are missing the most recent features of the state-of-art OGCMs but are less computationally demanding. These light-weight coupled models are sometimes called EMICs which is an acronym for Earth system models of intermediate complexity.

Vertical coordinate. Three major vertical coordinates are used in OGCMs: geopotential (z), isopycnal (ρ) and terrain-following (σ) coordinates. Each of them has its advantages and drawbacks. The choice of vertical coordinate is fundamental since it affects model's performance and capabilities and it is complicated to switch between two types. The z and ρ coordinates are commonly used in global models. The σ-coordinate is preferred in regional models. See Sec. 2.3.1 for more details.

Structure of the computational grid. The majority of OGCMs models is built upon structured Arakawa grids. Some OGCMs use unstructured spatial grids, e.g., FESOM [Danilov et al., 2004, 2017], FVCOM [Chen et al., 2003, Lai et al., 2010] and ICON [Korn, 2017]. The strength of these models is the accurate representation of complex coastlines. The grid is coarse on the deep ocean but it is smoothly refined in coastal areas. That is extremely useful for the regional OGCMs, especially in the presence of narrow straits [Fix, 1975, Le Provost, 1986]. On the other hand, there are still some open challenges in the use of unstructured grids in ocean modelling [Siedler et al., 2013].

An attentive reader might be surprised that we have not talked about tides so far. The reason is that tides were not considered by OGCMs for a long time. Certain technical issues complicated the implementation of tides into OGCMs. Tides have traditionally been modelled using the 2-D barotropic models which are based on the approximate shallow water equations. Despite their physical deficiencies, barotropic models proved to be a useful tool for modelling of ocean tides. Tidal models are used to calculate tidal corrections for studies of nontidal signals in satellite altimetry [Fu and Cazenave, 2001] and gravimetry [Visser et al., 2010, Seeber, 2003]. However, the advances in both computational technologies and ocean modelling itself have recently made the implementation of tides into OGCMs possible. It may improve the OGCM performance since tides contribute significantly to the ocean mixing [Munk and Wunsch, 1998, Egbert and Ray, 2000]. Müller et al. [2010] reported more realistic convection in the Labrador Sea, modified pathway of the North Atlantic Current and consequently a reduced North-Atlantic sea surface temperature bias in the climate model with tides included. Schiller and Fiedler [2007] performed a regional modelling around South-East Asia and Australia and they found a strong influence of tidal mixing on the mixed-layer in certain areas. There were also a few promising attempts to model baroclinic tides [Müller et al., 2012, Arbic et al., 2010, Simmons et al., 2004, Niwa and Hibiya, 2011] but it is still an open topic due to extremely high requirements on the spatial resolution, see Sec. 5.10.

The motivation for this thesis was a demand at our department for a global three-dimensional model for geophysical applications. In particular, a model that would replace the so-called sea level equation in the modelling of glacial isostatic adjustement. The desired model was expected to fit into the class of paleocean unstructured z-coordinate models. We intended to start with the ocean-only model and replace it by the ocean-atmosphere coupled model. In the spirit of EMIC modelling, we have chosen the simplified quasi-geostrophic ocean model LSG (see Sec. 3.1) and a one-layer energy balance atmospheric model. However, plans have changed when our team took part in the ESA satellite mission Swarm.

The Swarm mission was designed to precisely measure the Earth's magnetic field. It is a successor of POGO, Magsat (1979-1980), Oersted (1999-2008), Champ (2000-2008) and Sac-C (2000-2008) satellite missions. Swarm has been launched in 2013 and it is still operational. As its name suggests, the measurements are conducted by the "swarm" of three satellites. The two satellites are orbiting side-by-side at the mean altitude of 470 km, the third satellite is orbiting in a different plane and it also flies higher, with a mean altitude of 520 km. The primary objectives of the Swarm mission has been to improve the models of main [Finlay et al., 2016, Olsen et al., 2016], litospheric [Kotsiaros, 2016], magnetospheric and ionospheric [Chulliat et al., 2016, Laundal et al., 2016, Aakjær et al., 2016] fields and also enrich our knowledge about the electrical conductivity of the Earth's mantle. One of the secondary objectives of the mission was to identify the ocean-induced magnetic field (OIMF). It is not a simple task since the OIMF represents a weak signal (several nT) compared to the signal generated by the Earth's core, litosphere, magnetosphere and ionosphere. Another complication is that the OIMF contains contributions from both tidally-driven and wind-driven circulations. The wind-driven field has longer periods and it may erroneously be attributed to the litospheric field.

The modelling of ocean-induced magnetic field obviously requires a coupled model: the model of ocean circulation and the electromagnetic (EM) induction solver. A suitable ocean circulation model falls into the category of OGCMs for the present-day rather than paleo circulation. The capability to simulate not only the wind-driven but also the tidally-driven circulation is not required but it is beneficial. The first and key objective of this thesis was to create such model. As already mentioned, we started with the LSG model but we have rebuilt it completely and created a new model which we call LSOMG. The second objective of this thesis was to use an EM solver to study the OIMF. The spectrum of EM induction solvers is not as broad as the spectrum of OGCMs. Nevertheless, it encompasses “heavy but complete” 3-D solvers equiped with the full physics as well as certain “light-weight but aproximate” 2-D solvers based on approximate equations. It was clear that approximate solvers are less accurate but studies that would quantify the discrepancies were missing. We thus cooperated with our collegues from GFZ, DIAS, Freie Universität Berlin and CIRES and studied how the wind-driven OIMF is affected by certain modelling choices. We presented our results in Šachl et al. [2019]. We also participated in the companion paper Velímský et al. [2018] which studied the tidally-driven rather than wind-driven OIMF. Finally, we inspected the toroidal magnetic field using the first-ever coupled run in which both ocean model and EM induction solver were 3-D. The results of these calculations are summarized in Velímský et al. [2019].

We did not manage to identify the wind-driven OIMF in the Swarm data. It turned out that the model of magnetospheric field is the weak spot. Our group used the up-to-date Swarm Level 2 magnetospheric field model but its performance was not satisfactory. We participated in the creation of a competing magnetospheric field model that is better suited our purposes. The model is explained and tested in Martinec et al. [2017].

The thesis is structured as follows. The purpose of the first part is to provide a theoretical background in ocean modelling. Chapter 1 explains the physical principles on which OGCMs are based. Chapter 2 introduces numerical methods and schemes commonly used in ocean modelling. The second part describes the LSOMG model. Chapter 3 discusses our motivations and requirements on the ocean model which we outlined here in more details. It also provides a comparison between LSG and LSOMG models to demonstrate the number of improvements done in the LSOMG model. Chapter 4 continues with the barotropic part of the model. LSOMG is a 3-D baroclinic model but it can be run in a simplified 2-D barotropic version; the barotropic part composes a stand-alone model. Chapter 5 is devoted to the baroclinic part of the LSOMG model. The third and last part of the thesis contains the results of our simulations. Chapters 6 and 7 present the ocean-only simulations calculated by the LSOMG model. The results from simplified numerical tests are discussed in Chapter 6. Sec. 6.1 is based on Šachl et al. [2020]. The full LSOMG capabilities are demostrated in the realistic simulations in Chapter 7. Chapter 8 summarizes our study published in Šachl et al. [2019] on the numerical modelling of wind-driven OIMF. Paper Velímský et al. [2019] on the toroidal part of OIMF is included separately since I was the second not the first author.

Part I

Introduction to ocean modelling

1. Physical principles in OGCMs

OGCMs solve a set of so-called primitive equations that govern the dynamics of the system, see Sec. 1.1. The primitive equations are local versions of global balance laws which express the conservation of some physical quantity such as mass or linear momentum. In principle, the primitive equations are capable to describe even the very fine-scale dynamical processes, but we are limited by the available computational power of computers. We distinguish three classes of OGCMs with respect to the spatial resolution: The eddy-parameterized models with the horizontal resolution coarser than approximately 1°, the eddy-permitting models with the resolution finer than 1° but coarser than 1/6° and eddy-resolving models with the resolution finer than 1/6° [Siedler et al., 2013]. As the nomenclature suggests, the resolution of eddy-parameterized models is too coarse to resolve mesoscale processes such as ocean eddies, the circulation in eddy-permitting models is more vigorous with the presence of mesoscale activity but the fully developed mesoscale turbulence is present only in eddy-resolving models. Nonetheless, even nowadays state-of-art eddy-resolving ocean models are unable to capture relevant processes on the smallest scales and it is questionable if it might be ever possible in the future. The processes that occur on spatial scales that are smaller than the model grid spacing are called subgrid scale (SGS) processes. Ocean modellers use external parameterizations to include the SGS processes into the OGCMs. We discuss the SGS processes and their parameterizations in the following text, see Secs. 1.2 and 1.3.

1.1 Governing equations of the OGCMs

1.1.1 Primitive equations

The primitive equations are derived within the framework of the continuum mechanics, see Martinec [2019]. It is common to apply certain approximations such as hydrostatic and Boussinesq approximations. The hydrostatic approximation assumes that the ocean is close to the hydrostatic balance which reduces the vertical component of the momentum equation to a balance between the vertical pressure gradient and the buoyancy force [Pedlosky, 1987].

The non-Boussinesq primitive equations under the hydrostatic approximation are the horizontal momentum equation, hydrostatic balance (vertical momentum equation), continuity equation and evolution equations for tracers and vertical-column mass budget,

$$\mathbf{u}_{,t} + \nabla \cdot (\mathbf{v} \otimes \mathbf{u}^{\rho}) + M\mathbf{e}_3 \times \mathbf{v}^{\rho} = -f\mathbf{e}_3 \times \mathbf{v} - \frac{\nabla_h p}{\rho_0} + \mathbf{F}^{(\mathbf{u})}, \tag{1.1}$$

$$p_{,z} = -\rho g, \tag{1.2}$$

$$\rho_{,t} + \rho_0 \nabla \cdot \mathbf{v} = 0, \tag{1.3}$$

$$(\rho C)_{,t} + \rho_0 \nabla \cdot (\mathbf{v}C) = -\rho_0 \nabla \cdot \mathbf{F} + \rho S^C, \tag{1.4}$$

$$(h\bar{\rho}^z)_{,t} = -\rho_0 \nabla_h \cdot \mathbf{U} + \rho_0 q_w, \tag{1.5}$$

where $\mathbf{v} = \mathbf{u} + w\mathbf{e}_3$ is the complete velocity vector, $\mathbf{u} = u\mathbf{e}_1 + v\mathbf{e}_2$ is the horizontal velocity, $\mathbf{e}_1$ and $\mathbf{e}_2$ are orthogonal unit vectors in the horizontal plane and $\mathbf{e}_3$ is the unit vector parallel to the local vertical direction, M is the advective metric frequency, f is the Coriolis parameter,

$$f = 2\Omega \sin\phi, \tag{1.6}$$

where Ω is the angular velocity of the Earth's rotation and ϕ is the latitude, p is pressure, g is the gravitational acceleration, ρ is the density of water, ρ_0 is the constant reference density, $\mathbf{v}^{\rho}$ is the velocity defined by the linear momentum density,

$$\rho\mathbf{v}^{\rho} = \rho_0\mathbf{v}, \tag{1.7}$$

C is the tracer (typically temperature or salinity), $\mathbf{U}$ is the vertically integrated horizontal velocity, $\mathbf{F}^{(\mathbf{u})}$ is the friction force, $\mathbf{F}$ is the turbulent tracer flux, respectively, S^C is the volume source of tracer C, h is the water-column height, q_w is the surface water flux, $a_{,t}$ and $a_{,z}$ denote partial derivatives of a with respect to time and vertical coordinate z, respectively, $\bar{a}^z$ is vertically averaged quantity a, ∇ is the three-dimensional (3-D) gradient operator and subscript $_h$ denotes horizontal component, i.e., ∇_h is the two-dimensional (2-D) horizontal gradient operator [Griffies, 2004].

The whole system is completed by the equation of state which characterizes the material properties of the continuum and it is derived from measurements, see Sec. 1.4.

The Boussinesq approximation means that the true density ρ is replaced by the reference density ρ_0 everywhere except for the gravitational force and equation of state [McWilliams, 2006]. The primitive equations under the Boussinesq and hydrostatic approximations are

$$\mathbf{u}_{,t} + \nabla\cdot(\mathbf{v}\otimes\mathbf{u}) + M\mathbf{e}_3\times\mathbf{v} = -f\mathbf{e}_3\times\mathbf{v} - \frac{\nabla_h p}{\rho_0} + \mathbf{F}^{(\mathbf{u})}, \tag{1.8}$$

$$p_{,z} = -\rho g, \tag{1.9}$$

$$\nabla\cdot\mathbf{v} = 0, \tag{1.10}$$

$$C_{,t} + \nabla\cdot(\mathbf{v}C) = -\nabla\cdot\mathbf{F} + S^C, \tag{1.11}$$

$$\eta_{,t} = -\nabla_h\cdot\mathbf{U} + q_w, \tag{1.12}$$

where η is the sea surface height (SSH) [Griffies, 2004]. Eq. (1.10) is sometimes called the incompressibility condition and we call Eq. (1.12) the SSH equation.

Ocean models have traditionally employed the hydrostatic and Boussinesq approximations and it is still the most common implementation of the primitive equations. Hence, we will focus on hydrostatic Boussinesq models hereinafter. Nevertheless, it is good to keep in mind that some models attempt to omit these assumptions, e.g., the Massachusetts Institute of Technology General Circulation Model (MITgcm) has a non-hydrostatic capability [Adcroft et al., 2014] and the Geophysical Fluid Dynamics Laboratory (GFDL) Modular Ocean Model (MOM) allows employing non-Boussinesq kinematics [Griffies, 2012].

1.1.2 Semi-discrete form of the primitive equations

Consider the boundary conditions at the ocean surface, $z = \eta$, and at the ocean bottom, $z = -H$, in the form,

$$w = \frac{d\eta}{dt} - q_w = \eta_{,t} + \mathbf{u} \cdot \nabla\eta - q_w \qquad \text{at } z = \eta, \tag{1.13}$$

$$w = \frac{d(-H)}{dt} = -\mathbf{u} \cdot \nabla H. \qquad \text{at } z = -H, \tag{1.14}$$

If we recall that the normal to the implicitly given surface $S(x, y, z) = 0$ is ∇S, we can rewrite boundary conditions (1.13) and (1.14) into the equivalent form,

$$\mathbf{N} \cdot \mathbf{v} = \eta_{,t} - q_w \qquad \text{at } z = \eta, \tag{1.15}$$

$$\mathbf{N} \cdot \mathbf{v} = 0 \qquad \text{at } z = -H, \tag{1.16}$$

where $\mathbf{N}$ is the normal to the ocean surface ($z - \eta = 0$) and ocean bottom ($z + H = 0$),

$$\mathbf{N} = -\nabla\eta + \mathbf{e}_3 \qquad \text{at } z = \eta, \tag{1.17}$$

$$\mathbf{N} = \nabla H + \mathbf{e}_3 \qquad \text{at } z = -H. \tag{1.18}$$

It is useful to transform the primitive equations into the semi discrete form before discretizing them in the numerical model. Griffies [2004] vertical integrates the momentum and tracer equations and applies the boundary conditions to derive the semi-discrete forms of the respective equations. The Leibniz integration rule is used in the derivation to exchange the time differentiation and the vertical integration,

$$\int\limits_{z_2}^{z_1} C_{,t} dz = \left(\int\limits_{z_2}^{z_1} C dz \right)_{,t} + C(z_1) z_{1,t} + C(z_2) z_{2,t}, \tag{1.19}$$

where C is a scalar, and to exchange the spatial divergence and the vertical integration,

$$\begin{aligned} \int\limits_{z_2}^{z_1} \nabla \cdot \mathbf{v} dz &= \nabla_h \cdot \int\limits_{z_2}^{z_1} \mathbf{u} dz - \mathbf{u}(z_1) \cdot \nabla_h z_1 + \mathbf{u}(z_2) \cdot \nabla_h z_2 + w(z_1) - w(z_2) \\ &= \nabla_h \cdot \int\limits_{z_2}^{z_1} \mathbf{u} dz + (\mathbf{v} \cdot \mathbf{N})(z_1) - (\mathbf{v} \cdot \mathbf{N})(z_2), \end{aligned} \tag{1.20}$$

where $\mathbf{v}$ is a 3-D vector, $\mathbf{u}$ is its projection onto the horizontal plane and w is its vertical component. The derivation is performed for a z-coordinate (see Sec. 2.3.1 for further details) model. The numbering of layers in the model is depicted in Fig. 5.3. The total number of layers in the model is k_{max}. We summarize the results in the following text. In order to shorten the notation, we write A_k instead of $A(z_k)$, where A is an arbitrary quantity.

1.1.3 Semi-discrete form of the primitive equations: Tracer budget for a grid cell

The tracer budget of the k-th interior grid cell is

$$\partial_t (hC)_k = -\nabla_h \cdot (h\mathbf{u}C + h\mathbf{F}^h)_k - (wC)_{k-1} + (wC)_k - (F^z_{k-1} - F^z_k) + (hS^C)_k, \tag{1.21}$$

where $\mathbf{F}^h$ and F^z are horizontal and vertical components of the turbulent tracer flux, respectively,

$$\mathbf{F} = (\mathbf{F}^h, F^z). \tag{1.22}$$

Surface grid cells need to be treated more carefully. First, it is due to the interaction with atmosphere or ice. Second, the volume of a surface grid cell changes in time due to the SSH variations in time. The tracer budget of the surface grid cell can be expressed using the surface boundary condition (1.15) in the form,

$$\partial_t (hC)_1 = -\nabla_h \cdot (h\mathbf{u}C + h\mathbf{F}^h)_1 + (wC)_1 + F_1^z - F_C + (hS^C)_1, \tag{1.23}$$

where F_C is the total tracer flux which crosses the ocean surface,

$$F_C = -\left[q_w C_0 - (\mathbf{F} \cdot \mathbf{N})_0\right]. \tag{1.24}$$

The ocean model can not provide sufficient information to evaluate this flux. It needs to be supported by a boundary layer model or parameterization. Boundary layer models give tracer flux Q_C crossing the ocean surface from other components of the climate system such as atmosphere, rivers and sea ice. The form of Q_C is given by

$$Q_C = -q_w C_w + Q_C^{turb}, \tag{1.25}$$

where C_w is the tracer concentration in the fresh water and Q_C^{turb} is the turbulent flux. If we assume a continuous tracer flux at the ocean surface,

$$F_C = Q_C, \tag{1.26}$$

we can rewrite Eq. (1.23) using information from the boundary layer model,

$$\partial_t (hC)_1 = -\nabla_h \cdot \left(h\mathbf{u}C + h\mathbf{F}^h\right)_1 + (wC + F^z)_1 + \left[q_w C_w - Q_C^{turb}\right] + (hS)_1. \tag{1.27}$$

Eq. (1.27) can be equivalently written as

$$\begin{aligned} h_1 \partial_t C_1 = &- \nabla_h \cdot \left(h\mathbf{u}C + h\mathbf{F}^h\right)_1 + (wC + F^z)_1 + q_w \left(C_w - C_1\right) - Q_C^{turb} \\ &+ (hS)_1 + C_1 \nabla_h \cdot \mathbf{U}, \end{aligned} \tag{1.28}$$

which is the form used if the time evolution of tracer concentration instead of thickness weighted tracer concentration.

Remark that the only information about the tracer concentration in fresh water C_w and turbulent flux Q_C^{turb} is needed to close the tracer budget of a surface grid cell. Let us focus on Q_C. The turbulent flux Q_C^{turb} in the Eq. (1.25) can be written in the form

$$Q_C^{turb} = V_{piston} \left(C_1 - C^{data}\right) + Q_C^{turb,0}, \tag{1.29}$$

where the first term is the restoring flux and the second term is the turbulent flux from data or another model. In Eq. 1.29, C^{data} is the data prescribed tracer concentration and V_{piston} is the so-called piston velocity,

$$V_{piston} = \gamma_C h_1, \tag{1.30}$$

where γ_C is the inverse restoring time. The larger piston velocity, the stronger restoring of tracer concentration to the data prescribed tracer concentration. Indeed, if $C_1 > C^{data}$, then $V_{piston}(C_1 - C^{data})$ is positive and it acts as a tracer flux out of the model which damps larger values of ocean surface tracer towards C^{data}. Similarly for $C_1 < C^{data}$.

Consider now two special cases of potential temperature and salinity. Temperature is a neutral tracer,

$$C_w \approx C_1. \tag{1.31}$$

For neutral tracers, the explicit contribution of fresh water influx disappears from Eq. (1.28), although it is still present implicitly via $\nabla_h \cdot \mathbf{U}$. Salinity does not generally cross the ocean surface (with the exception of ocean-ice interactions), $F_C = Q_C = 0$, which causes the salt content in the whole ocean to remain reasonably constant. One can thus prescribe a fresh water flux to eliminate the salt flux,

$$q_w = V_{piston}\left(1 - \frac{S^{data}}{S_1}\right), \tag{1.32}$$

where we set $Q_C^{turb,0} = 0$.

1.1.4 Semi-discrete form of the primitive equations: Momentum budget for a grid cell

The momentum budget of the k-th interior grid cell is

$$\begin{aligned}(\partial_t + f\mathbf{e}_3\times)(h\mathbf{u})_k = &- (hM\mathbf{e}_3 \times \mathbf{u})_k - \nabla_h \cdot (h\mathbf{u}\otimes\mathbf{u})_k - h_k\frac{\nabla_h p_k}{\rho_0} + \left(h\mathbf{F}_H^{(\mathbf{u})}\right)_k \\ &- [(w\mathbf{u})_{k-1} - (w\mathbf{u})_k] + [(A_V\mathbf{u}_{,z})_{k-1} - (A_V\mathbf{u}_{,z})_k],\end{aligned} \tag{1.33}$$

where the friction force $\mathbf{F}^{(\mathbf{u})}$ has been split into horizontal $\mathbf{F}_H^{(\mathbf{u})}$ and vertical $\mathbf{F}_V^{(\mathbf{u})}$ friction,

$$\mathbf{F}^{(\mathbf{u})} = \mathbf{F}_H^{(\mathbf{u})} + \mathbf{F}_V^{(\mathbf{u})}. \tag{1.34}$$

The vertical friction in (1.33) is considered in the form

$$\mathbf{F}_V^{(\mathbf{u})} = (A_V\mathbf{u}_{,z})_{,z}, \tag{1.35}$$

where A_V is the non-negative vertical viscosity.

The momentum budget of the surface grid cell can be expressed using the surface boundary condition (1.15) in the form,

$$\begin{aligned}(\partial_t + f\mathbf{e}_3\times)(h\mathbf{u})_1 = &- (hM\mathbf{e}_3 \times \mathbf{u})_1 - \nabla_h \cdot (h\mathbf{u}\otimes\mathbf{u})_1 - h_1\frac{\nabla_h p_1}{\rho_0} + \left(h\mathbf{F}_H^{(\mathbf{u})}\right)_1 \\ &+ (w\mathbf{u})_1 - (A_V\mathbf{u}_{,z})_1 - \mathbf{F}_0^z,\end{aligned} \tag{1.36}$$

where $\mathbf{F}_0^z$ is the vertical flux of horizontal momentum at the sea surface,

$$\mathbf{F}_0^z = -\left[q_w\mathbf{u}_0 + (A_V\mathbf{u}_{,z})_0\right]. \tag{1.37}$$

The negative sign is used in order to have a positive flux (outflow from the ocean), if $q_w < 0$ $(w > 0)$, or if horizontal velocity decreases upward. The first term in

Eq. (1.37) is the vertical advective flux of horizontal momentum and the second term is the vertical diffusive flux of horizontal momentum that parameterizes subgrid scale processes.

Notice that the momentum budget of the surface grid cell looks formally the same as the momentum budget of the interior cell in which the vertical advection velocity at the sea surface is equal to the negative fresh-water flux, $w_0 = -q_w$. The thickness h_1 of the surface grid cell is, of course, not constant because it depends on the SSH.

Similar to the tracer budget, neither horizontal velocity $\mathbf{u}_0$ nor the vertical shear $(\mathbf{u}_{,z})_0$ at the sea surface can be determined from the ocean model. The solution of the problem is to employ a boundary layer model that is capable of providing the total momentum flux $\mathbf{Q}_{mom}$ across the ocean surface and assume that the total flux is continuous across the ocean surface,

$$\mathbf{Q}_{mom} = -\mathbf{F}_0^z. \tag{1.38}$$

The momentum flux $\mathbf{Q}_{mom}$ is usually written as

$$\mathbf{Q}_{mom} = q_w \mathbf{u}_w + \frac{\boldsymbol{\tau}_w}{\rho_0}, \tag{1.39}$$

where $\mathbf{u}_w$ is the fresh water velocity and $\boldsymbol{\tau}_w$ is the surface wind stress, see Sec. 5.14.4. The flux $\mathbf{F}_0^z$ in Eq. (1.36) can now be expressed using Eqs. (1.38) and (1.39),

$$\begin{aligned}(\partial_t + f\mathbf{e}_3\times)(h\mathbf{u})_1 = &- (hM\mathbf{e}_3 \times \mathbf{u})_1 - \nabla_h \cdot (h\mathbf{u} \otimes \mathbf{u})_1 - h_1 \frac{\nabla_h p_1}{\rho_0} + \left(h\mathbf{F}_H^{(\mathbf{u})}\right)_1 \\ &+ (w\mathbf{u})_1 - (A_V \mathbf{u}_{,z})_1 + \left[q_w \mathbf{u}_w + \frac{\boldsymbol{\tau}_w}{\rho_0}\right].\end{aligned} \tag{1.40}$$

We may further apply the assumption that the fresh water velocity is equal to the horizontal velocity $\mathbf{u}_1$ which is already computed by the ocean model,

$$\mathbf{u}_w = \mathbf{u}_1. \tag{1.41}$$

An alternative approach is to step forward the velocity $\mathbf{u}$ instead of the thickness weighted velocity $h\mathbf{u}$,

$$\begin{aligned}h_1(\partial_t + f\mathbf{e}_3\times)\mathbf{u}_1 = &- (hM\mathbf{e}_3 \times \mathbf{u})_1 - \nabla_h \cdot (h\mathbf{u} \otimes \mathbf{u})_1 - h_1 \frac{\nabla_h p_1}{\rho_0} + \left(h\mathbf{F}_H^{(\mathbf{u})}\right)_1 \\ &+ (w\mathbf{u})_1 - (A_V \mathbf{u}_{,z})_1 + \left[-\mathbf{u}_1 \eta_{,t} + q_w \mathbf{u}_w + \frac{\boldsymbol{\tau}_w}{\rho_0}\right].\end{aligned} \tag{1.42}$$

The SSH equation (1.12) is further used to express $\eta_{,t}$,

$$\begin{aligned}h_1(\partial_t + f\mathbf{e}_3\times)\mathbf{u}_1 = &- (hM\mathbf{e}_3 \times \mathbf{u})_1 - \nabla_h \cdot (h\mathbf{u} \otimes \mathbf{u})_1 - h_1 \frac{\nabla_h p_1}{\rho_0} + \left(h\mathbf{F}_H^{(\mathbf{u})}\right)_1 \\ &+ (w\mathbf{u})_1 - (A_V \mathbf{u}_{,z})_1 + \left[\mathbf{u}_1 \nabla_h \cdot \mathbf{U} + q_w(\mathbf{u}_w - \mathbf{u}_1) + \frac{\boldsymbol{\tau}_w}{\rho_0}\right].\end{aligned} \tag{1.43}$$

Notice that under the assumption (1.41), the term $q_w(\mathbf{u}_w - \mathbf{u}_1)$ is equal to zero and the surface water flux is then not explicitly present in Eq. (1.43). However, the surface water flux still influences the horizontal velocity in the surface grid cell by the change of term $\nabla_h \cdot \mathbf{U}$ in Eq. (1.43) through the SSH equation (1.12).

Finally, consider the bottom grid cell, $k = k_{max}$. The derivation is similar to the derivation for the surface grid cell, however, the thickness is usually assumed to be constant and there is no flux of fresh water into the ocean across the bottom. Hence, Eqs. (1.37) and (1.39) reduce for the bottom grid cell to

$$\mathbf{F}^z_{k_{max}} = -(A_V \mathbf{u}_{,z})_{k_{max}}, \tag{1.44}$$

$$\mathbf{Q}_{mom} = \boldsymbol{\tau}_b, \tag{1.45}$$

where $\boldsymbol{\tau}_b$ is the bottom friction, see Sec. 4.3.

1.2 Friction in ocean models

According to [Griffies and Hallberg, 2000], there are two central roles of friction:

- Friction in ocean models parameterizes the effect of frictional dissipation of SGS processes in the presence of turbulence and hydrodynamic instabilities on the scales which are resolved by the model.
- Numerical closure to suppress numerical instabilities.

As a consequence of the second point, the frictional dissipation in ocean models is much larger than in real oceans. The friction in ocean models is tuned and it should be kept as low as possible. The need to tune the friction can be one of the weak points in the ocean-model construction. It is known that certain phenomena such as the Gulf Stream separation point [Chassignet and Garraffo, 2001] or the equatorial undercurrent strength [Large et al., 2001] are affected by the friction. Generally speaking, there is no purely physically motivated closure for linear momentum in ocean models [Griffies and Hallberg, 2000]. A straightforward choice is to apply a linear momentum closure in the form of a diffusion of linear momentum. However, the SGS transport of linear momentum differ from the tracer transport because of the pressure effects [Griffies, 2004]. Hence, the frictional dissipation in the form of diffusion of linear momentum is questionable.

1.2.1 Form of the friction force

The friction force can be expressed as a divergence of a tensor,

$$\mathbf{F}^{(\mathbf{u})} = \nabla \cdot \boldsymbol{\sigma}, \tag{1.46}$$

where $\boldsymbol{\sigma}$ is a deviatoric stress tensor,

$$\sigma_{11} + \sigma_{22} + \sigma_{33} = 0. \tag{1.47}$$

We consider a Newtonian fluid, for which a linear relation between stress and strain is assumed, i.e., the stress tensor is assumed to follow the generalized Hooke's Law,

$$\frac{\boldsymbol{\sigma}}{\rho} = \mathbf{A} : \mathbf{e}, \tag{1.48}$$

where **A** is the viscosity tensor and **e** is the strain-rate tensor,

$$\mathbf{e} = \frac{1}{2}\left[\nabla\mathbf{v} + (\nabla\mathbf{v})^T\right]. \tag{1.49}$$

We further assume that the friction does not change the angular momentum. It also means that the friction needs to vanish for the solid body rotation and under uniform translations on a plane. It can be proved that the stress tensor must be symmetric if the angular momentum is conserved [Martinec, 2019].

Finally, we assume that the ocean is in a hydrostatic balance or very close to it. In this case, σ_{33} should be negligible [Williams, 1972] and thus we set it equal to zero, $\sigma_{33} = 0$.

If we consider the dissipative feature of friction, it is straightforward to choose the friction force in the form of a Laplacian operator acting on velocity. Unfortunately, the Laplacian friction suffers from certain deficiencies.

First, it has not been derived from the first principles.

Second, the above mentioned assumptions are not completely fulfilled. Wajsowicz [1993] derived the correct form of the friction force under the constraints given above. Assume for simplicity a fluid transversely isotropic with respect to the vertical coordinate axis with constant horizontal and vertical viscosities, A_H and A_V, respectively. The zonal component of the friction force in the spherical coordinates is given by

$$F_\lambda^{(\mathbf{u})} = A_H \Delta_h u + A_V \frac{\partial^2 u}{\partial z^2} + A_H \left(\frac{1 - \tan^2\phi}{a^2}\right) u - A_H \frac{2\sin\phi}{a^2\cos^2\phi}\frac{\partial v}{\partial\lambda}, \tag{1.50}$$

where a is the Earth's radius, λ is the longitude and ϕ is the latitude. The last two terms in Eq. (1.50) are missing if the standard Laplacian operator is considered. Another example is a transversely isotropic fluid in the Cartesian geometry with spatially varying viscosities. The x component of the friction force is given by

$$F_x^{(\mathbf{u})} = \frac{\partial}{\partial x}\left(A_H\frac{\partial u}{\partial x}\right) + \frac{\partial}{\partial y}\left(A_H\frac{\partial u}{\partial y}\right) + \frac{\partial}{\partial z}\left(A_V\frac{\partial u}{\partial z}\right) + \frac{\partial A_H}{\partial y}\frac{\partial v}{\partial x} - \frac{\partial A_H}{\partial x}\frac{\partial v}{\partial y}. \tag{1.51}$$

The last two terms in Eq. (1.51) are needed, otherwise a solid body rotation generates a viscous stress [Wajsowicz, 1993].

Third, as already mentioned at the beginning of this section, it is desirable to have the friction force that removes a minimal amount of kinetic energy from the scales of physical interest. Nonetheless, Griffies and Hallberg [2000] mentioned that the Laplacian operator removes both kinetic energy and enstrophy over a broad range of spatial scales. Consequently, for a high-resolution model, they suggested to use the biharmonic operator which has better scale-selective properties.

1.2.2 Viscosity

The viscosity tensor can not be arbitrary, it has to meet three constraints:

- The strain tensor is symmetric, which implies that the viscosity tensor needs to have the symmetry,

$$A_{mnpq} = A_{mnqp}, \tag{1.52}$$

since

$$0 = (\mathbf{A} : \mathbf{e})_{mn} - (\mathbf{A} : \mathbf{e}^\intercal)_{mn} = A_{mnpq}e_{pq} - A_{mnpq}e_{qp} = (A_{mnpq} - A_{mnqp})e_{pq} \tag{1.53}$$

must hold for arbitrarily chosen strain tensor.

- The symmetry of the stress tensor implies that

  $$A_{mnpq} = A_{nmpq}, \tag{1.54}$$

  which can be proved in a similar way as the previous symmetry relation (1.52).

- The last constraint comes from the horizontal kinetic energy budget. If we require the friction to act in a dissipative manner at each point of the fluid, the strain tensor must have the property,

  $$A_{mnpq} = A_{pqmn}. \tag{1.55}$$

The simplest approach is to use a constant viscosity. However, Griffies et al. [2000] pointed out a problem if the spherical coordinates are used. A viscosity which is appropriate for low latitudes may become too large for high latitudes since meridians converge and the zonal grid spacing decreases. To overcome this problem, we may taper the viscosity to smaller values at higher latitudes [Gent et al., 1998]. Similarly, the viscosity can be prescribed to vary with the grid spacing d. A quadratic dependence d^2 can be used for the Laplacian friction and a cubic dependence d^3 can be used for the biharmonic friction.

Smagorinsky [1963, 1993] suggested to set the viscosity values according to the velocity resolved in the model. More specifically, the horizontal Smagorinsky viscosity is a function of the horizontal tension D_T and the horizontal shearing strain D_S,

$$D_T = e_{11} - e_{22}, \tag{1.56}$$

$$D_S = 2e_{12}, \tag{1.57}$$

where e_{ij} are the strain rate components.

Leith [1968] and Leith [1996] proposed an alternative method to the approach of Smagorinsky. It is based on the theory of the 2-D turbulence and the enstrophy flux. The approach should theoretically outperform the previous one since Smagorinsky assumed a 3-D isotropic turbulence whereas the ocean is closer to the quasi 2-D geostrophic turbulence. However, the results of tests in which both viscosities were employed showed only little difference. Moreover, the Leith viscosity is less convenient to calculate. As a consequence, this parameterization is not frequently used in ocean modelling [Griffies et al., 2000].

It is common to assume that the ocean is transversely isotropic with respect to the vertical axis. However, other possibilities have also been inspected. For example, Large et al. [2001] suggested to use two horizontal viscosities instead of a single one. This concept has improved their simulations especially currents in the equatorial region.

1.3 Neutral physics

The tracer transport in the ocean interior occurs predominantly along neutral directions, which are the directions tangent to the local potential density surface. As a consequence, the mass of fluid living between two isopycnals remains nearly constant. The processes in the neutral direction are often called epineutral whereas the processes that cross the neutral directions are called dianeutral. The diffusion of tracers in the neutral direction and their stirring by mesoscale eddies are called neutral physics.

1.3.1 SGS tracer transport tensor

The turbulent tracer fluxes $\mathbf{F}$ in Eq. (1.11) may be written in the form

$$\mathbf{F} = -\mathbf{J} \cdot \nabla C, \tag{1.58}$$

where $\mathbf{J}$ is the second-order tracer transport tensor, which is generally a function of the fluid flow and tracer field. Eq. (1.58) fulfills the compatibility condition that $\nabla \cdot \mathbf{F} = 0$ if the tracer field is constant everywhere. Each second-order tensor can be decomposed to its symmetric part $\mathbf{K}$ and antisymmetric part $\mathbf{R}$,

$$\mathbf{J} = \mathbf{K} + \mathbf{R}. \tag{1.59}$$

If we combine Eq. (1.58) and (1.59) and insert them into Eq. (1.11), we obtain

$$C_{,t} + \nabla \cdot (\mathbf{v}C) = \nabla \cdot \left[(\mathbf{K} + \mathbf{R}) \cdot \nabla C\right], \tag{1.60}$$

where the source term S^C has been dropped out.

We further define the global tracer variance ν,

$$\nu = \int\limits_V C^2 \widetilde{\rho} dV - \left[\int\limits_V C \widetilde{\rho} dV\right]^2, \tag{1.61}$$

where $\widetilde{\rho}$ is the normalized density,

$$\widetilde{\rho} = \frac{\rho}{\int\limits_V \rho dV} = \frac{\rho}{m}. \tag{1.62}$$

If we assume a global ocean with the constant fluid mass m and constant tracer mass, the time evolution of tracer variance is governed by the first term in Eq. (1.61). If we further neglect the effect of the boundary terms, the time tendency of tracer variance is expressed by

$$m\nu_{,t} = 2\rho_0 \int \mathbf{F} \cdot \nabla C dV. \tag{1.63}$$

The term $\mathbf{F} \cdot \nabla C$ is rewritten using Eqs. (1.58) and (1.59) to yield,

$$\mathbf{F} \cdot \nabla C = -\nabla C \cdot (\mathbf{R} + \mathbf{K}) \cdot \nabla C = -\nabla C \cdot \mathbf{K} \cdot \nabla C, \tag{1.64}$$

since $\mathbf{R}$ is an asymmetric tensor. We require the tracer variance ν to decrease in time which requires tensor $\mathbf{K}$ to be positive semidefinite,

$$\nabla C \cdot \mathbf{K} \cdot \nabla C \geq 0. \tag{1.65}$$

Note that the tracer flux $-\mathbf{R}\cdot\nabla C$ is directed perpendicular to the tracer gradient since $(-\mathbf{R}\cdot\nabla C)\cdot\nabla C = -\nabla C\cdot\mathbf{R}\cdot\nabla C = 0$. The fluxes with this orientation are called skew fluxes. They are related to the advection; they are stirring tracers without mixing.

The local tracer extremum satisfies $\nabla C = \mathbf{0}$. If we insert this condition into Eq. (1.60), we get the evolution equation

$$C_{,t} = \mathbf{K} : \nabla(\nabla C), \tag{1.66}$$

where : stands for a double dot product of tensors. It means that tracer extrema are unaffected by advection and skew diffusion but they are blurred and smoothed by diffusion.

1.3.2 Neutral diffusion

Consider three orthogonal unit vectors $\mathbf{e}_1$, $\mathbf{e}_2$, $\mathbf{e}_3$, where $\mathbf{e}_1$, $\mathbf{e}_2$ are horizontal vectors and $\mathbf{e}_3$ is the pointing in the vertical direction and it is positive upwards, see also Sec. 5.1. Vectors $\mathbf{e}_1$, $\mathbf{e}_2$, $\mathbf{e}_3$ are base vectors of a coordinate frame which we call the z frame. In order to mathematically express the neutral diffusion of tracers, it is useful to introduce another coordinate frame, the so-called neutral frame. It is given by another triplet of orthogonal unit vectors, $\overline{\mathbf{e}}_1$, $\overline{\mathbf{e}}_2$, $\overline{\mathbf{e}}_3$,

$$\overline{\mathbf{e}}_1 = \frac{\mathbf{e}_3\times\nabla\rho}{|\mathbf{e}_3\times\nabla\rho|}, \tag{1.67}$$

$$\overline{\mathbf{e}}_2 = \overline{\mathbf{e}}_3\times\overline{\mathbf{e}}_1, \tag{1.68}$$

$$\overline{\mathbf{e}}_3 = \frac{\nabla\rho}{|\nabla\rho|}, \tag{1.69}$$

where the density gradient $\nabla\rho$ is computed with pressure held fixed (locally referenced),

$$\nabla\rho = \nabla\theta\left(\frac{\partial\rho}{\partial\theta}\right)_{S,p} + \nabla S\left(\frac{\partial\rho}{\partial S}\right)_{\theta,p} = \rho(-\alpha_T\nabla\theta + \beta_S\nabla S), \tag{1.70}$$

where α_T and β_S are the thermal expansion and saline contraction coefficients, respectively,

$$\alpha_T = -\frac{1}{\rho}\left(\frac{\partial\rho}{\partial\theta}\right)_{S,p}, \qquad \beta_S = \frac{1}{\rho}\left(\frac{\partial\rho}{\partial S}\right)_{\theta,p}. \tag{1.71}$$

Since the z frame and the neutral frame are orthogonal, the transformation between them is provided by the orthogonal rotation matrix $\mathbf{\Lambda}$ where $\Lambda_{mn} = \mathbf{e}_m\cdot\overline{\mathbf{e}}_n$. It can be proved that the transformation matrix is equal to

$$\mathbf{\Lambda} = \begin{pmatrix} \frac{s_y}{s} & \frac{s_x}{s\sqrt{1+s^2}} & \frac{-s_x}{\sqrt{1+s^2}} \\ -\frac{s_x}{s} & \frac{s_y}{s\sqrt{1+s^2}} & \frac{-s_y}{\sqrt{1+s^2}} \\ 0 & \frac{s}{\sqrt{1+s^2}} & \frac{1}{\sqrt{1+s^2},} \end{pmatrix}, \tag{1.72}$$

where s is the magnitude of the vector $\mathbf{s}$ which is the neutral direction slope with respect to the horizontal,

$$\mathbf{s} = s_x\mathbf{e}_1 + s_y\mathbf{e}_2 = \nabla_\rho z = -\frac{\nabla_h\rho}{\rho_{,z}} = \frac{-\alpha_T\nabla\theta + \beta_S\nabla S}{-\alpha_T\theta_{,z} + \beta_S\nabla S_{,z}}, \tag{1.73}$$

where ∇_ρ is the horizontal gradient taken along the neutral direction. It can be shown that

$$\nabla_\rho = \nabla_h + \mathbf{s}\partial_z. \tag{1.74}$$

Redi [1982] suggested to write the diffusion tensor $\overline{\mathbf{K}}$ in the neutral frame in a diagonal form,

$$\overline{\mathbf{K}} = \begin{pmatrix} K_H & 0 & 0 \\ 0 & K_H & 0 \\ 0 & 0 & K_V \end{pmatrix}, \tag{1.75}$$

where K_H and K_V are non-negative epineutral and dianeutral diffusivities, respectively. Both diffusivities can be space and time dependent but the epineutral diffusivity K_H is generally much larger than the dianeutral diffusivity K_V,

$$\epsilon = \frac{K_V}{K_H} \approx 10^{-8}. \tag{1.76}$$

The diffusion tensor $\mathbf{K}$ in the z frame is called the Redi diffusion tensor and it is obtained by transforming the diffusion tensor $\overline{\mathbf{K}}$ from the neutral frame to the z frame,

$$\mathbf{K} = \mathbf{\Lambda}\overline{\mathbf{K}}\mathbf{\Lambda}^T = \frac{K_H}{(1+s^2)} \begin{pmatrix} 1 + s_y^2 + \epsilon s_x^2 & (\epsilon - 1)s_x s_y & (1-\epsilon)s_x \\ (\epsilon - 1)s_x s_y & 1 + s_x^2 + \epsilon s_y^2 & (1-\epsilon)s_y \\ (1-\epsilon)s_x & (1-\epsilon)s_y & \epsilon + s^2 \end{pmatrix}, \tag{1.77}$$

where superscript T denotes the transposition. Gent and McWilliams [1990] derived a small slope approximation of the Redi tensor,

$$\mathbf{K}_{ssa} = K_H \begin{pmatrix} 1 & 0 & s_x \\ 0 & 1 & s_y \\ s_x & s_y & \epsilon + s^2 \end{pmatrix}. \tag{1.78}$$

Note that the term s^2 is retained in the (3,3) element. It is small under the small slope approximation but it is not negligible with respect to ϵ.

The corresponding small slope diffusive flux in the z frame is

$$\begin{aligned} \mathbf{F}_d &= -\mathbf{K}_{ssa} \cdot \nabla C = -\mathbf{K}_{ssa} \cdot (\nabla_h C + \mathbf{e}_3 C_{,z}) = -\mathbf{K}_{ssa} \cdot (\nabla_\rho C - \mathbf{s}C_{,z} + \mathbf{e}_3 C_{,z}) \\ &= -K_H \nabla_\rho C + (-K_H \mathbf{s} \cdot \nabla_\rho C - K_V C_{,z})\, \mathbf{e}_3, \end{aligned} \tag{1.79}$$

where we used Eq. (1.74) in the third equality. It is possible to prove that the errors in the neutral and dianeutral fluxes due to the use of the small slope approximation are of the order of $K_H s^2$ and $K_V s^2$, respectively. Remark that the dianeutral diffusive term under the small slope approximation reduces to a vertical downgradient diffusive flux.

Note that if we used the form of the diffusion tensor given by Eq. (1.75) also in the z-frame instead of the small slope approximation (1.78), we would introduce first- and second-order errors in slope in the off-diagonal and diagonal terms, respectively. The most significant, however, would be the error in the (3,3) element since it may seriously change the dianeutral diffusion.

1.3.3 Stirring by mesoscale eddies

Tracer transport in the ocean is a challenging process to be modelled. Large-scale ocean currents and mesoscale eddies are the dominant mechanisms for the tracer transport in the ocean. In the ocean interior, the tracers are mostly stirred by mesoscale eddies and tracer gradients are dissipated by small scale mixing processes. The eddy-parameterized ocean models do not resolve mesoscale eddies and thus they need to parameterize the effect of stirring. However, the so-called neutral physics schemes (see below) are important even for the eddy-permitting ocean models and it is generally recommended to use them since, as already mentioned, there still remain unresolved scales.

Gent and McWilliams [1990] and Gent et al. [1995] proposed the SGS stirring of tracers based on the following assumptions:

- mesoscale eddies locally provide an adiabatic sink of available potential energy
- mesoscale eddies act on all tracers in the same fashion

They suggest to use an eddy-induced velocity $\mathbf{v}^*$ which is divergence free,

$$\nabla \cdot \mathbf{v}^* = 0, \tag{1.80}$$

and it is written in the form,

$$\mathbf{v}^* = -\partial_z(\kappa \mathbf{s}) + \mathbf{e}_3 \nabla_h \cdot (\kappa \mathbf{s}), \tag{1.81}$$

where κ is a positive diffusivity. The velocity $\mathbf{v}^*$ is simply added to the velocity $\mathbf{v}$ resolved in the model when advecting tracers.

Griffies [1998] presented an alternative form by exploiting the relation between the advective and skew fluxes. The velocity $\mathbf{v}^*$ is divergence free, hence it can be expressed by a vector stream function $\boldsymbol{\gamma}$,

$$\mathbf{v}^* = \nabla \times \boldsymbol{\gamma}. \tag{1.82}$$

The stream function is not unique because a gradient of an arbitrary scalar function μ can be added to $\boldsymbol{\gamma}$,

$$\overline{\boldsymbol{\gamma}} = \boldsymbol{\gamma} + \nabla \mu, \tag{1.83}$$

without changing the value of $\mathbf{v}^*$ because

$$\nabla \times \nabla \mu = 0. \tag{1.84}$$

This property is called a gauge freedom and the function μ is called a gauge function. Consider the advective flux $\mathbf{F}_e^a$ due to the eddy-induced velocity,

$$\mathbf{F}_e^a = \mathbf{v}^* C, \tag{1.85}$$

and the skew flux $\mathbf{F}_e^s$,

$$\mathbf{F}_e^s = -\nabla C \times \boldsymbol{\gamma} = -\mathbf{R} \cdot \nabla C, \tag{1.86}$$

where $\mathbf{R}$ is the second-order tensor,

$$\mathbf{R} = \begin{pmatrix} 0 & \gamma_3 & -\gamma_2 \\ -\gamma_3 & 0 & \gamma_1 \\ \gamma_2 & -\gamma_1 & 0 \end{pmatrix}. \tag{1.87}$$

The dynamical effects of the advective flux $\mathbf{F}_e^a$ and the skew flux $\mathbf{F}_e^s$ on the tracer evolution are identical since

$$\begin{aligned} \nabla \cdot \mathbf{F}_e^s &= -\nabla \cdot (\nabla C \times \boldsymbol{\gamma}) = \nabla \cdot \Big[(\nabla \times \boldsymbol{\gamma})C - \nabla \times (C\boldsymbol{\gamma})\Big] \\ &= \nabla \cdot \Big[(\nabla \times \boldsymbol{\gamma})C\Big] = \nabla \cdot (\mathbf{v}^* C) = \nabla \cdot \mathbf{F}_e^a, \end{aligned} \tag{1.88}$$

where we used Eq. (1.82) and the second and third equalities are due to vector identities. Consequently, if we knew the generating stream function $\boldsymbol{\gamma}$, we could use the skew-flux form instead of the advective-flux form. Griffies [1998] showed that the stream function associated with the velocity $\mathbf{v}^*$ given by Eq. (1.81) can be written as

$$\boldsymbol{\gamma}_{gm} = \mathbf{e}_3 \times (\kappa \mathbf{s}), \tag{1.89}$$

which implies

$$\mathbf{R}_{gm} = \begin{pmatrix} 0 & 0 & -\kappa s_x \\ 0 & 0 & -\kappa s_y \\ \kappa s_x & \kappa s_y & 0 \end{pmatrix}. \tag{1.90}$$

Thus, for an arbitrary tracer, the skew flux which is dynamically equivalent to the advective flux induced by $\mathbf{v}^*$ is equal to

$$\mathbf{F}_e^s = \kappa \Big[\mathbf{s} C_{,z} - \mathbf{e}_3 (\mathbf{s} \cdot \nabla_h C)\Big]. \tag{1.91}$$

If we combine the stirring by mesoscale eddies and neutral diffusive mixing, we end up with the tracer flux,

$$\begin{aligned} \mathbf{F} = \mathbf{F}_d + \mathbf{F}_e^s &= \mathbf{s}\kappa C_{,z} - K_H(\nabla_h C + \mathbf{s} C_{,z}) \\ &\quad - \mathbf{e}_3 \Big[K_H \left(\mathbf{s} \cdot \nabla_h C + s^2 C_{,z}\right) + K_V C_{,z} + \kappa \mathbf{s} \cdot \nabla_h C\Big] \end{aligned} \tag{1.92}$$

If the diffusivities associated with the stirring and neutral diffusion are equal, $K_H = \kappa$, the tracer flux simplifies,

$$\mathbf{F} = -K_H \nabla_h C - \mathbf{e}_3 \Big[K_H (2\mathbf{s} \cdot \nabla_h C + s^2 C_{,z}) + K_V C_{,z}\Big]. \tag{1.93}$$

According to Griffies [2004], Eq. (1.93) provides two key benefits:

- The computation cost of the combination of these two schemes is less than the cost of either one alone due to the simplicity of the horizontal flux. In fact, the tracer flux (1.93) and the standard downgradient tracer flux given by tensor (1.75) in the z frame differ only in the vertical component. The neutral diffusion and stirring by eddies added the term $K_H(2\mathbf{s} \cdot \nabla_h C + s^2 C_{,z})$ to the vertical component.

- The discretized skew flux can be less prone to discretization errors relative to the advective flux.

1.4 Density in ocean models

1.4.1 State equation of sea water

The first attempts to derive a reliable state equation of sea water date back to the beginning of the 20th century. The first equation of state (EOS) was built on the efforts of Knudsen [1901], density measurements of Forch et al. [1902] and high pressure measurements of Ekman [1908] for the deep waters. It is known as the Knudsen formula. It became a standard and it has been used for many years. Nevertheless, certain problems of this EOS has been discovered over time. Thompson and Wirth [1931] reported 2×10^{-2} kg m^{-3} discrepancies between the Knudsen formula and their own measurements. Later on, Cox et al. [1970], Kremling [1972] and Millero et al. [1976] pointed out that systematic differences are introduced when using the Knudsen formula.

Consequently, it became clear that a more suitable representation of the sea water properties is needed. The work of Millero and Poisson [1981a], Millero and Poisson [1981b], Millero et al. [1980] and Millero et al. [1981] has finally led to the formulation of the new International Equation of State of Seawater (EOS-80) approved by the Joint Panel for Oceanographic Tables and Standards in 1980. The density ρ is computed as a function of in-situ temperature T, salinity S and pressure p,

$$\rho(S,T,p) = \frac{\rho(S,T,0)}{1 - \frac{p}{K(S,T,p)}} \tag{1.94}$$

where $\rho(S,T,0)$ is given by the one atmosphere International Equation of State 1980 and $K(S,T,p)$ is the secant bulk modulus. The expressions for $\rho(S,T,0)$ and $K(S,T,p)$ can be found in the previously mentioned papers and they are summarized in UNESCO [1981]. The overall standard error of EOS-80 estimated by Millero et al. [1980] and Fofonoff [1985] is 9×10^{-3} kg m^3, the error reduces to 5×10^{-3} kg m^3 in the oceanographic ranges of temperature, salinity and pressure.

From the ocean-modeling point of view, there are at least two problems with EOS-80. First, the equation may become computationally expensive. Wright [1997] reported that the evaluation of the full EOS-80 consumes approximately a half of the computation time in the low-order climate model developed by Wright and Stocker [1991]. Second, EOS-80 is formulated in terms of the in-situ temperature T which is in contrast to the representation in ocean models where the potential temperature θ is typically used. Hence, it would be useful to have the EOS formulated directly in the potential temperature.

Bryan and Cox [1972] proposed an algorithm to improve the EOS computational requirements. The algorithm was originally designed for the Knudsen formula, however, it can also be applied to EOS-80. The idea is to replace the general formula at each depth level in the model by an approximate formula which is less computationally demanding. The depth levels are supposed to be determined in advance. The density in the k-th depth level is then computed as

$$\begin{aligned}\rho_k(S,T) = \rho_{0k} + \Big[& x_{1k}\Delta T + x_{2k}\Delta S + x_{3k}(\Delta T)^2 \\ & + x_{4k}(\Delta S)^2 + x_{5k}(\Delta T \Delta S) + x_{6k}(\Delta T)^3 \\ & + x_{7k}(\Delta S)^2 \Delta T + x_{8k}(\Delta T)^2 \Delta S + x_{9k}(\Delta S)^3 \Big] \times 10^{-3},\end{aligned} \tag{1.95}$$

where $x_{1k}, x_{2k}, \ldots, x_{9k}$ are level-specific coefficients, $\Delta T = (T - T_{0k})$ and $\Delta S = (S - S_{0k})$. The coefficients are determined for the chosen range of temperatures and salinities (see table 1 in the paper) with T_{0k}, S_{0k} and ρ_{0k} corresponding to the mid-point values. Two versions of the proposed scheme applied to the Knudsen formula were tested: A simplified scheme which contains only three coefficients and a full scheme with all nine coefficients. The maximum error in density of the nine-coefficient formula is approximately one order better than the error of the three-coefficient formula. Both approximate formulas are more accurate at greater depths where temperature and salinity ranges are narrower.

Unfortunately, the algorithm proposed by Bryan and Cox [1972] is not universal. For example, it can not be applied to a sigma-coordinate ocean model, where levels of constant vertical coordinate does not correspond to constant depth levels. This motivated Mellor [1991] to derive an approximate but less computationally expensive formula to the full EOS-80 formula. Additionally, the input variable is the potential temperature instead of the in-situ temperature. The proposed form is

$$\rho(S, \theta, p) = \rho(S, \theta, 0) + 10^4 \frac{p}{c_m^2} \left(1 - 0.2 \frac{p}{c_m^2}\right), \tag{1.96}$$

where

$$c_m = 1449.2 + 1.34(S - 35) + 4.55\theta - 0.045\theta^2 + 0.00821p + 15 \times 10^{-9} p^2 \tag{1.97}$$

and $\rho(S, \theta, 0)$ is the same as in the original EOS-80 formula because $\theta = T$ for $p = 0$. The units of ρ, S, θ and p in Eqs. 1.96 and 1.97 are kg m^{-3}, parts per thousand, °C and decibars, respectively. The new formula is compared with EOS-80 using the conversion relation $\theta = \theta(S, T, p)$ from in-situ to potential temperature provided by the formula of Bryden [1973]. The maximum density error reaches 7×10^{-3} kg m^{-3} in the deepest waters which is of the same order as the standard error of the full formula. The maximum errors in calculating the density gradients are about 1%. They are also located in the deepest waters and decrease with decreasing depth.

Wright [1997] proposed another approximate formula which is more computationally efficient than EOS-80. It is formulated in the potential density and it is based on the Tumlirz equation of state,

$$\rho = \frac{p + p_w}{\lambda_w + \alpha_w (p + p_w)}, \tag{1.98}$$

where α_w, p_w and λ_w are given by

$$\begin{aligned}
\alpha_w &= a_0^w + a_1^w \theta + a_2^w S, & (1.99)\\
p_w &= b_0^w + b_1^w \theta + b_2^w \theta^2 + b_3^w \theta^3 + b_4^w S + b_5^w S\theta, & (1.100)\\
\lambda_w &= c_0^w + c_1^w \theta + c_2^w \theta^2 + c_3^w \theta^3 + c_4^w S + c_5^w S\theta, & (1.101)
\end{aligned}$$

where a_i^w, b_i^w and c_i^w are coefficients. Their values are determined and given in table 1 in the paper for two parameter ranges, the full range,

$$\begin{aligned}
0 \text{ Pa} \leq & p \leq 10^8 \text{ Pa}, & (1.102)\\
-2°\text{C} \leq & \theta \leq 40°\text{C}, & (1.103)\\
0 \text{ PSU} \leq & S \leq 40 \text{ PSU} & (1.104)
\end{aligned}$$

and the reduced range,

$$0 \text{ Pa} \leq p \leq 5 \times 10^7 \text{ Pa}, \tag{1.105}$$

$$-2°\text{C} \leq \theta \leq 30°\text{C}, \tag{1.106}$$

$$28 \text{ PSU} \leq S \leq 38 \text{ PSU}. \tag{1.107}$$

The root-mean-square (RMS) and maximum errors in density obtained for the full parameter range are 1.5×10^{-2} kg m^{-3} and 7.6×10^{-2} kg m^{-3}, respectively. The both errors decrease if the fit is performed for the reduced range. The RMS and maximum errors are then equal to 2.1×10^{-3} kg m^{-3} and 1.1×10^{-2} kg m^{-3}, respectively.

Wright's formula is efficient. Its rational-polynomial form contains only 15 coefficients which is a significant reduction from the original 41 coefficients of the EOS-80 formula. In fact, the author claims that the formula reduced the computation time to the less than one half even when compared with the formula of Mellor [1991]. However, the Wright's formula is used rarely due to its reduced accuracy [McDougall et al., 2003].

The third formula which modified EOS-80 was proposed by Jackett and McDougall [1995]. In contrast to Mellor's and Wright's formulas, this formula does not decrease the computation time of EOS-80 since it has the same form as EOS-80. The advantage of Jackett's and McDougall's formula is that the input variable is the potential temperature, instead of the in-situ temperature,

$$\rho(S, \theta, p) = \frac{\rho(S, \theta, 0)}{1 - \frac{p}{K(S, \theta, p)}} \tag{1.108}$$

It is accomplished by slightly adjusting the coefficients of the EOS-80 formula. In fact, only the coefficients of the secant bulk modulus need to be changed because $\rho(S, \theta, 0) = \rho(S, T, 0)$ due to $\theta = T$ for $p = 0$. The unchanged form of the formula is justified by the fact that the potential and in-situ temperatures differ by much less than a degree over most of the ocean. The parameter ranges in which the fit is performed are chosen to be

$$0 \text{ ba} \leq p \leq 1000 \text{ ba}, \tag{1.109}$$

$$-2°\text{C} \leq T \leq 40°\text{C}, \tag{1.110}$$

$$0 \text{ PSU} \leq S \leq 42 \text{ PSU}. \tag{1.111}$$

The RMS and maximum absolute errors with respect to the EOS-80 formula are 5.8×10^{-4} kg m^{-3} and 6.7×10^{-3} kg m^{-3}, respectively. The maximum error of Jackett's and McDougall's EOS is of the same magnitude as the standard error of EOS-80, which means that it is a suitable replacement of EOS-80. The modified values of the coefficients are given in table A1 in the paper.

Feistel [1993] described how to determine the Gibbs thermodynamic potential from the measurements and how to use it to compute physical quantities such as potential temperature, specific heat or chemical potential. Feistel and Hagen [1995] employed this method and derived the EOS from the Gibbs function (also called specific free enthalpy, Gibbs energy, Gibbs free energy, or free energy [Feistel, 2003]). Two important input data sets were included to improve the accuracy of the new EOS, data on the temperature of maximum density [Caldwell, 1978] and sound speed data [Del Grosso, 1974]. The resulting EOS outperforms EOS-80, but it is even more computationally demanding and it is not expressed as a function of S, θ, p.

This motivated McDougall et al. [2003] to choose a suitable form of EOS with S, θ, p as input variables and fit it to the EOS of Feistel and Hagen [1995]. The EOS form is similar to the one used by Wright [1997], however, more terms are included to improve its accuracy. The new formula has 25 coefficients, the Wright's formula has only 15 coefficients. The coefficient values together with three check values are given in Appendix B of the paper. The formula performs well. It is faster than the modified EOS-80 of Jackett and McDougall [1995] and it is significantly more accurate than the Wright's formula. The maximum error is four times smaller than the error of EOS-80 and 15 times smaller than the error of Wright's formula when compared to the EOS of Feistel and Hagen [1995]. Specifically, the maximum error of the formula of McDougall et al. [2003] is not larger than 3×10^{-3} kg m^{-3}.

The EOS of McDougall et al. [2003] is further improved by Jackett et al. [2006]. The accuracy improvement is due to Feistel [2003] who updated the Gibbs potential. The update consists mainly of incorporation of new data and addition of higher-order terms in the formula. The Gibbs potential of Feistel [2003] contains 101 coefficients instead of 89 coefficients used by Feistel and Hagen [1995]. Additionally, there are some minor improvements such as the incorporation of the triple point of water in the fit of the Gibbs function. Jackett et al. [2006] followed the same methodology as McDougall et al. [2003]. They used rational functions and found the coefficients that give the best fit to the EOS of Feistel [2003]. Despite the increased number of coefficients in the Gibbs potential, the form and number of terms in the rational functions that are used for the fit are kept unchanged. The errors between the resulting EOS and the EOS of Feistel [2003] are larger by 20%-160% than the errors between the EOS of McDougall et al. [2003] and the EOS of Feistel and Hagen [1995]. The RMS and maximum errors in density are 2.4×10^{-3} kg m^{-3} and 6.5×10^{-3} kg m^{-3}, respectively. These errors are of the same order as the errors already contained in the EOS of Feistel [2003]. Note, that the attempts to reduce the errors by changing the powers in the rational functions (5.44) and (5.45) are caused only minor improvements. The updated values of rational-function coefficients as well as three check values are given in Appendix A of the paper.

Nonetheless, the updated values of coefficients are not the only contribution of Jackett et al. [2006]. They argued that the ocean model temperature should be interpreted as conservative temperature Θ instead of commonly used potential temperature θ. Consequently, they also derived the EOS in the form $\rho = \rho(S, \Theta, p)$. The rational-function representation is again used and it is given by Eqs. (5.43), (5.44) and (5.45) where the potential temperature is replaced by the conservative temperature. The coefficient values together with two check values are given in Appendix B of the paper.

1.4.2 Conversions between different temperatures

It has been already noted that EOSs formulated in potential temperature are beneficial since temperature is commonly represented by the potential temperature in OGCMs. However, the results of temperature measurements, which are used as initial conditions, are provided in in-situ temperature. Hence, it is necessary to convert them from in-situ to potential temperature.

One possibility is to use the polynomial formula $\theta = \theta(S, T, p)$ of Bryden [1973],

$$\begin{aligned}\theta = p\Big\{&3.6504 \times 10^{-4} \\ &+ T\left[8.3198 \times 10^{-5} + T(-5.4065 \times 10^{-7} + 4.0274 \times 10^{-9}T)\right]\Big\} \\ &- p(S-35)(1.7439 \times 10^{-5} - 2.9778 \times 10^{-7}T) \\ &- p^2\left[8.9309 \times 10^{-7} + T(-3.1628 \times 10^{-8} + 2.1987 \times 10^{-10}T)\right] \\ &+ 4.1057 \times 10^{-9}p^2(S-35) \\ &- p^3\left(-1.6056 \times 10^{-10} + 5.0484 \times 10^{-12}T\right), \qquad (1.112)\end{aligned}$$

where S, T and p are in parts per thousand, °C and decibars, respectively.

Another method is provided by McDougall et al. [2003] and it is consistent with their EOS. The potential temperature θ of a water parcel with respect to the reference pressure p_r is computed by solving the equation,

$$\sigma_e(S, \theta, p_r) = \sigma_e(S, T, p), \qquad (1.113)$$

where σ_e is the specific entropy, which can be derived from the Gibbs function

$$G(S, T, p)$$

,

$$\sigma_e = -\left(\frac{\partial G}{\partial T}\right)_{S,p}. \qquad (1.114)$$

The numerical procedure is described in details in Sec. 5.14.

Jackett et al. [2006] provided improved values (see Sec. 1.4.1) of the coefficients in Eq. (5.197), the initial estimate of $\left(\frac{\partial \sigma_e}{\partial T}\right)_{S,p}$ remained unchanged. The algorithm that enables to compute the conservative temperature as a function of salinity and potential temperature was also provided. It is based on the definition of conservative temperature,

$$\Theta \equiv \frac{h_p(S, \Theta)}{C_p^0}, \qquad (1.115)$$

where

$$C_p^0 \equiv \frac{h_e(S = 35, \theta = 25, p_r = 0)}{25°\mathrm{C}} \approx 3992.103 \text{ J kg}^{-1}\text{K}^{-1}, \qquad (1.116)$$

where h_e is the enthalpy and h_p is the potential enthalpy. The potential enthalpy is expressed using the power series,

$$\begin{aligned}h_p = {}& d_0^h + d_1^h\mathscr{T} + d_2^h\mathscr{T}^2 + d_3^h\mathscr{T}^3 + d_4^h\mathscr{T}^4 + d_5^h\mathscr{T}^5 + d_6^h\mathscr{T}^6 + d_7^h\mathscr{T}^7 \\ &+ d_8^h s + d_9^h s\mathscr{T} + d_{10}^h s\mathscr{T}^2 + d_{11}^h s\mathscr{T}^3 + d_{12}^h s\mathscr{T}^4 + d_{13}^h s\mathscr{T}^5 \\ &+ d_{14}^h s^{1.5} + d_{15}^h s^{1.5}\mathscr{T} + d_{16}^h s^{1.5}\mathscr{T}^2 + d_{17}^h s^{1.5}\mathscr{T}^3 + d_{18}^h s^{1.5}\mathscr{T}^4 \\ &+ d_{19}^h s^2 + d_{20}^h s^{2.5} + d_{21}^h s^3 + d_{22}^h s^{3.5}, \qquad (1.117)\end{aligned}$$

where $s = S/40$ is scaled salinity and $\mathscr{T} = \theta/40°\mathrm{C}$ is scaled potential temperature. The coefficient values and four check values are given in appendix B of the paper. The enthalpy is computed from the Gibbs function,

$$h_e(S, T, p) = G - (T + 273.15\ °\mathrm{C}) \left(\frac{\partial G}{\partial T} \right)_{S,p} . \tag{1.118}$$

2. Numerics in OGCMs

2.1 Horizontal grids (Arakawa grids)

A horizontal grid needs to be chosen in both 2-D barotropic and 3-D baroclinic ocean models. The right choice is of fundamental importance because the grid serves as a foundation stone or a framework for the discretization. As a consequence, it affects the properties of the discrete form of the governing equations. Additionally, it is usually not easy to switch from one grid to another.

Ocean modelers often use the so-called Arakawa grids. Those grids are traditionally used with the finite difference method in which a continuous spatial derivative is replaced with the finite difference approximation based on the Taylor expansion. Arakawa grids were introduced by Arakawa and Lamb [1977]. There are five Arakawa grids which are denoted by capital letters A-E. Fig. 2.1 depicts Arakawa grids B, C and E, which are used in ocean modelling. Arakawa grids provide a regular distribution of scalar (SSH, temperature, salinity, etc.) and vector (velocity, friction force, tidal force, etc.) quantities. Grid A is a simple collocated grid. Grids B-E are staggered, which means that different physical quantities are discretized at different grid points (i.e., a staggered grid is composed of several collocated grids). For example, grids B and E contain vector points where the complete velocity vector is discretized and scalar points where scalar quantities are discretized. A different placement of grid points with discretized physical quantities results in a different discretization of the terms in the governing equations and a different accuracy in modelling certain physical processes.

Randall [1994] discussed the discretization of linearized shallow-water equations in terms of inertia-gravity (Poincaré) waves on an f-plane, i.e., the discretization of the Coriolis, pressure gradient and divergence terms is targeted. An important aspect is the necessity of averaging these terms on the particular grid as summarized in Table 2.1. Generally speaking, it is desirable to avoid averaging. The extensive averaging in the D-grid discretization is thus very unfavourable and the D-grid behaves badly in numerical simulations. Similarly, the A-grid solutions are extremely noisy and so it is recommended to avoid A-grid as well. There is no averaging of pressure gradient and divergence on the C-grid, but the troublemaker is the Coriolis term in which the averaging is inevitable. The opposite is the B-grid where the discretization of the Coriolis term is simple, but the pressure gradient and divergence needs averaging. However, the averaging used on the B-grid acts perpendicular to the direction of the differentiation while the averaging used on the A-grid acts in the same direction as the differentiation. The A-grid differentiation may average out oscillatory behaviour of the field in this direction. The E-grid seems to be a perfect choice since no averaging is needed but the E-grid collapses to the A-grid if the solution is uniform in one direction. To sum it up, the most promising are grids B and C. Their dispersion relations are studied for two values of the grid spacing d, $d = R_r/2$ and $d = 10R_r$, where R_r is the Rossby radius of deformation. It is found that the C-grid performs well for $d = R_r/2$, however, it has serious problems when $d = 10R_r$. The B-grid behaviour is different. The B-grid has problems for both grid spacings

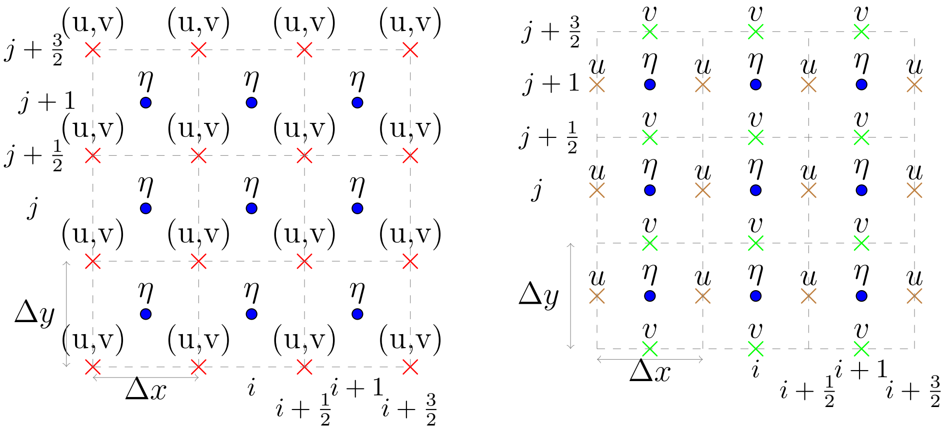
(a) Arakawa grid B

(b) Arakawa grid C

(b) Arakawa grid E

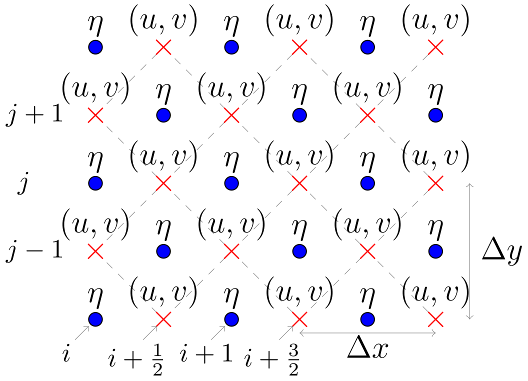

Figure 2.1: Sketches of Arakawa grids B, C and E.

tested, however, these problems are only moderate.

Grid	Coriolis	Pressure gradient	Divergence
A	no	yes	yes
B	no	yes	yes
C	yes	no	no
D	yes	yes	yes
E	no	no	no

Table 2.1: Averaging needed for the discretization of the Coriolis, pressure gradient and divergence terms on Arakawa grids A-E.

Batteen and Han [1981] examined consequences of the distorted dispersion relation on the solution in the initial-value problems. They report a checkerboard pattern of noise regardless of the ratio d/R_r on the B-grid, whereas the dependence on d/R_r is present in the C-grid solution with the concentric noise for large d/R_r (coarse grid). The incorrect behaviour of the B-grid is attributed to the averaging of the pressure gradient which causes wrong treatment of inertia-gravity waves. The C-grid problems are attributed to the averaging of the Coriolis force. The authors also show how the diffusion can suppress the computational noise on the B-grid and that the diffusion does not help much in suppressing the noise on the C-grid. The final conclusion is made to use the B-grid with diffusion in coarse-resolution models ($d > 100$ km) and C-grid in fine-resolution models ($d < 50$ km).

Dukowicz [1995] extended the ideas of Wajsowicz [1986] and studied the dispersion relation of Rossby waves rather than the inertia-gravity waves. The dynamics of Rossby waves is described in the quasi-geostrophic, β-plane approximation [Gill, 1982] instead of the linearized shallow water equations on an f-plane used in the previously mentioned studies. The focus is on the grids B and C. It is pointed out that the B-grid outperforms the C-grid in modelling Rossby waves for both resolved and unresolved Rossby radius. This is a surprising conclusion if we consider the results for inertia-gravity waves.

Finally, we mention a different treatment of the boundary conditions on grids B and C. The B-grid naturally implements the no-slip boundary conditions because both velocity components are discretized at the same grid point. In contrast, the C-grid discretization allows for a straightforward implementation of the free-slip boundary conditions with a possibility to implement the no-slip boundary conditions as well. The free-slip boundary conditions are probably more realistic. Hsieh et al. [1983] reported more serious problems in the alongshore behaviour of the baroclinic Kelvin waves under poor resolution on the B-grid than on the C-grid.

Motivated by all these aspects, ocean modellers usually choose either the B-grid or the C-grid. Of course, there are exceptions. The CANDIE model is available in A-grid and C-grid versions [Sheng et al., 1998]; the MITgcm model supports C-grid and C-D-grid [Adcroft et al., 1999]; and the LSG model, which was a base for the LSOMG model, is build on the E-grid [Maier-Reimer and Mikolajewicz, 1992].

2.2 Generalized horizontal coordinates

Roberts et al. [2006] define five properties that a coordinate grid which is suitable for ocean modelling should satisfy:

1. Orthogonality
2. Smooth spatial variations in grid spacing
3. east-west alignment of grid parallels near the Equator
4. Placement of singularities sufficiently away from the ocean
5. Grid cell aspect ratios close to unity

Strictly speaking, property 1) is not completely necessary. However, it greatly simplifies the numerics because the two coordinate directions are independent of each other and also metric terms in the momentum equations are simplified [Griffies, 2004]. It is a commonly used assumption. Property 2) is required to maintain the accuracy of the finite difference solution. Property 3) is useful to numerically better resolve equatorial ocean dynamics. The importance of properties 4) and 5) is discussed below in the context of spherical coordinates (SC).

Ocean models used to employ the SC, but the SC grid fulfills only first three properties. The main problem is the convergence of meridians at the poles: both South and North Poles are singular points of the SC. The South-Pole singularity does not cause any inconveniences because of Antarctica. Antarctica is a land area and so it is not a part of the computational domain of an ocean model. On the contrary, the North Pole is located in the Arctic ocean and it needs a special treatment. The point singularity can be bypassed by including a small artificial island at the North Pole. Unfortunately, this adjustment solves the problem only partially because the artificial island distorts dynamics in the polar region. Besides, the zonal grid spacing changes with latitude as $\cos\phi$ and it decreases when approaching a pole. The decrease of zonal grid spacing is not critical near the South Pole because the Antarctica covers the area south of approximately 80°S, but it may result in a serious restriction of time step near the North Pole due to the Courant–Friedrichs–Lewy (CFL) criterion. Certain methods have been proposed to remedy this problem. A popular solution was the application of Fourier filtering to selectively damp the shorter wavelengths which cause the main troubles. This is obviously not a neat treatment and it may produce some undesired phenomena such as static instabilities, noisy vertical velocities and small perturbations in the horizontal velocities [Murray and Reason, 2002]. Besides that, Murray and Reason [2001] pointed out that the aspect ratio of grid cells near the North Pole is large which is not a positive feature of the computation grid. Such a grid is computationally inefficient and may not capture the oceanic physical processes accurately.

There are several possibilities that allow for keeping the SC while improving their most salient drawbacks. Straightforward idea is to rotate the whole grid. Semtner [1976], Hibler III and Bryan [1987] and Semtner [1987] used a rotated SC grid with both South and North Poles located on the Equator for modelling the Arctic Ocean. This configuration might be useful for the Arctic-Ocean modelling, however, it is not suitable for the grid of a global ocean model. Murray [1996] referred that the land antipodes account for only 10% of the world's land area and nowhere lie sufficiently far inland, see also Fig. 1 in his paper. As a consequence, a rotated SC grid can never fully accomplish property 4) and may violate property 3). Deleersnijder et al. [1993] and Eby and Holloway [1994] proposed another solution. A composite grid was used instead of a single coordinate grid. The Arctic and North Atlantic Oceans were modeled on a SC grid rotated by 90°. The rotated grid was joined to the standard SC grid on the Equator. The problem is that the poles of the rotated grid lied in the North Pacific and Indian Oceans. Hence, the SC grid was used in this region but it can not be joined properly to the rotated grid at the Bering Strait. Additionally, according to Murray and Reason [2001], this composite grid suffers from a possibly inadequate resolution in the Arctic when used in coarse-resolution simulations and a discontinuity in grid spacing at the join. Eby and Holloway [1994] and Coward et al. [1994] argued that the distortion of ocean dynamics due to the latter issue is negligible. Although this grid is used in the Ocean Circulation and Climate Advanced Modelling Project (OCCAM) model, in which a simple channel model is used in Bering Strait, more flexible and general approach is needed. It is provided by the orthogonal curvilinear grids.

A solution to the pole problem is provided by the orthogonal curvilinear grids with relocated poles. The general idea is to relocate the coordinate singularity from oceans to continents. The computational domain of an OGCM does not contain continental areas and thus the presence of coordinate singularities is not disturbing there. The orthogonal curvilinear grids with relocated poles can be divided into two main categories: Dipolar grids which contain two poles and tripolar grids which contain three poles. The dipolar grids have more in common with the standard SC grid. Tripolar grids are slightly different, probably more complicated but they may have better properties. The representatives of dipolar grids are the dipolar reprojected grid of Murray [1996] and the grid of Roberts et al. [2006]. The examples of tripolar grids are the tripolar reprojected grid of Murray [1996] and the tripolar confocal grid of Murray [1996]. A dipolar grid has been supported, e.g., by the MPIOM [Marsland et al., 2003] and POP [Smith et al., 2010] models. Nevertheless, it seems that the trend is to prefer the tripolar grids. For example, the up-to-date versions of the MPIOM and POP models as well as the NEMO [Madec, 2012] and MOM [Griffies, 2012] models use tripolar grids.

2.3 Vertical discretization

The discretization in a barotropic model is completed by choosing the horizontal grid. However, the additional choice of an appropriate vertical coordinate has to be made in a baroclinic model. There are three most common types of vertical coordinates used in ocean models, geopotential (z) coordinate, isopycnal (ρ) coordinate and terrain-following (σ) coordinate, see the figures on the NOM group webpage (`https://www.oc.nps.edu/nom/modeling/vertical_grids.html`) for illustration. Each coordinate type is advantageous in a particular region of the global ocean and experiences problems elsewhere. Consider the following three parts of the ocean: The surface mixed layer, the ocean interior and the bottom.

The surface mixed layer provides a transition zone between the ocean and the other parts of the climate system, such as the atmosphere, sea ice or rivers. It is a region where ocean waters are efficiently mixed by turbulent convective processes, so the stratification is very weak. The resolution needed to capture these turbulent processes is on the scale of meters or even shorter. Such small scales are impossible to reach even in high-resolution state-of-art ocean models, hence parameterizations are required. The description of the surface mixed layer is natural in the z coordinate.

The ocean interior is different. Tracer transport processes that occur here are predominantly directed along surfaces of constant potential density. In other words, the isopycnal mixing is much stronger that the diapycnal. Consequently, it is suitable to use the ρ coordinate in this region.

The last part is the ocean bottom. We must capture the shape of the bottom topography because it influences the direction of currents. Moreover, similar to the surface boundary, there exists a turbulent bottom boundary layer (BBL) where so-called overflows occur. These density driven near-bottom currents may cross ridges of sills between ocean basins or slide down the continental slopes affecting the deep water [Beckmann and Döscher, 1997]. σ coordinate provides a suitable framework for the BBL and representation of the bathymetry. We discuss each vertical coordinate in more details in the following text based on Griffies [2004].

2.3.1 z coordinate

The most straightforward choice is the z-coordinate. Undisturbed ocean surface is given by $z = 0$ in this representation. Vertical axis is traditionally oriented upwards, so that the bottom is given by $z = -H$. Bryan [1969], Semtner [1974] and Cox [1984] established the basic methods for the z-coordinate models. Their efforts finally lead to the MOM ocean model which is currently available to the community in version 6 [Adcroft et al.]. The z-coordinate is the most extensive choice of ocean modellers throughout the history. Many renowned models are based on it. We mention the MITgcm model, the Los Alamos Parallel Ocean Program (POP), the Southampton Oceanography Centre OCCAM model and ocean part of the Hadley Centre Global Environmental Model (HadGEM) model. The main advantages of the z-coordinate are:

- Simple numerical discretization.
- World-wide use of this model class reflects in decent knowledge about their pitfalls and ways how to (at least partly) overcome them.
- Natural parameterization of the surface mixed layer.
- State equation of sea water, which is a nonlinear function of pressure, temperature and density, can be accurately expressed.
- No problems with the horizontal pressure gradients (see σ-coordinate models).

Unfortunately, there are also disadvantages:

- The precise representation of bottom topography is troublesome. The Bryan [1969] "full cell" ("staircase") approach can be modified to the "partial cell" and "shaved cell" approaches [Adcroft et al., 1997, Pacanowski and Gnanadesikan, 1998]. However, the representation of the BBL processes remains difficult.

- The cell thickness of the first grid cell is not completely arbitrary. The depressed ocean surface is not allowed to cause negative thickness of the first grid cell. This may restrict the high resolution of the model when tidal simulation is intended or when coupling to the sea ice model.

- Tracer advection and diffusion driven by mesoscale eddies in the interior of the ocean requires special care. Horizontal diffusion results in an unphysically large diapycnal mixing, therefore it is necessary to perform a transformation into isopycnal direction.

2.3.2 σ coordinate

Phillips [1957] first suggested to use the σ-coordinate. His motivation was to find a coordinate system for an atmospheric model in which the ground is a coordinate surface. He proposed to define this coordinate as

$$\sigma = \frac{p}{p_g}, \tag{2.1}$$

where p is the pressure and p_g is the pressure at the ground level. In ocean models, it is common to define the σ-coordinate in a slightly different way,

$$\sigma = \frac{z - \eta}{H + \eta}. \tag{2.2}$$

Hence, $\sigma = 0$ and $\sigma = -1$ at the ocean surface, $z = \eta$, and at the bottom, $z = -H$, respectively. Additionally, σ is a monotonic function of z, which means that there exists a unique mapping between the space and time dependent interval $\langle -H(\lambda, \phi), \eta(\lambda, \phi, t) \rangle$ in the z-coordinate and the constant interval $\langle -1, 0 \rangle$ in the σ-coordinate. Note that the space and time dependencies have moved to the transformation rule.

The σ-coordinate brings the following advantages:

- The representation of the bottom is smooth and representation of the BBL natural.

- The accurate representation of the state equation of sea water.

The main disadvantages are:

- The representation of the surface mixed layer may be imperfect. The distance between isolines grow with the increasing ocean depth which may result in an insufficient coverage in the mixed layer. Song and Haidvogel [1994] provided an example of a coastal model with 21 σ-levels which gives a sufficient mixed-layer resolution of 4 m on the shelf but a crude resolution of 230 m in the depth of 4600 m. As a remedy, he designed the s-coordinate which is a generalized σ-coordinate:

$$z = \eta(1+s) + H_c s + (H - H_c) C_s(s, a_s, b_s), \tag{2.3}$$

where s is in range $1 \leq s \leq 0$, H_c is the minimum depth and $C_s(s, a_s, b_s)$ is the nonlinear function of coordinate s given by

$$C_s(s, a_s, b_s) = (1 - b_s)\frac{\sinh(a_s s)}{\sinh a_s} + b_s \frac{\tanh[a_s(s + 1/2)] - \tanh(a_s/2)}{2\tanh(a_s/2)}, \tag{2.4}$$

which can be tuned by control parameters a_s and b_s in ranges

$$0 \leq a_s \leq 20, \tag{2.5}$$

$$0 \leq b_s \leq 1. \tag{2.6}$$

The s-coordinate becomes the σ-coordinate in the limit $a_s \to 0$. There are three terms in the definition Eq. (2.3). Their purpose is to follow the free surface, prevent possible linear instability and stretch the interior coordinate plus follow the bottom, respectively. It is shown that the resolution in the surface layer is significantly improved if s-coordinate is used, see Figs. 1b, 1c of Song and Haidvogel [1994].

- σ-coordinate models experience similar problems as the z-coordinate models in modelling isopycnal advection and diffusion. However, the problem is more serious here. The isopycnal surfaces are usually only slightly inclined so that they are close to the z-coordinate surfaces. In contrast, the σ-coordinate surfaces in the ocean interior may be inclined much more if the bottom-topography is steep.

- The accurate computation of horizontal pressure gradients is a controversial issue [Haney, 1991, Berntsen, 2002]. The horizontal pressure gradient is a sum of two terms

  $$\nabla_h p = \nabla_\sigma p + \rho g \nabla_\sigma z, \tag{2.7}$$

  where ∇_σ is a gradient along surfaces of constant σ. The magnitude of the two terms may become of the same order in certain ocean regions (next to continental shelves and sea mounts). Hence, it requires to compute both terms very accurately.

The first σ-coordinate ocean model was designed by Blumberg and Mellor [1987]. Well-known σ-coordinate models are the Princeton Ocean Model (POM) and the Regional Ocean Modeling System (ROMS). The models from this class have been traditionally used in regional and coastal ocean studies. There exist studies that apply σ-coordinate models to basin-scale problems, e.g., Ezer and Mellor [1994], Haidvogel et al. [2000], Willebrand et al. [2001], but these models are usually not used for studies of the global ocean. As far as we know, the only σ-coordinate models that have been used to study the world ocean circulation are the INMOM [Gusev and Diansky, 2014] and MASNUM [Lei, 2014] models.

2.3.3 ρ coordinate

The isopycnal models use the potential density as the vertical coordinate. It is defined as the density that a fluid parcel would have if moved adiabatically and with constant composition to a reference pressure ([Vallis, 2006], page 25). The potential density is a valid vertical coordinate if it is a monotonic function of ocean depth. This assumption is valid if a simplified equation of state is used.

The main advantages are:

- The isopycnal models are able to capture the physics of ocean interior. For example, the problems with diapycnal mixing that occur in the z-coordinate and σ-coordinate models are implicitly solved in isopycnal models.
- The overflow simulations in isopycnal models show good results. There is certain superiority over the z-coordinate models [Legg et al., 2006].

The main disadvantages are:

- It is difficult to include a realistic state equation. The potential density surfaces are also material surfaces in an adiabatic fluid. However, there is no available materially conserved density coordinate if we employ a realistic state equation.
- The resolution of an isopycnal model in a particular region is governed by the present potential-density stratification. It means that the model has enhanced resolution in dynamically important regions where density gradients are strong. On the other hand, the resolution is poor in the well-mixed regions. The latter is the case of the surface mixed layer. In order to solve this problem, the bulk parameterizations of the surface mixed layer are used [Bleck et al., 1992, Oberhuber, 1993a].

The representants of this model class are the Hallberg Isopycnal Model (HIM), the Miami Isopycnic Model (MICOM) and the OPYC (junction of Ocean and isoPYCnal coordinates) model.

2.4 Advection schemes

The advection in the evolution equation for tracers (1.11) can be discretized using various numerical schemes. The individual schemes differ by the discretization of a tracer on the grid-cell face. We distinguish between linear and nonlinear advection schemes. In linear schemes, the coefficients for interpolation of the advected tracer are linear and they are functions of the flow, not the tracer field itself [Adcroft et al., 2014]. We discuss the centered second-order, centered fourth order, first-order upwind and upwind biased third-order (QUICK) linear advection schemes in this section. The nonlinear schemes are discussed in Sec. 5.7. We also distinguish whether the advection scheme is positive or not. If the scheme is positive (positive definite), then it guarantees that negative tracer values will not appear if the initial tracer distribution was strictly positive. The schemes that are not positive are not recommended for passive tracers. It is also desirable to use the same scheme for both active and passive tracers [Madec, 2012]. Finally, the scheme is called monotonic, if the initial monotonic tracer distribution remains monotonic after the advection process.

In this section, we assume for simplicity that the grid is 1-D and regular with a unit grid spacing. We define the differencing and averaging operators, δ_i and $\overline{}^{i}$, respectively,

$$\delta_i A = A_{i+\frac{1}{2}} - A_{i-\frac{1}{2}}, \tag{2.8}$$

$$\overline{A}^{i} = \frac{A_{i+\frac{1}{2}} + A_{i-\frac{1}{2}}}{2}, \tag{2.9}$$

where A is an arbitrary scalar quantity. If we neglect the terms with turbulent tracer fluxes and the source term in Eq. (1.11), the evolution equation for tracers reduces to

$$C_{,t} + \delta_i F = 0, \tag{2.10}$$

where $F = uC$ is the tracer flux.

2.4.1 Centered second-order scheme

The centered second-order scheme is simple, the tracer flux is given by

$$F_{i+\frac{1}{2}} = u_{i+\frac{1}{2}} \overline{C}^{i+\frac{1}{2}}. \tag{2.11}$$

The scheme is non diffusive and so it conserves the tracer variance, but it is very noisy due to its dispersive nature. It must be used in conjunction with an explicit diffusion operator to produce a meaningful solution [Madec, 2012]. It may lead to unphysical oscillatory behaviour in an implicit solution or to a disastrous nonconvergence in an explicit computation in regions where convection strongly dominates diffusion [Leonard, 1979]. The centered second-order scheme can be used with the leapfrog time stepping scheme but it is unstable with the explicit Euler time stepping scheme.

2.4.2 First-order upwind scheme

Another simple scheme with virtually opposite characteristics to the centered second-order scheme is the first-order upwind scheme,

$$F_{i+\frac{1}{2}} = u_{i+\frac{1}{2}} C_I, \tag{2.12}$$

where index I depends on the sign of advecting velocity

$$I = \begin{cases} i & \text{if } u_{i+\frac{1}{2}} > 0, \\ i+1 & \text{if } u_{i+\frac{1}{2}} < 0. \end{cases} \tag{2.13}$$

The scheme is known to be very diffusive. Gerdes et al. [1991] refers that the upwind scheme is too diffusive to be of practical use except in coarse-resolution models. On the other hand, it is a positive and monotonic scheme [Guan and Zhang, 2004]. Some more sophisticated schemes which are nearly monotonic are based on the first-order upwind scheme [Durran, 1999]. Remark that explicit time scheme is necessary for the upwind scheme regardless of its order (first-order, third-order, etc.) due to the diffusive nature of the upwind scheme. The prove for a simplified 1-D tracer equation with constant velocities and without diffusion terms can be found in Griffies [2004].

2.4.3 Centered fourth-order scheme

The centered fourth-order scheme,

$$F_{i+\frac{1}{2}} = u_{i+\frac{1}{2}} \overline{\left(C - \frac{1}{6}\delta_i \delta_{i+\frac{1}{2}} C\right)}^{i+\frac{1}{2}}, \tag{2.14}$$

may be appealing for high-resolution simulations where dynamical scales are well resolved. However, the scheme is noisy similar to the centered second-order scheme and certain amount of diffusion is again needed. The biharmonic diffusion is recommended because it is more scale selective [Adcroft et al., 2014].

2.4.4 Quadratic Upstream Interpolation for Convective Kinematics (QUICK)

The QUICK scheme is also known as the Upwind-Biased Scheme (UBS). It is based on the third-order upwind-biased quadratic interpolation [Leonard, 1979],

$$F_{i+\frac{1}{2}} = u_{i+\frac{1}{2}} \overline{\left(C - \frac{1}{8}\delta_i \delta_{i+\frac{1}{2}} C\right)}^{i+\frac{1}{2}} + \frac{1}{16}\left|u_{i+\frac{1}{2}}\right| \delta_{i+\frac{1}{2}} \delta_i \delta_{i+\frac{1}{2}} C. \tag{2.15}$$

The scheme is not positive but it offers a relatively good compromise between the accuracy and smoothness [Adcroft et al., 2014]. It is less diffusive than the standard upwind scheme and less dispersive than the centered second-order scheme [Prange et al., 2003]. The over-shooting inherent in the centered second-order advection scheme is significantly reduced [Pacanowski and Griffies, 2000].

The scheme is unstable if leapfrog or explicit Euler time stepping schemes are employed. Farrow and Stevens [1995] suggested to use a two time level predictor-corrector time integration scheme with the centered second-order scheme for the predictor step. Another possibility implemented in the NCAR model is to use the leapfrog time stepping scheme but evaluate the intrinsic diffusive term in the previous not the current time step [Holland et al., 1998]. This modification solves the stability issue and it less computationally expensive.

2.4.5 Summary

The existence of different advection schemes suggests that it might be tricky to find the best option. Indeed, Adcroft et al. [2014] argued that there is no perfectly universal advection scheme and the determination of the most suitable scheme for the particular application is often a matter of trial. The model resolution could also be decisive. In a coarse-resolution model, Adcroft et al. [2014] suggested that the simplest scheme might be the best one. In a high-resolution model, they preferred either a higher-order scheme with (optionally) scale-selective diffusion or the flux limited methods (see Sec. 5.7).

Figures 2.13, 2.14 and 2.15, 2.16, 2.17 in Adcroft et al. [2014] may also provide useful hints for the right choice of the advection scheme. Figures 2.13, 2.14 depict a comparison between different advection schemes in one dimension for the Courant numbers 0.05 and 0.89. Figures 2.15, 2.16, 2.17 show the advection of a Gaussian bell in a rectangular basin for the Courant numbers 0.01, 0.27 and 0.47.

Part II

Ocean model LSOMG

3. Introduction

3.1 Motivations and requirements

The LSOMG model is a z-coordinate baroclinic OGCM. It solves the primitive equations under the Boussinesq, hydrostatic and shallow ocean approximations, see Sec. 1.1. Our motivation for the development of the LSOMG model was the intention to have an OGCM that is

- a global primitive-equation ocean model
- fully 3-D not only barotropic and thus it is capable of generating the 3-D distribution of 3-D velocities (important, for example, for the modelling of toroidal magnetic field in the ocean)
- open for modifications
- understood on a code level by our group
- usable for geophysical purposes, such as modelling the ocean induced magnetic field

We have chosen the LSG ocean model which was developed at the Max–Planck–Institut für Meteorologie in Germany. The main reason for our choice was the model designation for large-scale long-term simulations, for example, climate studies. Such model is certainly not suitable for regional studies of eddy activity but its complexity could be sufficient for the geophysical applications. On top of that, a simplified numerical core implies faster computations and a light-weight tool for the user/programmer.

The model fulfils our first and second requirements. The third requirement is also fulfilled. We obtained the LSG code from Dr. Butzin and we were free to modify it. The fourth requirement is fulfilled only partly. The model is described in Maier-Reimer and Mikolajewicz [1992]. The text is meant to be the LSG manual but it is incomplete. The code is not commented frequently either, which makes its understanding difficult. The fifth requirement is invalid. It turned out during the development that the LSG model is obsolete. We have gradually rewritten the whole code with the exception of several parts, such as the advection scheme QUICK or the sea-ice model. The major modifications are summarized in Sec. 3.2 and in Table 3.1. As a consequence, we call the resulting model LSOMG since the original acronym LSG is now inaccurate and misleading. The LSOMG is the shortcut for the "Libor Sachl Ocean Model for Geophysics".

Note that the LSOMG model is fully 3-D but it can also be run in a barotropic version. We call this version LSOMG-BT. The LSOMG-BT model is described in details in Sec. 4. It can be used to test the barotropic part of the LSOMG model, see Sec. 6.1, or to model the tidal circulation, see Sec. 7.1.

3.2 Summary of differences between the LSG and LSOMG models

Both the LSG and LSOMG models discretize the governing equations using the finite difference method. The LSG model uses the Arakawa E-grid while the LSOMG model is build on the Arakawa C-grid. The main motivation to switch from the E-grid to C-grid was to avoid the coexistence of two solutions that evolve independently of each other on the E-grid . A more natural treatment of boundary conditions and simpler indexing of grid points are additional advantages. Barotropic LSOMG-BT also supports Arakawa grids B and E for certain time stepping schemes as an alternative to the default C-grid.

The governing equations in the LSG model are expressed in the spherical coordinates. It is a valid option but it is not free of deficiencies, as discussed in Sec. 2.2. In the LSOMG model, we rather implemented the governing equations in their general form using the metric coefficients of the particular coordinate system. Consequently, the LSOMG model is able to handle arbitrary orthogonal horizontal coordinates. The suitable coordinate grids are listed in Sec. 2.2. There are three generalized grids available in the LSOMG model, see Sec. 5.11. The tripolar reprojected grid of Murray [1996] is our preferred choice. Note that apart from the general forms of operators in the model, the programs that regrid data on the computational grids also need special attention. We calculate the model bathymetry by averaging data values within model grid cells which requires an algorithm to determine the position of data point with respect to the particular grid cell, see Sec. 5.14.1. Besides that, vector data such as 10-m wind speed need to be rotated into the direction of coordinate axes of the chosen coordinate system, see Sec. 5.14.4.

The ad-hoc choice of vertical layers in the LSG model has been replaced by a semi-automatically generated distribution of vertical layers in the LSOMG model. The distribution is determined from a prescribed smooth distribution of level depths and thicknesses. The scheme is not fully automatic because it contains one tunable parameter, see Sec. 5.3.

The original LSG model propagates the barotropic part of the momentum equation in time using the implicit time stepping scheme. The implicit scheme allows to step the model forward in time with a significantly larger time step than the explicit scheme. On the other hand, the implicit scheme requires to solve a system of linear equations in each time step. Our primary goal was to model the wind- and buoyancy-driven ocean circulation but we also intended to force the model by tides. The accurate tidal modelling requires the time step to be "small enough" to resolve the tidal periods. The period of principal lunar semidiurnal M_2 tide is approximately 12.4 hours, which means that a tidally-driven model needs to resolve much finer time scales than a purely wind-driven model. The implicit time-stepping scheme with a short time step could become time consuming due to the need to repeatedly solve the system of linear equations. The explicit time-stepping scheme is thus better suited for the tidal modelling. The time-stepping schemes for the barotropic system that are available in the LSOMG model are discussed in Sec. 4.1.

The baroclinic circulation is forced by the vertically dependent forcing terms in the momentum equation. The baroclinic forcing in the original LSG model includes pressure gradient and horizontal friction force while the vertical friction force and nonlinear terms are neglected. Both terms are now available:

- The nonlinear terms are expressed either in the vector invariant form, see Eq. (5.16), or in the flux form, see Eq. (5.18). The implementation follows Madec [2012].
- The vertical friction arises from the vertical shears of horizontal velocities. The term is discretized implicitly in time to ensure stability even for large vertical eddy viscosity.

The horizontal friction force has already been present in the LSG model, however, its implementation has been improved. The LSG models uses the horizontal friction in the form of a Laplacian. The LSOMG model retains this option but a more appropriate form given by Murray and Reason [2001] is also available. Similarly, horizontal viscosities are constant in LSG but LSOMG enables viscosities which adapt according to the actual velocity field [Smagorinsky, 1963, 1993], see Sec. 1.2.2 and 5.6 for more details.

The form of diffusion operator has also been improved. There are two options available for the tracer diffusion operator at present. It is either the original Laplacian operator or the epineutral (isopycnal) operator. The Laplacian is a somewhat ad-hoc form, on the contrary, the epineutral operator is based on oceanographic measurements and observations and it is thus physically justified, see Sec. 1.3 for details. The implementation of epineutral operator is based on the triad algorithm of Griffies et al. [1998] with modifications introduced by Madec [2012] and it is combined with the parameterization of tracer stirring by mesoscale eddies as explained in Sec. 1.3.3.

The surface heat fluxes are represented by a simple relaxation towards the prescribed distribution of sea surface temperature in the LSG model. This option is retained in the LSOMG model but it is supplemented with more realistic bulk formulas for shortwave, longwave, sensible and latent heat fluxes. The bulk formulas of Kara et al. [2002], Kondo [1975] and Large and Yeager [2004] are available.

The tidal forcing is expressed in the form of a gradient of the second-degree tidal potential. The implementation is adopted from the DEBOT model. The LSOMG also includes parameterizations of two important physical phenomena:

- The internal wave drag caused by the breaking of internal tidal waves. The parameterization of Jayne and St. Laurent [2001] has been implemented.
- The change of gravity field due to the effect of self attraction and loading (SAL). The scalar approximation of SAL has been implemented into the LSOMG model.

See Sec. 4.4 for further details.

New tracer advection schemes have been implemented to the LSOMG model. The original QUICK scheme from the LSG model has been supplemented (replaced) with three schemes with flux limiters: The Lax-Wendroff scheme, third-order direct space time scheme [Adcroft et al., 2014] and the scheme of Smith et al. [2010]. The splitting method of Adcroft et al. [2014] has been implemented to handle the multidimensional tracer advection.

The original EOS-80 state equation [UNESCO, 1981] has been replaced by the state equation of [Jackett et al., 2006], see Sec. 1.4 for further discussion. The initial potential temperature distribution is obtained from the in-situ temperature distribution following the method described in Sec. 5.14.5.

The convective adjustment scheme used in the LSG model checks the stability of a water column from top to bottom and if instability is found, the scheme mixes the content of two neighbouring grid cells. The procedure is finished when it reaches the bottom cell, it is not repeated. It is a simple and computationally favourable scheme but it does not guarantee to stabilize an unstable water column (although it may work fine in certain cases). The LSOMG model thus employs a scheme of Rahmstorf [1993] which truly guarantees to stabilize an arbitrary unstable water column.

The LSG ocean model is coded in the old fashioned way in FORTRAN 77 with common blocks and static arrays. The LSOMG model is coded in Fortran 90 with modules and allocatable arrays, see Sec. 5.13.

The LSG ocean model is not parallelized at all and it does not utilize any numerical library (e.g., a system of linear equations is solved using a hand-made Gaussian elimination without pivotation). The LSOMG model is parallelized using the MPI standard and it benefits from the sophisticated Intel MKL library if certain parts of the model are active, see Sec. 5.13..

The Coriolis term is discretized implicitly in the LSG ocean model. It increases the model stability at no additional computational costs. On the contrary, the discretization of the Coriolis term in both space and time is a delicate issue on the Arakawa C-grid. The Coriolis term in the LSOMG model is discretized using the Adams-Bashforth method in time and there are several spatial schemes available. However, none of the discretizations is completely free of the grid-scale noise. In order to remedy this problem, we implemented the divergence damping and the dual-step five-point-involved spatial smoothing method of Han [2014] into the LSOMG model. See Sec. 5.8 for more details.

For the reader's convenience, we summarize the key differences between LSG and LSOMG models in Table 3.1.

	LSG	LSOMG
Horizontal grid	Arakawa E grid	Arakawa C grid
Horizontal coord.	spherical	generalized
Vertical grid	manually generated	semi-auto generated
Time stepping	no splitting, collocated	splitting, staggered
Barotropic part	implicit	explicit (PC, FBgen)
Horiz. friction	“rotated” Laplacian	Laplacian, “full” form
Vert. friction	no	yes (explicit, implicit)
Nonlinear terms	no	yes (2 formulations)
Isopycnal mixing	no	yes
GM stirring	no	yes
State equation	UNESCO [1981]	Jackett et al. [2006]
Tidal forcing	no	yes (from DEBOT)
Heat fluxes	relaxation	relaxation, bulk formulas
Tidal parameterizations	no	yes
Advection scheme	QUICK	QUICK, LW, DST3
Coriolis term	implicit	Adams-Bashforth
Convective adj.	one sweep	[Rahmstorf, 1993]
Programming	FORTRAN 77	Fortran 90
Parallelization	no	MPI, (OpenMP)

Table 3.1: Summary of major differences between LSG and LSOMG models. See the main text for more details. PC = predictor-corrector, FBgen = generalized forward-backward, LW = Lax-Wendroff, DST3 = third-order direct space time

4. Barotropic LSOMG-BT model

The LSOMG-BT model is the barotropic version of the LSOMG model. The governing equations of the barotropic ocean model are the so-called shallow water equations (SWE), see Einšpigel and Martinec [2015] for their detailed derivation. SWE can be expressed in two equivalent forms, the flux form and advective form [Williamson et al., 1992]. The advective form expressed in the barotropic velocity $\bar{\mathbf{u}}$ is

$$\bar{\mathbf{u}}_{,t} + \bar{\mathbf{u}} \cdot \nabla_h \bar{\mathbf{u}} + f\mathbf{e}_3 \times \bar{\mathbf{u}} + g\nabla_h \eta = \mathbf{F}, \tag{4.1}$$

$$\eta_{,t} + \nabla_h \cdot (h\bar{\mathbf{u}}) = 0, \tag{4.2}$$

the flux form expressed in the vertically integrated transport $\mathbf{U} = h\bar{\mathbf{u}}$ is

$$\mathbf{U}_{,t} + \nabla_h \cdot \left(\frac{\mathbf{U} \otimes \mathbf{U}}{h}\right) + f\mathbf{e}_3 \times \mathbf{U} + gh\nabla_h \eta = h\mathbf{F}, \tag{4.3}$$

$$\eta_{,t} + \nabla_h \cdot \mathbf{U} = 0. \tag{4.4}$$

where $\mathbf{F}$ denotes forcing. In the LSOMG-BT model, $\mathbf{F}$ contains the horizontal friction $\mathbf{F}_H^{(\mathbf{u})}$, bottom friction $\boldsymbol{\tau}_b$, wind stress $\boldsymbol{\tau}_w$ and tidal forcing $\mathbf{F}_{tid}$,

$$\mathbf{F} = \mathbf{F}_H^{(\mathbf{u})} + \frac{\boldsymbol{\tau}_w}{\rho_0 h} - \frac{\boldsymbol{\tau}_b}{h} + \mathbf{F}_{tid}, \tag{4.5}$$

see Secs. 5.6, 4.2, 4.3 and 4.4.

The LSOMG-BT model neglects nonlinear advection in the momentum equation which is represented by the second term on the left-hand side of Eqs. (4.1) and (4.3). As already mentioned in Sec. 3.1, the expected usage of LSOMG-BT is either testing of the barotropic part of the full LSOMG model or modelling of barotropic tidal circulation. Considering the first case, the nonlinear advection terms are computed in the baroclinic part of the model and then inserted into the barotropic part as the vertically integrated baroclinic contribution. Considering the second case, the linear SWE are commonly used in the barotropic tidal models. The nonlinearities become important in shallow coastal regions but on the deep ocean they can be neglected.

The governing equations are discretized using the finite difference method in the LSOMG-BT model. Spatial derivatives are approximated using the centered differences on Arakawa grids [Arakawa and Lamb, 1977], see Sec. 2.1. We consider two types of boundary conditions:

$$\begin{aligned} \text{Free slip: } & \eta = 0, \; \bar{\mathbf{u}} \cdot \mathbf{n} = 0. \\ & \eta = 0, \; \mathbf{U} \cdot \mathbf{n} = 0. \end{aligned} \tag{4.6}$$

$$\begin{aligned} \text{No slip: } & \eta = 0, \; \bar{\mathbf{u}} = \mathbf{0}. \\ & \eta = 0, \; \mathbf{U} = \mathbf{0}, \end{aligned} \tag{4.7}$$

where $\mathbf{n}$ is the outer normal to the ocean-land boundary. The LSOMG-BT model supports Arakawa grids B, C and E, see Fig. 2.1 . We apply free-slip boundary conditions on the Arakawa grid C and no-slip boundary conditions on Arakawa grids B and E. Free-slip boundary conditions (or its modification) are probably more appropriate, however, Griffies and Hallberg [2000] refer that a natural formulation of free-slip on the B-grid does not exist. The grid configuration affects the design of the numerical schemes and their performance as we will discuss later.

In the following sections, we discuss the time stepping schemes which are available in the LSOMG-BT model, implementation of tidal force and tidal parameterizations for a barotropic tidal model and also the grid-scale noise on the Arakawa grids B and E.

Note that the overbars in the symbols for barotropic velocities are dropped out in the rest of this chapter in order to simplify the notation.

4.1 Time stepping schemes in the LSOMG-BT model

The LSOMG-BT model provides four time-stepping schemes: The Euler implicit scheme (IMP), the modified Crank-Nicolson (CNmod) scheme [Campin et al., 2004], the forward-backward (FB) scheme [Gadd, 1974, Mesinger, 1977] (or its modification the predictor-corrector (PC) scheme) and the generalized forward-backward (FBgen) scheme [Shchepetkin and McWilliams, 2005, 2008]. However, the total number of spatio-temporal configurations available in the model is not 3 × 4 since some schemes are applicable at particular spatial grids only. The available model configurations are FB on the grid B, FB (or PC), FBgen and CNmod on the grid C and FB (or PC) and IMP on the grid E.

4.1.1 Euler implicit time-stepping scheme from the LSG model (IMP)

The IMP scheme is the time-stepping scheme originally used in the LSG model and we use it only on the Arakawa grid E. The scheme employs SWE in the flux form and integrates them implicitly in time,

$$\mathbf{u} + f\left(\mathbf{k} \times \mathbf{u}\right)\Delta t = \mathbf{u}^n - g\nabla\eta\Delta t + \mathbf{F}^n\Delta t, \tag{4.8}$$

$$\eta = \eta^n - \nabla \cdot \left(h^n\mathbf{u}\right)\Delta t, \tag{4.9}$$

where Δt is the time step. The quantities with superscript n are evaluated in the previous time step, otherwise they are evaluated in the current time step. The SSH in Eq. (4.8) is expressed using Eq (4.9),

$$\mathbf{u} + f\left(\mathbf{k} \times \mathbf{u}\right)\Delta t - g\nabla\nabla \cdot \left(h^n\mathbf{u}\right)\left(\Delta t\right)^2 = \mathbf{u}^n - g\nabla\eta^n\Delta t + \mathbf{F}^n\Delta t. \tag{4.10}$$

At the start, we solve Eq. (4.10) for the barotropic velocity. The third term on the left hand side of Eq. (4.10) contains horizontal velocity in the actual time step within a differential operator. It introduces coupling between grid points if differential operators are approximated using the finite difference method. The system of linear algebraic equations needs to be solved, see Appendix. A.1. The system matrix is non-symmetric but sparse with at most eight nonzero elements in each row of the matrix. We use the restarted generalized minimal residual method (GMRES), which is an iterative method suitable for solving a linear system of equations with a general non-symmetric matrix [Saad and Schultz, 1986]. When the barotropic velocity is know, the SSH is calculated from Eq. (4.9).

Note that the original implementation of the IMP scheme in the LSG model neglects the SSH in the water-column height. For the purpose of this paper, we include the SSH explicitly into the water-column height, see h^n in Eq. (4.9). The modified scheme is semi-implicit rather than implicit. The scheme could be kept implicit by using h instead of h^n in Eq. (4.9). In that case, we would solve both the momentum and SSH equations simultaneously for the barotropic velocity and SSH. We have not tested this implementation.

4.1.2 Modified Crank-Nicolson time-stepping scheme (CNmod)

The scheme is based on two key ideas, the use of Crank-Nicolson time-stepping scheme and the treatment of the SSH and water-column height as two independent variables. The resulting scheme is unconditionally stable and it is claimed to conserve total mechanical energy (kinetic plus potential energy). The complete derivation of the scheme is given in Campin et al. [2004], and so we merely summarize the key steps of the computational process below.

1. Update the water-column height,

$$h = h^n - \nabla \cdot \left(h^n \mathbf{u}^n\right) \Delta t. \tag{4.11}$$

2. Compute the auxiliary velocity $\mathbf{u}^*$,

$$\mathbf{u}^* = \mathbf{u}^n + f\left(\mathbf{k} \times \mathbf{u}^{n+\frac{1}{2}}\right) \Delta t - (1-\gamma_c) g \nabla \eta \Delta t + \mathbf{F}^n \Delta t, \tag{4.12}$$

   where $\mathbf{u}^{n+\frac{1}{2}}$ is the velocity extrapolated using the third-order Adams-Bashforth method (see Eq. 4.18).

3. Update the SSH using the new water-column height from step 1 and auxiliary velocities from step 2,

$$\eta + \beta_c \gamma_c g \nabla \cdot \left(h \nabla \eta\right) (\Delta t)^2 = (h - H) - \beta_c \nabla \cdot \left(h \mathbf{u}^*\right) \Delta t. \tag{4.13}$$

4. Update the barotropic velocity using the auxiliary velocity from step 2 and the new SSH from step 3,

$$\mathbf{u} = \mathbf{u}^* - \gamma_c g \nabla \eta \Delta t. \tag{4.14}$$

Parameters β_c and γ_c are both equal to 0.5, which corresponds to the Crank-Nicolson time-stepping scheme.

Similar to Eq. (4.10), the left hand side of Eq. (4.13) contains the SSH in the actual time step within a differential operator and so a system of linear equation needs to be solved, see Appendix. A.2. We solve it using the GMRES method as in the IMP scheme. The computational demands of IMP and CNmod matrix problems are, however, different. First, the number of unknowns in the CNmod problem is approximately half than in the IMP problem, since Eq. (4.13) is a scalar equation, while Eq. (4.10) is a vector equation. Second, the number of nonzero elements is smaller in the CNmod scheme, with a maximum of five nonzero elements in one row of the CNmod matrix. Both properties reduce the computational time.

4.1.3 Forward-backward time-stepping scheme (FB)

The main idea of the FB scheme is to advance the velocity (vertically integrated transport) and the SSH gradually, i.e., solve the momentum equation using the explicit (forward in time) scheme first and then solve the SSH equation using the implicit (backward in time) scheme.

The FB scheme is second-order accurate similar to the commonly used leapfrog scheme [Mesinger and Arakawa, 1976]. However, the FB scheme has certain favourable properties [Mesinger and Popovic, 2010, Lei, 2014]. The FB scheme is a two-time-level scheme, hence, it does not suffer from the computational mode that is present in the three-time-level leapfrog scheme. Both FB and leapfrog time steps are constrained by the CFL criterion for the external gravity waves,

$$\Delta t \sqrt{gh\left[\frac{1}{(\Delta x)^2}+\frac{1}{(\Delta y)^2}\right]}\Bigg|_{\max} < C_m, \tag{4.15}$$

where Δx and Δy denote lateral grid spacings. However, the C_m in the FB scheme is $C_m = 1$, which is twice as large as in the leapfrog scheme.

The LSOMG implementation of the FB scheme depends on the discretization of the Coriolis term. The components of velocity (vertically integrated transport) are discretized at the same points on Arakawa grids B/E but they are spatially separated on the Arakawa grid C. As a consequence, the Coriolis term on the Arakawa grid C needs to be treated more carefully. We start with the B/E–grid implementation. We use the semi-implicit discretization of the Coriolis term in time,

$$\mathbf{U} + f\mathbf{k}\times\left(\frac{\mathbf{U}^n+\mathbf{U}}{2}\right)\Delta t = \mathbf{U}^n - gh^n\nabla\eta^n\Delta t + h^n\mathbf{F}^n\Delta t, \tag{4.16}$$

$$\eta = \eta^n - (\nabla\cdot\mathbf{U})\,\Delta t. \tag{4.17}$$

The momentum equation constitutes a system of two linear equations for the components of barotropic transport that can be solved analytically (see Griffies [2004]).

On the Arakawa grid C, the default is the Adams-Bashforth extrapolation of the third order. However, in Sec. 6.1, we use the method of Sielecki [1968] and Beckers and Deleersnijder [1993] in order to make the FB scheme more distinct from the FBgen scheme. The spatial and temporal discretization of the Coriolis term on the C-grid is discussed in more details in Sec. 5.8.

Note that the FB scheme may solve the SWE in the opposite order; start with the SSH equation and then continue with the momentum equation. Let us call this version SSH–MOM and the other one MOM–SSH. Mesinger [1973] showed that the amplification factors of both versions are the same. He also argued that the MOM–SSH version should be more suitable for an atmospheric model but then he reported that there were hardly any differences between the two solutions in a realistic run. Consequently, we use the MOM–SSH version in the LSOMG-BT model and we have not tested the SSH–MOM version.

4.1.4 Generalized forward-backward time-stepping scheme (FBgen)

The FBgen scheme generalizes the FB scheme by implementing a combination of a third-order Adams-Bashforth (AB3) step with a fourth-order Adams-Moulton (AM4) step. The scheme consists of four steps:

1. The AB3 extrapolation of the SSH and velocities,
$$\begin{pmatrix}\eta\\ \mathbf{u}\end{pmatrix}^{n+\frac{1}{2}} = \left(\frac{3}{2}+\beta_f\right)\begin{pmatrix}\eta\\ \mathbf{u}\end{pmatrix}^{n} - \left(\frac{1}{2}+2\beta_f\right)\begin{pmatrix}\eta\\ \mathbf{u}\end{pmatrix}^{n-1} + \beta_f\begin{pmatrix}\eta\\ \mathbf{u}\end{pmatrix}^{n-2}. \tag{4.18}$$
2. Updating η by the SSH equation (4.2),
$$\eta = \eta^n - \nabla\cdot\left(h^{n+\frac{1}{2}}\mathbf{u}^{n+\frac{1}{2}}\right)\Delta t, \tag{4.19}$$
where $h^{n+\frac{1}{2}} = H + \eta^{n+\frac{1}{2}}$.
3. Computing the provisional η' for the momentum equation using the AM4 interpolation,
$$\eta' = \left(\frac{1}{2}+\gamma_f+2\epsilon_f\right)\eta + \left(\frac{1}{2}-2\gamma_f-3\epsilon_f\right)\eta^n + \gamma_f\eta^{n-1} + \epsilon_f\eta^{n-2}. \tag{4.20}$$
4. Updating u and v using the provisional η' from the previous step,
$$\mathbf{u} = \left[h^n\mathbf{u}^n - f\mathbf{k}\times\left(h^{n+\frac{1}{2}}\mathbf{u}^{n+\frac{1}{2}}\right)\Delta t - gh^n\nabla\eta'\Delta t + h^n\mathbf{F}^n\Delta t\right]/h. \tag{4.21}$$

The FBgen scheme is second-order accurate for any values of β_f, γ_f and ϵ_f, and is third-order accurate for $\beta_f = 5/12$ and even up to a fifth-order accuracy can be achieved, however the scheme can easily become unstable. For practical purposes, Shchepetkin and McWilliams [2005, 2008] recommend $\beta_f = 0.281105$, $\gamma_f = 0.088$ and $\epsilon_f = 0.013$ to obtain the scheme with a large stability range for waves, advection, and the Coriolis term. However, the scheme is still constrained by the CFL criterion (4.15) with $C_m \approx 0.89$ for the setting above. Note that the constrain is slightly more restrictive than in the FB scheme. For more detailed information about the FBgen scheme, see Shchepetkin and McWilliams [2005, 2008].

4.1.5 Predictor-corrector time-stepping scheme (PC)

The PC scheme is another modification of the FB scheme. The vertically integrated transport (velocity) and the SSH are computed in three steps. In the first (predictor) step, the SSH is advanced in time using the explicit scheme,

$$\eta^p = \eta^n - \left(\nabla\cdot\mathbf{U}^n\right)\gamma_{pc}\Delta t, \tag{4.22}$$

where γ_{pc} is the parameter. The computed SSH η^p is not the SSH in the actual time step, it is only its "prediction". Second, the vertically integrated transport (velocity) is computed using the "predicted" η_p,

$$\mathbf{U} + f\mathbf{k}\times\mathbf{U}^{n+\frac{1}{2}}\Delta t = \mathbf{U}^n - gh^n\nabla\eta^p\Delta t + h^n\mathbf{F}^n\Delta t, \tag{4.23}$$

where $\mathbf{U}^{n+\frac{1}{2}}$ is the AB3-extrapolated transport, see (4.18). Third, the SSH is "corrected" using the barotropic transport (velocity) from the second step using Eq. (4.17).

If $\gamma_{pc} = 0$, the predicted SSH equals the SSH from the previous time step, $\eta^p = \eta^n$. In that case, the FB and PC schemes are the same. If $\gamma_{pc} \neq 0$, the scheme gains some added dissipation. It can be shown that the scheme damps fast gravity gravity waves. It is also scale-selective, the damping is more rapid for small scales. This is the key benefit of the PC scheme with respect to the FB scheme. At the expense of one additional SSH equation, the PC scheme selectively damps the grid-scale noise. The scheme is used in the BT part of the full baroclinic LSOMG model.

4.2 Wind stress

The wind stress is generated by the wind blowing over the ocean surface. It is calculated from the wind velocity at 10 m height. Trenberth et al. [1990] and Timmermann et al. [2009] use the bulk formula,

$$\boldsymbol{\tau}_w = \rho_a C_D \left|\mathbf{u}_w\right| \mathbf{u}_w, \tag{4.24}$$

where ρ_a is the density of air, C_D is the drag coefficient and $\mathbf{u}_w$ is the wind velocity at 10 meters. Pacanowski [1987] suggests to use a more complex formula:

$$\boldsymbol{\tau}_w = \rho_a C_D \left|\mathbf{u}_w - \mathbf{u}\right| (\mathbf{u}_w - \mathbf{u}), \tag{4.25}$$

where the ocean surface velocity is not neglected with respect to the wind velocity.

The drag coefficient is either constant as in Timmermann et al. [2009], or it depends on the wind speed u_w, $u_w = |\mathbf{u}_w|$, as in Yelland and Taylor [1996] and Yelland et al. [1998],

$$C_D = \begin{cases} 10^{-3}\left(0.29 + \frac{3.1}{u_w} + \frac{7.7}{u_w^2}\right) & \text{if } 3 \leq u_w \leq 6 \text{ m/s}, \\ 10^{-3}\left(0.60 + 0.071 u_w\right) & \text{if } 6 \leq u_w \leq 26 \text{ m/s}. \end{cases} \tag{4.26}$$

In the baroclinic LSOMG model, the drag coefficient can also be computed from rather sophisticated bulk formulas in which the stability of atmosphere, its temperature etc. are taken into consideration, see Sec. 5.14.6.

4.3 Bottom friction

The bottom friction $\boldsymbol{\tau}_b$ is commonly parameterized by either a linear or a nonlinear form. The linear form is simply given by

$$\boldsymbol{\tau}_b = r\mathbf{u}, \tag{4.27}$$

where r is the friction parameter. The value of r is estimated as

$$r = \frac{H}{\tau_{dec}}, \tag{4.28}$$

where τ_{dec} is the typical decay time. Weatherly [1984] suggested to use the decay time between 100 and 200 days, which results in the friction-parameter values around 10^{-4} m s^{-1}.

The LSOMG uses the nonlinear form,

$$\boldsymbol{\tau_b} = C_b \left|\mathbf{u}\right| \mathbf{u}, \tag{4.29}$$

where C_b is the dimensionless friction coefficient. The typical values are between 1×10^{-3} and 3×10^{-3} [Adcroft et al., 2014]. For example, 2.5×10^{-3} in Timmermann et al. [2009]and 1×10^{-3} in Treguier [1992].

In order to avoid numerical instabilities, we follow Einšpigel and Martinec [2015] and Backhaus [1983] and use a semi-implicit discretization of the bottom friction. Consider, for example, the FBgen scheme,

$$\frac{h\mathbf{u} - h^n\mathbf{u}^n}{\Delta t} = -C_b\mathbf{u}|\mathbf{u}^n| + X, \tag{4.30}$$

where X denotes other terms in the momentum equation. The velocity in the current time step is

$$\mathbf{u} = \frac{h^n\mathbf{u}^n + X\Delta t}{h + C_b|\mathbf{u}^n|\Delta t}, \tag{4.31}$$

which reduces to Eq. (4.21) if there is no bottom friction.

Note that some models, which do not include tides explicitly, add the effect of tides into the bottom friction,

$$\boldsymbol{\tau_b} = C_b\mathbf{u}\sqrt{\left|\mathbf{u}\right|^2 + \left|\mathbf{u}_{tid}\right|^2}, \tag{4.32}$$

where $\mathbf{u}_{tid}$ is the horizontal velocity due to tides [Rivière et al., 2004]. Willebrand et al. [2001] and Griffies [2012] used $|\mathbf{u}_{tid}| = 0.05$ m s^{-1}.

4.4 Tidal forcing and tidal parameterizations

The tidal force $\mathbf{F}_{tid}$ can be expressed in terms of the second-degree tidal potential V_2 [Melchior, 1983],

$$\begin{aligned} V_2 = \frac{3}{4}\frac{GMa^2}{l^3} \Bigg[&\cos^2\phi\cos^2\delta\cos(2\tau) + \sin(2\phi)\sin(2\delta)\cos\tau \\ &+ 3\left(\sin^2\phi - \frac{1}{3}\right)\left(\sin^2\delta - \frac{1}{3}\right)\Bigg], \end{aligned} \tag{4.33}$$

where G is the gravitational constant, M is the mass of the celestial body, a is the Earth's radius, l is the geocentric distance between the Earth and the celestial body, δ is the declination of a celestial body and τ is the local hour angle, $\tau = \Omega t_G + \lambda - \alpha$, where t_G is the Greenwich sidereal mean time, λ is the longitude and α is the right ascension of a celestial body. We consider the gravitational attraction of two celestial bodies, the Moon and the Sun. The lunisolar tidal force has the form

$$\mathbf{F}_{tid} = \gamma_T\nabla(V_2^{Moon} + V_2^{Sun}), \tag{4.34}$$

where V_2^{Moon} and V_2^{Sun} are tidal potentials of the Moon and the Sun, respectively, and γ_T is the so called diminishing factor,

$$\gamma_T = 1 + k_T - h_T, \tag{4.35}$$

where k_T and h_T are the second-degree body tide Love numbers. The diminishing factor accounts for the elastic response of the Earth to tidal forcing. Values of the Love numbers are chosen to be equal to $k_T = 0.302$ and $h_T = 0.612$ [Melchior, 1983]. The values of α, δ and l, which determine the positions of the Moon and Sun, are found at each time step by the package of subroutines NOVAS F3.1 provided by the U.S. Naval Observatory [Kaplan et al., 2011].

The tidal force is applied only in the barotropic system. It means that we do not consider vertical variations of tidal force within the ocean since they are negligible. The implementation is adopted from the DEBOT model with the following speed improvements. The zonal and meridional components of the gradient of the tidal potential are

$$(\nabla V_2)_\lambda = -\frac{3}{4}\frac{GMa}{l^3}\Big[2\cos\phi\cos^2\delta\sin(2\tau) + 2\sin\phi\sin(2\delta)\sin\tau\Big], \tag{4.36}$$

$$\begin{aligned}(\nabla V_2)_\phi = \frac{3}{4}\frac{GMa}{l^3}\Big[&- \sin(2\phi)\cos^2\delta\cos(2\tau) + 2\cos(2\phi)\sin(2\delta)\cos\tau \\ &+ \sin(2\phi)(3\sin^2\delta - 1)\Big].\end{aligned} \tag{4.37}$$

The gradient of the tidal potential is computed at each time step. The formulas contain goniometric functions which makes the computation time consuming. Fortunately, it is not necessary to compute all the goniometric functions repeatedly. Consider that

$$\sin\tau = \sin(\Omega T_{Gr} - \alpha)\cos\lambda + \cos(\Omega T_{Gr} - \alpha)\sin\lambda, \tag{4.38}$$

$$\cos\tau = \cos(\Omega T_{Gr} - \alpha)\cos\lambda - \sin(\Omega T_{Gr} - \alpha)\sin\lambda \tag{4.39}$$

and analogically for $\sin(2\tau)$ and $\cos(2\tau)$. We thus have

$$\begin{aligned}(\nabla V_2)_\lambda = -\frac{3}{2}\frac{GMa}{l^3}\Big\{ &\cos\phi\Big[\cos^2\delta\sin[2(\Omega T_{Gr} - \alpha)]\cos(2\lambda) \\ &\quad + \cos^2\delta\cos[2(\Omega T_{Gr} - \alpha)]\sin(2\lambda)\Big] \\ &+ \sin\phi\Big[\sin(2\delta)\sin(\Omega T_{Gr} - \alpha)\cos\lambda \\ &\quad + \sin(2\delta)\cos(\Omega T_{Gr} - \alpha)\sin\lambda\Big]\Big\},\end{aligned} \tag{4.40}$$

$$\begin{aligned}(\nabla V_2)_\phi = \frac{3}{4}\frac{GMa}{l^3}\Big\{ &\sin(2\phi)\Big[-\cos^2\delta\cos[2(\Omega T_{Gr} - \alpha)]\cos(2\lambda) \\ &\quad + \cos^2\delta\sin[2(\Omega T_{Gr} - \alpha)]\sin(2\lambda) \\ &\quad + (3\sin^2\delta - 1)\Big] \\ &+ 2\cos(2\phi)\Big[\sin(2\delta)\cos(\Omega T_{Gr} - \alpha)\cos\lambda \\ &\quad - \sin(2\delta)\sin(\Omega T_{Gr} - \alpha)\sin\lambda\Big]\Big\}.\end{aligned} \tag{4.41}$$

The goniometric functions of δ and $(\Omega T_{Gr} - \alpha)$ are time dependent and are thus computed repeatedly at each time step. Nevertheless, these terms do not depend on geographic coordinates of a grid point and so they represent a small computation burden of a few numbers. On the other hand, the goniometric functions of λ and ϕ have to be evaluated on the computational grid but they are constant in time. It is thus sufficient to compute them once at the beginning and store them for the later use. It means that the time consuming computation of goniometric functions on a grid can be efficiently reduced to the multiplication of precomputed terms. The algorithm is especially useful if the model uses the generalized horizontal coordinates since the grid is irregular and longitudes and latitudes of points do not repeat.

As noted in Introduction, the attempts to model tides in a full OGCM exist but it is still not a common practice. Nevertheless, the tidal modelling itself is well established and the modern data-constrained models are able to predict tides, especially on the deep ocean, with reasonable accuracy, see Stammer et al. [2014]. Many tidal models are based on the barotropic models, e.g., FES2012 [Carrère et al., 2012], HAMTIDE12 [Taguchi et al., 2014] and TPXO8 [Egbert and Erofeeva, 2002]. Nevertheless, the experience has shown that the barotropic models based on the pure SWE are inaccurate. The reason is that the SWE are missing two important physical phenomena, the effect of self-attraction and loading and the tidal dissipation due to the breaking of internal tides. The SWE need to be supplemented with suitable parameterizations of these processes. In both cases, an additional term is added to the right-hand side of the momentum equation,

$$\mathbf{u}_{,t} = \cdots + \boldsymbol{\tau}_{sal} + \boldsymbol{\tau}_{iwd}, \tag{4.42}$$

where $\boldsymbol{\tau}_{sal}$ denotes the self-attraction and loading term and $\boldsymbol{\tau}_{iwd}$ denotes the internal wave drag term.

The self attraction and loading (SAL) describes the change of gravity field when the load is applied to the non-rigid Earth. In tidal modelling, the load is represented by water masses uplifted or pushed below the equilibrium surface. The gravity field is changed by the following three processes [Hendershott, 1972]:

- deformation of the Earth's surface when the load is applied
- displacement of the Earth's masses when the load is applied
- self-gravitation of the load itself

The computation of SAL effect should involve the spherical harmonic decomposition of the tidal SSH. This procedure is numerically demanding especially because it should be repeated at each time step. The LSOMG-BT model rather uses the so-called scalar approximation of SAL [Accad and Pekeris, 1978] in which $\boldsymbol{\tau}_{sal}$ is proportional to the SSH gradient,

$$\boldsymbol{\tau}_{sal} = \beta_s g \nabla \eta. \tag{4.43}$$

The coefficient β_s may in principle be spatially dependent but it is a constant in the LSOMG-BT model. The value of β_s varies from 0.060 to 0.095 in the literature, see Table 4.1. The default value in the LSOMG-BT model is 0.09

Paper	β_s
Buijsman et al. [2015a]	0.095
Arbic et al. [2010]	0.060
Arbic et al. [2004]	0.094
Thomas et al. [2001]	0.085
Accad and Pekeris [1978]	0.085

Table 4.1: Values of SAL coefficient β_s used by other authors.

which is approximately the average of values in Table 4.1 if we exclude somewhat anomalously low value of 0.06 used in Arbic et al. [2010].

In the process of tidal dissipation, a part of the tidal energy is transferred from the barotropic to baroclinic tides. The baroclinic tides then propagate in the ocean interior in the form of internal waves and they are losing their energy when breaking on rough topography. The $\boldsymbol{\tau}_{iwd}$ can be expressed as

$$\boldsymbol{\tau}_{iwd} = -\frac{\mathbf{C}_{iwd} \cdot \mathbf{u}}{h}, \tag{4.44}$$

where $\mathbf{C}_{iwd}$ is the internal wave drag tensor. The term has the form of a linear friction and so it is called the "internal wave drag" (IWD) or the "internal tide drag". Contrary to the bottom drag coefficient, the IWD tensor is not constant, it is spatially varying.

Several forms of the IWD tensor have been proposed. The LSOMG-BT model implements the scheme of Jayne and St. Laurent [2001] in which the IWD tensor is approximated by a scalar,

$$C_{iwd} = \frac{\pi}{L}\hat{H}^2 N_b, \tag{4.45}$$

where $\hat{H}$ is the bottom roughness, N_b is the buoyancy frequency at the sea bed and L is a tunable parameter. We set $L = 10$ km in the LSOMG-BT model in accordance with Green and Nycander [2013] and Buijsman et al. [2015b]. The buoyancy frequency is computed from the definition,

$$N^2 = -\left(\frac{g}{\rho_0}\right)\frac{\partial\rho}{\partial z}, \tag{4.46}$$

using the World Ocean Atlas 2013 [Locarnini et al., 2013, Zweng et al., 2013] temperature and salinity data. The density gradient in Eq. 4.46 is either computed using the chain rule,

$$\frac{\partial\rho}{\partial z} = \frac{\partial\rho}{\partial\theta}\frac{\partial\theta}{\partial z} + \frac{\partial\rho}{\partial S}\frac{\partial S}{\partial z}, \tag{4.47}$$

or it can alternatively be computed from the formula,

$$\frac{\partial\rho}{\partial z} = \frac{\rho^*(z) - \rho(z+\Delta z)}{\Delta z}, \tag{4.48}$$

where $\rho^*(z)$ is the density of a water parcel that was adiabatically displaced from depth z to $z+\Delta z$ [Smith et al., 2010]. We numerical proved that both approaches give virtually the same results.

The computed spatial distribution of buoyancy frequency is depicted in Fig. 4.1 (left panel). We compared our map with the result of Michael Schindelegger who computed the buoyancy frequency from the older World Atlas Ocean 2005. The resolutions of Schindelegger's and our maps are 1° and 0.25°, respectively. The Schindelegger's map is thus less detailed but the large-scale structures are qualitatively the same (not shown).

We have also computed the map of buoyancy frequency according to the approximate formula of Zaron and Egbert [2006],

$$N_b = N_{b0} \exp\left(\frac{z}{1300}\right), \tag{4.49}$$

where $N_{b0} = 5.24 \times 10^{-3}$. The result is depicted in Fig. 4.1 (right panel). There is a significant mismatch between the "full" and "approximate" maps. The full map contains small scale features that are missing in the approximate map and also the amplitudes are significantly larger in the full map in many regions. The approximation of Zaron and Egbert [2006] is merely a 1-D depth profile that is applied globally. The discrepancies are thus expected but they are surprisingly large.

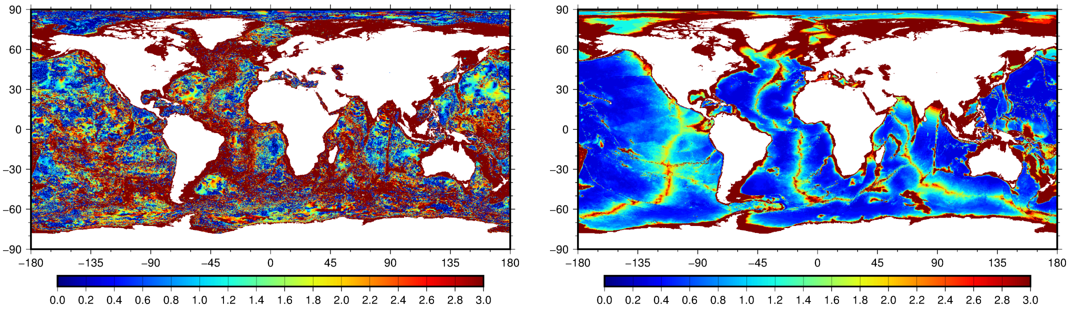

Figure 4.1: Buoyancy frequency [hour^{-1}] computed using the full formula (left panel) and approximate formula of Zaron and Egbert [2006] (right panel).

The bottom roughness $\hat{H}$ at the point with the geographic coordinates λ, ϕ is computed as a standard deviation of bathymetry data,

$$\hat{H}(\lambda, \phi) = \sqrt{\frac{1}{n} \sum_{\lambda', \phi'} \left[H(\lambda, \phi) - H(\lambda', \phi')\right]^2}, \tag{4.50}$$

where the summation goes over all wet grid points within the 1° × 1° rectangle centered to the point (λ, ϕ) and n is the total number of grid point in the summation.

The bottom roughness computed from the GEBCO [IOC, IHO and BODC, 2003] bathymetry data is depicted in the left panel of Fig. 4.2. We have not found any bottom-roughness maps in the literature thus we could not validate our map. However, if we compare the bottom roughness with the bottom topography, see the right panel of Fig. 4.2, the roughness seems to be correct. For example, the sharp bathymetry features in the West Pacific have large roughness while the ridges in the East Pacific are clearly visible in the bathymetry figure but their roughness is small since they are rising slowly from the deep ocean.

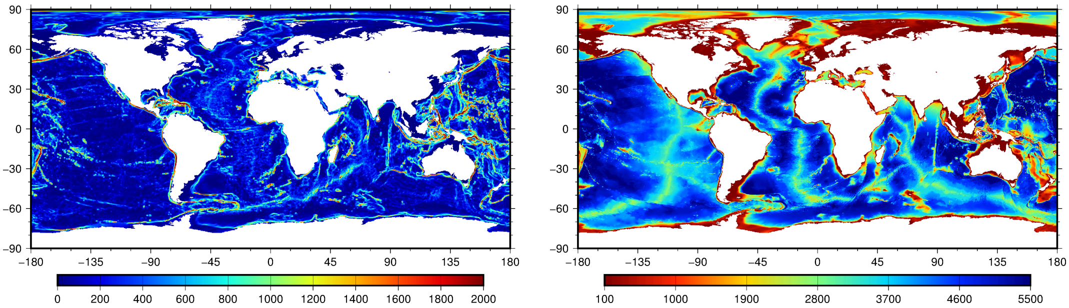

Figure 4.2: Bottom roughness [m] (left panel) computed from the GEBCO data and the GEBCO bathymetry [m] (right panel) on a 0.25° grid.

Note that Green and Nycander [2013] tested four fairly different schemes, the scheme of Nycander [2005] (NY), Jayne and St. Laurent [2001] (JS), Zaron and Egbert [2006] (ZE) and Baines [1982] (BA). The NY, JS and ZE schemes produce realistic global tidal dissipations around 1 TW, the BA scheme is out of range with 10 TW. The JS scheme has certain flaws. It is empirical (based on dimensional analysis) and the spatial structure of its dissipation rate below the 500-m depth is different than in the NY and ZE schemes. Nonetheless, Green and Nycander [2013] compared the computed SSH with the satellite measurements and the results were favourable. The best RMS difference of 7 cm was achieved by the NY scheme, the JS and ZE schemes achieved similar RMSs of 11 cm and 12 cm. We do not consider these differences to be significant for our purposes. On top of that, the IWD tensor is frequency-dependent in the NY and ZE schemes, which makes these schemes suitable for the frequency-domain models but not for the time-domain models such as LSOMG-BT.

4.5 Suppression of grid-scale noise on Arakawa grids B and E

Both Arakawa grids B and E are prone to generate grid-scale noise that affects velocity (vertically integrated transport) and SSH fields. In both cases, the noise has a checkerboard pattern, which is rotated by 45° on the Arakawa grid E.

On Arakawa grid B, the problem is caused by averaging present in the discrete form of the pressure gradient term. The pressure gradient of a two-grid-interval (checkerboard-like) wave is zero. The B-grid thus allows the stationary two-grid-interval wave to be a legitimate gravity-wave solution of the linear SWE without the Coriolis term. If the Coriolis term is present, the two-grid-interval waves appear as low-frequency inertia waves [Mesinger and Arakawa, 1976].

Janjic [1974] showed that the gravity-wave part of the linear SWE is fully discretized on the Arakawa grid C. The Arakawa grid E is composed of two Arakawa grids C which are shifted in a diagonal direction with respect to each other. The solutions on these subgrids are independent of each other and they may freely separate. In the full nonlinear SWE, there is communication between the subgrids via the Coriolis and advection terms, but the typical time-scale is much larger [Mesinger and Arakawa, 1976].

In the LSOMG model, we implement an additional term F_s on the right-hand side of the SSH equation to suppress the grid-scale noise. Griffies [2004] suggested to use a biharmonic operator on Arakawa grid B,

$$F_s = -\nabla_h \cdot A_s \nabla_h (\nabla_h \cdot A_s \nabla_h \eta), \tag{4.51}$$

where A_s is a spatially varying diffusivity. We express the governing equations in the geographic coordinates and use a diffusivity that scales with the quadrate of zonal grid spacing. The largest (equatorial) diffusivity is chosen to be lower than the maximum stable value A_s^{max} of the diffusivity for centered differences and explicit discretization in time [Griffies et al., 2000], $A_s^{max} = (\Delta x_{eq})^2/\sqrt{32\Delta t}$.

On the Arakawa grid E, we also use the biharmonic operator, but in the form,

$$F_s = -\nabla_h^\times \cdot A_s \nabla_h^\times (\nabla_h^\times \cdot A_s \nabla_h^\times \eta), \tag{4.52}$$

where $\nabla_h^\times$ is the nabla operator rotated by 45°. Note that Mesinger and Popovic [2010] derived a form of the smoothing term which is suitable for the Arakawa grid E,

$$F_s = -\frac{gh(\Delta t)^2}{4}\left(\Delta_h^\times \eta^n - \Delta_h \eta^n\right), \tag{4.53}$$

where Δ_h is the standard horizontal Laplacian and $\Delta_h^\times$ is the horizontal Laplacian rotated by 45°. However, the scheme was unstable in our computations unless we multiplied F_s by a suitable diminishing factor. Consequently, we rather use the biharmonic smoothing where the stability limits for the diffusivity are clearly stated.

4.6 Global singularity-free grids

We discussed the properties of the SC grid and introduced the dipolar/tripolar grids with relocated poles in Sec. 2.2. The SC grid as well as the dipolar/tripolar grids with relocated poles have singularities. The SC grid has singularities on poles. The grids with relocated poles have singularities in land areas which is favourable for the ocean modelling on the Earth since land areas are out of model's computational domain. However, if our task was to calculate the flow on a planet which is completely covered by oceans, there would be nowhere to relocate the poles. The so-called aqua-planet simulations require global grids that are free of singularities.

There exist several global singularity-free grids such as the cubed-sphere grid and the icosahedral grid. The cubed sphere grid is used in the MITgcm model Adcroft et al. [2014]. However, neither cubed-sphere grid nor icosahedral grid are orthogonal. We have rather chosen two different grids, the Yin-Yang (YY) grid and the reduced spherical coordinate (RSC) grid, and implemented them into the LSOMG model.

So far, we have tested both grids only in simple barotropic numerical tests that are presented in Sec. 6.2. Nevertheless, global singularity-free grids could also be useful for coupled simulations and paleocean models:

- The ocean model is typically coupled to the atmospheric model for which the computational domain covers the whole surface of the Earth. The relocation of singularities does not help similar to aqua-planet simulations. It is possible to use a different grid in each model and interpolate results, but the interpolation may introduce errors and reduce the accuracy of calculations.

- Paleocean models are sometimes used for long simulations. The land mask in these simulations may change due to melting of ice sheets. A fixed dipolar/tripolar configuration may not be suitable for such a simulation.

We bare these possible future applications in mind when we assess the performance of YY and RSC grids in our simple numerical tests.

4.6.1 Yin-Yang grid

The YY grid was introduced by Kageyama and Sato [2004]. Its name comes from the Chinese symbol for complementarity since the YY consists of two identical parts that are rotated by 90° and put together to cover the whole sphere.

The YY grid can either be non-optimized or optimized. The difference is that Yin and Yang subgrids overlap in certain regions in the non-optimized YY grid while there are no overlaps in the optimized YY grid. The Yin part (λ^i, ϕ^i) of non-optimized YY grid is a rectangle in the spherical coordinates (SC):

$$45^\circ \leq \lambda^i \leq 315^\circ, \qquad -45^\circ - \delta_1 \leq \phi^i \leq 45^\circ + \delta_2 \tag{4.54}$$

see the left panel in Fig. 4.3 and fig. 3 in Kageyama and Sato [2004]. The parameters δ_1 and δ_2 are discussed below.

There is an infinite number of optimized YY grids. We have chosen the YY grid which resembles a baseball, see the right panel in Fig. 4.3 and figs. 3 (a,c) in Kageyama and Sato [2004].

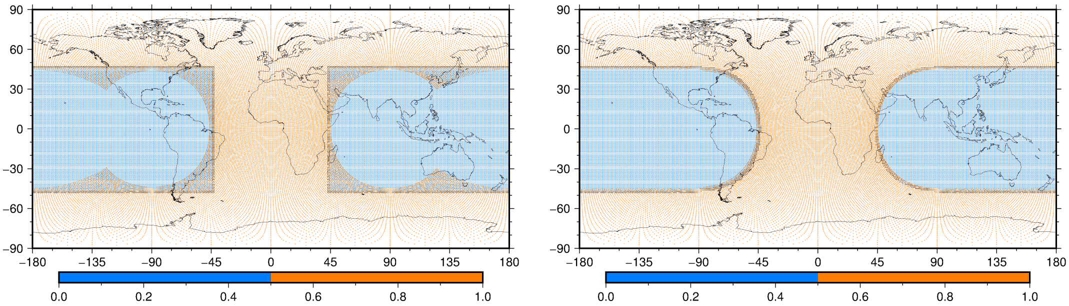

Figure 4.3: Non-optimized (left panel) and optimized (right panel) Yin (blue) and Yang (red) subgrids with Yin halo regions (black).

The transformation between Yin (λ^i, ϕ^i) and Yang (λ^a, ϕ^a) subgrids is [Baba et al., 2010]:

$$\phi^a = \arcsin(\cos\phi^i \sin\lambda^i) \tag{4.55}$$

$$\lambda^a = \arcsin\left(\frac{\sin\phi^i}{\cos\phi^a}\right) \tag{4.56}$$

The optimized YY grid is created from the non-optimized YY grid by dismissing all grid points that fulfill

$$\left|\lambda^i\right| < 90^\circ, \qquad |\phi^a| < 45^\circ - \delta_3, \tag{4.57}$$

where ϕ^a is computed from Eq. (4.55) and the parameter δ_3 is discussed below.

Both Yin and Yang parts of the YY grid are covered with the spherical coordinates. It brings two benefits. First, YY grid has a good grid cell aspect ratio. The SC grid has bad grid cell aspect ratio in polar regions that are not considered in the YY grid. Second, the usage of SC coordinates simplifies the implementation into the LSOMG model.

On the other hand, the use of a staggered C-grid complicates the implementation of YY grid into the LSOMG model since there are four types of grid points instead of only one. We construct the S-point grid first. The U-, V- and C-point grids are constructed from the S-point grid. The respective Yin part is shifted in zonal and/or meridional direction according to the point type and the Yang part is then constructed according to Eqs. (4.55) and (4.56). The consequence of our procedure is that all C-, S-, U- and V-point grids have the same number of inner and halo grid points. This may not be true if the individual grids were constructed independently to each other.

The Yin and Yang grids are coupled through their halo regions. We tested the bilinear and the inverse-distance-weighting (IDW) interpolations. Both interpolation techniques are described in Appendix D.1. Moreover, we have to consider that the Yin and Yang base vectors are mutually rotated. A similar problem is mentioned in Secs. 5.11.5 and 5.14.4. Let $\mathbf{u} = u^i \mathbf{e}^i_\lambda + v^i \mathbf{e}^i_\phi = u^a \mathbf{e}^a_\lambda + v^a \mathbf{e}^a_\phi$ be a vector, where $\mathbf{e}^i_\lambda$, $\mathbf{e}^i_\phi$and $\mathbf{e}^a_\lambda$, $\mathbf{e}^a_\phi$ are SC base vectors in Yin and Yang parts, respectively. Kageyama and Sato [2004] derived the transformation between the Yin and Yang vector components,

$$\begin{pmatrix} u^a \\ v^a \end{pmatrix} = R \begin{pmatrix} u^i \\ v^i \end{pmatrix} = \begin{pmatrix} -\sin\lambda^i \sin\lambda^a & \cos\lambda^i / \cos\phi^a \\ -\cos\lambda^i / \cos\phi^a & -\sin\lambda^i \sin\lambda^a \end{pmatrix} \begin{pmatrix} u^i \\ v^i \end{pmatrix}, \tag{4.58}$$

where R is the rotation matrix from Yin to Yang coordinate systems. The transformation from Yang to Yin components has exactly the same form only the Yin and Yang coordinates are exchanged since the Yin and Yang parts are complementary to each other. A further complication of C-grid is that zonal and meridional components are located at different points; U and V points. To compute zonal component at halo U points, we interpolate both zonal and meridional components to the U points, rotate the vector components at the U-points at keep the zonal component. The procedure is analogical at V points.

Eqs. (4.54) and (4.57) with $\delta_1 = \delta_2 = \delta_3 = 0$ can be used to successfully create Yin and Yang segments on a sphere. However, if a grid with a finite grid spacing is considered, it may happen that some Yin halo grid points will not be surrounded by four Yang inner grid points and vice versa. The requirement of four points is given by bilinear and IDW interpolations, it could be different for other interpolation types. The purpose of parameters δ_1, δ_2 and δ_3 is to adjust the YY grid. Parameters δ_1 and δ_2 are chosen in multiples of grid spacing d and δ_3 is a suitable positive real number. Notice that due to the rotation of vector components mentioned above, we have to check not only the interpolation at C-, S-, U- and V-point grids but also the interpolation from U- to V-point grids and vice versa.

For example, consider 1° resolution. The choice $\delta_1 = d$, $\delta_2 = 0$, $\delta_3 = 0.2$ leads to a correct S- and V-point grids but C- and U-point grids still contain problematic halo grid points. If we further set $\delta_2 = d$, C- and U-point grids become also correct. We use another setup which is given by $\delta_1 = \delta_2 = 0$, $\delta_3 = 1.1$ in our numerical tests. The reason is that the number of inner and halo grid points in this YY grid is lower than in the previous case.

Finally, the Coriolis term on the YY grid has the same form as on the SC grid. The proof is provided in Appendix D.2. The SWE are thus implemented as on the SC grid.

4.6.2 Reduced spherical coordinate grid

The RSC grid was introduced by Gates and Riegel [1962] and Kurihara [1965]. It is a modified SC grid. The key idea is to reduce the number of grid points in the zonal direction with the increasing latitude to increase the zonal grid spacing in higher latitudes. The early attempts to implement the RSC grid using the finite difference method were not successful due to large numerical errors in polar regions. The problem was attributed to the increased curvature of the parallel in the polar regions [Staniforth and Thuburn, 2012]. However, Starius [2014] argued that the real culprit is not the curvature but the small number of grid-points along the parallel.

Consider a standard SC grid with I grid points in the zonal direction and $J = I/2$ grid points in the meridional direction. The both latitudinal and longitudinal spacings are constant, $\Delta\lambda = \Delta\phi = 2\pi/I$. The RSC grid has the same number of parallels and thus also the same latitudinal spacing. The RSC grid of Staniforth and Thuburn [2012] is constructed from segments of parallels. The number of grid points on a parallel is constant within each segment and it is determined from the condition that the zonal grid interval is $\sqrt{2}$ times smaller/larger than the meridional grid step at maximum,

$$\frac{1}{\sqrt{2}} \leq \frac{\Delta\phi}{\cos\phi\Delta\lambda} \leq \sqrt{2}, \tag{4.59}$$

where $\Delta\lambda = (2\pi/I)/2^{n-1}$ in the n-th segment. The first segment is located around equator. Notice that the number of grid points on a parallel does not change gradually with increasing latitude. Instead, it is halved if the zonal grid step becomes too small. The segment which is closest to the South/North Pole always contains a single parallel with 8 grid points. The next two segments contain two parallels with 16 grid points and four parallels with 32 points, respectively. The RSC grid with C, S, U and V points is shown in Fig. 4.4.

Fig. 4.5 depicts a section of a RSC grid which corresponds to the five northernmost parallels. For simplicity, we depicted only S (blue circles) and U (red circles) points since C and V points are treated analogously. If a parallel has twice as many grid grid points as its neighbouring parallel, we call it a "dense" parallel and its neighbour a "coarse" parallel. The parallels $J-3$ and $J-1$ are dense, parallels $J-2$ and J are coarse, see Fig. 4.5.

It is straightforward to use the standard finite difference schemes in each segment of the RSC grid. However, a special attention is needed at bounding parallels of each segment since particular grid points in the neighbouring parallel could be missing. Let us start with S points. We interpolate in the zonal direction on coarse parallels to get values at "missing" S points. In Fig. 4.5, the missing S points have indeces $(3, J-2)$, $(7, J-2)$ and $(5, J)$ and are denoted by blue

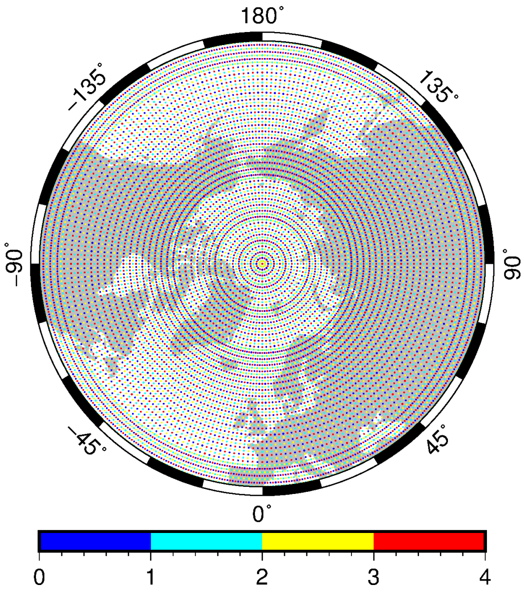

Figure 4.4: The reduced spherical coordinate grid viewed from the North Pole with C (blue), S (light blue), U (yellow) and V (red) points.

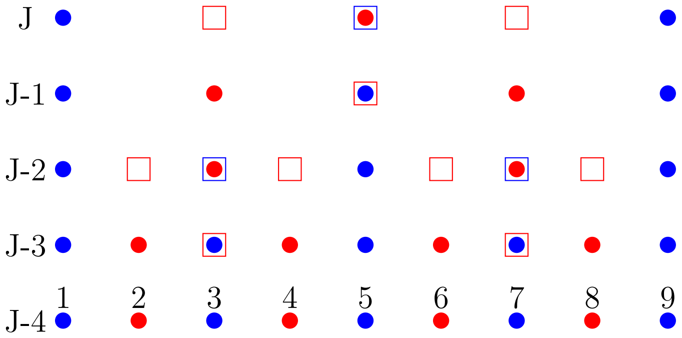

Figure 4.5: Sketch of the reduced spherical grid. Computational S and U points are denoted by blue and red circles, respectively. The S and U points at which we interpolate are denoted by blue and red squares, respectively.

squares. We use eight-point interpolation formula (D.23) as suggested in Starius [2014]. If C-grid was a collocated grid, no other considerations would be necessary. However, C-grid is a staggered grid and we also need to consider U points. Each U point is located in between two S points on a parallel. Consequently, U-point locations in coarse parallels are zonally shifted with respect to the U-point locations in dense parallels. We thus need to interpolate in both coarse and dense parallels to correctly couple U-point segments. We again use Eq. (D.23) to interpolate on coarse parallels but we use Eq. (D.24) to interpolate on dense parallels and get the missing U-point values.

If we linearize SWE (4.3), (4.4) and express them in spherical coordinates, we get:

$$U_{,t} - fV + \frac{gH}{a\cos\phi}\eta_{,\lambda} = HF_{\lambda}, \tag{4.60}$$

$$V_{,t} + fU + \frac{gH}{a}\eta_{,\phi} = HF_{\phi}, \tag{4.61}$$

$$\eta_{,t} + \frac{1}{a\cos\phi}\left[U_{,\lambda} + (\cos\phi\, V)_{,\phi}\right] = 0. \tag{4.62}$$

Function $(\cos\phi)^{-1}$ in Eqs. (4.60) and (4.62) goes to infinity at the poles. Our solution is to cover the whole sphere with S-point cells. Eqs. (4.60) and (4.62) can then be numerically solved in all U and S points. There is a V point on both North and South Poles. It would be possible to calculate meridional velocity components using Eq. (4.61) at the poles. The problem is that velocity is a vector quantity and vector directions are well defined in the vicinity of the poles in the SC coordinates but not at the poles. Starius [2014] suggested to project the polar cap onto the plane which is tangent to the sphere at the pole and replace the SC with the Cartesian coordinates. Let $\mathbf{e}_x$, $\mathbf{e}_y$ be the base vectors of the Cartesian coordinate system. The projection P of the base SC vectors to the Cartesian base is

$$P\mathbf{e}_{\lambda} = \cos\lambda\mathbf{e}_x + \sin\lambda\mathbf{e}_y, \tag{4.63}$$

$$P\mathbf{e}_{\phi} = (-\sin\lambda\mathbf{e}_x + \cos\lambda\mathbf{e}_y)\sin\phi \tag{4.64}$$

and thus the SC velocity components U, V transform to the Cartesian velocity components $\tilde{U}$, $\tilde{V}$ according to

$$\begin{pmatrix} \tilde{U} \\ \tilde{V} \end{pmatrix} = \begin{pmatrix} \cos\lambda & -\sin\lambda \\ \sin\lambda & \cos\lambda \end{pmatrix} \begin{pmatrix} U \\ V\sin\phi \end{pmatrix}. \tag{4.65}$$

Motivated by Starius [2014], we apply transformation (4.65) and then interpolate in the meridional direction using Eqs. (D.26) and (D.25) from U and V points to the poles, respectively. We use 16 meridians which correspond to the eight U and eight V points in the parallels closest the poles. Finally, we average the interpolated vector components to get one single vector at the pole. The inverse transformation is then used to determine the meridional component in the SC coordinates along the particular meridian. The truth is that the neat way is to transform Eqs. (4.60) and (4.61) into the Cartesian coordinates and solve the SWE on the tangent plane. We have not tested it. It is doable on a collocated grid but it is complicated on a staggered grid since we would need to average or interpolate the missing vector component and then use transformation (4.65). We suspect that especially the averaging of the zonal component in the zonal direction could be harmful due to the high curvature of parallels close to the poles.

5. Baroclinic LSOMG model

The LSOMG model solves the primitive equations 1.8-1.12 with the following boundary conditions at the surface,

$$w = \eta_{,t} - q_w, \tag{5.1}$$

$$q_w \mathbf{u} + A_V \mathbf{u}_{,z} = q_w \mathbf{u}_w + \frac{\boldsymbol{\tau}_w}{\rho_0}, \tag{5.2}$$

$$p = 0, \tag{5.3}$$

$$q_w C - \mathbf{F} \cdot \mathbf{N} = q_w C_w - \gamma_C h_1 \left(C_1 - C^{data} \right) + Q_C^{turb,0}, \tag{5.4}$$

at the bottom,

$$w = 0, \tag{5.5}$$

$$A_V \mathbf{u}_{,z} = \boldsymbol{\tau}_b, \tag{5.6}$$

$$\mathbf{F} \cdot \mathbf{N} = 0, \tag{5.7}$$

and at lateral boundaries,

$$\mathbf{u} \cdot \mathbf{N} = \mathbf{F}^{(\mathbf{u})} \cdot \mathbf{N} = \mathbf{F} \cdot \mathbf{N} = 0, \tag{5.8}$$

where N is the normal to the particular boundary. The boundary conditions are in accordance with Sec. 1.1 with the exception of boundary conditions (5.1) and (5.5) for the vertical velocity, see Sec. 1.1.2. The reason is that the equations presented in the first chapter are written for a model with a fully non-linear free surface while the LSOMG model uses an approximate linear free surface. The difference is that the barotropic transport $\mathbf{U}$ takes the full form $\mathbf{U} = \int_{-H}^{\eta} \mathbf{u} dz$ in the non-linear free surface approach but it is approximated by $\mathbf{U} = \int_{-H}^{0} \mathbf{u} dz$ in the linear free surface. At the same time, the horizontal advective and diffusive tracer fluxes above the reference surface $z = 0$ should be neglected, see secs. 4.5.1 and 5.2.1 in Smith et al. [2010] for further details.

5.1 Primitive equations in curvilinear coordinates

In order to discretize the primitive equations, which were described and discussed in Sec. 1.1, in the ocean model, they need to be written in certain coordinates. Consider a general orthogonal curvilinear coordinates with grid variables ξ_1, ξ_2, ξ_3. According to [Martinec, 2011], the unit base vectors $\mathbf{e_1}$, $\mathbf{e_2}$, $\mathbf{e_3}$ of the coordinate system are given by

$$\mathbf{e}_k = \frac{1}{h_k} \frac{\partial \mathbf{r}}{\partial \xi_k}, \qquad k \in \{1, 2, 3\} \tag{5.9}$$

where $\mathbf{r}$ is the radius vector and metric coefficients (or Lamé coefficients) h_1, h_2, h_3 are determined as follows,

$$h_k = \sqrt{\frac{\partial \mathbf{r}}{\partial \xi_k} \cdot \frac{\partial \mathbf{r}}{\partial \xi_k}}, \qquad k \in \{1, 2, 3\}, \tag{5.10}$$

In LSOMG, we suppose that $\mathbf{e}_3$ is parallel to the local vertical direction (positive upwards) and thus $\mathbf{e}_1$ and $\mathbf{e}_2$ are located in the horizontal plane tangent to the Earth's surface. The examples of horizontal coordinate grids were mentioned in Sec. 2.2. See also Sec. 5.11.

If the mapping between the orthogonal curvilinear system and the geographic coordinate system is known analytically, we can compute the metric terms analytically. Madec [2012] expresses $\mathbf{r}$ in the Cartesian base $\tilde{\mathbf{e}}_x$, $\tilde{\mathbf{e}}_y$, $\tilde{\mathbf{e}}_z$ using the geographic coordinates,

$$\mathbf{r} = (a+z)\left(\cos\phi\cos\lambda\mathbf{e}_x + \cos\phi\sin\lambda\mathbf{e}_y + \sin\phi\mathbf{e}_z\right) \tag{5.11}$$

and compute the metric coefficients from Eq. 5.10,

$$h_1 = (a+z)\sqrt{\left(\frac{\partial\lambda}{\partial\xi_1}\cos\phi\right)^2 + \left(\frac{\partial\phi}{\partial\xi_1}\right)^2}, \tag{5.12}$$

$$h_2 = (a+z)\sqrt{\left(\frac{\partial\lambda}{\partial\xi_2}\cos\phi\right)^2 + \left(\frac{\partial\phi}{\partial\xi_2}\right)^2}, \tag{5.13}$$

$$h_3 = \frac{\partial z}{\partial\xi_3}, \tag{5.14}$$

where he assumed that $\mathbf{e}_3$ is parallel to the local vertical direction (positive upwards). The horizontal metric coefficients h_1, h_2 are then independent of ξ_3,

$$\frac{\partial h_1}{\partial\xi_3} = \frac{\partial h_2}{\partial\xi_3} = 0. \tag{5.15}$$

Additionally, term $a+z$ in Eqs. 5.12 and 5.13 can be approximated by a since the value of z within the ocean is small with respect to the Earth's radius. This approximation is called the shallow ocean approximation (do not mix it up with the shallow water approximation) .

The supplementary programs that generate the computational grid for the LSOMG model do not use the analytic formulas 5.12-5.14. The reason is simple. We do not know the mapping between the orthogonal curvilinear system and the geographic coordinate system analytically for the grids listed in Sec. 5.11. We thus compute the metric coefficients numerically from Eq. 5.10 and the LSOMG model reads them from the input file.

If metric coefficients of a coordinate system are known, they can be used to express the differential operators in the governing equations. Murray and Reason [2001] and Madec [2012] provide forms of the individual terms which appear in the primitive equations (1.8)-(1.12) in the curvilinear coordinates that fulfil Eq. (5.15):

The momentum advection terms in Eq. (1.8) are expressed either in the so-called vector invariant form or the flux form. The vector invariant form is given by

$$[\nabla\cdot(\mathbf{v}\otimes\mathbf{v})]_h = \left[(\nabla\times\mathbf{v})\times\mathbf{v} + \frac{1}{2}\nabla(\mathbf{v}\cdot\mathbf{v})\right]_h = \zeta\mathbf{e}_3\times\mathbf{u} + \frac{1}{2}\nabla_h(\mathbf{u}\cdot\mathbf{u}) + \frac{1}{h_3}w\frac{\partial\mathbf{u}}{\partial\xi_3}, \tag{5.16}$$

where subscript h means the horizontal components of the 3-D vector and ζ is the relative vorticity defined by

$$\zeta = \mathbf{e}_3 \cdot (\nabla \times \mathbf{v}) = \frac{1}{h_1 h_2}\left[\frac{\partial(h_2 v)}{\partial \xi_1} - \frac{\partial(h_1 u)}{\partial \xi_2}\right]. \tag{5.17}$$

The nonlinear advection in the vector invariant form is thus composed of the relative vorticity term, the gradient of the kinetic energy and the vertical advection term. Note that the vector invariant form is natural on the C-grid, but it is not common in the B-grid models since it requires a larger grid stencil [Griffies et al., 2000]. The flux form yields

$$\begin{aligned}
&[\nabla \cdot (\mathbf{v} \otimes \mathbf{v})]_h = \nabla \cdot (\mathbf{v} \otimes \mathbf{u}) + M\mathbf{e}_3 \times \mathbf{v} \\
&= [\nabla \cdot (\mathbf{v}u) + Mv]\,\mathbf{e_1} + [\nabla \cdot (\mathbf{v}v) - Mu]\,\mathbf{e_2} \\
&= \left\{\frac{1}{h_1 h_2 h_3}\left[\frac{\partial}{\partial \xi_1}(h_2 h_3 uu) + \frac{\partial}{\partial \xi_2}(h_1 h_3 vu)\right] + \frac{1}{h_3}\frac{\partial}{\partial \xi_3}(wu) + (L_1 u - L_2 v)\right\}\mathbf{e_1} \\
&+ \left\{\frac{1}{h_1 h_2 h_3}\left[\frac{\partial}{\partial \xi_1}(h_2 h_3 uv) + \frac{\partial}{\partial \xi_2}(h_1 h_3 vv)\right] + \frac{1}{h_3}\frac{\partial}{\partial \xi_3}(wv) + (L_2 v - L_1 u)\right\}\mathbf{e_2},
\end{aligned} \tag{5.18}$$

where M is the advective metric frequency, $M = L_1 u - L_2 v$, and L_1 and L_2 are the grid-dependent coefficients,

$$L_1 = \frac{1}{h_1 h_2}\frac{\partial h_1}{\partial \xi_2}, \qquad L_2 = \frac{1}{h_1 h_2}\frac{\partial h_2}{\partial \xi_1}, \tag{5.19}$$

which are proportional to the divergence of grid lines in the directions of $\mathbf{e}_2$ and $\mathbf{e}_1$ vectors, respectively. Note that in the special case of spherical coordinates, the coefficient L_2 is equal to zero since the parallels do not converge,

$$L_1 = -\frac{\tan\phi}{a}, \qquad L_2 = 0. \tag{5.20}$$

Each component of the momentum advection in Eq. (5.18) is composed of two terms: The divergence of momentum flux and the horizontal advective metric term. That is the reason why it is called the flux form. In Eq. 5.18, the divergence of momentum flux is further expanded to the horizontal advective term (first term) and vertical advection of horizontal momentum (second term) in each component.

Horizontal pressure gradients normalized by the reference density in Eq. (1.8) are expressed as

$$-\frac{\nabla_h p}{\rho_0} = -\frac{1}{\rho_0}\left(\frac{1}{h_1}\frac{\partial p}{\partial \xi_1}\mathbf{e_1} + \frac{1}{h_2}\frac{\partial p}{\partial \xi_2}\mathbf{e_2}\right). \tag{5.21}$$

The continuity equations (1.10) becomes:

$$\nabla \cdot \mathbf{v} = \frac{1}{h_1 h_2 h_3}\left[\frac{\partial(h_2 h_3 u)}{\partial \xi_1} + \frac{\partial(h_1 h_3 v)}{\partial \xi_2}\right] + \frac{1}{h_3}\frac{\partial w}{\partial \xi_3} = 0. \tag{5.22}$$

The advective term in Eq. (1.11) has the form:

$$\nabla \cdot (\mathbf{v}C) = \frac{1}{h_1 h_2 h_3}\left[\frac{\partial(h_2 h_3 uC)}{\partial \xi_1} + \frac{\partial(h_1 h_3 vC)}{\partial \xi_2}\right] + \frac{1}{h_3}\frac{\partial(wC)}{\partial \xi_3}. \tag{5.23}$$

If we use the small slope diffusive flux (1.79), the diffusive term in Eq. (1.11) is

$$\begin{aligned}\nabla \cdot \mathbf{F} = \frac{1}{h_1 h_2 h_3} \Bigg\{ & \frac{\partial}{\partial \xi_1} \left[h_2 h_3 \left(K_H \frac{1}{h_1} \frac{\partial C}{\partial \xi_1} + K_H s_x \frac{1}{h_3} \frac{\partial C}{\partial \xi_3} \right) \right] \\ & + \frac{\partial}{\partial \xi_2} \left[h_1 h_3 \left(K_H \frac{1}{h_2} \frac{\partial C}{\partial \xi_2} + K_H s_y \frac{1}{h_3} \frac{\partial C}{\partial \xi_3} \right) \right] \Bigg\} \\ + \frac{1}{h_3} \frac{\partial}{\partial \xi_3} & \left[K_H \left(s_x \frac{1}{h_1} \frac{\partial C}{\partial \xi_1} + s_y \frac{1}{h_2} \frac{\partial C}{\partial \xi_2} \right) + (K_H s^2 + K_V) \frac{1}{h_3} \frac{\partial C}{\xi_3} \right], \end{aligned} \tag{5.24}$$

where $\mathbf{s}$ is given by Eq. (1.73) in which the gradients of temperature and salinity are expressed similarly to the pressure gradient (5.21). If we combine the neutral diffusion with the stirring by eddies according to Eq. 1.93, we obtain

$$\begin{aligned}\nabla \cdot \mathbf{F} = \frac{1}{h_1 h_2 h_3} & \left[\frac{\partial}{\partial \xi_1} \left(h_2 h_3 K_H \frac{1}{h_1} \frac{\partial C}{\partial \xi_1} \right) + \frac{\partial}{\partial \xi_2} \left(h_1 h_3 K_H \frac{1}{h_2} \frac{\partial C}{\partial \xi_2} \right) \right] \\ + \frac{1}{h_3} \frac{\partial}{\partial \xi_3} & \left[2 K_H \left(s_x \frac{1}{h_1} \frac{\partial C}{\partial \xi_1} + s_y \frac{1}{h_2} \frac{\partial C}{\partial \xi_2} \right) + (K_H s^2 + K_V) \frac{1}{h_3} \frac{\partial C}{\xi_3} \right]. \end{aligned} \tag{5.25}$$

The convergence of the barotropic transport in Eq. (1.12) is given by

$$-\nabla_h \cdot \mathbf{U} = -\frac{1}{h_1 h_2} \left[\frac{\partial (h_2 U)}{\partial \xi_1} + \frac{\partial (h_1 V)}{\partial \xi_2} \right], \tag{5.26}$$

where $\mathbf{U} = U \mathbf{e}_1 + V \mathbf{e}_2$.

5.2 Time stepping

The LSOMG model is using a linear free surface. Contrary to the rigid-lid method that was commonly used in the OGCMs in the past, the linear free surface allows modelling of tides. However, the wave field is richer in the free-surface model which makes the numerical solution of the governing equations more complicated. In particular, the incompressibility condition 1.10 excludes sound waves, but the surface (external) gravity waves (such as tidal waves) are retained, they are filtered out only if the rigid-lid method is used. Unfortunately, the surface gravity waves are rather fast. It can be shown by solving the linear SWE that these nondispersive waves propagate with the speed of $v_g = \sqrt{gH}$. The speed of surface gravity waves may thus reach 200 m/s in the regions where the ocean is deep. Consequently, the presence of surface gravity waves severely restricts the time step of explicit time-stepping schemes via the CFL criterion (4.15).

Madala and Piacseki [1977], Berntsen et al. [1981] and Killworth et al. [1991] suggested to use the split-explicit scheme in which they split the fast (barotropic, external) and slow (baroclinic, internal) dynamical modes and evolve them with different time steps. The speed of the fastest (first) baroclinic mode is approximately 2 m/s which is about two orders of magnitude smaller than the speed of the barotropic mode. A stable baroclinic time step is thus much larger than the stable barotropic time step (or the time step of the unsplitted system) provided the advective and diffusive CFL criteria are less restrictive. Besides that, the

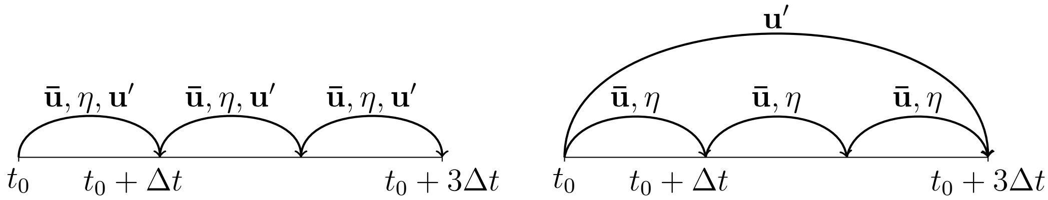

Figure 5.1: Time stepping of the barotropic velocity $\bar{\mathbf{u}}$, the barotropic SSH η and the baroclinic velocity $\mathbf{u}'$ in the unsplitted (left panel) and split-explicit (right panel) scheme. In the unsplitted scheme, both the barotropic and baroclinic time steps are the same. In the split-explicit scheme, the baroclinic time step is extended and the barotropic system is subcycled.

baroclinic system is 3-D but the barotropic system is only 2-D. The split-explicit scheme thus allows us to evolve the 3-D part of the system with a significantly extended time step. The unsplitted and split-explicit schemes are compared in Fig. 5.1.

In the LSOMG model, we separate the barotropic modes by vertical averaging of the governing equations. It is known that this method is not flawless, the vertically averaged system is the same as the barotropic system only in an idealized case, see Sec. 4.3 in Smith et al. [2010]. Nonetheless, the experience from other OGCMs proves that the split by vertical averaging is useful and the energy leakage between the vertically averaged and baroclinic systems is not a critical issue. Let us write the momentum equation 1.8 in the form:

$$\mathbf{u}_{,t} + f\mathbf{e}_3 \times \mathbf{v} = -g\nabla_h\eta + \mathbf{F}_{tid} + \mathbf{G}, \tag{5.27}$$

where the first term on the right-hand side is the surface pressure gradient, $\mathbf{F}_{tid}$ is the tidal force and $\mathbf{G}$ is the baroclinic forcing which contains all the terms in the momentum equation that depend on the vertical coordinate,

$$\mathbf{G} = -\frac{\nabla_h p}{\rho_0} + \mathbf{F}_H^{(\mathbf{u})} + \mathbf{F}_V^{(\mathbf{u})} - \left[\nabla \cdot (\mathbf{v} \otimes \mathbf{v})\right]_h, \tag{5.28}$$

where p denotes the baroclinic part of the total pressure,

$$p(z) = g \int_z^0 \rho(z')dz'. \tag{5.29}$$

The vertically integrated momentum equation and the evolution equation for the SSH compose the barotropic system,

$$\bar{\mathbf{u}}_{,t} + f\mathbf{e}_3 \times \bar{\mathbf{u}} = -g\nabla\eta + \mathbf{F}_{tid} + \bar{\mathbf{G}}, \tag{5.30}$$

$$\eta_{,t} = -\nabla_h \cdot (H\bar{\mathbf{u}}), \tag{5.31}$$

where $\bar{\mathbf{G}}$ is assumed to be constant during one time step. Note that the barotropic system is equivalent to the linear SWE with forcing $\mathbf{F}_{tid} + \bar{\mathbf{G}}$ on the right-hand side of the vertically integrated momentum equation.

The baroclinic velocities $\mathbf{u}'$ are computed in two steps. First, the provisional velocities $\mathbf{u}_p$ are computed from the momentum equation without the depth-independent surface pressure gradient and tidal forcing on the right-hand side,

$$\mathbf{u}_{p,t} + f(\mathbf{k} \times \mathbf{u}_p) = \mathbf{G}, \tag{5.32}$$

where the baroclinic forcing $\mathbf{G}$ is evaluated explicitly in time using the actual velocities $\mathbf{v}$ not the provisional velocities $\mathbf{u}_p$. The baroclinic velocities are then computed from the provisional velocities by removing their vertical mean,

$$\mathbf{u}' = \mathbf{u}_p - \bar{\mathbf{u}}_p. \tag{5.33}$$

The LSOMG model propagates the velocity, SSH, temperature and salinity in time. We use the time stepping scheme described in Griffies [2004] in which the physical quantities are staggered in time. The barotropic and baroclinic velocities are discretized on integer time steps, whereas the SSH, tracer C (temperature and salinity) and thus also density and pressure are discretized on half integer time steps. The time staggering ensures the second-order accurate discretization in time. One model time step is depicted in Fig. 5.2.

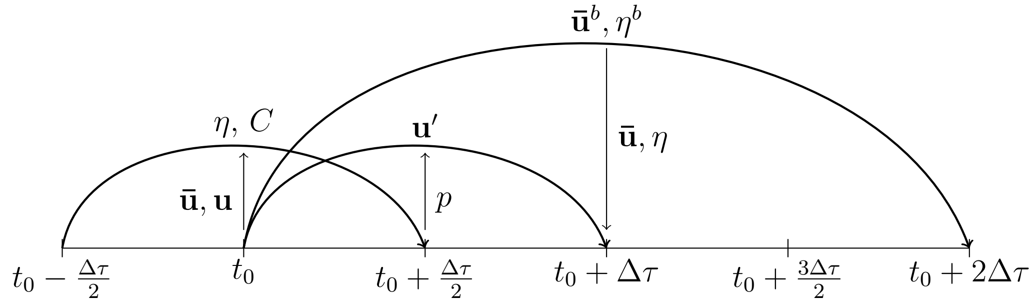

Figure 5.2: Time stepping used in the LSOMG model.

The SSH and tracer values are known at time $t = t_0 - \frac{\Delta\tau}{2}$, where $\Delta\tau$ is the baroclinic time step, and velocities are known at $t = t_0$. We first advance surface elevations to $t = t_0 + \frac{\Delta\tau}{2}$ using the barotropic velocities at $t = t_0$ and modify the thicknesses of the surface-layer cells by the newly computed elevations. We then compute temperature and salinity fields at $t = t_0 + \frac{\Delta\tau}{2}$ using the total velocities at $t = t_0$. The density at $t = t_0 + \frac{\Delta\tau}{2}$ is computed from the updated temperature and salinity distributions. Baroclinic forcing such as the pressure gradients is computed at $t = t_0 + \frac{\Delta\tau}{2}$. We compute the vertical average of the baroclinic forcing and advance the barotropic system in time. As already mentioned, the LSOMG model uses the split-explicit method which means that the barotropic system is discretized explicitly in time and thus the barotropic time step Δt is small but the baroclinic time step $\Delta\tau$ is significantly larger. We typically use the baroclinic time step that is 60 times larger than the barotropic time step. In the practical usage, there can arise some stability issues. We thus propagate the barotropic system not only to $t = t_0 + \Delta\tau$ but to $t = t_0 + 2\Delta\tau$ and then average the barotropic quantities computed during subcycling to obtain the final value at $t = t_0 + \Delta\tau$,

$$\bar{\mathbf{u}}(t + \Delta\tau) = \frac{1}{N} \sum_{n=0}^{N-1} \bar{\mathbf{u}}^b(t + n\Delta t), \tag{5.34}$$

$$\eta(t + \Delta\tau) = \frac{1}{N+1} \sum_{n=0}^{N} \eta^b(t + n\Delta t), \tag{5.35}$$

where $\bar{\mathbf{u}}^b$ and η^b are barotropic velocities and SSH computed in the barotropic system prior to the averaging and N is the total number of barotropic subcycles per one baroclinic time step,

$$N = \frac{2\Delta\tau}{\Delta t}. \tag{5.36}$$

The averaging ensures the stability of the splitting method. Finally, the baroclinic velocities are advanced to $t = t_0 + \Delta\tau$ using the baroclinic forcing from $t = t_0 + \frac{\Delta\tau}{2}$ and the total velocities are assembled by adding barotropic and baroclinic velocities together.

5.3 Vertical grid

The LSOMG model provides two options how to set up the vertical grid, see Fig. 5.3. The first option is to give the depths of tracer points (blue dots in the figure). The depths of vertical-velocity points (blue crosses in the figure) are then computed, the vertical-velocity points are located exactly between the two neighbouring tracer points. The second option is to do this in an exactly opposite way; the depths of vertical-velocity points are defined and the depths of tracer points are computed.

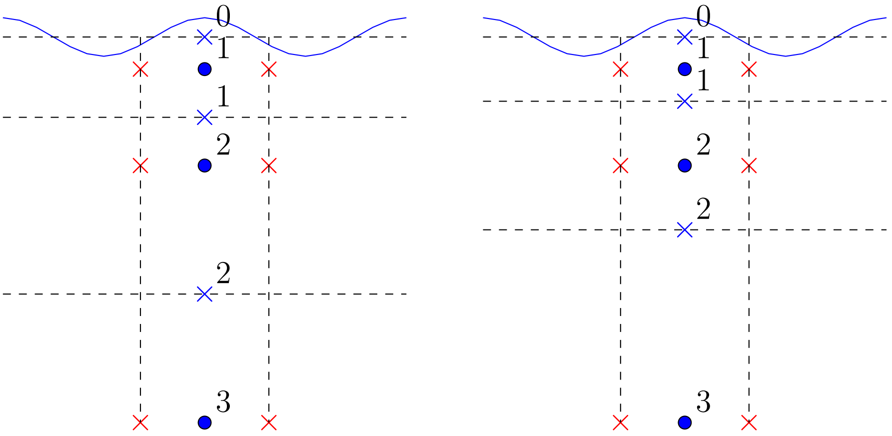

Figure 5.3: Vertical grid-point discretizations available in the LSOMG model. Tracers (temperature and salinity), density and pressure are discretized at blue dots. Horizontal and vertical velocities are discretized at red and blue crosses, respectively. The discretization in the left panel is used in the LSG model. It is retained also in the LSOMG model, but LSOMG uses the discretization in the right panel by default.

The first option was used in the original LSG model. In the LSOMG model, we prefer the second option since it is more suitable for the computation of vertical velocity and tracers are discretized in the middle of tracer cells, which is assumed in the implemented tracer advection schemes.

The original ad-hoc choice of vertical layers has been replaced by a semi-automatically generated distribution. The purpose is to provide a better distribution of layer thicknesses that varies smoothly with depth. It is determined from prescribed smooth distributions of thicknesses h and level depths z of Madec

[2012],

$$h(K) = \left| -h_a - h_b \tanh\left(\frac{K - h_{th}}{h_{cr}}\right) \right|, \tag{5.37}$$

$$z(K) = h_{sur} - h_a K - h_b h_{cr} \log\left[\cosh\left(\frac{K - h_{th}}{h_{cr}}\right)\right]. \tag{5.38}$$

Eqs. (5.37) and (5.38) contain four unknowns h_a, h_b, h_{th}, h_{sur} and a tunable parameter h_{cr}. The smooth thickness and depth distributions have to fulfill the following four conditions,

$$h(0.5) = h_3(1), \tag{5.39}$$

$$h(k_{max} - 0.5) = h_3(k_{max}), \tag{5.40}$$

$$z(0) = 0, \tag{5.41}$$

$$z(k_{max}) = H_{max}, \tag{5.42}$$

where k_{max} is the total number of layers, $h_3(1)$ and $h_3(k_{max})$ are thicknesses of the first and last layer, respectively, and H_{max} is the maximum depth. Eqs (5.39)-(5.42) constitute a system of four nonlinear equations for the four unknown variables. We solve the system in Matlab using the Levenberg-Marquardt algorithm with the initial guess taken from Madec [2012]. Fig. 5.4 shows results for $k_{max} = 11$, $h_3(1) = 50$ m, $h_3(k_{max}) = 1000$ m, $h_{cr} = 2.3$ and $H_{max} = 5000$ m in the left panel and $k_{max} = 22$, $h_3(1) = 25$ m, $h_3(k_{max}) = 500$ m, $h_{cr} = 3$ and $H_{max} = 5000$ m in the right panel.

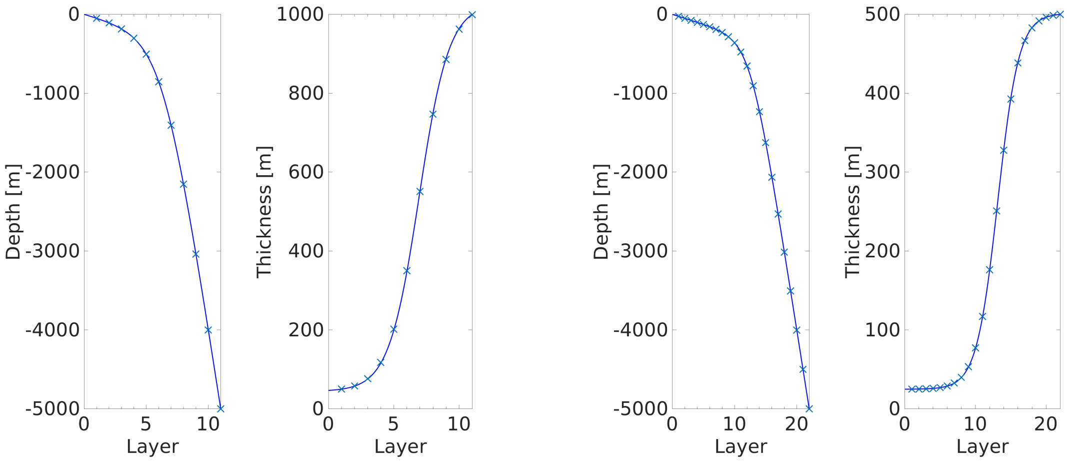

Figure 5.4: Computed depth and thickness distributions. Left panels: $k_{max} = 11$, $h_3(1) = 50$ m, $h_3(k_{max}) = 1000$ m, $h_{cr} = 2.3$ and $H_{max} = 5000$ m. Right panels: $k_{max} = 22$, $h_3(1) = 25$ m, $h_3(k_{max}) = 500$ m, $h_{cr} = 3$ and $H_{max} = 5000$ m.

Note that the LSOMG model uses the partial bottom cells. It means that the depth of vertical layers are the same in each water column with the exception of the bottom face of the deepest wet cell. This cell is allowed to stretch or shrink to fit the bathymetry. However, the shift of bottom face is limited by the positions of the nearest tracer points.

5.4 Density and related variables

5.4.1 Density

The state equation in the LSOMG model is the EOS of McDougall et al. [2003] with the values of coefficients from Jackett et al. [2006] . The density is expressed in the rational form,

$$\rho(S,\theta,p) = \frac{P_1(S,\theta,p)}{P_2(S,\theta,p)}, \tag{5.43}$$

where $P_1(S,\theta,p)$ and $P_2(S,\theta,p)$ are polynomials,

$$\begin{aligned} P_1 &= a_0 + a_1\theta + a_2\theta^2 + a_3\theta^3 + a_4 S + a_5 S\theta + a_6 S^2 + a_7 p + a_8 p\theta^2 \\ &\quad + a_9 pS + a_{10} p^2 + a_{11} p^2\theta^2, \qquad (5.44) \\ P_2 &= b_0 + b_1\theta + b_2\theta^2 + b_3\theta^3 + b_4\theta^4 + b_5 S + b_6 S\theta + b_7 S\theta^3 + b_8 S^{\frac{3}{2}} \\ &\quad + b_9 S^{\frac{3}{2}}\theta^2 + b_{10} p + b_{11} p^2\theta^3 + b_{12} p^3\theta, \qquad (5.45) \end{aligned}$$

where S, θ and p are expressed in PSU, °C and db, respectively. The polynomials P_1 and P_2 are evaluated numerically using the Horner scheme to reduce the number of multiplications,

$$\begin{aligned} P_1 &= a_0 + \theta\left[a_1 + \theta\left(a_2 + a_3\theta\right)\right] + S\left(a_4 + a_5\theta + a_6 S\right) \\ &\quad + p\left[a_7 + a_8\theta^2 + a_9 S + p\left(a_{10} + a_{11}\theta^2\right)\right], \qquad (5.46) \\ P_2 &= b_0 + \theta\left\{b_1 + \theta\left[b_2 + \theta(b_3 + b_4\theta)\right]\right\} \\ &\quad + S\left[b_5 + \theta\left(b_6 + b_7\theta^2\right) + S^{1/2}\left(b_8 + b_9\theta^2\right)\right] \\ &\quad + p\left[b_{10} + p\left(b_{11}\theta^2 + b_{12} p\right)\theta\right]. \qquad (5.47) \end{aligned}$$

Further details about this EOS, such as its accuracy and comparison with the EOS-80 which is the EOS used in the LSG model, can be found in Sec 1.4.1.

5.4.2 Thermal expansion and saline contraction coefficients

Thermal expansion and saline contraction coefficients are needed for the computation of neutral direction slopes according to Eq. (1.73). In fact, only the ratio of the two coefficients is needed since

$$\mathbf{s} = \frac{-\frac{\alpha_T}{\beta_S}\nabla\theta + \nabla S}{-\frac{\alpha_T}{\beta_S}\theta_{,z} + S_{,z}}. \tag{5.48}$$

The ration α_T/β_S is expressed using the definition (1.71),

$$\frac{\alpha_T}{\beta_S} = -\frac{\left(\frac{\partial\rho}{\partial\theta}\right)_{S,p}}{\left(\frac{\partial\rho}{\partial S}\right)_{\theta,p}} = -\frac{\frac{\partial P_1}{\partial\theta} - \rho\frac{\partial P_2}{\partial\theta}}{\frac{\partial P_1}{\partial S} - \rho\frac{\partial P_2}{\partial S}}, \tag{5.49}$$

where we inserted the density in the rational form (5.43). The derivatives in Eq. (5.49) are expressed using Eqs. (5.46) and (5.47) as

$$\frac{\partial P_1}{\partial \theta} = a_1 + \theta(2a_2 + 3a_3\theta) + a_5 S + 2p\theta(a_8 + a_{11}p), \tag{5.50}$$

$$\begin{aligned}\frac{\partial P_2}{\partial \theta} &= b_1 + \theta\left[2b_2 + \theta(3b_3 + 4b_4\theta)\right] + S\left[b_6 + \theta(3b_7\theta + 2b_9\sqrt{S})\right] \\ &\quad + p^2(3b_{11}\theta^2 + b_{12}p),\end{aligned} \tag{5.51}$$

$$\frac{\partial P_1}{\partial S} = a_4 + a_5\theta + 2a_6 S + a_9 p, \tag{5.52}$$

$$\frac{\partial P_2}{\partial S} = b_5 + \theta\left(b_6 + b_7\theta^2\right) + 1.5\sqrt{S}\left(b_8 + b_9\theta^2\right). \tag{5.53}$$

5.5 Diffusion of tracers

5.5.1 Form of diffusion term

In the LSOMG model, tracers are diffused either in the horizontal-vertical directions or in the epineutral-vertical directions. In both cases:

- The diffusion is characterized by two diffusivity values: The diffusivity in the horizontal/epineutral direction and the diffusivity in the vertical direction.
- The horizontal/epineutral diffusion is treated explicitly in time while the vertical diffusion is treated implicitly in time. The implicit discretization in time is used to ensure numerical stability even for large values of vertical diffusivity. In certain LSOMG configurations, large vertical diffusivities are prescribed in gravitationally unstable grid cells to substitute the unresolved convection processes, see Sec. 5.9.

In the horizontal-vertical diffusion, the horizontal diffusion is represented by the Laplacian operator. The epineutral-vertical diffusion is more complicated. The epineutral diffusion in the LSOMG is implemented under the small slope approximation (see Sec. 1.3.2) and it is combined with the parameterization of mesoscale eddies of Gent and McWilliams [1990], Gent et al. [1995] (see Sec. 1.3.3). The resulting tracer flux is available in two forms in the LSOMG model. The general form is given by Eq. (1.92). However, if the epineutral and eddy-induced diffusivities are the same, the simplified form given by Eq. (1.93) is also directly available.

The standard C-grid discretization of epineutral flux contains combined differencing and averaging of the tracer in one direction. The resulting operator has a null space and it does not damp the two-grid-interval noise in that particular direction. It can be used in combination with certain adjustments such as the filtering of neutral direction slopes. We rather implemented a different technique. It is the triad algorithm of Griffies et al. [1998]. The algorithm is similar to the EEN scheme for the Coriolis term in 5.8. In contrast to the standard discretization of epineutral flux, the tracer gradient is multiplied by other terms before it is averaged to the grid-cell face which solves the null-space problem. In more details, the flux is computed as an area-weighted average from four terms from the neighbouring points. Each term contain the differencing (gradient) of tracer multiplied by the diffusivity and the component of the slope (or its quadrate). The algorithm is called the triad algorithm since each slope component is computed from three points. The horizontal gradients in the numerator of (1.73) are computed at the horizontal faces of tracer cells without averaging. Similarly, the vertical gradients in the denominator of (1.73) are computed at the vertical faces of tracer cells without averaging. The algorithm is explained in details in Madec [2012].

5.5.2 Diffusivity

Vertical diffusivity

The LSOMG model provides two options for the vertical diffusivity. It is either the vertical profile of Bryan and Lewis [1979] or the Richardson-number based parameterization of Pacanowski and Philander [1981].

A constant vertical diffusivity is a crude approximation of the real distribution in the ocean, which varies in both lateral and vertical directions. The first-order approximation is a vertical diffusivity which varies with depth. Bryan and Lewis [1979] suggested to use a depth-dependent vertical diffusivity in the form

$$K_V = 10^{-4}\left\{0.8 + \frac{1.05}{\pi}\arctan\left[4.5\times10^{-3}(|z|-2500)\right]\right\}. \qquad (5.54)$$

The dependency (5.54) is based on the measurements of Gregg [1977] that showed a minimum vertical mixing in the thermocline and its increase down to the abyss. The surface value of vertical diffusivity, 3×10^{-5} m^2/s, is based on the work of Rooth and Östlund [1972] and the value in the deep ocean, 1.3×10^{-4} m^2/s, was suggested by Munk [1966] for the deep Pacific ocean. Griffies et al. [2005] preferred slightly different values. They use 1.2×10^{-4} m^2/s in the deep ocean. In the upper ocean, they use either 1×10^{-5} m^2/s or 3×10^{-5} m^2/s; the higher value is used in high latitudes.

$$K_V = 10^{-4}\left\{0.647 + \frac{1.160}{\pi}\arctan\left[4.5\times10^{-3}(|z|-2500)\right]\right\} \quad \text{in low latitudes,} \qquad (5.55)$$

$$K_V = 10^{-4}\left\{0.748 + \frac{0.949}{\pi}\arctan\left[4.5\times10^{-3}(|z|-2500)\right]\right\} \quad \text{in high latitudes.} \qquad (5.56)$$

The choice of latitudinal dependence of vertical diffusivity is based on observations. However, Griffies et al. [2005] also noted that the main motivation was to reduce the model bias in the subpolar North Atlantic which they found to be caused by the biased wind stress.

The LSOMG model adopts the vertical profile from the LSG model,

$$K_V = 10^{-4}\left\{0.95 + \frac{0.75}{\pi}\arctan\left[4.5\times10^{-3}(|z|-2500)\right]\right\}. \qquad (5.57)$$

The values in the deep ocean are similar to the original (5.57) but the upper ocean is more diffusive than in the original or the MOM implementation, see Fig. 5.5.

The major flaw of the vertical profile of Bryan and Lewis [1979] is that the lateral dependence is completely neglected. Pacanowski and Philander [1981]

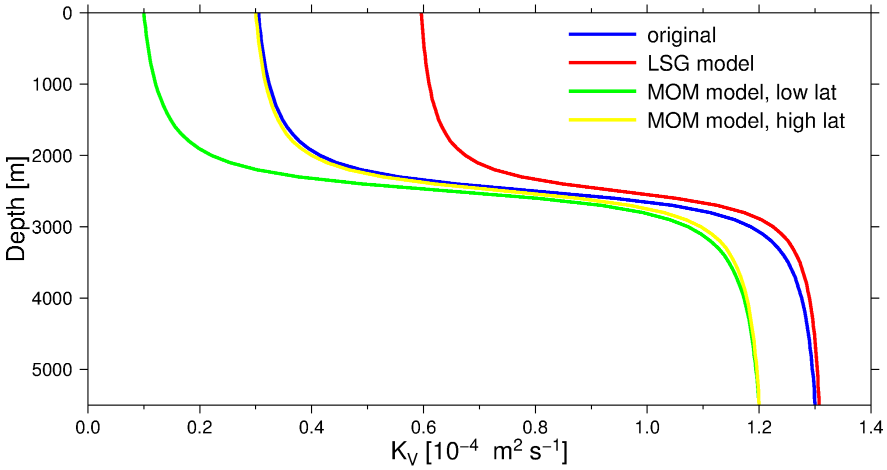

Figure 5.5: Comparison of depth profiles of vertical diffusivity according to Bryan and Lewis [1979] and the implementations in the LSG and MOM models.

suggested to use a parameterization in which both vertical viscosity and diffusivity depend on the Richardson number Ri,

$$Ri = \frac{N^2}{|\mathbf{u}_{,z}|^2}, \tag{5.58}$$

where N is the buoyancy frequency given by Eq. (4.46).

$$A_V = \frac{A_{V0}}{(1+5Ri)^2} + A_{Vb}, \tag{5.59}$$

$$K_V = \frac{A_V}{1+5Ri} + K_{Vb} \tag{5.60}$$

where A_{Vb} and K_{Vb} are constant background values of vertical viscosity and diffusivity, respectively, and A_{V0} is a tunable parameter. Pacanowski and Philander [1981] used $A_{Vb} = 1 \times 10^{-4}$ m^2/s, $K_{Vb} = 1 \times 10^{-5}$ m^2/s and proposed to use A_{V0} between 5×10^{-3} m^2/s and 1.5×10^{-2} m^2/s.

The implementations in the CLIO, MPI-OM and NEMO models use slightly modified equations. They keep Eq. (5.59) for the viscosity but Eq. (5.60) for the diffusivity is replaced by

$$K_V = \frac{K_{V0}}{(1+5Ri)^3} + K_{Vb}. \tag{5.61}$$

All three implementations attempt to increase the mixing in the surface mixed layer. However, the methods how it is done and how the mixed-layer depth is calculated are different.

- In the CLIO model, A_{V0} and K_{V0} are not constant [Goosse et al., 1999]. They are both set equal to 1×10^{-2} m^2/s from the bottom to 50 m depth and then they increase to the surface value of 1×10^{-1} m^2/s. Minimum surface values are also prescribed, $A_V = 1 \times 10^{-3}$ m^2/s and $K_V = 3 \times 10^{-5}$ m^2/s. The background vertical viscosity is $A_{Vb} = 1 \times 10^{-4}$ m^2/s and the vertical profile of Bryan and Lewis [1979] type is used for the vertical diffusivity.

Paper	A_{V0} [10^{-2} m^{2}s^{-1}]	A_{Vb} [10^{-4} m^{2}s^{-1}]	K_{Vb} [10^{-5} m^{2}s^{-1}]
PP81	0.5-1.5	1	1
G99	1	1	profile
M2003	1	1	1
L2001	0.5	0.5	0.1
F2017	0.5	0.01	0.01

Table 5.1: Comparison of coefficient values used in different implementations of the Richardson number based parameterization of Pacanowski and Philander [1981] in the deep ocean. PP81=Pacanowski and Philander [1981], G99=Goosse et al. [1999], M2003=Marsland et al. [2003], L2001=Lermusiaux [2001], F2017=Federico et al. [2017]

- The implementation in the MPI-OM model as explained in Marsland et al. [2003] use constant A_{V0} and K_{V0}, $A_{V0} = K_{V0} = 1 \times 10^{-2}$ m^2/s. The mixing is the surface mixed layer is increased by adding an additional term in both Eqs. (5.59) and (5.61). The new term represents a wind induced contribution that is proportional to the cube of wind speed (with a factor 5×10^{-4} m^2/s) and it decays exponentially with depth. The penetration depth in which the wind-induced mixing decreases to e^{-1} is chosen to be 40 m. The local static stability and ice cover are also taken into consideration. The background values are $A_{Vb} = 1 \times 10^{-4}$ m^2/s and $K_{Vb} = 1 \times 10^{-5}$ m^2/s.

- The implementation in the NEMO model is based on the paper of Lermusiaux [2001]. The scheme is also discussed in Federico et al. [2017]. The quantities A_{V0}, K_{V0}, A_{Vb} and K_{Vb} are constant as in the MPI-OM model but their values are different: $A_{V0} = K_{V0} = 5 \times 10^{-3}$ m^2/s in both Lermusiaux [2001] and Federico et al. [2017], $A_{Vb} = 5 \times 10^{-5}$ m^2/s, $K_{Vb} = 1 \times 10^{-6}$ m^2/s in Lermusiaux [2001] and $A_{Vb} = 1 \times 10^{-6}$ m^2/s, $K_{Vb} = 1 \times 10^{-7}$ m^2/s in Federico et al. [2017]. The mixed-layer depth is given by the Ekman depth H_E,

  $$H_E = C_E \frac{u_f}{f}, \tag{5.62}$$

  where C_E is the empirical parameter and u_f is the turbulent friction velocity,

  $$u_f = \sqrt{\frac{|\boldsymbol{\tau}|}{\rho_0}}. \tag{5.63}$$

  Lermusiaux [2001] uses $C_E = 0.04$ but Federico et al. [2017], Madec [2012] and Griffies [2012] use $C_E = 0.7$. Within the surface mixed layer, Lermusiaux [2001] used $A_V = 1.5 \times 10^{-3}$ m^2/s, $K_V = 7.5 \times 10^{-5}$ m^2/s and Federico et al. [2017] used $A_V = 1.5 \times 10^{-3}$ m^2/s, $K_V = 5 \times 10^{-4}$ m^2/s.

The values of A_{V0}, A_{Vb} and K_{Vb} used in the above mentioned papers are summarized in Table 5.1 for a quick reference.

The LSOMG model offers the simple implementation with a constant mixed-layer depth from the CLIO model and the more sophisticated implementation from the NEMO model.

Epineutral (horizontal) diffusivity

The epineutral (horizontal) diffusivity in the LSOMG model is given by the vertical profile of Bryan and Lewis [1979],

$$K_H = K_{Hb} + (K_{Hs} - K_{Hb})e^{-\frac{|z|}{500}}, \tag{5.64}$$

where K_{Hb} is the epineutral diffusivity in the deep ocean (to be exact for z→ $-\infty$) and K_{Hs} is the epineutral diffusivity at the ocean surface. Contrary to the vertical diffusivity, the epineutral diffusivity is decreasing with depth according the this profile. The same profile was used in the LSG model and we also kept the same values of coefficients, $K_{Hs} = 1000$ m^2/s, $K_{Hb} = 500$ m^2/s.

5.6 Friction force

5.6.1 Form of friction force

The friction force in the LSOMG model is implemented according to Murray and Reason [2001]. The partial bottom cells are not considered in the original paper but we discuss in Appendix B.1 that the formulas remain valid. The fluid is assumed to be transversely isotropic with respect to the vertical coordinate ξ_3. The friction force can then be written as

$$\begin{aligned}
\mathbf{F}^{(\mathbf{u})} \cdot \mathbf{e}_1 = \frac{1}{h_1 h_2 h_3} \Bigg\{ & \frac{1}{h_2} \frac{\partial}{\partial \xi_1} \left\{ h_2^2 h_3 A_H \left[\frac{h_2}{h_1} \frac{\partial}{\partial \xi_1} \left(\frac{u}{h_2} \right) - \frac{h_1}{h_2} \frac{\partial}{\partial \xi_2} \left(\frac{v}{h_1} \right) \right] \right\} \\
& + \frac{1}{h_1} \frac{\partial}{\partial \xi_2} \left\{ h_1^2 h_3 A_H \left[\frac{h_2}{h_1} \frac{\partial}{\partial \xi_1} \left(\frac{v}{h_2} \right) + \frac{h_1}{h_2} \frac{\partial}{\partial \xi_2} \left(\frac{u}{h_1} \right) \right] \right\} \Bigg\} \\
+ \frac{1}{h_3} \frac{\partial}{\partial \xi_3} & \left(\frac{A_V}{h_3} \frac{\partial u}{\partial \xi_3} \right),
\end{aligned} \tag{5.65}$$

$$\begin{aligned}
\mathbf{F}^{(\mathbf{u})} \cdot \mathbf{e}_2 = \frac{1}{h_1 h_2 h_3} \Bigg\{ & \frac{1}{h_2} \frac{\partial}{\partial \xi_1} \left\{ h_2^2 h_3 A_H \left[\frac{h_2}{h_1} \frac{\partial}{\partial \xi_1} \left(\frac{v}{h_2} \right) + \frac{h_1}{h_2} \frac{\partial}{\partial \xi_2} \left(\frac{u}{h_1} \right) \right] \right\} \\
& - \frac{1}{h_1} \frac{\partial}{\partial \xi_2} \left\{ h_1^2 h_3 A_H \left[\frac{h_2}{h_1} \frac{\partial}{\partial \xi_1} \left(\frac{u}{h_2} \right) - \frac{h_1}{h_2} \frac{\partial}{\partial \xi_2} \left(\frac{v}{h_1} \right) \right] \right\} \Bigg\} \\
+ \frac{1}{h_3} \frac{\partial}{\partial \xi_3} & \left(\frac{A_V}{h_3} \frac{\partial v}{\partial \xi_3} \right).
\end{aligned} \tag{5.66}$$

The terms that contain viscosity A_H represent the horizontal friction, the terms that contain viscosity A_V represent the vertical friction in accordance with Eqs. 1.34 and 1.35. Eqs. (5.65) and (5.66) can be expressed in a more compact form,

$$\begin{aligned}
\mathbf{F}^{(\mathbf{u})} \cdot \mathbf{e}_1 = {} & \frac{1}{h_1 h_2 h_3} \left[\frac{1}{h_2} \frac{\partial}{\partial \xi_1} \left(h_2^2 h_3 A_H D_T \right) + \frac{1}{h_1} \frac{\partial}{\partial \xi_2} \left(h_1^2 h_3 A_H D_S \right) \right] \\
& + \frac{1}{h_3} \frac{\partial}{\partial \xi_3} \left(\frac{A_V}{h_3} \frac{\partial u}{\partial \xi_3} \right),
\end{aligned} \tag{5.67}$$

$$\begin{aligned}
\mathbf{F}^{(\mathbf{u})} \cdot \mathbf{e}_2 = {} & \frac{1}{h_1 h_2 h_3} \left[\frac{1}{h_2} \frac{\partial}{\partial \xi_1} \left(h_2^2 h_3 A_H D_S \right) - \frac{1}{h_1} \frac{\partial}{\partial \xi_2} \left(h_1^2 h_3 A_H D_T \right) \right] \\
& + \frac{1}{h_3} \frac{\partial}{\partial \xi_3} \left(\frac{A_V}{h_3} \frac{\partial v}{\partial \xi_3} \right),
\end{aligned} \tag{5.68}$$

where the horizontal tension D_T and the horizontal shearing strain D_S given by Eqs. (1.56) and (1.57) are equal to

$$D_T = \frac{h_2}{h_1}\frac{\partial}{\partial \xi_1}\left(\frac{u}{h_2}\right) - \frac{h_1}{h_2}\frac{\partial}{\partial \xi_2}\left(\frac{v}{h_1}\right), \tag{5.69}$$

$$D_S = \frac{h_2}{h_1}\frac{\partial}{\partial \xi_1}\left(\frac{v}{h_2}\right) + \frac{h_1}{h_2}\frac{\partial}{\partial \xi_2}\left(\frac{u}{h_1}\right). \tag{5.70}$$

Notice that although the transverse isotropy is described by five independent eddy viscosities, Eqs. (5.67) and (5.68) contain only two viscosities, A_H and A_V. The number is reduced by the trace-free condition for the stress tensor, Eq. (1.47), the incompressibility condition, Eq. (1.10), and the quasi-hydrostatic approximation (the last assumption in Sec. 1.2.1).

From the numerical point of view, the choice of Arakawa grid C is advantageous since both D_T and D_S can be discretized without any averaging. The D_T term is discretized at SSH points (S points in the left panel of Fig. 5.10) and the D_S term is discretized at the corners of elementary grid cells (C points in the left panel of Fig. 5.10). The friction force itself can then be also computed without averaging. Note that we set the D_S term equal to zero at dry points, the D_T term is equal to zero at dry points automatically from its definition.

The friction force given by Eqs. (5.67) and (5.68) can also be used in the purely barotropic LSOMG-BT ocean model if we consider that the barotropic fluid is moving as a whole column without any variations in the vertical direction. According to this view, the third metric coefficient is replaced by the water-column height and the horizontal tension and shearing strain are calculated using the barotropic velocities. The vertical shears of horizontal velocities are zero in the whole water column except for the ocean surface and bottom where their values are prescribed through boundary conditions (5.2) and (5.6) which gives rise to the second and third term on the right-hand side of Eq. (4.5). A more rigorous derivation in the spherical coordinates and with a constant eddy viscosity A_H is provided in Einšpigel and Martinec [2015], see Appendix B.2.

The friction force can also be written in an alternative form,

$$\begin{aligned} \mathbf{F}^{(\mathbf{u})} \cdot \mathbf{e}_1 = {} & \nabla_h \left(A_H \nabla_h u\right) + \frac{1}{h_3}\frac{\partial}{\partial \xi_3}\left(\frac{A_V}{h_3}\frac{\partial u}{\partial \xi_3}\right) \\ & + \left(M_1 \frac{\partial v}{\partial \xi_1} - M_2 \frac{\partial v}{\partial \xi_2}\right) + (N_1 u + N_2 v), \end{aligned} \tag{5.71}$$

$$\begin{aligned} \mathbf{F}^{(\mathbf{u})} \cdot \mathbf{e}_2 = {} & \nabla_h \left(A_H \nabla_h v\right) + \frac{1}{h_3}\frac{\partial}{\partial \xi_3}\left(\frac{A_V}{h_3}\frac{\partial v}{\partial \xi_3}\right) \\ & + \left(M_1 \frac{\partial u}{\partial \xi_1} - M_2 \frac{\partial u}{\partial \xi_2}\right) + (N_1 v + N_2 u). \end{aligned} \tag{5.72}$$

The first two terms in Eqs. (5.71) and (5.72) represent the classical Laplacian diffusion of linear momentum. The terms in the first and second bracket are the first- and second-order metric terms, respectively. The particular form of M_1, M_2, N_1 and N_2 can be found in Murray and Reason [2001]. In the special case of spherical coordinates and constant viscosity, Eq. (5.71) reduces to Eq. (1.50). In the special case of Cartesian coordinates, Eq. (5.71) reduces to Eq. (1.51).

The horizontal friction $\mathbf{F}_H^{(\mathbf{u})}$ is discretized explicitly in time in the LSOMG model. The vertical friction $\mathbf{F}_V^{(\mathbf{u})}$ can be discretized either explicitly or implicitly in time, both discretizations are available in the LSOMG model. The implicit discretization ensures a stable computation. If it is selected, the coupling between cells within one water column arises for each component of the momentum equation. Consequently, the system of linear equations needs to be solved to obtain the velocities within each water column. The system matrix is tridiagonal. The problem is similar to the implicit treatment of vertical diffusion of temperature and salinity.

5.6.2 Viscosity

Horizontal viscosity

The horizontal viscosity A_H is set according to Smagorinsky [1963] and Smagorinsky [1993],

$$A_H = \left(k_H \frac{d}{\pi}\right)^2 D, \tag{5.73}$$

where d is the local grid spacing, k_H is the dimensionless scaling parameter and D is the deformation rate,

$$D = \sqrt{D_T^2 + D_S^2}. \tag{5.74}$$

The local grid spacing d is computed according to Griffies and Hallberg [2000] as a minimum of the grid spacings along the horizontal directions $\mathbf{e}_1$, $\mathbf{e}_2$,

$$d = \min\left(h_1 \Delta\xi_1, h_2 \Delta\xi_2\right). \tag{5.75}$$

The value of viscosity is tuned by parameter k_H. Griffies and Hallberg [2000] suggest values from 2.2 to 4. The default value in the LSOMG model is $k_H = 4$.

The Smagorinsky viscosity is physically more correct than the constant viscosity. It is computed from the tension and shearing strain and thus it is automatically increased when the flow becomes vigorous and it is kept low otherwise. It is also quite appealing from the numerical point of view since both D_T and D_S need to be computed anyway to evaluate the horizontal friction, see Eqs. 5.67 and 5.68.

The value of viscosity is bounded by three criteria in the LSOMG model. One criterion limits the maximum and the other two criteria the minimum allowed value of viscosity.

- The horizontal friction is discretized explicitly in time in LSOMG. Consequently, the viscosity can not exceed the value given by the CFL criterion,

  $$A_H < \frac{d^2}{4\Delta t}, \tag{5.76}$$

  otherwise the scheme would become unstable.

- The model needs to resolve the viscous boundary layer. [Munk, 1950] has shown that the boundary-layer width L_M is equal to

  $$L_M = \frac{\pi}{\sqrt{3}} \left(\frac{A_H}{\beta}\right)^{\frac{1}{3}}, \tag{5.77}$$

where β is the meridional gradient of planetary vorticity. In order to resolve the Munk boundary layer, the grid spacing d needs to be smaller than the width of the boundary layer, $d < L_M$. If the grid spacing is given, it restricts the horizontal viscosity,

$$A_H > \beta \left(\frac{d\sqrt{3}}{\pi} \right)^3 . \tag{5.78}$$

Griffies and Hallberg [2000] notes that it is a common practice to resolve the Munk layer by at least two grid points.

- Besides the minimum viscosity limit imposed by the presence of Munk boundary layer, there is a condition based on the grid Reynolds number. Bryan et al. [1975] showed that for centered finite-difference schemes, it is desirable to ensure that

  $$A_H > \frac{U_R d}{2}, \tag{5.79}$$

  otherwise the viscosity is not large enough to dissipate the noise generated by the advection term and the solution becomes noisy. The coefficient U_R represents the advection velocity. The default value of U_R in the LSOMG model is 0.4 m/s according to Smith and McWilliams [2003].

Fig. 5.6 shows the minimum viscosity according to the Munk and grid Reynolds criteria at the Equator. The grid Reynolds criterion is more restrictive than the Munk criterion even for the 2° resolution. Since we do not expect to run the LSOMG model for coarser resolutions than 2°, the Munk criterion should not be decisive.

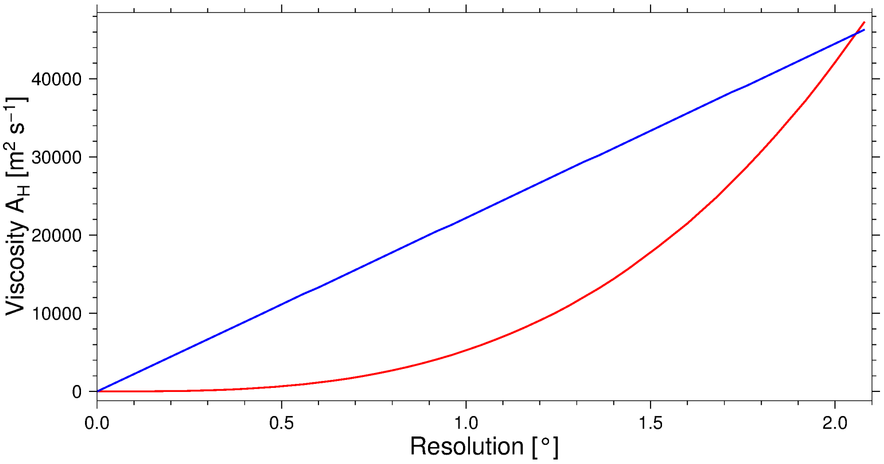

Figure 5.6: Minimum viscosity according to the Munk (red) and grid Reynolds (blue) criteria.

Table 5.2 summarizes the values of horizontal viscosity used in other OGCMs. Models are run using different resolutions, the viscosity values are thus not directly comparable. In order to do such comparison, we recompute the viscosity values to 1° resolution assuming the viscosity is proportional to the grid size squared, $A_H \propto d^2$, as in Eq. (5.73). The viscosity based on the grid Reynolds number is equal to $A_H = 2.2 \times 10^4$ m^2/s which is roughly comparable to the recomputed constant viscosities used in other OGCMs.

OGCM	Resolution	A_H [m^{2}s^{-1}]	A_H^{1dg} [m^{2}s^{-1}]	Paper
HadGEM1	1/3°	2.0×10^3	1.80×10^4	Johns et al. [2006]
CLIMBER-3	3.75°	3.2×10^5	2.28×10^4	Montoya et al. [2005]
UVIC	3.6°	2.5×10^5	1.93×10^4	Weaver et al. [2001]
NCAR CSM	2.3°	8.0×10^4	1.51×10^4	Gent et al. [1998]
CLIO	3.0°	1.0×10^5	1.11×10^4	Campin and Goosse [1999]
MITgcm	0.9°	5.0×10^3	6.20×10^3	Adcroft [1995]
LSG	3.5°	4.0×10^5	3.27×10^4	Weijer et al. [2002]
LSG	3.5°	5.0×10^4	4.08×10^3	Maier-Reimer et al. [1993]
MOM	4.0°	1.0×10^6	6.25×10^4	Danabasoglu et al. [1994]
DYNAMO	1.2°	8.0×10^3	5.56×10^3	Gulev et al. [2003]

Table 5.2: Values of horizontal viscosity used in other OGCMs. The value A_H^{1dg} is the original value A_H recomputed to 1° resolution.

Vertical viscosity

The vertical viscosity in the ocean is several orders of magnitude smaller than the horizontal viscosity. Montoya et al. [2005], Gulev et al. [2003], Weaver et al. [2001] and Gent et al. [1998] used a constant vertical viscosity $A_V = 1 \times 10^{-3}$ m^2/s. Larger values has also been used in the community. Danabasoglu et al. [1994] used $A_V = 2 \times 10^{-3}$ m^2/s and the default constant (background) viscosity in the NEMO 3.4 model is $A_V = 2 \times 10^{-3}$ m^2/s [Madec, 2012]. The default value in the LSOMG model is $A_V = 1 \times 10^{-3}$ m^2/s.

5.7 Advection schemes

The original LSG model uses the QUICK advection scheme of Leonard [1979], see Sec. 2.4.4. Its implementation follows Farrow and Stevens [1995]. The scheme is third-order accurate in space and second-order accurate in time. The QUICK advection scheme is an acceptable choice, but artificial numerical overshoots may occur in the solution since the scheme does not contain flux limiters.

We mentioned in Sec. 2.4 that simple schemes such as the centered second-order or first-order upwind schemes are not suitable for a realistic OGCM. On the other hand, the higher-order schemes have their own drawbacks. Godunov [1959] showed that only the first-order schemes can be monotonic. The purpose of flux limiter is to combine the first-order and higher-order advection schemes and take the best of both. If the solution is smooth without steep gradients and jumps, it is possible to use a higher order (e.g., second-order or third-order) advection scheme. On the other hand, if steep gradients and jumps are present, a flux limiter switches the scheme back to the first-order advection scheme. The truth is that a flux limiter reduces amplitudes of advected tracers due to the diffusive nature of the first-order advection scheme. However, a good flux limiter reduces amplitudes only little.

A flux limiter should also be total-variation diminishing (TVD) where total variation ν_{tot} in 1-D is defined as

$$\nu_{tot} = \int_a^b \left| \frac{\partial C}{\partial x} \right| dx. \tag{5.80}$$

If we consider an equidistant grid with n grid points, the total variation ν_{tot} is equal to

$$\nu_{tot} = \sum_{i=1}^{n} \left| C_i - C_{i-1} \right|. \tag{5.81}$$

A higher total variation thus corresponds to a more oscillatory function. A TVD scheme does not increase total variation of the tracer when it is stepped forward in time,

$$\nu_{tot}(t + \Delta t) \leq \nu_{tot}(t). \tag{5.82}$$

We have implemented three new advection schemes with flux limiters into the LSOMG model.

5.7.1 Lax-Wendroff scheme

The scheme is based on the Lax-Wendroff algorithm,

$$F_{i+\frac{1}{2}} = F^{up}_{i+\frac{1}{2}} + \frac{|u_{i+\frac{1}{2}}|}{2} \left(\frac{\Delta x_I - |u_{i+\frac{1}{2}}| \Delta t}{\Delta x_{i+\frac{1}{2}}} \right) \delta_{i+\frac{1}{2}} C, \tag{5.83}$$

where $F^{up}_{i+\frac{1}{2}}$ is the first-order upwind flux (2.12) and index I is defined by Eq. (2.13). The Lax-Wendroff scheme can be viewed as the upwind scheme with the correction term added. Eq. (5.83) represents its general form, it is valid for both equidistant and non-equidistant grids. The Lax-Wendroff scheme is stable with explicit time-stepping schemes but it produces spurious oscillations [Leonard, 1991].

It is thus necessary to add a flux limiter ψ,

$$F_{i+\frac{1}{2}} = F^{up}_{i+\frac{1}{2}} + \psi(\gamma_{i+\frac{1}{2}}) \frac{|u_{i+\frac{1}{2}}|}{2} \left(\frac{\Delta x_I - |u_{i+\frac{1}{2}}| \Delta t}{\Delta x_{i+\frac{1}{2}}} \right) \delta_{i+\frac{1}{2}} C, \tag{5.84}$$

where

$$\gamma_{i+\frac{1}{2}} = \begin{cases} \frac{C_i - C_{i-1}}{C_{i+1} - C_i} & \text{if } u_{i+\frac{1}{2}} > 0, \\ \frac{C_{i+2} - C_{i+1}}{C_{i+1} - C_i} & \text{if } u_{i+\frac{1}{2}} < 0. \end{cases} \tag{5.85}$$

A good flux limiter can not be an arbitrary function of γ although there is a rich variety of flux limiters. We mention the van Leer [Van Leer, 1974], van Albada [Van Albada et al., 1997], minmod [Roe, 1986] and Barth-Jespersen [Barth and Jespersen, 1989] flux limiters. In order to achieve a TVD advection scheme, the flux limiter has to fall into the TVD region in the Sweby diagram [Sweby, 1984],

$$0 \leq \psi(\gamma) \leq 2, \tag{5.86}$$

$$0 \leq \frac{\psi(\gamma)}{\gamma} \leq 2, \tag{5.87}$$

$$r \leq \psi(\gamma) \leq 1 \quad \text{for } \gamma \leq 1, \tag{5.88}$$

$$1 \leq \psi(\gamma) \leq r \quad \text{for } \gamma \geq 1. \tag{5.89}$$

The Superbee and minmod limiters represent extreme cases since they follow the boundary of the TVD region. The Superbee limiter is the least diffusive and the minmod limiter is the most diffusive.

The LSOMG model uses the Superbee flux limiter,

$$\psi(\gamma) = \max\left[0, \min(1, 2\gamma), \min(2, \gamma)\right], \tag{5.90}$$

for the horizontal fluxes as it is done in MITgcm Adcroft et al. [2014]. We do not use the Superbee flux limiter in the vertical direction since Eq. (5.90) is derived for an equidistant grid. The computational grid can be non-equidistant in both horizontal and vertical directions but it is expected that the change is more abrupt in the vertical direction even though we use a thickness distribution that is changing smoothly, see Sec. 5.3.

We implemented the van Leer flux limiter,

$$\psi(\gamma) = \frac{\gamma + |\gamma|}{1 + |\gamma|}, \tag{5.91}$$

the Koren flux limiter,

$$\psi(\gamma) = \max\left[(0, \min(2\gamma, \frac{2+\gamma}{3}, 2)\right], \tag{5.92}$$

and the MC flux limiter,

$$\psi(\gamma) = \max\left[0, \min(2\gamma, \frac{1+\gamma}{2}), 2\right], \tag{5.93}$$

for the vertical flux. The van Leer flux limiter seems to work surprisingly well even for the non-equidistant grid according to the example with linear data in Berger et al. [2005], section III, paragraph C. The Koren and MC flux limiters were chosen as a compromise between van Leer and Superbee flux limiters. We argue that Koren flux limiter is the best choice for the vertical advection based on the tests in Sec. 6.5, but the differences between the tested flux limiters are relatively small.

5.7.2 Third order direct space time (DST3) scheme with flux limiters according to Adcroft et al. [2014]

The DST3 scheme is given be

$$F_{i+\frac{1}{2}} = \begin{cases} u_{i+\frac{1}{2}}\left[C_i + d_0(C_{i+1} - C_i) + d_1(C_i - C_{i-1})\right] & \text{if } u_{i+\frac{1}{2}} > 0, \\ u_{i+\frac{1}{2}}\left[C_{i+1} - d_0(C_{i+1} - C_i) - d_1(C_{i+2} - C_{i+1})\right] & \text{if } u_{i+\frac{1}{2}} < 0. \end{cases} \tag{5.94}$$

where

$$d_0 = \frac{(2-c)(1-c)}{6}, \tag{5.95}$$

$$d_1 = \frac{(1-c)(1+c)}{6}. \tag{5.96}$$

and

$$c = \frac{\left|u_{i+\frac{1}{2}}\right| \Delta t}{\Delta x_{i+\frac{1}{2}}} \tag{5.97}$$

is the Courant number. Note that the scheme reduces to the third order upwind method if Courant number is equal to zero, $c = 0$. Otherwise, the dependence on the flow through the coefficients d_0 and d_1 acts in a similar way as the diffusion added to the centered second-order advection in the Lax-Wendroff scheme. The scheme is stable for $0 \leq c \leq 1$ and it must be implemented with explicit time stepping scheme. The scheme has a remarkable property that its accuracy increases with the Courant number, hence it is extremely accurate for large Courant numbers with only minor overshoots Adcroft et al. [2014].

The flux limiter is implemented in a following way into the DST3 scheme,

$$F_{i+\frac{1}{2}} = F^{up}_{i+\frac{1}{2}} + \left|u_{i+\frac{1}{2}}\right| \psi\left(\gamma_{i+\frac{1}{2}}\right) \delta_{i+\frac{1}{2}} C \tag{5.98}$$

where ψ is the Sweby limiter

$$\psi(\gamma) = \max\left\{0, \min\left[\min(1, d_0 + d_1\gamma), \frac{1-c}{c}\gamma\right]\right\}. \tag{5.99}$$

Currently, we apply this scheme only in the horizontal direction in the LSOMG model. We use the Lax-Wendroff advection scheme with appropriate flux limiter in the vertical direction.

5.7.3 Lax-Wendroff scheme with flux limiters according to Smith et al. [2010]

The scheme is based on the Lax-Wendroff scheme. The flux limiter is the ULTIMATE flux limiter of Leonard [1979]. The limiter is constructed in such a way that the new tracer values are limited by the actual values in the upwind direction. We consider the advective flux

$$F_{i+\frac{1}{2}} = F^{up}_{i+\frac{1}{2}} + \left|u_{i+\frac{1}{2}}\right| \psi_{i+\frac{1}{2}} \delta_{i+\frac{1}{2}} C, \tag{5.100}$$

which is the flux introduced in Eq. (5.98) where $\psi\left(\gamma_{i+\frac{1}{2}}\right)$ is replaced by $\psi_{i+\frac{1}{2}}$. We changed the notation to emphasize that the form of the flux limiter is not always the same, it depends on the direction of velocity on the grid-cell face and the direction of velocity in the upwind direction. The following three cases are considered:

- If $u_{i+\frac{1}{2}} > 0$, $u_{i-\frac{1}{2}} > 0$, then

  $$\psi_{i+\frac{1}{2}} = \max\left[0, \min\left(1, \psi^0_{i+\frac{1}{2}}, \frac{\Delta x_i - u_{i-\frac{1}{2}}\Delta t}{u_{i+\frac{1}{2}}\Delta t}\gamma_i\right)\right], \tag{5.101}$$

  where $\psi^0_{i+\frac{1}{2}}$ represents the flux without the flux limiter applied, i.e., it corresponds to the Lax-Wendroff scheme,

  $$\psi^0_{i+\frac{1}{2}} = \frac{1}{2}\left(\frac{\Delta x_I - |u_{i+\frac{1}{2}}|\Delta t}{\Delta x_{i+\frac{1}{2}}}\right). \tag{5.102}$$

- If $u_{i+\frac{1}{2}} < 0$, $u_{i+\frac{3}{2}} < 0$, then

$$\psi_{i+\frac{1}{2}} = \max\left[0, \min\left(1, \psi^0_{i+\frac{1}{2}}, -\frac{\Delta x_{i+1} + u_{i+\frac{3}{2}}\Delta t}{u_{i+\frac{1}{2}}\Delta t}\gamma_{i+1}\right)\right]. \tag{5.103}$$

- If $u_{i+\frac{1}{2}} > 0$, $u_{i-\frac{1}{2}} < 0$, then the flux limiters at both grid-cell faces of i-th tracer volume needs to be set at the same time,

$$\psi_{i-\frac{1}{2}} = \max\left[0, \min\left(1, \psi^0_{i-\frac{1}{2}}, -\frac{u_{i+\frac{1}{2}}}{u_{i-\frac{1}{2}}}\frac{\max\left[0, \min\left(1, \psi^0_{i+\frac{1}{2}}\right)\right]}{\gamma_i}\right)\right], \tag{5.104}$$

$$\psi_{i+\frac{1}{2}} = -\frac{u_{i-\frac{1}{2}}\psi_{i-\frac{1}{2}}}{u_{i+\frac{1}{2}}\gamma_i}. \tag{5.105}$$

$$\tag{5.106}$$

The $u_{i+\frac{1}{2}} < 0$, $u_{i+\frac{3}{2}} > 0$ case is not considered since it is equivalent to the case $u_{i+\frac{1}{2}} > 0$, $u_{i-\frac{1}{2}} > 0$ with shifted indeces.

5.7.4 Splitting method of Adcroft et al. [2014]

The flux limiters that were introduced in previous sections are designed for a 1-D advection. The advection in the LSOMG model is, of course, fully 3-D. However, it is difficult to derive a 3-D limiter for a 3-D advection. On the other hand, if we treat the advection independently in each direction, we may compromise the properties of the scheme such as monotonicity. The preferred way is the multi-dimensional splitting method described in Adcroft et al. [2014]. It is a variant of operator splitting technique and allows us to couple the three dimensions without the need for a 3-D flux limiter.

Consider for simplicity a 3-D advection in the Cartesian coordinates. The evolution equation for tracers without turbulent fluxes and source terms is then

$$C_{,t} + \partial_x F_x + \partial_y F_y + \partial_z F_z = 0, \tag{5.107}$$

where $F_x = uC$, $F_y = vC$ and $F_z = wC$. We gradually advect the tracer concentration in the directions of x, y and z axes.

$$C^{n+\frac{1}{3}} = C^n - \Delta t\left[\partial_x F_x\left(C^n\right) + C^n\partial_x u\right], \tag{5.108}$$

$$C^{n+\frac{2}{3}} = C^{n+\frac{1}{3}} - \Delta t\left[\partial_y F_y\left(C^{n+\frac{1}{3}}\right) + C^n\partial_y v\right], \tag{5.109}$$

$$C^{n+\frac{3}{3}} = C^{n+\frac{2}{3}} - \Delta t\left[\partial_z F_z\left(C^{n+\frac{2}{3}}\right) + C^n\partial_z w\right]. \tag{5.110}$$

where C^n is the actual tracer concentration and $C^{n+\frac{1}{3}}$, $C^{n+\frac{2}{3}}$ and $C^{n+\frac{3}{3}}$ are tracer concentrations after the first, second and third advection. Terms $C^n\partial_x u$, $C^n\partial_y v$ and $C^n\partial_z w$ arise due to the fact that the velocity vector is divergence-free but its components are not. The individual terms do not contribute to $C^{n+\frac{3}{3}}$ directly,

$$C^{n+\frac{3}{3}} = C^n - \Delta t\left[\partial_x F_x(C^n) + \partial_y F_y\left(C^{n+\frac{1}{3}}\right) + \partial_z F_z\left(C^{n+\frac{2}{3}}\right)\right], \tag{5.111}$$

however, they modify tracer concentrations $C^{n+\frac{1}{3}}$ and $C^{n+\frac{2}{3}}$ which in turn affects fluxes F_y and F_z and thus also the final tracer distribution $C^{n+\frac{3}{3}}$.

5.8 Coriolis term on the C-grid

The components of velocity (vertically integrated transport) are discretized at the same points on Arakawa grids B/E but they are spatially separated on the Arakawa grid C. As a consequence, the both spatial and temporal discretization of the Coriolis term on the Arakawa grid C needs to be treated carefully.

Let us start with the spatial discretization. The Coriolis term in the zonal (meridional) component of the momentum equation requires the meridional (zonal) component of velocity. In order to collocate the both velocity components, some kind of averaging procedure is needed. The simplest choice is

$$(fv)_{i+\frac{1}{2},j} = f\overline{v}^{i+\frac{1}{2},j}, \tag{5.112}$$

$$-(fu)_{i,j+\frac{1}{2}} = -f\overline{u}^{i,j+\frac{1}{2}}. \tag{5.113}$$

Unfortunately, the Coriolis term then contributes to the total kinetic energy which is not physical, see Eq. (C.2). More sophisticated schemes that conserve certain physical variables have been designed. The following schemes are available in the LSOMG model:

- The energy conserving scheme ENE of Madec [2012],

$$(fv)_{i+\frac{1}{2},j} = \frac{1}{h_1}\overline{\frac{f}{h_3}\overline{(h_1h_3v)}^{i+\frac{1}{2}}}^{j}, \tag{5.114}$$

$$-(fu)_{i,j+\frac{1}{2}} = -\frac{1}{h_2}\overline{\frac{f}{h_3}\overline{(h_2h_3u)}^{j+\frac{1}{2}}}^{i}. \tag{5.115}$$

- The energy conserving scheme ENE2 of Shchepetkin and McWilliams [2005],

$$(fv)_{i+\frac{1}{2},j} = \frac{1}{h_3}\overline{fh_3\overline{v}^{j}}^{i+\frac{1}{2}}, \tag{5.116}$$

$$-(fu)_{i,j+\frac{1}{2}} = -\frac{1}{h_3}\overline{fh_3\overline{u}^{i}}^{j+\frac{1}{2}}. \tag{5.117}$$

- The enstrophy conserving scheme ENS of Madec [2012],

$$(fv)_{i+\frac{1}{2},j} = \frac{1}{h_1}\frac{\overline{f}^{j}}{h_3}\overline{(h_1h_3v)}^{i+\frac{1}{2},j}, \tag{5.118}$$

$$-(fu)_{i,j+\frac{1}{2}} = -\frac{1}{h_2}\frac{\overline{f}^{i}}{h_3}\overline{(h_2h_3u)}^{i,j+\frac{1}{2}}. \tag{5.119}$$

- The energy and enstrophy conserving scheme EEN of Madec [2012],

$$\begin{aligned}
&(fv)_{i+\frac{1}{2},j}\\
&= \frac{1}{h_1}\Big[T^{-,-}_{i+\frac{1}{2},j+\frac{1}{2}}(h_1h_3v)_{i,j+\frac{1}{2}} + T^{+,-}_{i+\frac{1}{2},j+\frac{1}{2}}(h_1h_3v)_{i+1,j+\frac{1}{2}}\\
&\qquad + T^{-,+}_{i+\frac{1}{2},j-\frac{1}{2}}(h_1h_3v)_{i,j-\frac{1}{2}} + T^{+,+}_{i+\frac{1}{2},j-\frac{1}{2}}(h_1h_3v)_{i+1,j-\frac{1}{2}}\Big],
\end{aligned} \tag{5.120}$$

$$\begin{aligned}
&-(fu)_{i,j+\frac{1}{2}}\\
&= -\frac{1}{h_2}\Big[T^{+,-}_{i-\frac{1}{2},j+\frac{1}{2}}(h_2h_3u)_{i-\frac{1}{2},j} + T^{+,+}_{i-\frac{1}{2},j+\frac{1}{2}}(h_2h_3u)_{i-\frac{1}{2},j+1}\\
&\qquad + T^{-,-}_{i+\frac{1}{2},j+\frac{1}{2}}(h_2h_3u)_{i+\frac{1}{2},j} + T^{-,+}_{i+\frac{1}{2},j+\frac{1}{2}}(h_2h_3u)_{i+\frac{1}{2},j+1}\Big],
\end{aligned} \tag{5.121}$$

where $T_{I,J}^{i_p,j_p}$ is a triad,

$$T_{I,J}^{i_p,j_p} = \frac{1}{12}\left[\left(\frac{f}{h_3}\right)_{I+i_p,J} + \left(\frac{f}{h_3}\right)_{I,J} + \left(\frac{f}{h_3}\right)_{I,J+j_p}\right], \tag{5.122}$$

where I, J are grid indeces of the particular C-point and i_p, j_p are either $+1$ or -1. We write only the signs of i_p and j_p in Eqs. 5.120, 5.121 to simplify the notation.

We also need to concern the temporal discretization of the Coriolis term. On the Arakawa grids B/E, the semi-implicit discretization of the Coriolis term in time is commonly used. Such discretization is stable and it does not increase the computational demands since it does not introduce coupling between neighbouring grid points. The original discretization of the Coriolis term in the LSG model is implicit in time. The implicit discretization was preferred to the semi-implicit one since it allows for larger time steps in the model.

On the Arakawa grid C, the both semi-implicit and implicit discretizations of the Coriolis term in time may in principle be also used. The problem is that the spatial separation of velocity components results in coupling between the neighbouring grid points (see Eqs. 5.112-5.122) and the momentum equation transforms to a system of linear equations that needs to be solved. If the split-explicit time stepping scheme is used, which is the case of the LSOMG model, the time step is limited by the CFL criterion and the usage of semi-implicit or implicit discretization of the Coriolis term becomes costly.

The straightforward explicit discretization of the Coriolis term is not recommended either. The stability analysis of inertial oscillations shows that such a discretization is formally stable, but growing modes may appear [Durran, 1999]. Note that this is true for the two-time-level schemes that advance velocities from time step n to time step $n+1$. The explicit discretization may be used together with the leap-frog time stepping scheme, which is a three-time-level scheme that advances velocities from time step $n-1$ to $n+1$. The discretization of the Coriolis term on time level n is stable. However, the leap-frog time stepping scheme has its own problems such as the existence of a computational mode [Griffies et al., 2000].

The LSOMG model is using two time levels and thus neither explicit, semi-implicit or implicit discretizations are suitable. One solution of the problem is to apply the Adams-Bashforth extrapolation. The MITgcm model is using the quasi-second-order Adams-Bashforth extrapolation,

$$u_{AB} = \left(\frac{3}{2} + \epsilon_{AB}\right) u^n - \left(\frac{1}{2} + \epsilon_{AB}\right) u^{n-1}, \tag{5.123}$$

where ϵ_{AB} is a small number that stabilizes the method with respect to oscillatory terms [Adcroft et al., 2014]. The Adams-Bashforth extrapolation of the third-order is used in the FBgen scheme, see Eq. (4.18), and it is also the default method in the LSOMG model. Another possibility is to use the method of Sielecki [1968] and Beckers and Deleersnijder [1993] that somehow mimics the implicit discretization. Similar to the forward-backward scheme, the method is based on the idea of gradual update of components of the momentum equation (not momentum and SSH equations as in the FB scheme). In time step n, the

Coriolis term is discretized explicitly in the zonal component and implicitly in the meridional component of the momentum equation. The zonal component is thus computed first and the computation of the meridional component follows. In time step $n+1$, the discretization in time and the computation order are swapped between the components.

Unfortunately, even the sophisticated discretizations in space and time does not cure all the difficulties. The Coriolis term is prone to generate a grid-scale noise on the C-grid. Consider the simplest scheme given by Eqs. 5.112 and 5.113. The Coriolis term is equal to zero for a velocity field in the form of a checkerboard pattern with alternating $+1$ and -1 values. The averaging operators used in Eqs. 5.112 and 5.113 thus have a null space and does not "see" the checkerboard noise. The other discussed schemes (ENE, ENE2, ENS and EEN schemes) suffer from a similar problem since each of them is in fact a weighted average of four neighbouring grid points.

The noise is generated at the boundaries. In fact, an unrealistic numerical boundary layers develop along solid boundaries [Jamart and Ozer, 1986]. The noise generation can be somewhat suppressed if the averaging procedure distinguishes between wet and dry points. On the other hand, if dry points are not considered in the scheme, the conservation of the particular quantity (energy, enstrophy etc.) is violated. The LSOMG model thus does not exclude the dry points from the proposed schemes. Instead, we have implemented the so-called divergence damping method.

The divergence damping of order $2q$ adds an additional term into the momentum equation,

$$\mathbf{u}_{,t} = \cdots + (-1)^{q+1} \nabla_h \left(A_d \nabla_h^{2q-1} \cdot \mathbf{u} \right), \tag{5.124}$$

where $q \geq 1$ is a positive integer and A_d is the damping coefficient. The LSOMG uses the second-order method,

$$\mathbf{u}_{,t} = \cdots + \nabla_h \left(A_d \nabla_h \cdot \mathbf{u} \right). \tag{5.125}$$

If we apply the rotation operator $\nabla_h \times$ to Eq. (5.125), the newly added term vanishes since $\nabla_h \times \nabla_h \mathbf{A} = 0$, where $\mathbf{A}$ is an arbitrary vector function. It means that the vorticity dynamics (rotational motions) is unaffected. However, if we apply the divergence operator $\nabla_h \cdot$ to Eq. (5.125), we obtain

$$\mathscr{D}_{,t} = \cdots + \Delta_h \left(A_d \mathscr{D} \right), \tag{5.126}$$

where $\mathscr{D}$ is a divergence of horizontal velocity, $\mathscr{D} = \nabla_h \cdot \mathbf{u}$. The divergence equation thus has an additional diffusion term. Consequently, the divergence damping method selectively damps inertia-gravity waves (associated with the divergent part of the flow) and controls numerical noise [Adcroft, 1995, Jablonowski and Williamson, 2011].

Additionally, we may use some kind of a spatial smoother. We require the smoother to act on the small-scale features which are supposed to represent noise and keep the larger scales unaffected. We implemented the dual-step five-point-involved (DFP) smoother of Lei [2014]. In the first step, we compute the provisional velocity $\tilde{u}$,

$$\tilde{u}_{i+\frac{1}{2},j} = u_{i+\frac{1}{2},j} + \frac{s}{4} W_{i+\frac{1}{2},j} \left(u_{i+\frac{3}{2},j} + u_{i-\frac{1}{2},j} + u_{i+\frac{1}{2},j+1} + u_{i+\frac{1}{2},j-1} - K u_{i+\frac{1}{2},j} \right) \tag{5.127}$$

and in the second step, the provisional velocity is used to calculate the final DFP-smoothed velocity,

$$\hat{u}_{i+\frac{1}{2},j} = \tilde{u}_{i+\frac{1}{2},j} - \frac{s}{4} W_{i+\frac{1}{2},j} \left(\tilde{u}_{i+\frac{3}{2},j} + \tilde{u}_{i-\frac{1}{2},j} + \tilde{u}_{i+\frac{1}{2},j+1} + \tilde{u}_{i+\frac{1}{2},j-1} - K \tilde{u}_{i+\frac{1}{2},j} \right). \tag{5.128}$$

The parameter s in the DFP smoother determines the level of smoothing. The smoother strength is thus not fixed but it can be adjusted to the particular situation. We use $s = 0.1$ as the default value according to Lei [2014].

The benefit of the divergence damping combined with the DFP filter is demonstrated in Fig. 5.7. The both panels depict zonal surface velocities from the wind-driven baroclinic LSOMG simulation after one year. However, the velocities in the left panel are computed without the divergence damping and DFP smoother while both options are enabled in the right panel. The divergence damping with the DFP smoother successfully suppress the grid-scale noise around Antarctica, Greenland or Iceland. The noise is virtually gone. At the same time, the flow details are preserved, which is the requested behaviour.

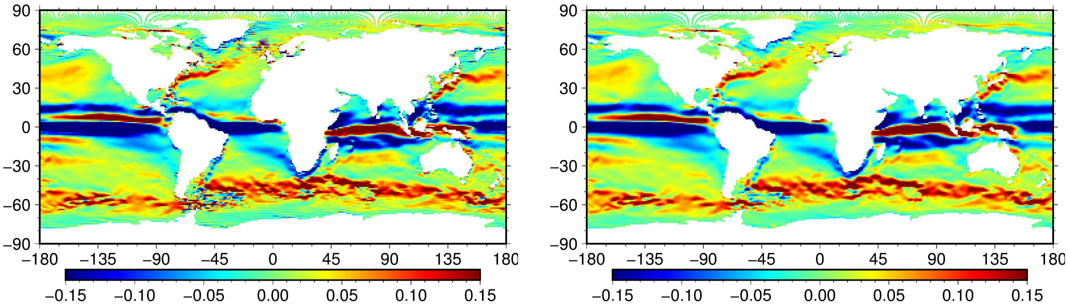

Figure 5.7: The suppression of grid-scale noise in the zonal component of surface velocity [m/s] using the divergence damping and the DFP smoother. Both options are switched off in the left panel while they are active in the right panel.

5.9 Convective adjustment scheme

The LSOMG model uses the hydrostatic approximation which reduces the vertical component of the momentum equation to the hydrostatic pressure balance. It is a suitable approximation since the global ocean is close to the hydrostatic equilibrium in most regions. However, the unresolved convection processes may result in gravitationally unstable water columns in certain regions. The purpose of the so-called convective adjustment scheme is to ensure that all water columns in the model are gravitationally stable. If instability is found, the scheme mixes the water in model cells in order to make the column stable.

Note that the mixing process affects the temperature and salinity rather than the density itself. If we mix two water parcels, the resulting density could be lower than the initial density of each water parcel due to the non-linearity of state equation of sea water [Rahmstorf, 1993].

The stability of two model cells is determined by comparison of density of adiabatically displaced water mass from the upper cell and the density of water mass from the lower cell. The density of adiabatically displaced water mass is calculated from the state equation using the temperature and salinity of the displaced water mass and the pressure at the interface between the two cells.

The original convective adjustment scheme used in the LSG model checks the stability of each pair of model cells in the water column. The scheme starts with the upper most pair and continues to the deeper parts of the water column. The process is not repeated after processing the whole water column. The scheme is simple but there is no guarantee that the water column will be stable. According to Maier-Reimer et al. [1993], around 5% of convective regions remain unstable after the single sweep in the realistic configuration. The entire process could be repeated but the number of repetitions could be very large to stabilize the water column. It may not be a critical issue but we rather implemented the scheme of Rahmstorf [1993] in which the stabilization of water column is guaranteed.

The key idea of the Rahmstorf's scheme is that the mixing of multiple model cells is allowed. The scheme goes through the water column from top to bottom. If instability is found, the unstable cells are mixed and they are joined into one cell. The stability of the joined cell with respect to the next lower cell is then checked. If instability is found, the joined cell is mixed with this cell, the joined cell is enlarged and the scheme proceeds to the next lower cell. If the scheme reaches a cell that is stable with respect to the joined cell, the stability between the joined cell and the cell just above it is checked since the instability could have been introduced. If there is no instability, it continues down the water column to find the next unstable part of the water column. If there is instability, the mixing process is repeated to remove this instability but the joined cell is still considered to be a one cell. The Rahmstorf's scheme is obviously more complicated than the original LSG scheme since it is necessary to remember which cells are joined.

An alternative to the convective adjustment scheme is to increase the vertical diffusion to some large value if instabilities are found and let the diffusive process to mix the water parcels. In LSOMG, this method is automatically enabled if the Richardson-number based viscosities and diffusivities are used, see Sec. 5.5.2. If the Richardson number is negative, both vertical diffusivity and viscosity are increased to $A_V = K_V = 50\ \mathrm{m}^2/\mathrm{s}$. Recall that the vertical diffusion and friction are treated implicitly which assures the stability.

5.10 Tides in the baroclinic LSOMG

Tides is one of physical processes that were neglected in OGCMs for a long time. The reasons were mainly technical such as the popular rigid-lid approximation, which filters out gravity waves (see Sec. 5.2) by assuming that the ocean surface does not evolve in time which directly precludes the modelling of tides, and insufficient resolution in space and time. Instead of modelling tides properly, it was believed that the effect of tides is negligible for climate studies due to their periodic nature and much shorter time scales. However, Munk and Wunsch [1998] estimated that 2.1 TW are required to maintain the global ocean circulation and they pointed out that the wind stresses can not be the only source of energy. They attributed about half of the total power to the tidal dissipation in the deep ocean. Egbert and Ray [2000] confirmed this estimate using satellite altimeter data from Topex/Poseidon. Nowadays, there is a growing interest in tidal effects in the OGCM's community. Müller et al. [2010] showed that tides improved the skill of a climate model. [Müller et al., 2012, Arbic et al., 2010, Simmons et al., 2004, Niwa and Hibiya, 2011] presented results from the modelling of baroclinic tides.

Laurent et al. [2002] were one of the first modelling teams who included tides into an OGCM. He did not implement tides directly, he rather suggested a parameterization suitable for models with implicit time stepping schemes. His idea is to modify the vertical diffusivity by adding a new term. The tidally induced diffusivity depends on the internal wave energy map derived from a barotropic tidal model, buoyancy frequency and depths. For further details see Jayne [2009] who used this parameterization in the POP model.

However, a more natural approach is to implement tides directly as a forcing on the right-hand side of the momentum equation. This approach was followed by Schiller and Fiedler [2007], Müller et al. [2010, 2012] and Arbic et al. [2010]. Schiller and Fiedler [2007] and Arbic et al. [2010] implemented eight dominant constituents of the semi-diurnal (M_2, S_2, N_2 and K_2) and diurnal (K_1, O_1, P_1, Q_1) tides into the MOM and HYCOM models, respectively, and Müller et al. [2010, 2012] implemented the full lunisolar tidal forcing into the MPI-OM model (the resulting model is called STORMTIDE). We also prefer this approach and thus tides are implemented directly in the LSOMG model, see Sec. 4.4.

What about the tidal parameterization discussed in Sec. 4.4, especially IWD? Is IWD needed also in the baroclinic model? In principle, a baroclinic model should be able to model the breaking of internal tides. However, the problem is the resolution. According to Arbic et al. [2010], the wavelength of the first baroclinic M_2 internal tide is approximately 100 km in mid-latitudes. As a rule of thumb, eight grid points per wavelength are needed. If we consider that the wavelength of n-th mode decreases with $1/n$, we realize that even the first few modes require a resolution than is beyond the limits of the most powerful supercomputers in terms of OGCMs. Consequently, the IWD parameterization is needed also in the baroclinic model. However, the situation in the full OGCM is more complicated than in the tidal barotropic model. The input for the IWD parameterization is the vertically integrated tidal flow. That is natural for the tidal barotropic model but the OGCM which is forced by tides and fluxes of momentum, heat and fresh water generates the flow which is a superposition of both tidal and non-tidal (surface currents, meridional overturning circulation, etc.) circulations. The key issue is thus the separation of these two circulation types.

Arbic et al. [2010] suggested to use the 25-hour running mean. Tidal velocities are considered to be deviations from the running mean. Similarly, tidal heights are thought to be deviations from the dynamic height. Unfortunately, our experience with the LSOMG model has shown that the implemented split-explicit scheme considerably damps the amplitudes of tidal circulation. It is the consequence of averaging of barotropic quantities in time that ensures the stability of the scheme. We thought that the problem could be solved by decreasing the length of the baroclinic time step which reduces the number of barotropic subcycles per one baroclinic time step, see Eq. 5.36. However, the method was not proved to be useful since we were unable to get rid of the damping. On top of that, it increases the computational demands and so it devalues the main advantage of the split-explicit scheme.

We have rather decided to follow an alternative way and implemented a barotropic linear tidal model into LSOMG according to Sakamoto et al. [2013]. The idea is to have two barotropic systems instead of just one. The first barotropic system contains all the forcing (surface pressure gradients and the vertically integrated baroclinic forcing, see Eqs. 5.30 and 5.28) except for the tidal force. The second barotropic system is forced by tides and it computes merely the tidal circulation. It is thus simple to implement the tidal parameterizations. This is the primary barotropic tidal effect. The baroclinic part of the model provides the secondary tidal effect. The SSHs and vertically integrated velocities from the both barotropic systems are added together. The barotropic and baroclinic velocities are added to get total velocities. The total velocities are stronger due to the presence of tides. The transports of temperature and salinity are also larger which effects the density, pressure and finally the pressure gradients. The pressure gradients provide a forcing to the momentum equation, which in turn affects the velocities, see Fig. 5.8.

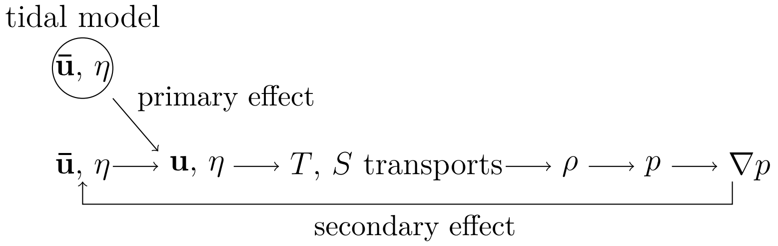

Figure 5.8: Scheme illustrating the implementation of tidal model into the LSOMG model. The primary effect stands for the barotropic response and the secondary effect stands for the baroclinic response.

Note that the second (tidal) barotropic system is not affected by the baroclinic part of the LSOMG model, it is running independently. Indeed, it is a separate model that is running together with the baroclinic LSOMG. Consequently, there is no need to ensure the stability of barotropic-baroclinic splitting and so no averaging in time is needed in the second barotropic system. That is the principal benefit of this approach. One may, of course, argue that the one-way coupling between the models is not correct since the baroclinic response should affect barotropic tides in return. There is no clear argument against this statement but according to Sakamoto et al. [2013] such interactions have not been reported. Nevertheless, they anticipate that the proposed scheme is not suitable for a shallow coastal regions where nonlinearities become important.

5.11 Horizontal coordinates

An arbitrary orthogonal coordinate grid may in principle be used in the LSOMG model if grid-point positions and metric coefficients are provided in the input file. We mentioned several orthogonal coordinate grids in Sec. 2.2. Apart from the standard SC grid, the dipolar grid of Roberts et al. [2006], the tripolar confocal grid of Murray [1996] and the tripolar reprojected grid of Murray [1996] are available in the LSOMG model, see Fig. 5.9. The construction of these grids is explained in details in the original papers, we thus merely highlight the key ideas and summarize the formulas. We also discuss the implementation of tripolar grids such as the tripolar reprojected grid of Murray [1996] into the LSOMG model, especially the way how to enclose grid at the North Pole.

5.11.1 Dipolar grid of Roberts et al. [2006]

Roberts et al. [2006] proposed a global dipolar grid. Roughly speaking, the grid looks like a SC grid that is "tilted" towards the new relocated North Pole. The grid is composed of two parts, the SC grid from the South Pole to the join latitude ϕ_{JN} and the "tilted" grid from the join latitude northward. The "tilted" grid gradually adjusts with increasing latitude to relocate the North Pole to the new position with longitude λ_P and latitude ϕ_P.

The grid construction is based on the stereographic projection and reprojection technique. The central point of the reprojection is the Earth's North Pole. The grid parallels and meridians are projected to the tangent plane, shifted and reprojected back to the sphere. Note that the grid parallels are actually constructed first, the grid meridians are then constructed from the orthogonality property (meridians are orthogonal to the parallels). We report eight steps to construct the grid as they are listed in the appendix of Roberts et al. [2006]:

1. Consider a point with geographic coordinates λ_c, ϕ_c. Project the point on the tangent plane. Its polar coordinates r, θ_1 on the tangent plane are

$$r = \frac{\tan(\frac{\pi}{2} - \phi_c)}{\tan(\frac{\pi}{2} - \phi_{JN})}, \tag{5.129}$$

$$\theta_1 = \lambda_c. \tag{5.130}$$

   Notice that $0 \le r \le 1$ since $r = 0$ for $\phi_c = \pi/2$ and $r = 1$ for $\phi_c = \phi_{JN}$.

2. Rotate the point in the tangent plane,

$$\theta_2 = \theta_1 - \lambda_P, \tag{5.131}$$

   while keeping θ_2 within $0 \le \theta_2 \le 2\pi$.

3. Choose function f that controls the shift of grid-point circles in the tangent plane. We require

$$f(1) = 0, \qquad f(0) = a, \tag{5.132}$$

   where

$$a = \frac{\tan(\frac{\pi}{2} - \phi_P)}{\tan(\frac{\pi}{2} - \phi_{JN})}. \tag{5.133}$$

   According to Eqs. (5.141) and (5.142), the $\phi_c = \phi_{JN}$ parallel is then left unchanged and the North Pole is relocated to $x = a$ and $y = 0$.

4. Compute the integration constant c,

$$\theta_2 \in \{0, \pi\} \qquad \Rightarrow \qquad c = -\ln\left|\tan\frac{\theta_2}{2}\right| + F(1), \tag{5.134}$$

$$\theta_2 \notin \{0, \pi\} \qquad \Rightarrow \qquad c = 0, \tag{5.135}$$

   where

$$F(r) = \int \frac{df(\rho)}{d\rho}\frac{1}{\rho}d\rho. \tag{5.136}$$

5. Update θ,

$$\theta_2 = 0 \qquad \Rightarrow \qquad \theta_3 = 0, \tag{5.137}$$

$$0 < \theta_2 < \pi \qquad \Rightarrow \qquad \theta_3 = 2\arctan\left[e^{F(r)-c}\right], \tag{5.138}$$

$$\theta_2 = \pi \qquad \Rightarrow \qquad \theta_3 = \pi, \tag{5.139}$$

$$\pi < \theta_2 < 2\pi \qquad \Rightarrow \qquad \theta_3 = 2\pi - 2\arctan\left[e^{F(r)-c}\right]. \tag{5.140}$$

6. Compute Cartesian coordinates of the point on the tangent plane,

$$x_4 = f(r) + r\cos\theta_3, \tag{5.141}$$

$$y_4 = r\sin\theta_3. \tag{5.142}$$

7. Remove the rotation that was applied in point 2,

$$x_5 = x_4\cos\lambda_P - y_4\sin\lambda_P, \tag{5.143}$$

$$y_5 = x_4\sin\lambda_P + y_4\cos\lambda_P. \tag{5.144}$$

8. Reproject the point back from the tangent plane to the sphere, its new geographic coordinates are

$$\lambda_s = \text{atan2}(y_5, x_5), \tag{5.145}$$

$$\phi_s = \frac{\pi}{2} - \arctan\left[\sqrt{x_5^2 + y_5^2}\tan\left(\frac{\pi}{2} - \phi_{JN}\right)\right]. \tag{5.146}$$

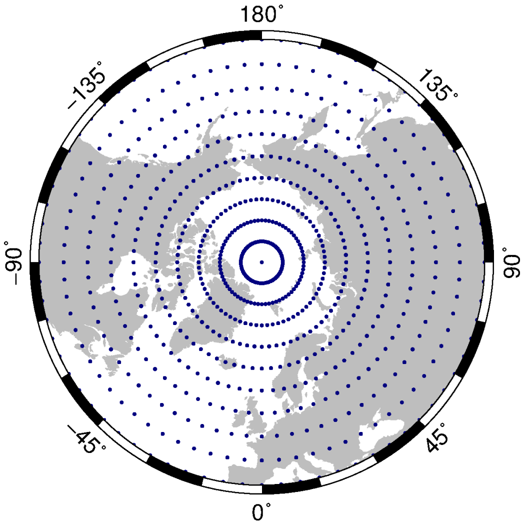
(a) spherical coordinates

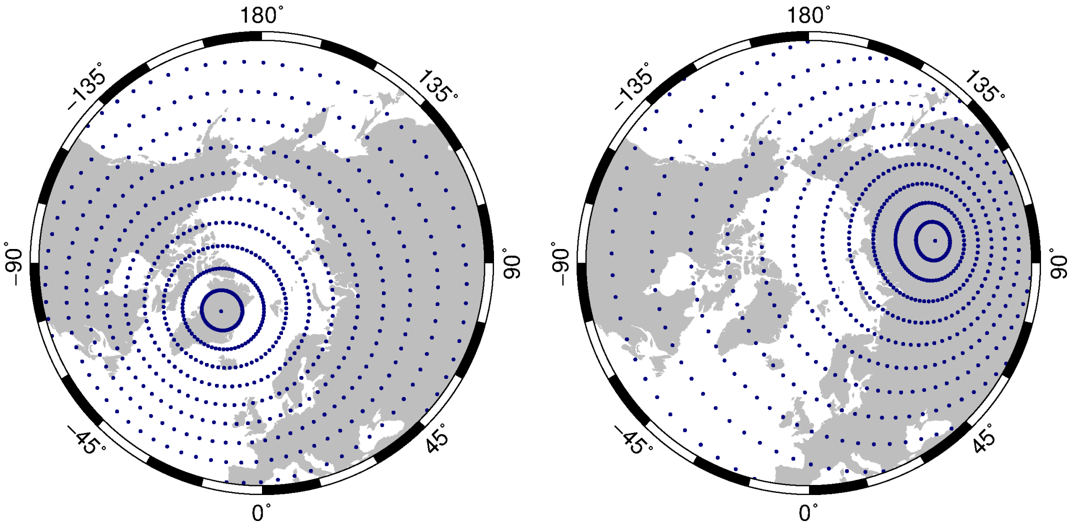
(b) Roberts et al. [2006], Greenland

(c) Roberts et al. [2006], Asia

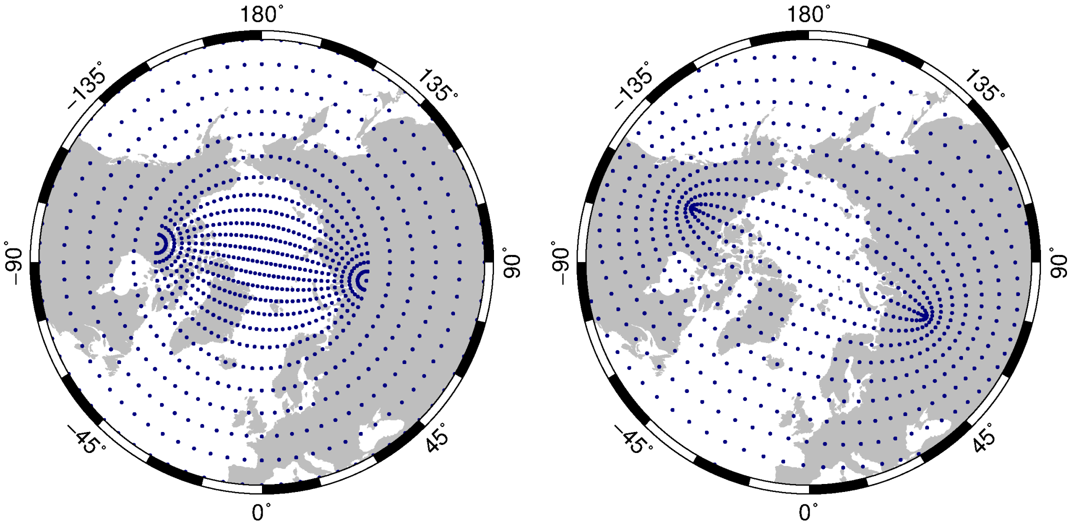
(d) reprojected Murray [1996]

(e) confocal Murray [1996]

Figure 5.9: Horizontal grids available in the LSOMG model.

The choice of $f(r)$ is up to the user. Roberts et al. [2006] proposed either polynomial functions or the cosine function. They tested three polynomial functions, the linear, parabolic and cubic functions. The best performance is achieved for the parabolic function, which provides a smooth transition at the join and small latitudinal grid spacing near the grid pole. The linear case leads to a step in the latitudinal grid spacing at the join and the cubic function causes the largest change in the latitudinal grid spacing near the grid pole, see Fig. 5b in Roberts et al. [2006]. The benefit of using the cosine function is questionable. On one hand metrics are continuous across the pole, on the other hand the grid spacing is larger in the polar region than in the case of polynomial functions.

The $f(r)$ and $F(r)$ are

$$f(r) = a(1-r)^2, \tag{5.147}$$

$$F(r) = 2a\left(r - \ln r\right), \tag{5.148}$$

for the parabolic function and

$$f(r) = a\frac{1+\cos(r\pi)}{2}, \tag{5.149}$$

$$F(r) = -\frac{a\pi \mathrm{Si}(r\pi)}{2}, \tag{5.150}$$

for the cosine function, where $Si(z)$ is the Sine Integral,

$$\mathrm{Si}(z) = \int\limits_0^z \frac{\sin t}{t} dt = \sum_{n=0}^{\infty} \frac{(-1)^n z^{2n+1}}{(2n+1)(2n+1)!} \tag{5.151}$$

according to Abramowitz and Stegun [1968].

The dipolar grid of Roberts et al. [2006] is depicted in Fig. 5.9, panels (b) and (c). The North Pole is relocated to Greenland, 40° W and 75° N, in panel (b) and to Asia, 60° W and 100° N, in panel (c). The parabolic function f and join at the Equator are used in the both cases.

5.11.2 Tripolar reprojected grid of Murray [1996]

Murray [1996] constructed a dipolar grid with relocated poles using the stereographic projection and reprojection (the form is slightly different than in Sec. 5.11.1) that is applied to the standard SC grid. First, the SC grid is stereographically projected from the (grid) sphere onto the tangent plane. The central point of the projection, which is the point where the plane touches the sphere, is at the Equator. The grid projected on the tangent plane is then reprojected onto the second (real) sphere. The central points of projection and reprojection are the same but the radius of the second sphere is larger. Finally, the reprojected grid can be shifted and rotated. The key part of the outlined transformation is that the both projection and reprojection are conformal (angle-preserving) which implies that the orthogonality of the original SC grid is preserved.

Consider a general transformation with North and South Poles relocated to (λ_1, ϕ_1) and (λ_2, ϕ_2), respectively, and assume without any loss of generality that the diameter of the second sphere is equal to unity. The diameter of the first sphere is given by the required stretching of the transformation. Let χ_P be the half of angular distance between the transformed poles then the diameter of the first sphere is $\tan(\chi_P/2)$. The transformation is given by the following steps:

1. Determine the parameters of the transformation: The longitude λ_Q and colatitude $\vartheta_Q = \frac{\pi}{2} - \phi_Q$ of the central point, the angular distance χ_P and the angle β which expresses the rotation applied after the reprojection. All these parameters can be computed from the positions of the North and South Poles after the transformation,

$$\begin{aligned} \chi_P &= \frac{1}{2} f_c(\lambda_1 - \lambda_2, \vartheta_2, \vartheta_1), && (5.152)\\ \alpha &= f_t(\lambda_1 - \lambda_2, \vartheta_2, \vartheta_1), && (5.153)\\ \lambda_Q &= \lambda_1 - f_t(\alpha, \chi_P, \vartheta_1), && (5.154)\\ \vartheta_Q &= f_c(\alpha, \vartheta_1, \chi_P), && (5.155)\\ \beta &= f_t(\alpha, \vartheta_1, \chi_P), && (5.156) \end{aligned}$$

   where f_t and f_c are functions in a spherical triangle with vertices A, B and C opposite to sides a, b and c, respectively, defined by

$$\begin{aligned} f_c(A, b, c) &= \cos^{-1}(\cos A \sin b \sin c + \cos b \cos c), && (5.157)\\ f_t(A, b, c) &= \operatorname{atan2}\left[\sin A, \left(\frac{\sin c}{\tan b} - \cos c \cos A\right)\right]. && (5.158) \end{aligned}$$

2. Transform geographic coordinates λ_c, ϕ_c of the point on the Earth surface into the natural variables of the projection, θ_c and χ_c,

$$\begin{aligned} \chi_c &= \cos^{-1}(\cos \lambda_c \cos \phi_c), && (5.159)\\ \theta_c &= \operatorname{atan2}(\sin \lambda_c, \tan \phi_c), && (5.160) \end{aligned}$$

   where $\operatorname{atan2}(x, y)$ has the meaning of the FORTRAN `atan2` function.

3. Apply projection and reprojection which transforms χ_c to χ_s,

$$\chi_s = 2 \tan^{-1}\left(\tan \frac{\chi_P}{2} \tan \frac{\chi_c}{2}\right). \qquad (5.161)$$

4. Rotate by angle β,

$$\theta_s = \theta_c + \beta. \qquad (5.162)$$

5. Shift the whole result to have the central point at coordinates (λ_Q, ϕ_Q) and compute the new longitude λ_s and latitude ϕ_s of the point,

$$\begin{aligned} \lambda_s &= \lambda_Q + f_t(\theta_s, \chi_s, \vartheta_Q), && (5.163)\\ \phi_s &= \frac{\pi}{2} - f_c(\theta_s, \chi_s, \vartheta_Q). && (5.164) \end{aligned}$$

The dipolar grid has the third property from the list in Sec. 2.2 only if the poles are located on the same meridian and at equal latitudes. Therefore, Murray [1996] proposed to use this dipolar grid in a composite tripolar grid. It consists of the SC grid from the South Pole to the join latitude ϕ_{JN} on the northern hemisphere and the dipolar grid from the join latitude to the North Pole. The dipolar-grid poles are located opposite to each other on the join latitude, $\lambda_2 = \lambda_1 + \pi$, $\vartheta_1 = \vartheta_2 = \vartheta_{JN}$. The special positions of poles significantly simplifies Eqs. (5.163) and (5.164),

$$\lambda_s = \lambda_1 - \theta_c = \lambda_1 - \operatorname{atan2}(\sin\lambda_c, \tan\theta_c), \tag{5.165}$$

$$\phi_s = \frac{\pi}{2} - \chi_s = \frac{\pi}{2} - 2\tan^{-1}\left(\tan\frac{\vartheta_1}{2}\tan\frac{\chi_c}{2}\right), \tag{5.166}$$

since $\chi_P = \vartheta_1$, $\alpha = 0$, $\lambda_Q = \lambda_1$, $\vartheta_Q = 0$, $\beta = 0$. Let $\Delta\lambda_c$ and $\Delta\phi_c$ be the zonal and meridional grid spacings of the SC grid in the composite grid, respectively, and $\Delta\lambda_s$ and $\Delta\phi_s$ be the zonal and meridional grid spacings of the dipolar grid before the transformation, respectively. The meridians of the dipolar grid are treated as parallels in the composite grid and the parallels are treated as meridians. The choice of meridional grid spacing of the dipolar grid before the transformation is thus clear, $\Delta\phi_s = \Delta\lambda_c$. The zonal grid spacing of the dipolar grid before the transformation is chosen to be slightly larger than $\Delta\phi_c$ to improve the continuity of grid spacing in the meridional direction on the join of the composite grid, $\Delta\lambda_s = \Delta\phi_c/\cos\phi_{JN}$.

The tripolar reprojected grid of Murray (1996) is depicted in Fig. 5.9 (d). The two poles in the bipolar part of the grid are located at (10° ± 90°) W and 65° N.

5.11.3 Tripolar confocal grid of Murray [1996]

The tripolar confocal grid is constructed from families of confocal ellipses and hyperbolae. The ellipses represent parallels and hyperbolae represent meridians. It looks similar to the tripolar reprojected grid of Murray [1996] that was described in Sec. 5.11.2 but it is constructed as a global grid and thus it is free of discontinuities at the join of two parts of the grid. Similar to Secs. 5.11.1 and 5.11.2, the grid construction is based on the stereographic projection technique. The key difference is that the reprojection step is missing. The grid is constructed in the tangent plane and then it is simply reprojected on the sphere with the central point at the North Pole.

The ellipses with foci at $(-r_F, 0)$ and $(r_F, 0)$ in Cartesian coordinates are given by the equation

$$\frac{x^2}{r_F^2\cosh\psi_c} + \frac{y^2}{r_F^2\sinh\psi_c} = 1, \tag{5.167}$$

where ψ_c is a parameter which distinguishes the individual ellipses. Similarly, the hyperbolae with the same foci are given by the equation

$$\frac{x^2}{r_F^2\sin^2\lambda_c} - \frac{y^2}{r_F^2\cos^2\lambda_c} = 1, \tag{5.168}$$

where λ_c is a parameter which distinguishes the individual hyperbolae. It can be shown that these two sets of curves compose a grid that is equidistant in both λ_c and ψ_c. Combining Eq. (5.167) for the ellipses and Eq. (5.168) for the hyperbolae we obtain the Cartesian coordinates of points on their intersection,

$$x = r_F\sin\lambda_c\cosh\psi_c, \tag{5.169}$$

$$y = r_F\cos\lambda_c\sinh\psi_c. \tag{5.170}$$

Additionally, the grid can be constructed to be equiangular in latitude on the Prime Meridian. This condition is expressed by

$$r_F \sinh \psi_c = \tan\left(\frac{\vartheta_c}{2}\right), \tag{5.171}$$

where we equated the length of minor axis of ellipse with the parameter ψ_c and the distance of the point with the colatitude ϑ_c from the central point on the tangent plane. If we insert Eq. (5.171) into Eqs. (5.169) and (5.170), we obtain the final Cartesian coordinates of grid points on the tangent plane,

$$x = \sin \lambda_c \sqrt{r_F^2 + \tan^2 \frac{\vartheta_c}{2}}, \tag{5.172}$$

$$y = \cos \lambda_c \tan \frac{\vartheta_c}{2}. \tag{5.173}$$

To sum it up, the confocal grid with foci at colatitude ϑ_F and longitudes λ_F and $\lambda_F + \pi$ is constructed in three steps:

1. Compute the distance of foci from the central point on the tangent plane, $r_F = \tan \frac{\vartheta_F}{2}$.
2. Compute Cartesian coordinates on the tangent plane of all grid points in the SC grid using Eqs. 5.172 and 5.173.
3. Reproject the grid points from the tangent plane back on the sphere and rotate the grid in the zonal direction to have foci at the desired positions

$$\lambda_s = \operatorname{atan2}(y, x) + \lambda_F, \tag{5.174}$$

$$\phi_s = \frac{\pi}{2} - 2 \arctan r. \tag{5.175}$$

The tripolar confocal grid of Murray (1996) is depicted in Fig. 5.9 (e). The two poles in the North hemisphere are located at (25° ± 90°) W and 60° N.

5.11.4 Construction of a C-grid type grid

There are four types of grid points on the Arakawa C-grid. We call them C, S, U and V points, see the left panel of Fig. 5.10. The grid is fully determined by the C-point positions since S-, U- and V-point positions are computed from the C-point positions The positions of two neighbouring C points on a cell side are averaged to determine the positions of U and V points. S-point positions are then determined by averaging the U-point positions. The averaging of two points means that the new point is equally distant from both original points and all three points are located on the same great circle. Points with geographic coordinates $(-90°, 80°)$ and $(90°, 80°)$ are thus averaged to a point with coordinates $(0°, 90°)$ not $(0°, 80°)$. The complete tripolar reprojected C-grid of Murray [1996] is shown in the right panel of Fig. 5.10.

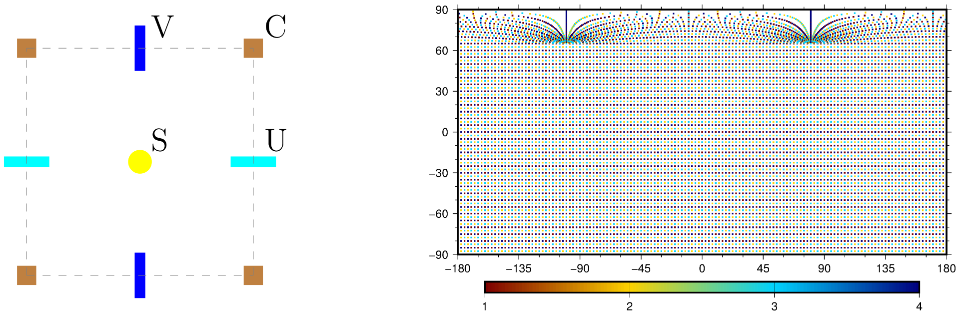

Figure 5.10: Left panel: Notation used for points on Arakawa C-grid. Right panel: The tripolar reprojected grid of Murray [1996] with Arakawa C-grid cells. The grid-point colors are the same as on the left panel.

5.11.5 Tripolar grids in the LSOMG model

The implementation of a dipolar orthogonal curvilinear grid (such as the dipolar grid of Roberts et al. [2006] in Sec. 5.11.1) into the SC ocean model requires two modifications:

1. The (re)formulation of the governing equations into the full form using the metric coefficients.
2. The input vector data needs to be rotated into the local directions of base vectors.

The first issue was discussed in Secs. 5.1 and 5.6.1, the second issue will be discussed in Sec. 5.14.4. No other special treatment of the North-Pole cap is needed since the nearest grid-point circles (grid points with the same grid coordinate j) around the relocated North Pole contain only dry grid points which corresponds to a SC grid with an artificial continent around the true North-Pole. The implementation of a tripolar grid is more complicated since there is no completely dry grid-point circle in the North-Pole cap. We explain the technique that is used in the LSOMG model to enclose the North-Pole cap on the example of the tripolar reprojected C-grid of Murray [1996].

We require the dipolar part of the tripolar grid to contain a reprojected C-point meridian which crosses the true North Pole. This meridian is called a symmetry meridian. The dipolar part is not constructed from the relocated grid-point circles but grid points located on two reprojected meridians equally distant from the symmetry meridian can be viewed as one grid-point circle since the number of grid points is the same. The numbering of C-point circles (="meridional" grid coordinate j) and the numbering of C points within each circle (="zonal" grid coordinate i) in the LSOMG code is shown in the left and right panels of Fig. 5.11, respectively.

As already mentioned, the dipolar grid needs to be enclosed in order to allow the two parts of the grid separated by the symmetry meridian to communicate with each other. Fig. 5.12 depicts the seam for a grid with only eight grid points in each grid-point circle. The grid is enclosed by adding two auxiliary grid-point circles. Consider a grid that originally contained $I \times J$ grid points. The values in the first auxiliary grid-point circle are:

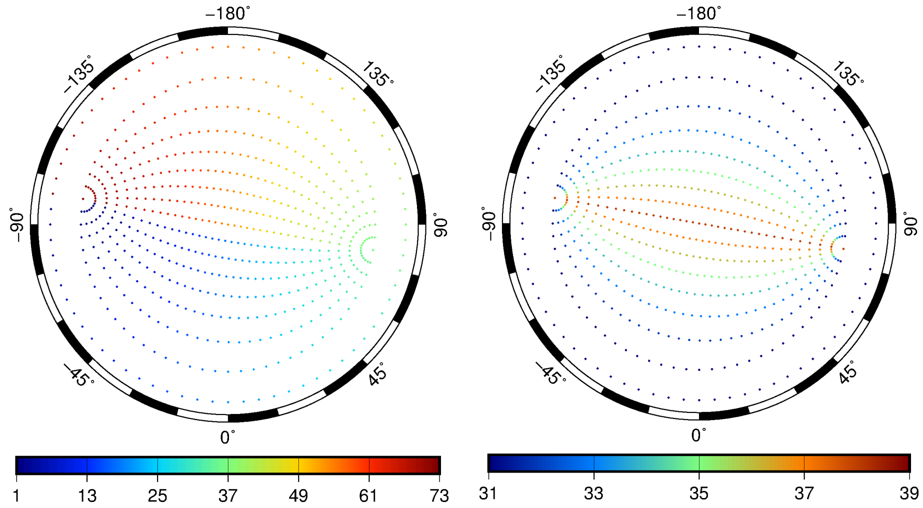

Figure 5.11: Zonal (right panel) and meridional (left panel) grid indeces (numbering of grid points) used in the LSOMG code in the dipolar part of the tripolar grid viewed from the true North Pole.

- Scalars s^C, s^S, s^U and s^V at C, S, U and V points, respectively:

$$s^C(i, J+1) = s^C(I-i, J-1), \tag{5.176}$$

$$s^S(i, J+1) = s^S(I-i+1, J), \tag{5.177}$$

$$s^U(i, J+1) = s^U(I-i, J), \tag{5.178}$$

$$s^V(i, J+1) = s^V(I-i+1, J-1). \tag{5.179}$$

- Components of vectors $\mathbf{v}^C$, $\mathbf{v}^S$, $\mathbf{v}^U$ and $\mathbf{v}^V$ at C, S, U and V points, respectively:

$$v_i^C(i, J+1) = -v_i^C(I-i, J-1), \tag{5.180}$$

$$v_i^S(i, J+1) = -v_i^S(I-i+1, J), \tag{5.181}$$

$$v_i^U(i, J+1) = -v_i^U(I-i, J), \tag{5.182}$$

$$v_i^V(i, J+1) = -v_i^V(I-i+1, J-1). \tag{5.183}$$

Note that the components of vectors change the sign when they cross the symmetry meridian while scalars do not. The reason is that the base vectors change their directions when we cross the symmetry meridian. Consequently, the general formulas for the components of tensors of the n-th order contain factor $(-1)^n$. Scalars and vectors are tensors of the zeroth and first order, respectively, and thus we multiply them (their components) by $(-1)^0$ and $(-1)^1$, respectively.

The formulas for the second auxiliary grid-point circle are not given explicitly. They are constructed analogously to those for the first auxiliary grid-point circle using grid points with meridional grid index $J-1$ (instead of J).

Besides that, there exist quantities that are not located at one particular type of grid points. These quantities are auxiliary coefficients which are introduced in the LSOMG model in order to speed up the computation. Consider, for example, the horizontal tension given by Eq. (5.69). The tension discretized on the Arakawa

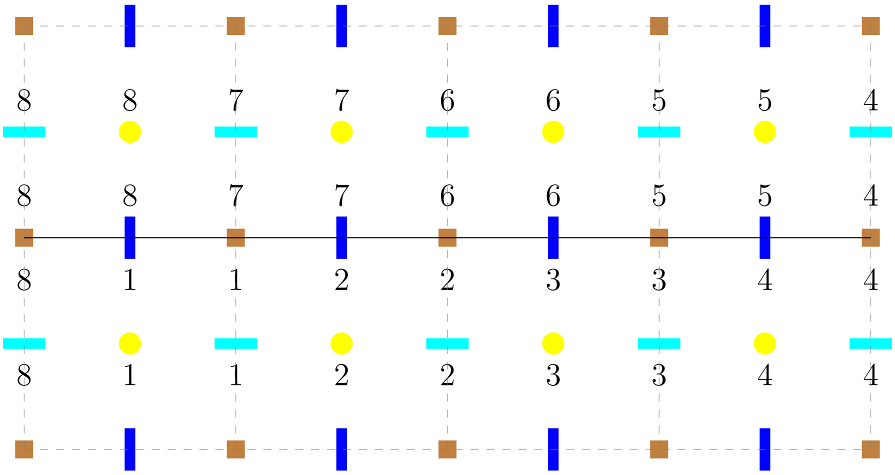

Figure 5.12: Sketch of the tripolar grid at the North-Pole seam. Numbers denote the zonal grid index used in the LSOMG code. The full line denotes the symmetry meridian.

C-grid has the form,

$$
\begin{aligned}
(D_T)_{i,j} = {} & \left(\frac{h_2}{h_1}\right)_{i,j} \left[\left(\frac{u}{h_2}\right)_{i+\frac{1}{2},j} - \left(\frac{u}{h_2}\right)_{i-\frac{1}{2},j} \right] \\
& - \left(\frac{h_1}{h_2}\right)_{i,j} \left[\left(\frac{v}{h_1}\right)_{i,j+\frac{1}{2}} - \left(\frac{v}{h_1}\right)_{i,j-\frac{1}{2}} \right] ,
\end{aligned}
\tag{5.184}
$$

where ξ_1 and ξ_2 are chosen such that $\Delta\xi_1 = \Delta\xi_2 = 1$. Eq. (5.184) can be rewritten,

$$
(D_T)_{i,j} = K_1 u_{i+\frac{1}{2},j} - K_2 u_{i-\frac{1}{2},j} - \left(K_3 v_{i,j+\frac{1}{2}} - K_4 v_{i,j-\frac{1}{2}} \right) ,
\tag{5.185}
$$

where K_i are coefficients,

$$
\begin{aligned}
K_1 &= \left(\frac{h_2}{h_1}\right)_{i,j} \left(\frac{1}{h_2}\right)_{i+\frac{1}{2},j} , \quad K_2 = \left(\frac{h_2}{h_1}\right)_{i,j} \left(\frac{1}{h_2}\right)_{i-\frac{1}{2},j} , \\
K_3 &= \left(\frac{h_1}{h_2}\right)_{i,j} \left(\frac{1}{h_1}\right)_{i,j+\frac{1}{2}} , \quad K_4 = \left(\frac{h_1}{h_2}\right)_{i,j} \left(\frac{1}{h_1}\right)_{i,j-\frac{1}{2}} ,
\end{aligned}
\tag{5.186}
$$

which are spatially varying but constant in time. In the LSOMG model, they are calculated only once during the initialization phase of the computation, stored in memory and then used in each time step. It is faster to compute tension using Eq. (5.185) since it requires less multiplications (divisions) than Eq. (5.184). The K_1 and K_2 coefficients contain metric coefficients from S and U points, the K_3 and K_4 coefficients contain metric coefficients from S and V points. The problem is that the grid indeces for the halo exchange are different for S, U and V points; compare Eqs. (5.177), (5.178) and (5.179). However, notice that K_1 and K_2 contain values from the same S point and neighbouring U points. We send K_1 and K_2 halos as if both coefficients were located at S points and then exchange their meridional halos. The same procedure is applied to the K_3 and K_4 coefficients.

5.12 Sea ice

The sea ice model used by the LSOMG model captures merely a simple thermodynamics, there is no sea-ice dynamics. If water in a surface cell is cooled below the freezing temperature T_{fr}, the water temperature is restored to the freezing temperature and a certain amount of sea ice is formed. On the other hand, if water in a surface model cell warms up above the freezing temperature in the presence of sea ice, the water temperature is restored to the freezing temperature and the excessive heat is used to melt certain amount of sea ice.

Consider a water with temperature T_w and mass m_w and sea-ice with temperature T_{fr} and mass m_i. If we put them together, the final equilibrium state depends on the sign of E_m,

$$E_m = m_w c_w (T_w - T_{fr}) - m_i l_f, \tag{5.187}$$

where c_w is the specific heat capacity of water and l_f is the latent heat of freezing or melting. The first term in Eq. (5.187) represents the heat that the water mass would release if it was cooled down to the freezing temperature and the second term represents (in absolute value) the heat needed to completely melt the ice.

If $E_m > 0$, the ice melts completely and the water with mass $m_w + m_i$ and temperature T,

$$T = T_{fr} + \frac{E_m}{(m_w + m_i)c_w}, \tag{5.188}$$

will remain.

If $E_m < 0$, the water cools down to temperature T_{fr} and the ice with mass m_m,

$$m_m = \frac{m_w c_w (T_w - T_{fr})}{l_f}, \tag{5.189}$$

will melt and the ice with mass m_i^{new},

$$m_i^{new} = m_i - m_m = -\frac{E_m}{l_f}, \tag{5.190}$$

will remain. Note that if the initial water temperature is below the freezing point, $T_w < T_{fr}$, Eq. (5.190) that determines the equilibrium ice mass remains valid. The ice grows rather than melts, $m_i^{new} > m_i$, since both terms in Eq. (5.187) are negative not just the second one.

5.13 Parallelization and other programming issues

The original LSG model is built on the FORTRAN 77 programming standard. It follows the FORTRAN 77 fixed format, global variables are accessed via common blocks and static arrays (their shape and size is specified during the compilation process) are used. We regard these features as obsolete and the LSOMG model is build on the Fortran 90 programming standard. The FORTRAN 77 fixed format, common blocks and static arrays are replaced by the Fortran 90 free format, modules and allocatable arrays, respectively. A programmer benefits from the

Fortran 90 free format that does not restrict the length of one line of the code (which is the case of Fortran 77 fixed format) and allows to write comments next to the Fortran code. A model user benefits from the use of allocatable arrays in higher resolution runs. The allocatable arrays are created on the heap that has no size limits contrary to the static arrays which are stored on the fixed-size stack.

Besides that, neither `go to` nor `equivalence` statement are used anymore. The `go to` statement is avoided since it produces a confusing spaghetti code. The `equivalence` statement is often used in the LSG model to "reshape" multidimensional arrays. For example, a 3-D array is made equivalent with a 1-D array. The reason is probably the possibility to collapse nested do loops into one loop in order to decrease the computation time. However, we tested this concept in the `Intel Fortran` compiler and the computation time stayed unchanged.

The LSG model is not parallelized. The LSOMG model is parallelized using the MPI standard. The majority of the LSOMG code is also parallelized using the OpenMP standard. We also tested the GPU parallelization using the OpenACC directives during the model development. The speed up with respect to the OpenMP parallelization depended on the particular task as well as the grid resolution. The OpenACC performed better in higher-resolution runs. The best scaling achieved in 1° E-grid version was approximately 2.8. We anticipate a further speed up in the eddy-permitting and eddy-resolving resolutions. The full GPU conversion of the code might be beneficial. However, it is beyond the scope of this PhD project given the number of other challenges. On top of that, the MPI is a well documented and established concept while the OpenACC is still under development.

The MPI parallelization is implemented using the regular domain decomposition and the master-slave model. Fig. 5.13 shows the domain decomposition for eight cores (threads) in the configuration 4×2 cores in the zonal and meridional directions, respectively. The yellow rectangle denotes the whole domain - the grid with $I \times J$ grid points. The dashed lines divide the whole domain to the smaller domains that belong to the individual cores. The gray-brown frame around the core domains are the so-called halo regions. The governing equations are discretized using the finite difference method in the LSOMG model. The discrete form of a differential operator written at the certain grid point includes not only that grid point but also the neighbouring grid points. Consequently, grid points that belong to the neighbouring core domains are needed to compute differential operators at the edges of a core domain. These grid points compose the halo region. The LSOMG halo regions are updated by calling one dedicated subroutine which invokes the MPI communication between the MPI threads.

The default width of the halo region is two grid points in the LSOMG model, which is sufficient for the second order centered differences. However, if a tripolar grid is used, the width of the eastern halo region has to be extended by one grid point. The two-point halo regions are sufficient for S (and V) points, see Fig. 5.14. The problem is caused by U (and C) points since their grid indeces are shifted by one for halo sends, compare Eqs. (5.177) and (5.178). Fig. 5.15 depicts a situation in which each core domain contains four grid points in the "zonal" direction. If we cross the symmetry meridian, the halo grid point $i = 6$ is paired with the halo grid point $i = -2$. Unfortunately, the standard two-point halo region does not

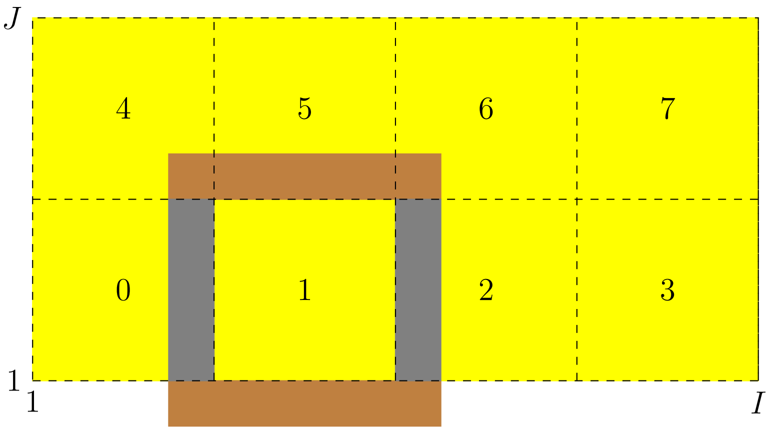

Figure 5.13: Regular decomposition of the domain (yellow) and the halo region (brown and gray) for the thread number 1.

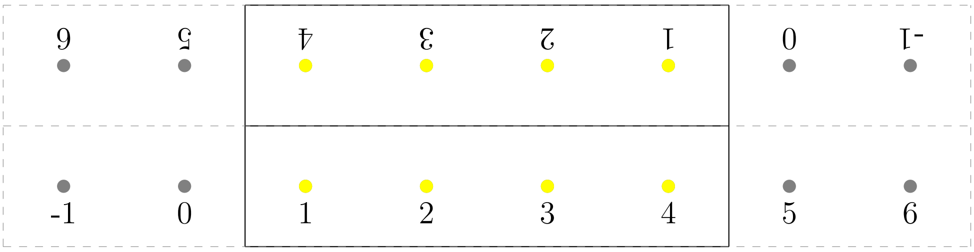

Figure 5.14: Two (parts of) S-point grids (solid lines and yellow points) with their halo regions (dashed lines and gray points) which belong to two cores and are separated by the symmetry meridian.

contain halo grid point $i = -2$ and so we have to enlarge the eastern halo region by one grid point. In the LSOMG model, zonal halos (gray region in Fig. 5.13) are updated first and the meridional halos (brown region in Fig. 5.13) are updated second. The meridional halo regions are not extended with respect to the SC version. We only send grid points $-2 \leq i \leq 5$ instead of $-1 \leq i \leq 6$.

The master-slave model means that the input data are read by master core (thread number 0) and then they are distributed to the other cores in the form of MPI messages. It is clear that the reading in the master-slave model could become a bottleneck if large data are read by a single core. We apply the master-slave model at the beginning of a computation to initialize the model. It simplifies the initializations and it does not slow down the computation since it is done only

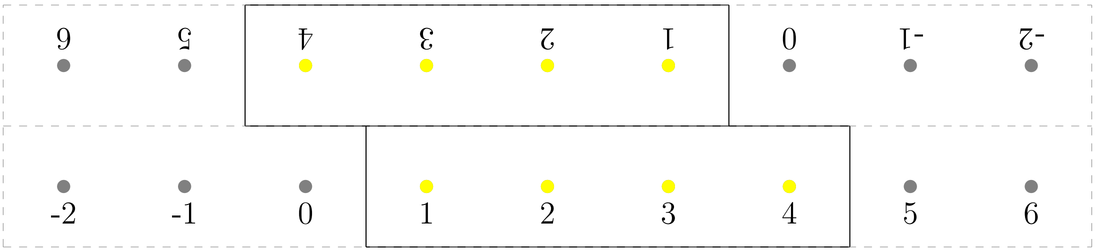

Figure 5.15: Two (parts of) U-point grids (solid lines and yellow points) with their halo regions (dashed lines and gray points) which belong to two cores and are separated by the symmetry meridian.

once. We update the boundary conditions (surface forcing) using the master-slave model only if the forcing is "sufficiently sparse" in time such as monthly values. Otherwise, the reading is also parallelized, each core is supplied with a separate data file.

We tested the performance of the MPI implementation in the LSOMG model on the Salomon supercomputer. The results are shown in Fig. 5.16. Panels (a) and (b) depict the performance of the 1° and 0.5° wind-driven LSOMG model, respectively. Panel (c) depicts the performance of the 0.25° tidally-driven LSOMG-BT model. Fig. 5.16 shows that, within the tested range, the performance of LSOMG and LSOMG-BT models may decrease but it does not saturate with the increasing number of cores. The ideal scaling is linear. The scaling in the 1° baroclinic version is linear up to 72 cores but then there is certain decrease in performance for higher number of cores. The 0.5° baroclinic version should be eight times (four times more grid points and halved time step) slower than the 1° baroclinic version. It is true up to 72 cores: 6.3, 11.9 and 16.4 years/hour in the 1° version and 0.6, 1.6 and 2.1 years/hour in the 0.5° version using 24, 48 and 72 cores, respectively. However, the scaling in the 0.5° baroclinic version is approximately linear up to the 144 cores. The 1° version with 144 cores computes 26.6 years/hour. The expected performance of 0.5° version with 144 cores is 3.3 years/hour but the actual performance is better, 4.2 years/hour. The scaling in the 0.25° barotropic version is superb. In fact, the performance curve is convex up to 192 cores which means that the scaling is better than the ideal one. It is either the consequence of measurement error or some unknown technical issue of the Salomon supercomputer.

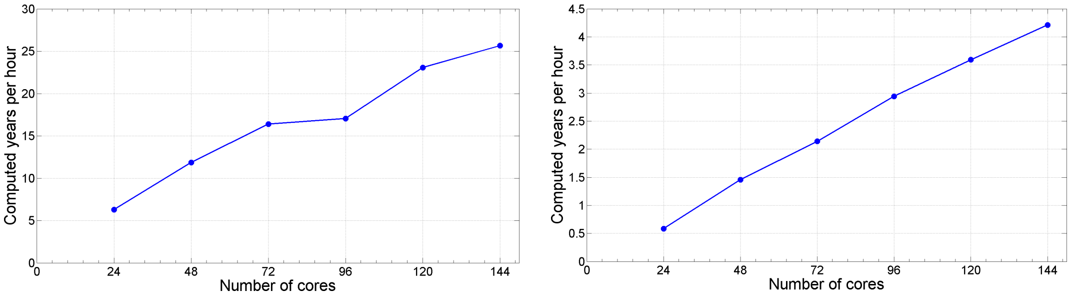
(a) 1°, LSOMG

(b) 0.5°, LSOMG

(c) 0.25°, LSOMG-BT

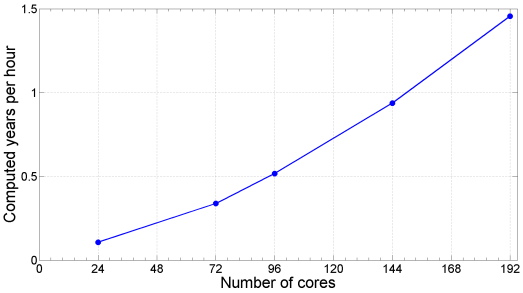

Figure 5.16: Performance of the LSOMG and LSOMG-BT models with respect to the number of cores: (a) 1° wind-driven LSOMG, (b) 0.5° wind-driven LSOMG, (c) 0.25° tidally-driven LSOMG-BT.

We consider the performance of the MPI version of the LSOMG model to be satisfactory. Nevertheless, it should be noted that it is not free of deficiencies. The regular domain decomposition is not optimal in the presence of continents. If the number of cores is large, the core domains are small and it may happen that all grid points assigned to certain cores are dry. These cores do not do any useful work. The performance of a particular domain decomposition is governed by the (largest) core-domain size and the complexity of MPI communication. It is desirable to reduce the size of core domains (less computations per each core) and/or reduce the MPI communications as much as possible to increase the performance of the MPI code.

The algorithm of Smith et al. [2010] reduces the size of core domains by using core subdomains. On the other hand, the number of MPI communications is increased at the same time. Smith et al. [2010] found the algorithm useful in the high-resolution runs. We have not implemented the algorithm of Smith et al. [2010] into the LSOMG model since the eddy-resolving configurations are probably unnecessary for the geophysical applications, which are the main focus of the LSOMG model.

Another possibility is to combine the MPI and OpenMP approaches in order to decrease the MPI communications. A low number of threads is used for the MPI parallelization with the regular domain decomposition. The OpenMP parallelization is then used in each core domain. The core domains are large, the ratio between the number of grid points in the core domain and halo region is large, which means that the MPI communications do not present a bottleneck. Additionally, a decreased total size of halo regions reduces memory requirements and the OpenMP shared memory architecture provides faster access to the memory than the MPI distributed memory architecture. The MPI + OpenMP concept is appealing and we tested it during the development of the LSOMG model. Unfortunately, we failed to achieve the expected speed up. In fact, the pure MPI version outperformed the MPI + OpenMP version of the LSOMG model.

5.14 Input data

An OGCM needs two types of input data. First, distributions of physical quantities in the entire volume of global ocean to prescribe the initial conditions. Second, distributions of physical quantities at the ocean surface to prescribe boundary conditions.

The initial conditions are given by temperature and salinity fields, velocities and sea surface heights. However, there is no need to provide measured distributions of velocities and SSHs. It is common to start the simulation from homogeneous initial conditions, $\mathbf{v} = 0$, $\eta = 0$ and run it under the proper forcing for a “sufficiently long” time. The procedure is called a spin-up. At the end of spin-up phase, the model should reach a quasi equilibrium in which the resulting velocities and SSHs are consistent with the model dynamics and there are no transients.

The boundary conditions are given by the fluxes of momentum, heat and fresh water. The momentum flux (wind stress) is generated by the wind blowing over the ocean surface. There are two options how to represent heat fluxes in the LSOMG model. The first option is to represent the heat fluxes by a strong Newtonian relaxation of temperature in the upper model layer to the climatological ocean surface temperature. A typical time scale used in our simulation with this option is 30 days. The second option is to calculate the heat fluxes from the input data using the bulk formulas according to Sec. 5.14.6, and apply only a weak relaxation of about 90 days to the climatological surface temperature. In the actual version of LSOMG, the water fluxes are not prescribed. The surface salinity is simply relaxed towards the climatological values.

Additionally, the ocean bathymetry, which determines the shape of computation domain, needs to be specified. The bathymetry is fixed in LSOMG simulations. The changes of coastal lines and uplift or drop of the ocean floor are neglected since time scales of these processes are much longer than time scales of tidally and wind driven currents which we are interested in.

5.14.1 Ocean bathymetry

The ocean bathymetry is derived from GEBCO [IOC, IHO and BODC, 2003] or ETOPO1 [Amante, 2009] data. The both data sets are provided on 1-minute SC grids covering the whole globe. The depth at the certain LSOMG grid point is computed as an average of data values from all data points within the LSOMG grid cell.

The main difficulty is to determine whether a given data point lies inside the model grid cell. It is the same task as the determination whether a point lies inside or outside of a polygon (point-in-polygon problem). The polygon is a quadrangle in our case. In the SC, the problem is simple since the grid cells are spherical isosceles trapezoids which are regularly aligned (no rotation) with respect to each other. In the GC, the situation can be much more complicated and a sophisticated algorithm needs to be used. There are several options.

The ray casting algorithm is based on a shooting rays from the point. In planar geometry, the ray crosses the polygon sides an odd number of times if it is inside the polygon. Despite a simple principle, we consider this algorithm difficult to implement because our polygon is located on a sphere not in a plane which may complicate the shooting of rays.

We have chosen a different algorithm. It is a variant of a winding number algorithm. For the given quadrangle ABCD and the data point Z, we compute sizes of angles $\sphericalangle AZB$, $\sphericalangle BZC$, $\sphericalangle CZD$ and $\sphericalangle DZA$ using the cosine formula for a spherical triangle, see Fig. 5.17. For example, the size of angle $\sphericalangle AZB$ is give by

$$|\sphericalangle AZB| = \arccos\left(\frac{\cos|AB| - \cos|BZ|\cos|AZ|}{\sin|BZ|\sin|AZ|}\right), \tag{5.191}$$

$$\cos|BZ| = \mathbf{r}_B \cdot \mathbf{r}_Z, \quad \cos|AZ| = \mathbf{r}_Z \cdot \mathbf{r}_A, \quad \cos|AB| = \mathbf{r}_A \cdot \mathbf{r}_B, \tag{5.192}$$

where $|BZ|$, $|AZ|$ and $|AB|$ are lengths of spherical-triangle sides and $\mathbf{r}_A$, $\mathbf{r}_B$ and $\mathbf{r}_Z$ are radius (position) vectors on a unit sphere. The sizes of angles $\sphericalangle BZC$, $\sphericalangle CZD$ and $\sphericalangle DZA$ are computed analogously. The data point lies inside the quadrangle if

$$|\sphericalangle AZB| + |\sphericalangle BZC| + |\sphericalangle CZD| + |\sphericalangle DZA| = 2\pi, \tag{5.193}$$

otherwise it is outside.

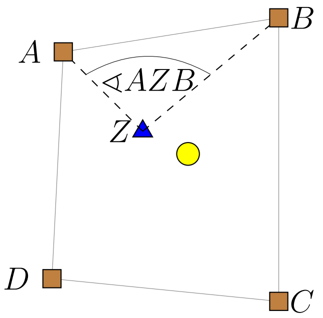

Figure 5.17: Data point Z (blue triangle) and the LSOMG grid cell (full lines). The grid cell is determined by grid-cell vertices A, B, C, D (brown squares) and it is centered to its grid point (yellow circle).

5.14.2 Initial temperature and salinity

The initial temperature and salinity distributions are taken from the World Ocean Atlas (WOA) 2013 [Locarnini et al., 2013, Zweng et al., 2013]. WOA data are provided on a SC grid with the horizontal resolution of 0.5°. The vertical resolution depends on a climatology. The annual and seasonal fields are discretized in 102 depth levels with the deepest layer in 5500 m. The monthly fields are discretized in 57 depth levels with the deepest layer in 1500 m. The first level is the ocean surface, the second layer is in 5 m for all three cases. We use annual fields as initial conditions.

We apply a different regridding scheme than in Sec. 5.14.1. The main reason is that WOA data are provided on a much coarser grid than bathymetry data. We may also argue that field quantities such as temperature and salinity require a different treatment than bathymetry. We apply the following procedure:

- We linearly interpolate WOA data in the vertical direction to the LSOMG depth levels. The interpolation use WOA values in the neighbouring upper and lower WOA depth levels, see Fig. 5.18. In the shallow coastal regions, it may happen that the upper WOA point is wet but the lower WOA point is dry (we do not consider the situation with a dry upper and a wet lower point). It would not be meaningful to interpolate land values. We simply use the value from the wet point, see Fig. 5.18.

  There are three special cases. If the LSOMG level is deeper than the last WOA level (5500 m), we use data from that last level (=nearest level). Similarly, if the LSOMG level is shallower than the second WOA level (5 m), we use data from that level. Finally, if there exists a WOA level which has exactly the same depth as the LSOMG level, no interpolation is needed and data from this level are used.

- The vertically interpolated data are then interpolated horizontally. The value at the model grid point is calculated from the neighbouring data points using either the bilinear or the IDW interpolation (see Appendix D.1). If all neighbouring data points are wet, we prefer the bilinear interpolation over the IDW interpolation since the interpolated field is smoother. If one or more data points are dry, their weights are set to zero and we apply the IDW interpolation.

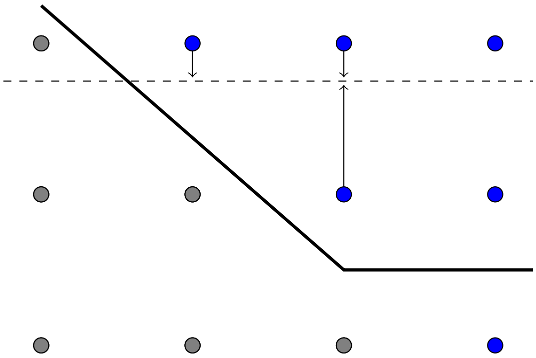

Figure 5.18: Vertical interpolation of data in the vertical cross section of data grid. Wet data points (blue dots), dry data points (gray dots), ocean bottom (thick line) and the LSOMG layer (dashed line). Arrows show how data points are used for the vertical interpolation.

> We consider three special cases. If the grid point is located at the side of the data cell, the grid-point value is calculated from the two data points on that particular cell side using the linear interpolation. If the grid point coincide with a particular data point, the value at this data point is taken. Finally, it may happen that the model and WOA bathymetries are not fully compatible and a wet grid point is surrounded by four dry data points. In that case, we search for the nearest data point and use its value.

The performance of the outlined procedure is demonstrated on initial temperatures in the depth of 221 m. The neighbouring WOA levels are level 25 in the depth of 200 m, and level 26 in the depth of 225 m. Fig. 5.19 (left) shows WOA temperature in level 26 and Fig. 5.19 (right) shows the final temperature interpolated to the LSOMG grid.

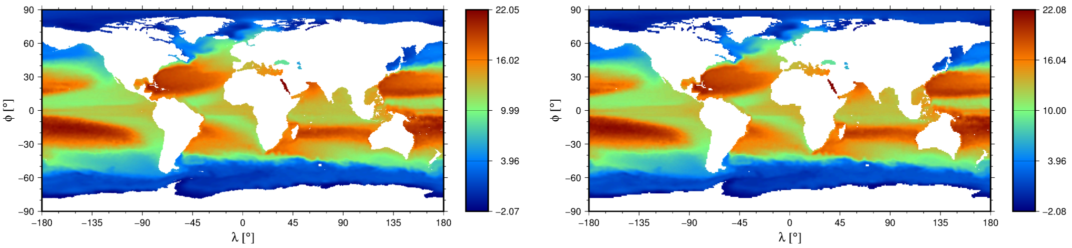

Figure 5.19: Left panel: Original WOA temperature distribution [°] in 225 m. Right panel: Temperature distribution [°] interpolated to the 1° spherical coordinate LSOMG grid in 221 m.

5.14.3 Climatological surface temperature and salinity

The surface temperature and salinity distributions are also taken from the WOA 2013. We use monthly fields from the database which are applied in a seasonal cycle. New data are read from the input file at the beginning of the 16th day of each month and horizontally interpolated to the LSOMG grid using the algorithm described in Sec. 5.14.2. The values between two months are not constant, we rather linearly interpolate data in time and continuously update the boundary values between two months.

5.14.4 Wind velocity

In early stages of this PhD project, we used the wind velocity data from the NCEP/NCAR Reanalysis 1 [Kalnay et al., 1996]. However, we have switched to ERA-Interim data [Dee et al., 2011] soon since the resolution of ERA data is much better: ERA-Interim data are provided on a 0.75° SC grid, while NCEP/NCAR data are provided on a 2.5° SC grid. Consequently, NCER/NCAR data capture main features but finer structures are missing as we can see in Fig. 5.20.

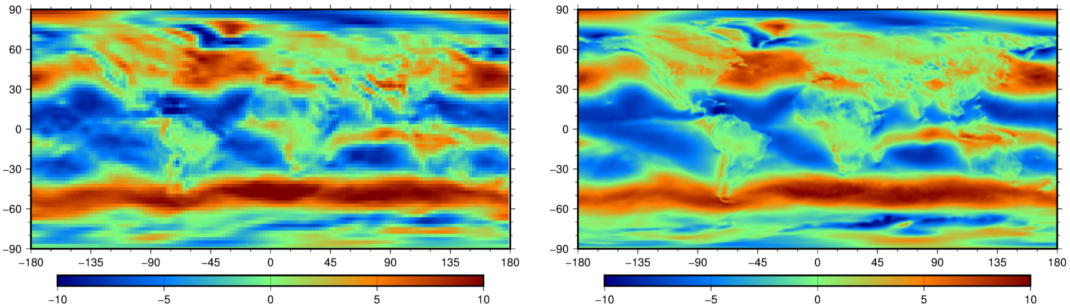

Figure 5.20: Zonal wind velocity [m/s] from the NCEP/NCAR Reanalysis 1 (left panel) and ERA-Interim (right panel) in January.

We also tested CORE-II data [Large and Yeager, 2009] as an alternative to ERA-Interim data, see Sec. 7. CORE-II data are provided on a T62 atmospheric grid with 192 × 94 grid points.

If the model uses the generalized horizontal coordinates (GC) instead of the SC, the components of wind velocity need to be recomputed (rotated) due to different directions of the GC and SC axes. Let $\mathbf{e}_\lambda$, $\mathbf{e}_\phi$ and $\mathbf{e}_1$, $\mathbf{e}_2$ be the base vectors of the SC and GC, respectively. The wind velocity can be expressed in both GC and SC,

$$\mathbf{u}_w = \tilde{u}_{w1}\mathbf{e}_\lambda + \tilde{u}_{w2}\mathbf{e}_\phi = u_{w1}\mathbf{e}_1 + u_{w2}\mathbf{e}_2, \tag{5.194}$$

where $\tilde{u}_{w1}$, $\tilde{u}_{w2}$ and u_{w1}, u_{w2} are the components of wind velocity in the SC and GC, respectively. The GC components are computed from the SC components,

$$\begin{pmatrix} u_{w1} \\ u_{w2} \end{pmatrix} = \begin{pmatrix} \cos\alpha_{sg} & \sin\alpha_{sg} \\ -\sin\alpha_{sg} & \cos\alpha_{sg} \end{pmatrix} \begin{pmatrix} \tilde{u}_{w1} \\ \tilde{u}_{w2} \end{pmatrix}, \tag{5.195}$$

where the rotation angle α_{sg} is the angle between $\mathbf{e}_1$ and $\mathbf{e}_\lambda$, see the left panel of Fig. 5.21. We compute its value numerically using Eq. (5.191).

The rotation angle computed for the tripolar reprojected grid of Murray [1996] is depicted in the right panel of Fig. 5.21. The angle is equal to zero at the reprojected equator and it changes sign when we cross the reprojected equator due to the symmetry. The departure between the GC and SC base vectors is increasing when we approach the symmetry meridian.

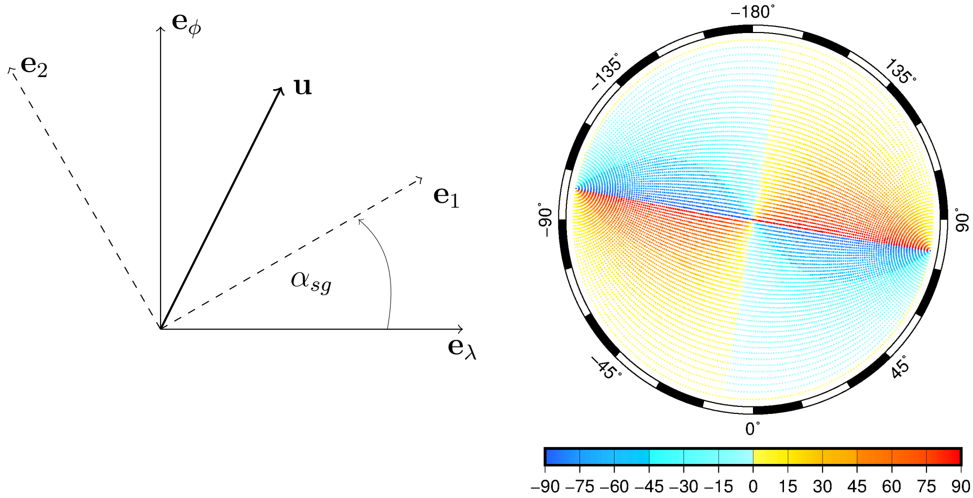

Figure 5.21: Rotation angle from the GC to the SC. Left panel: Sketch depicting the rotation angle α_{sg} from the SC (base vectors $\mathbf{e}_\lambda$, $\mathbf{e}_\phi$) to the GC (base vectors $\mathbf{e}_1$, $\mathbf{e}_2$). Right panel: Rotation angle computed for the tripolar reprojected grid of Murray [1996].

5.14.5 Conversion of in-situ temperature

As discussed in Sec. 1.4.1, the great advantage of EOS of McDougall et al. [2003] is that it is formulated in potential temperature. However, the WOA 2013 database provides only the in-situ temperatures. We thus need to convert the input WOA 2013 in-situ temperatures to potential temperatures.

The potential temperature is determined by solving the Eq. (1.113) following the procedure of McDougall et al. [2003]. The initial guess θ_0 is given by

$$\theta_0(S,T,p,p_r) = T + (p - p_r)P(S,T,p+p_r), \tag{5.196}$$

where $P(S,T,p+p_r)$ is a polynomial,

$$P(S,T,p+p_r) = a_1^d + a_2^d S + a_3^d(p+p_r) + a_4^d T + a_5^d ST + a_6^d T^2 + a_7^d T(p+p_r). \tag{5.197}$$

The values of coefficients and one check value are given in Appendix A of McDougall et al. [2003]. Next, the Newton-Raphson technique is applied to improve θ_0. The first iteration yields

$$\theta_1 = \theta_0 - \left[\frac{\sigma_e(S,\theta_0,p_r) - \sigma_e(S,T,p)}{13.9\ \mathrm{J\ kg^{-1}\ K^{-2}}}\right], \tag{5.198}$$

where 13.9 J kg^{-1} K^{-2} is the initial guess for $\left(\frac{\partial \sigma_e}{\partial T}\right)_{S,p}$ and we reference the potential temperature to the sea surface, $p_r = 0$. McDougall et al. [2003] tested the formula in the range of (0 PSU, 40 PSU) × (−3 °C, 40 °C) × (0 db, 10^4 db) with the reference pressure in the range (0 db, 10^4 db) and obtained the RMS and maximum errors 3×10^{-3} °C and 1.5×10^{-2} °C, respectively. As a consequence, they suggested to proceed one iteration further since the errors of the first iteration are still too large. The final estimate of the potential temperature θ_2 is

$$\theta_2 = \theta_0 - \left[\frac{\sigma_e(S,\theta_0,p_r) - \sigma_e(S,T,p)}{\left(\frac{\partial \sigma_e}{\partial T}\right)_{S,p}(S, \frac{\theta_0+\theta_1}{2}, p_r)}\right], \tag{5.199}$$

which requires no additional evaluations of entropy in the numerator. In total, one evaluation of $\left(\frac{\partial\sigma_e}{\partial T}\right)_{S,p}$ and two evaluations of σ_e are required. Feistel and Hagen [1995] and Feistel [2003] provide the equation to evaluate the Gibbs function,

$$G(S,T,p) = (G_{100}+G_{110}T_f)\cdot S_f^2 \ln S_f + \sum_{j=0}^{7}\sum_{k=0}^{5}\left(G_{0jk}+\sum_{i=2}^{7} G_{ijk}S_f^i\right) T_f^j p_f^k, \quad (5.200)$$

where G_{ijk} are coefficients and S_f, T_f and p_f are scaled variables given by $S = 40S_f^2$, $T = 40°\mathrm{C}\cdot T_f$ and $p = 100\mathrm{MPa}\cdot p_f$, respectively. Using the definition equation 1.114, the specific entropy is computed from Eq. (5.200) as

$$\begin{aligned}\sigma_e &= -\left(\frac{\partial G_f}{\partial T}\right)_{S,p} = -\left(\frac{\partial T_f}{\partial T}\right)_{S,p}\left(\frac{\partial G_f}{\partial T_f}\right)_{S,p} \\ &= -\frac{1}{40}\left[G_{110}S_f^2 \ln S_f + \sum_{j=1}^{7} j \sum_{k=0}^{5}\left(G_{0jk}+\sum_{i=2}^{7} G_{ijk}S_f^i\right) T_f^{j-1}p_f^k\right]. \quad (5.201)\end{aligned}$$

Similarly, the first derivative of specific entropy with respect to temperature is equal to

$$\left(\frac{\partial\sigma_e}{\partial T}\right)_{S,p} = -\frac{1}{40^2}\left[\sum_{j=2}^{7} j(j-1)\sum_{k=0}^{5}\left(G_{0jk}+\sum_{i=2}^{7} G_{ijk}S_f^i\right) T_f^{j-2}p_f^k\right]. \quad (5.202)$$

The values of coefficients G_{ijk} are given in Appendices of Feistel and Hagen [1995] and Feistel [2003].

Note that the whole procedure is repeated iteratively because Eq. (1.113) contains pressure which is not known at the beginning as it depends on density and thus on potential temperature and salinity distributions. We therefore insert hydrostatic pressure in the first iteration and refine the results in the following iterations.

5.14.6 Heat fluxes

The total heat flux Q is a sum of shortwave Q_{SW}, longwave Q_{LW}, latent Q_{LA} and sensible Q_{SN} heat fluxes,

$$Q = Q_{SW} + Q_{LW} + Q_{LA} + Q_{SN}. \quad (5.203)$$

Shortwave heat flux

The shortwave (SW) heat flux Q_{SW}, or solar radiation, includes wavelengths 0.3-3 μm [Large and Yeager, 2009]. The SW heat flux which penetrates through the ocean surface is computed from the incoming SW heat flux Q_{SW}^{down} by subtracting the portion Q_{SW}^{refl} of the incoming radiation that is reflected at the ocean surface back to the atmosphere,

$$Q_{SW} = Q_{SW}^{down} - Q_{SW}^{refl}. \quad (5.204)$$

The amount of reflected radiation depends on the SW albedo α_{SW} of the ocean surface,

$$Q_{SW}^{refl} = Q_{SW}^{down}\alpha_{SW}. \quad (5.205)$$

If we insert Eq. (5.205) into the Eq. (5.204), we obtain

$$Q_{SW} = Q_{SW}^{down}(1 - \alpha_{SW}). \tag{5.206}$$

The SW albedo in the LSOMG model is either set equal to a constant value $\alpha_{SW} = 0.1$ [Brunnabend, 2010] or its value varies with the Earth latitude,

$$\alpha_{SW} = 0.069 - 0.011\cos(2\phi) \tag{5.207}$$

according to Large and Yeager [2009]. If sea ice is present, the albedo has to be increased. We use a constant value $\alpha_{SW} = 0.75$ [Brunnabend, 2010].

Longwave heat flux

The longwave (LW) heat flux Q_{LW}, also thermal or terrestrial radiation, includes wavelengths 3-50 μm [Large and Yeager, 2009]. Similarly to the SW heat flux, the LW heat flux Q_{LW} is computed from the incoming LW heat flux Q_{LW}^{down} by subtracting the radiation Q_{LW}^{refl} that is reflected from the ocean surface and the radiation Q_{LW}^{emit} that is emitted from the ocean,

$$Q_{LW} = Q_{LW}^{down} - Q_{SW}^{refl} - Q_{LW}^{emit}. \tag{5.208}$$

The reflected LW radiation is computed analogously to the reflected SW radiation (see Eq. (5.205)),

$$Q_{LW}^{refl} = Q_{LW}^{down}\alpha_{LW}. \tag{5.209}$$

However, the reflected LW radiation is rather small. Brunnabend [2010] uses $\alpha_{LW} = 0.03$. Large and Yeager [2004] neglects the reflected LW radiation completely, $\alpha_{LW} = 0$. The outcoming radiation is computed from the Stefan-Boltzmann law which describes the black-body radiation,

$$Q_{LW}^{emit} = \epsilon_{LW}\sigma\left(\theta_s + 273.16\right)^4, \tag{5.210}$$

where θ_s is the sea surface temperature [1], ϵ_{LW} is the emissivity of the sea surface relative to the black body radiation and σ is the Stefan-Boltzmann constant, $\sigma \approx 5.67 \times 10^{-8}$ Wm^{-2}K^{-4}. In the radiative equilibrium,

$$\epsilon_{LW} = 1 - \alpha_{LW}. \tag{5.211}$$

If we insert Eqs. (5.209)-(5.211) into Eq. (5.208), we obtain the final expression for the LW radiation,

$$Q_{LW} = \epsilon_{LW}\left[Q_{LW}^{down} - \sigma\left(\theta_s + 273.16\right)^4\right]. \tag{5.212}$$

Latent and sensible heat fluxes

The both latent and sensible heat fluxes are turbulent heat fluxes and they are computed via bulk formulas,

$$Q_{LA} = \rho_a L_e C_E u_w (q_a - q_s), \tag{5.213}$$

$$Q_{SN} = \rho_a c_{pa} C_H u_w (\theta_a - \theta_s), \tag{5.214}$$

---

[1] in-situ or potential temperature, they are equal at the ocean surface

where ρ_a is the air density, L_e is the latent heat of vaporization, q_s is the saturated specific humidity at sea surface temperature, q_a is the surface air specific humidity, c_{pa} is the specific heat of air, θ_a is the air temperature and C_E, C_H are bulk transfer coefficients.

We currently use the ERA-Interim data that contain incoming SW and LW radiation heat flux, air temperature at 2 m height, dew point temperature at 2 m height, mean atmospheric pressure at sea level and wind velocity at 10 m height. The LSOMG model uses $c_{pa} = 1004$ Jkg^{-1}K^{-1} for the specific heat of air. The latent heat of evaporation L_e [J/kg], saturated specific humidity q_s [kg/kg] at sea surface temperature, surface air specific humidity q_a [kg/kg] and air density ρ_a [kg/m^3] need to be computed from the data formulas. Four different sets of data formulas were implemented into the LSOMG model.

- Formulas of Kara et al. [2002] (KRH):

$$q_s = \frac{0.62197 e_s}{p_a - 0.378 e_s}, \tag{5.215}$$

$$q_a = \frac{0.62197 e_a}{p_a - 0.378 e_a}, \tag{5.216}$$

$$\rho_a = \frac{100 p_a}{R_g(\theta_a + 273.16)(1 + 0.61 q_a)}, \tag{5.217}$$

$$L_e = (2.501 - 0.00237\theta_s)10^6, \tag{5.218}$$

  where e_s [hPa] is the saturated water vapor pressure, e_a [hPa] is the water vapor pressure at the sea surface, p_a [hPa] is the atmospheric pressure and R_g is the gas constant for dry air, $R_g = 287.1$ Jkg^{-1}K^{-1}. The air temperature θ_a is in [°C]. The vapor pressures e_s and e_a are equal to

$$e_s = 5.99902615 \exp\left[\frac{\left(18.729 - \frac{\theta_s}{227.3}\right)\theta_s}{\theta_s + 257.87}\right], \tag{5.219}$$

$$e_a = 6.1121 \exp\left[\frac{\left(18.729 - \frac{\theta_d}{227.3}\right)\theta_d}{\theta_d + 257.87}\right], \tag{5.220}$$

  where θ_d [°C] is the dew point temperature

- Modified formulas of Kara et al. [2002] (LY): The surface air specific humidity, air density and latent heat of evaporation are computed from Eqs. (5.216), (5.217) and (5.218), respectively. Eq. (5.215) for the saturated specific humidity at sea surface temperature is replaced by

$$q_s = 0.98 \frac{640380}{\rho_a} e^{-\frac{5107.4}{\theta_s + 273.16}}, \tag{5.221}$$

  where factor 0.98 is applied only over open water according to Large and Yeager [2004].

- Formulas of Kondo [1975] (KON): The formulas for the saturated specific humidity at sea surface temperature, surface air specific humidity and water vapor pressure at the sea surface are Eqs. (5.215), (5.216) and (5.220), respectively, as in Kara et al. [2002]. Eqs. (5.217) and (5.218) for the air density and latent heat of vaporization are replaced by

$$\rho_a = 1.205, \tag{5.222}$$

$$L_e = 4.186 \times 10^3 \, (594.9 - 0.5\theta_s) \tag{5.223}$$

and Eq. (5.219) for the saturated water vapor pressure is replaced by

$$e_s = 0.98 \times 6.1078 \times 10^{\frac{7.5\theta_s}{237.3+\theta_s}}. \tag{5.224}$$

- Formulas used in Brunnabend [2010] (BRU): The saturated specific humidity q_s at sea surface temperature is computed from Eq. (5.215),

$$q_a = \frac{3.80042 e_s^{\frac{A\theta_d}{\theta_d + B}}}{p_a}, \tag{5.225}$$

$$\rho_a = 1.3, \tag{5.226}$$

$$L_e = \begin{cases} 2.560 \times 10^6 & \text{open water,} \\ 2.834 \times 10^6 & \text{sea-ice,} \end{cases} \tag{5.227}$$

where the coefficients A and B in Eq. (5.225) are equal to

$$A = 17.3, \qquad B = 237.3^\circ \text{ C} \qquad \text{open water,} \tag{5.228}$$

$$A = 21.9, \qquad B = 265.5^\circ \text{ C} \qquad \text{sea ice .} \tag{5.229}$$

The particular form of bulk transfer coefficients is not unique. We implemented the bulk transfer coefficients of Kara et al. [2002], Kondo [1975] and Large and Yeager [2004] into the LSOMG model. Besides the bulk transfer coefficients C_E and C_H, all three methods provide formulas to compute the drag coefficient C_D. The drag coefficient C_D is used in the bulk formula (4.24) for the wind stress, which is a turbulent flux (of momentum) similar to the turbulent fluxes of latent and sensible heat.

We summarize all three methods in the following text in order to provide direct and complete instructions of how to implement them. The reason is that we have found some inconsistencies in the original papers. For example, step number seven in Large and Yeager [2004] is incorrect. In particular, the equations for C_H and C_E are incorrect. The correct equations are provided in Large [2006]. A reader of the original text may also overlook that the coefficients in Eqs. (5.258)-(5.260) are at the measurement height and stability while the coefficient in Eq. (5.266) is at 10 m for the neutral stability.

Coefficients used in Brunnabend [2010] (BRU)

Brunnabend [2010] uses the simplest form of bulk transfer coefficients, they are set equal to constant values,

$$C_D = \begin{cases} 1 \times 10^{-3} & \text{open water,} \\ 1.32 \times 10^{-3} & \text{sea-ice,} \end{cases} \tag{5.230}$$

$$C_E = C_H = 1.75 \times 10^{-3}. \tag{5.231}$$

Coefficients of Kara et al. [2002] (KRH)

Kara et al. [2002] suggests to compute the bulk transfer coefficients by evaluating the polynomials,

$$C_D = \left[C_{0D} + C_{1D}(\theta_s - \theta_a)\right]/1000, \tag{5.232}$$

$$C_E = \left[C_{0H} + C_{1H}(\theta_s - \theta_a)\right]/1000, \tag{5.233}$$

$$C_H = 0.95 C_E, \tag{5.234}$$

where

$$C_{0D} = 0.692 + 0.0710 u_w - 0.000700 u_w^2, \tag{5.235}$$

$$C_{1D} = 0.083 - 0.0054 u_w + 0.000093 u_w^2, \tag{5.236}$$

$$C_{0H} = 0.8195 + 0.0506 u_w - 0.0009 u_w^2, \tag{5.237}$$

$$C_{1H} = -0.0154 + \frac{0.5698}{u_w} - \frac{0.6743}{u_w^2}. \tag{5.238}$$

The wind speed u_w in [m/s] is limited to

$$2.5 \leq u_w \leq 32.5. \tag{5.239}$$

Coefficients of Kondo [1975] (KON)

Kondo [1975] computes the bulk transfer coefficients at height $z_{\theta q}$ where air temperature and humidity are measured. The coefficients are computed in three steps:

1. The bulk transfer coefficients at 10 m for the neutral atmospheric stability are computed,

$$C_{DN} = 10^{-3}\left[a_d + 10^{-2} b_d u_w^{p_d}\right], \tag{5.240}$$

$$C_{EN} = 10^{-3}\left[a_e + 10^{-2} b_e u_w^{p_e} + c_e\left(10^{-2} u_w - 8\right)^2\right], \tag{5.241}$$

$$C_{HN} = 10^{-3}\left[a_h + 10^{-2} b_h u_w^{p_h} + c_h\left(10^{-2} u_w - 8\right)^2\right]. \tag{5.242}$$

   The values of coefficients a_d, a_e, a_h, b_d, b_e, b_h, c_e, c_h, p_d, p_e, p_h are given in Kondo [1975]. The wind speed u_w in [m/s] is limited to

$$0.3 \leq u_w \leq 50. \tag{5.243}$$

2. The transfer coefficients are shifted to the measurement height $z_{\theta q}$,

$$C_{DNh} = \frac{\kappa^2}{\left[\frac{\kappa}{\sqrt{C_{DN}}} + \ln\left(\frac{z_{\theta q}}{z_{10}}\right)\right]^2}, \tag{5.244}$$

$$C_{HNh} = \frac{\kappa\sqrt{C_{DNh}}}{\kappa\frac{\sqrt{C_{DN}}}{C_{HN}} + \ln\left(\frac{z_{\theta q}}{z_{10}}\right)}, \tag{5.245}$$

$$C_{ENh} = \frac{\kappa\sqrt{C_{DNh}}}{\kappa\frac{\sqrt{C_{DN}}}{C_{EN}} + \ln\left(\frac{z_{\theta q}}{z_{10}}\right)}, \tag{5.246}$$

   where $z_{10} = 10$ m.

3. Finally, the stability s_a of the atmospheric boundary layer,

$$s_a = \frac{\theta_s - \theta_a}{\left[1 - \ln\left(\frac{z_{\theta q}}{z_{10}}\right)\right]^2 u_w^2} \tag{5.247}$$

is taken into consideration,

$$s_a < -3.3 \quad \Rightarrow \quad \begin{cases} C_D = 0, \\ C_E = 0, \\ C_H = 0, \end{cases} \tag{5.248}$$

$$-3.3 \leq s_a < 0 \quad \Rightarrow \quad \begin{cases} C_D = C_{DNh}\left[0.1 + 0.03 s_a + 0.9 e^{4.8 s_a}\right], \\ C_E = C_{ENh}\left[0.1 + 0.03 s_a + 0.9 e^{4.8 s_a}\right], \\ C_H = C_{HNh}\left[0.1 + 0.03 s_a + 0.9 e^{4.8 s_a}\right], \end{cases} \tag{5.249}$$

$$0 \leq s_a \quad \Rightarrow \quad \begin{cases} C_D = C_{DNh}\left[1.0 + 0.47\sqrt{s_a}\right], \\ C_E = C_{ENh}\left[1.0 + 0.47\sqrt{s_a}\right], \\ C_H = C_{HNh}\left[1.0 + 0.47\sqrt{s_a}\right]. \end{cases} \tag{5.250}$$

Coefficients of Large and Yeager [2004] and Large [2006] (LY)
Large and Yeager [2004] do not restrict the measurement heights. Let wind speed, potential air temperature and surface air specific humidity be measured at heights z_u, z_θ and z_q, respectively. However, all transfer coefficients are determined at height z_u where the wind speed is measured.

The coefficients are computed in an iterative process. To initialize the process, the wind speed u_{wN} at 10 m for the neutral stability is set equal to the wind speed measured at height z_u and limited according to Eq. (5.243),

$$u_{wN} = u_w(z_u). \tag{5.251}$$

The coefficients C_{DN}, C_{EN}, C_{HN} at 10 m for the neutral stability are computed,

$$C_{DN} = \frac{0.0027}{u_{wN}} + 0.000142 + 0.0000764 u_{wN}, \tag{5.252}$$

$$C_{EN} = 0.0346\sqrt{C_{DN}}, \tag{5.253}$$

$$C_{HN} = 0.0327\sqrt{C_{DN}} \tag{5.254}$$

and their values are used to initialize the transfer coefficients C_D, C_E and C_H,

$$C_D = C_{DN}, \qquad C_E = C_{EN}, \qquad C_H = C_{HN}. \tag{5.255}$$

Finally, the potential air temperature and specific humidity at height z_u are initialized with the measured values,

$$\theta_a(z_u) = \theta_a(z_\theta), \qquad q_a(z_u) = q_a(z_q). \tag{5.256}$$

The following seven steps are then repeated. According to Large and Yeager [2004], the maximum of five iterations is needed and usually only two iterations are sufficient since the ocean is close to the neutral stability.

1. Compute the virtual potential temperature θ_v,

$$\theta_v = \theta_a(z_u)\left[1 + 0.608 q_a(z_u)\right]. \tag{5.257}$$

2. Compute the turbulent scales u_*, θ_* and q_*,

$$u_* = \sqrt{C_D} u_w(z_u), \tag{5.258}$$

$$\theta_* = \frac{C_H}{\sqrt{C_D}}\left[\theta_a(z_\theta) - \theta_s\right], \tag{5.259}$$

$$q_* = \frac{C_E}{\sqrt{C_D}}\left[q_a(z_q) - q_s\right]. \tag{5.260}$$

3. Compute the stability parameters ζ_u, ζ_θ and ζ_q,

$$\zeta_u = \zeta(z_u), \quad \zeta_\theta = \zeta(z_\theta), \quad \zeta_q = \zeta(z_q), \tag{5.261}$$

   where the stability parameter $\zeta(z)$ is given by

$$\zeta(z) = \frac{\kappa g z}{u_*^2}\left(\frac{\theta_*}{\theta_v} + \frac{q_*}{q_a(z_q) + 0.608^{-1}}\right) \tag{5.262}$$

   and $\kappa = 0.4$ is the von Karman constant. The stability parameters in the LSOMG model are limited,

$$-2 \leq \zeta(z) \leq 1. \tag{5.263}$$

4. Compute integrals of the dimensionless flux profiles $\Psi_m(\zeta_u)$, $\Psi_h(\zeta_u)$, $\Psi_h(\zeta_\theta)$ and $\Psi_h(\zeta_q)$. The integral $\Psi_m(\zeta)$ corresponds to momentum and $\Psi_h(\zeta)$ to heat and moisture,

$$\zeta \geq 0 \quad \Rightarrow \quad \begin{array}{l} \Psi_m(\zeta) = -5\zeta, \\ \Psi_h(\zeta) = -5\zeta, \end{array} \tag{5.264}$$

$$\zeta < 0 \quad \Rightarrow \quad \begin{array}{l} \Psi_m(\zeta) = 2\ln\left(\frac{1+\zeta}{2}\right) + \ln\left(\frac{1+\zeta^2}{2}\right) - 2\tan^{-1}(\zeta) + \frac{\pi}{2}, \\ \Psi_h(\zeta) = 2\ln\left(\frac{1+\zeta^2}{2}\right). \end{array} \tag{5.265}$$

5. Convert the measured wind speed to the wind speed at 10 m and neutral stability and shift the measured air temperature and specific humidity to the height where the wind speed is measured,

$$u_{wN} = \frac{u_w(z_u)}{1 + \frac{\sqrt{C_{DN}}}{\kappa}\left[\ln\left(\frac{z_u}{z_{10}}\right) - \Psi_m(\zeta_u)\right]}, \tag{5.266}$$

$$\theta_a(z_u) = \theta_a(z_\theta) - \frac{\theta_*}{\kappa}\left[\ln\left(\frac{z_\theta}{z_u}\right) + \Psi_h(\zeta_u) - \Psi_h(\zeta_\theta)\right], \tag{5.267}$$

$$q_a(z_u) = q_a(z_q) - \frac{q_*}{\kappa}\left[\ln\left(\frac{z_q}{z_u}\right) + \Psi_h(\zeta_u) - \Psi_h(\zeta_q)\right], \tag{5.268}$$

   where $z_{10} = 10$ m.

6. Update the neutral stability coefficients at 10 m using Eqs. (5.252), (5.253) and

$$C_{HN} = \begin{cases} 0.0180\sqrt{C_{DN}} & \text{if } \zeta_\theta > 0, \\ 0.0327\sqrt{C_{DN}} & \text{if } \zeta_\theta \leq 0. \end{cases} \tag{5.269}$$

7. Compute the coefficients at the measurement height and stability,

$$C_D = \frac{C_{DN}}{\left\{1 + \frac{\sqrt{C_{DN}}}{\kappa}\left[\ln\left(\frac{z_u}{z_{10}}\right) - \Psi_m(\zeta_u)\right]\right\}^2}, \tag{5.270}$$

$$C_H = \frac{C_{HN}}{\left\{1 + \frac{C_{HN}}{\kappa\sqrt{C_{DN}}}\left[\ln\left(\frac{z_u}{z_{10}}\right) - \Psi_h(\zeta_u)\right]\right\}^2}, \tag{5.271}$$

$$C_E = \frac{C_{EN}}{\left\{1 + \frac{C_{EN}}{\kappa\sqrt{C_{DN}}}\left[\ln\left(\frac{z_u}{z_{10}}\right) - \Psi_h(\zeta_u)\right]\right\}^2}. \tag{5.272}$$

In the presence of sea ice, the algorithms of Kondo [1975] and Large and Yeager [2004] are modified. The bulk transfer coefficients at 10 m for the neutral atmospheric stability are set equal to constant values. Large and Yeager [2004] use

$$C_{DN} = C_{HN} = C_{EN} = 1.63 \times 10^{-3}, \tag{5.273}$$

Mellor and Kantha [1989] use

$$C_{DN} = 3.0 \times 10^{-3}, \tag{5.274}$$

$$C_{HN} = C_{EN} = 1.5 \times 10^{-3}. \tag{5.275}$$

We prefer the second option based on the suggestion in the MRI model manual [Tsujino et al., 2010].

Heat fluxes computed from the ERA-Interim data

We used ERA-Interim data to test and compare the methods described above. We decided to use daily data for this purpose. Unfortunately, daily data are not directly available, we thus constructed them from the available data. The SW and LW heat fluxes were computed by summing together the two twelve-hour long additive data products. The other variables were computed by averaging data sampled in six-hour long intervals, i.e., four data samples were averaged to get one daily value.

The heat fluxes presented in the following text are the climatological heat fluxes. We computed them from the one year long time series of daily heat fluxes which we averaged in time.

The climatological SW heat fluxes are depicted in Fig. 5.22. In the left panel, we used the constant SW albedo $\alpha_{SW} = 0.1$ while in the right panel, we computed the albedo from the Eq. (5.207). The overall pattern of the SW heat flux is the same in both panels, however, the SW heat flux is stronger in the right panel. The values of the SW albedo computed using Eq. (5.207) smoothly varies between 0.058 at the Equator and 0.080 at the poles. All values are thus smaller than constant $\alpha_{SW} = 0.1$ with the largest difference at the Equator and the smallest

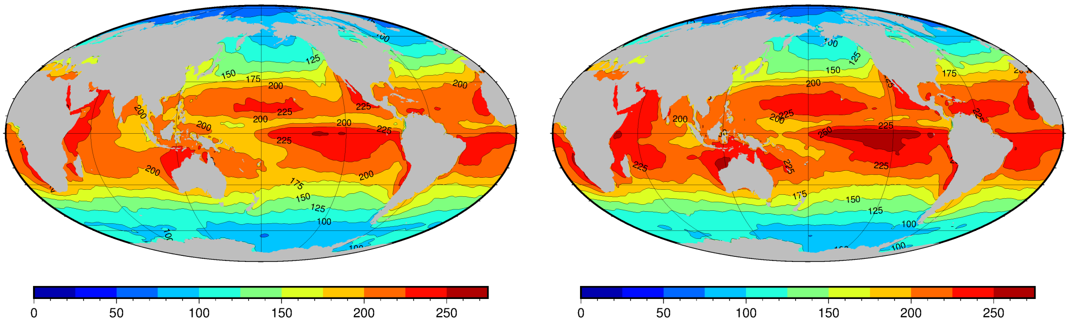

Figure 5.22: Climatological shortwave heat flux Q_{SW} [W/m^2] computed from ERA-Interim daily data. Left: $\alpha_{SW} = 0.1$. Right: α_{SW} computed using Eq. (5.207).

difference at the poles. The smaller amount of the reflected SW radiation results in the stronger SW heat flux that penetrates through the ocean surface. The maximum differences between the two SW heat fluxes are around 12 W/m^2.

The climatological LW heat fluxes are depicted in Fig. 5.23. Similar to Fig. 5.22, the left and right panels differ in the LW albedo used. The albedo is larger in the left panel, $\alpha_{LW} = 0.03$, than in the right panel, $\alpha_{LW} = 0$. The smaller albedo means larger emissivity. The LW heat flux is directly proportional to the emissivity and thus the flux is stronger in the right panel. The maximum differences between the two LW heat fluxes are around 5 W/m^2.

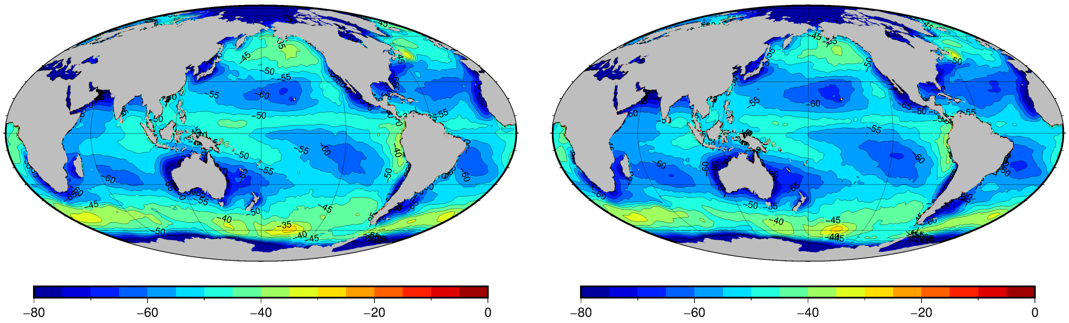

Figure 5.23: Climatological longwave heat flux Q_{LW} [W/m^2] computed from ERA-Interim daily data. Left panel: $\alpha_{LW} = 0.03$. Right panel: $\alpha_{LW} = 0$.

The climatological LA and SN heat fluxes are shown in Figs. 5.24 and 5.25, respectively. Panels (a), (b), (c) and (d) depicts results from LY, KRH, KON and BRU bulk formulas, respectively. The individual bulk formulas are used to compute both the bulk transfer coefficients and the values of q_s, q_a, ρ_a and L_e. The smallest amplitudes of LA and SN heat fluxes are computed using the KRH bulk formulas. The peak amplitudes of the LA fluxes of LY, KON and BRU are larger by approximately 35 W/m^2, 50 W/m^2 and 100 W/m^2, respectively. Similarly, the peak amplitudes of the SN fluxes of LY, KON and BRU are larger by approximately 3 W/m^2, 5 W/m^2 and 10 W/m^2, respectively. Note that the climatological LA fluxes are larger by approximately one order in magnitude than the climatological SN fluxes. In fact, the variations in the LA heat fluxes caused by the choice of particular bulk formula are larger than the SN fluxes itselves.

(a) LY (b) KRH

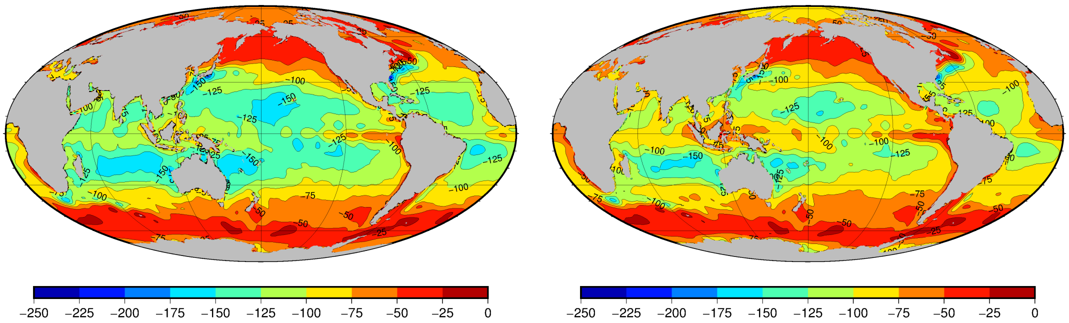

(c) KON (d) BRU

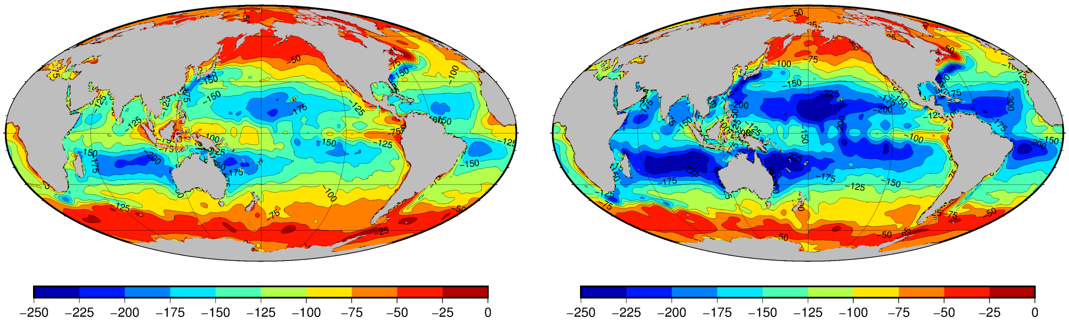

Figure 5.24: Climatological latent heat flux Q_{LA} [W/m^2] computed from ERA-Interim daily data using the LY, KRH, KON and BRU bulk formulas (both coefficients and data).

The climatological net heat fluxes are depicted in Fig. 5.26. The LW albedo is set to $\alpha_{LW} = 0$ in all presented bulk formulas. The SW albedo is set to $\alpha_{SW} = 0.1$ in the BRU solution and it is computed from Eq. (5.207) in the LY, KRH and KON solutions. The BRU net heat flux stands out from our set of computed heat fluxes, it is overly cold. The reason is that the positive SW heat flux has smaller amplitudes while the negative SN and especially the LA heat fluxes have larger amplitudes in the BRU solution than in the LY, KRH and KON solutions. As a consequence, the peak values, e.g., in the warm tongue west of South America does not reach 125 W/m^2 in the BRU net flux while the values larger than 125 W/m^2 compose a significant part of the warm tongue in the KON, LY and KRH solutions. In the KRH net heat flux, which is the warmest of the presented fluxes, even the values over 150 W/m^2 can be found. The LY, KRH and KON net heat fluxes are closer to each other, but differences between them are also visible. Consider the net heat flux in large ocean basins such as the Pacific Ocean. The BRU net heat flux is mostly negative in the Pacific Ocean. The KON net heat flux is significantly warmer, though the regions with negative heat flux are also extensive. The LY net heat flux is mostly positive and the KRH net heat flux is dominated by positive values.

We have already pointed out the large variations in the LA heat fluxes among the bulk formulas. In order to understand them more deeply, we investigate the sensitivity of the LA heat flux in the LY method on q_s, q_a, ρ_a and L_e. We have chosen the LY method because of two reasons. First, the LY bulk transfer coefficients are rather complex. Second, we supplement them with LY data as

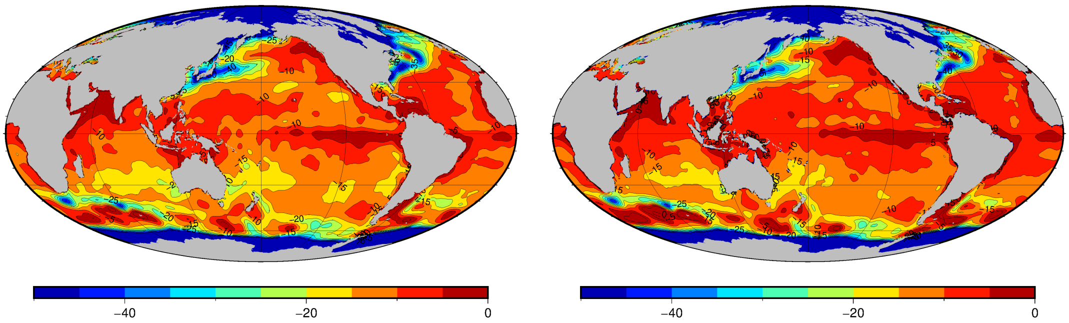

(a) LY

(b) KRH

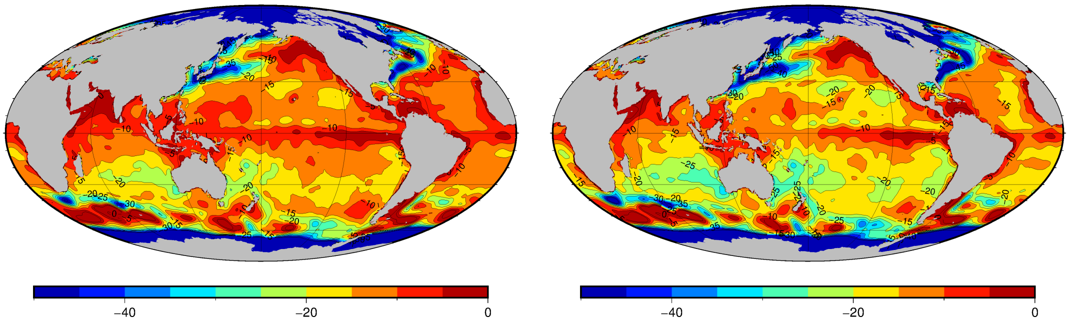

(c) KON

(d) BRU

Figure 5.25: Climatological sensible heat flux Q_{SN} [W/m^2] computed from ERA-Interim daily data using the LY, KRH, KON and BRU bulk formulas (both coefficients and data).

default but in the original paper Large and Yeager [2004] suggest to use

$$\rho_a = 1.22 \text{ kg/m}^3, \tag{5.276}$$

$$L_e = 2.5 \times 10^6 \text{ J/kg}, \tag{5.277}$$

instead of more sophisticated Eqs. (5.217) and (5.218) used in the LY method. The differences in Q_{LA} computed using KON, KRH and BRU data with respect to the reference flux computed using LY data are depicted in panels (b), (c) and (d) of Fig. 5.27, respectively. The reference flux in panel (a) is the same as in Fig. 5.24 (a). The largest differences are caused by the use of BRU data. Regions where the changes in the LA heat flux reach 35 W/m^2 are well pronounced. KON data has much smaller impact on the LA heat flux, the differences do not exceed 15 W/m^2. Nevertheless, regions where differences are larger than 10 W/m^2 are rather extensive. The use of KRH data has the smallest influence on the LA heat flux. That was anticipated since LY and KRH data are computed using the same equations except for the equation for saturated specific humidity at sea surface temperature. In the most regions, the changes in the LA flux are around 5-10 W/m^2.

To sum it up, different data formulas produce different LA heat fluxes but this is not the major source of large variations in LA heat fluxes among the considered methods. Equally important or even more influential are the bulk transfer coefficients. The LA heat fluxes computed using BRU data formulas are markedly different to the heat fluxes computed using other data formulas. The BRU method thus differ from other methods in both bulk transfer coefficients and data formulas.

(a) LY (b) KRH

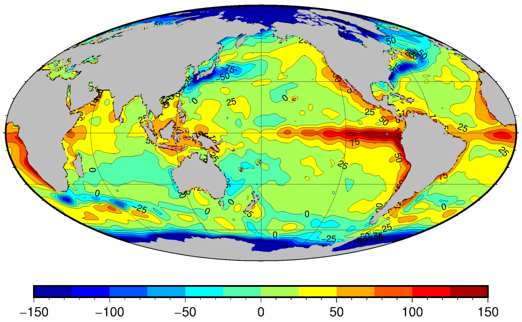

(c) KON (d) BRU

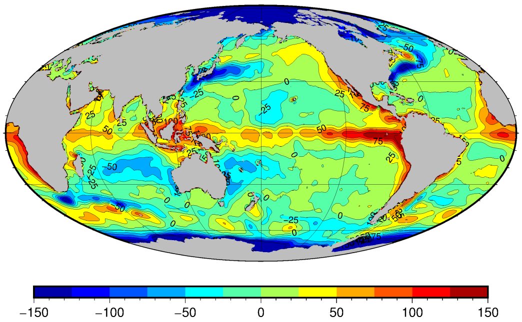

Figure 5.26: Climatological net heat flux Q [W/m^2] computed from ERA-Interim daily data using the LY, KRH, KON and BRU bulk formulas (both coefficients and data).

(a) $(Q_{LA})_{LY\,data}$ (c) $(Q_{LA})_{KON\ data} - (Q_{LA})_{LY\ data}$

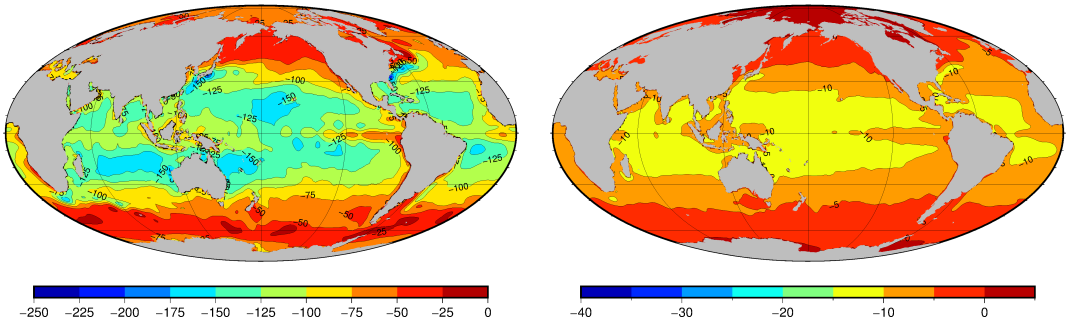

(e) $(Q_{LA})_{KRH\ data} - (Q_{LA})_{LY\ data}$ (g) $(Q_{LA})_{BRU\ data} - (Q_{LA})_{LY\ data}$

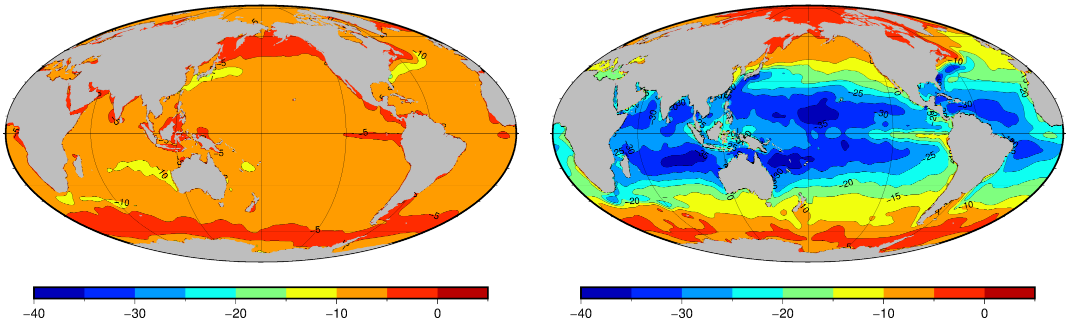

Figure 5.27: Latent heat flux [W/m^2] (a) computed using the LY bulk transfer coefficients and LY data. Panels (b),(c) and (d) depict the differences [W/m^2] between the latent heat fluxes computed using the LY bulk transfer coefficients and KON (b), KRH (c) and BRU (d) data with respect to the reference flux (a).

Part III

Numerical simulations of ocean and ocean-induced magnetic field

6. Numerical tests of the LSOMG model

We start with the barotropic numerical tests of the LSOMG-BT model in Sec. 6.1, 6.3 and 6.2. Sec. 6.1 is devoted to the simple numerical tests suitable for testing the tidal component of global ocean models. In Sec. 6.2, we use the modified versions of the tests from Sec. 6.1 to verify the implementation of the Yin-Yang grid and the reduced spherical coordinate grid in the LSOMG-BT model. In Sec. 6.3, the wind-driven circulation in a simple setup computed using the LSOMG-BT model is tested against the analytical solution. The rest of the chapter focuses on the baroclinic features of the LSOMG model. In Sec. 6.4, we verify the implementation of vertical friction in the momentum equation by inspecting the Ekman layer. In Sec. 6.5, we compare the performance of tracer advection schemes used in the LSOMG model.

6.1 Tsunami and tidal numerical tests

The following study is published as a paper Šachl et al. [2020]. It is a result of cooperation with my colleague David Einšpigel, the author of the DEBOT model.

6.1.1 Introduction

The performance of hydrodynamic tidal models is limited by several factors:

- Internal wave drag: We explained IWD in Sec. 4.4. We remind you the study of Green and Nycander [2013] that tested several IWD schemes. In Sec. 5.10 we discussed that even the present-day high-resolution baroclinic models resolve only the low baroclinic modes and thus they should also include a parameterized IWD [Arbic et al., 2010].

- Self attraction and loading: We explained SAL in Sec. 4.4. Recall that its calculation is numerically demanding and thus it is common to use the scalar approximation of Accad and Pekeris [1978] which simply lowers the value of surface pressure gradients in the governing equations, see Eq. (4.43).

- Bottom drag coefficient: It is common to use a constant value between 2.5×10^{-3} and 3×10^{-3} for the bottom drag coefficient. However, the studies of Wang et al. [2014] and Kagan and Timofeev [2015] suggest that a spatially varying bottom drag coefficient is a better choice, at least for regional tidal studies.

- Bathymetry: The ocean depth affects the speed of external gravity waves. The topographic roughness which enters the IWD parameterization is computed from bathymetry data. Consequently, the resolution and quality of bathymetry data are important factors for tidal studies. Nevertheless, Arbic et al. [2004] argued that the smaller spatial scales are missing in the present-day bathymetry data and tuned their IWD scheme by adding a multiplicative factor. Einšpigel and Martinec [2016] tested GEBCO [IOC, IHO and BODC, 2003] and ETOPO1 [Amante, 2009] data and they recommended to use GEBCO over ETOPO1.

- Numerical issues:
  - Splitting of tidal and non-tidal velocities: The IWD schemes are acting on the tidal velocities. However, standard OGCMs do not distinguish between tidal and non-tidal motions. Arbic et al. [2010] used a running 25-h average to separate them, although this separation may not be perfect. Sakamoto et al. [2013] used a linear tidal model that was running independently and which provided tidal velocities to the OGCM, see Sec. 5.10. The separation of tidal and non-tidal motions is then exact, but the scheme is probably not suitable for shallow coastal regions where nonlinearities become important.
  - Splitting of the barotropic and baroclinic systems: OGCMs commonly split the fast barotropic and slow baroclinic dynamical modes and evolve them with different time steps, see Sec. 5.2. The separation is realized by vertical averaging which is approximate, but sufficiently accurate. In order to suppress numerical instabilities, Griffies [2004] suggested to use time averaging in the barotropic system. A scheme is tested in the wind-driven runs but, according to our experience, it is damping tidal motions since their period is smaller, see Sec. 5.10.

The study of Stammer et al. [2014] confirms that the accuracy of purely (no-data constrained) hydrodynamic barotropic models is significantly lower than the accuracy of assimilative models that are constrained by data. This means that if a pure hydrodynamic barotropic model is tested against real data, a bug in the numerical model may not be found. It would be therefore useful to test the numerical model in a simplified numerical test. We expect that the growing interest in the effects of tidal forcing on the global-ocean circulation will continue in the future, which makes such numerical test even more valuable. While there are papers that inspect the performance of ocean models, it seems that there is no easily accessible numerical test appropriate for an OGCM with a tidal forcing.

Therefore, we present a set of numerical tests suitable for a global OGCM forced by tides. We build upon the work of Williamson et al. [1992], but we adapt it to oceanic conditions. We consider shallow water equations in our numerical tests, since the tidal force should be included into the barotropic part of the OGCM [Schiller and Fiedler, 2007]. Indeed, tidal force can be safely treated as a barotropic forcing since its vertical variations are negligible within the ocean. We also use the proposed numerical tests to inspect the performance of several time stepping schemes and computational grids which are used in the state-of-art OGCMs. Although the proposed numerical tests are simple compared to the realistic simulations, their analytic solutions are not available. We thus check the conservation of time invariants to ensure that the solution is physically meaningful. We also compare the time evolution of certain physical quantities and the differences in sea surface heights at particular time instants with respect to a reference solution.

6.1.2 Numerical setup

In total, six different configurations of the LSOMG-BT model are subject to the three numerical tests. We test FB on the grid B, FB, FBgen and CNmod on the grid C, and FB and IMP on the grid E, see Table 6.1. Note that these configurations are used in the following OGCMs: C–FB in MOM6 and HIM, C–FBgen in ROMS, C–CN in MITgcm, B–FB in MOM5, and E–IMP in LSG.

Configuration	Grid	Time-stepping scheme	Ocean model
C–FB	C	Forward-backward (FB)	MOM6, HIM
C–FBgen	C	Generalized forward-backward (FBgen)	ROMS
C–CN	C	Modified Crank-Nicolson (CNmod)	MITgcm
B–FB	B	Forward-backward (FB)	MOM5
E–FB	E	Forward-backward (FB)	-
E–IMP	E	Euler implicit (IMP)	LSG

Table 6.1: Model configurations considered in the numerical tests and ocean models which use these configurations.

The governing equations, time stepping schemes, tidal forcing and other numerical features used in the LSOMG-BT model are discussed in Sec. 4. The horizontal friction and bottom stress are set equal to zero in the numerical tests, since we inspect the energy conservation and dissipative terms would violate it. Besides that, neither SAL nor IWD parameterizations are used in the tests. Both terms are needed for a realistic modelling of barotropic tides as discussed in Sec. 4 but they are pointless in the simplified tests. Note that the contribution of advection terms should not be significant in our numerical tests according to the results of tests carried out by the full nonlinear DEBOT model.

Tsunami test (TSU)

The initial conditions in the TSU are given by zero velocities over the globe and a Gaussian-shape depression of the SSH,

$$\eta(\lambda, \phi, t = 0) = A_d \exp\left[-\frac{(\lambda_d - \lambda)^2 - (\phi_d - \phi)^2}{2\sigma_d^2}\right]. \tag{6.1}$$

The central point of the depression has longitude $\lambda_d = 60°$ and latitude $\phi_d = 0°$ in geographic coordinates. The maximum amplitude of the depression in the central point is $A_d = -100$ m and the standard deviation is equal to $\sigma_d = 5°$. Hence, the radius of a circle where the amplitude of the initial surface depression is equal to at least the half of maximum value is $\sigma_{1/2} = \sigma_d\sqrt{2\ln 2} \approx 6.9°$.

The deepest ocean bottom is H_{max} =3 790 m. In addition, there is a Gaussian-shape mountain which arises from the ocean bottom,

$$H(\lambda, \phi) = H_{max} - A_m \exp\left[-\frac{(\lambda_m - \lambda)^2 - (\phi_m - \phi)^2}{2\sigma_m^2}\right]. \tag{6.2}$$

The central point of the Gaussian mountain is at $\lambda_m = -60°$, $\phi_m = 0°$, maximum height of the mountain measured from the ocean bottom is $A_m = 6\ 000$ m and

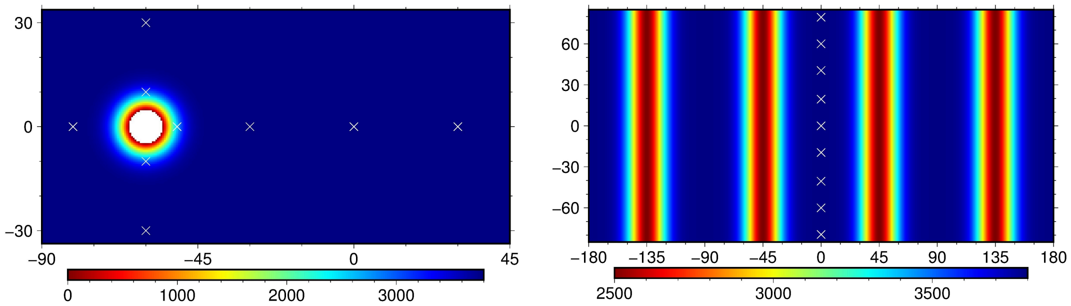

Figure 6.1: Bathymetry [m] and check-point positions (white crosses) in the TSU (left panel) and TIDa (right panel) numerical tests. In the left panel, we show only a part of the whole domain.

the mountain's standard deviation is $\sigma_m = \sigma_d = 5°$. The bathymetry is depicted in the left panel of Fig. 6.1.

We prescribe two continents at the poles for $\phi \geq \phi_{max}$ and $\phi \leq -\phi_{max}$, where ϕ_{max} is 84.75°, i.e., latitudes of bounding wet SSH points on the Arakawa grid C are 84.5° and -84.5°. On the Arakawa grid E, we choose the bounding wet SSH points to have latitudes 84.75° and -84.75°. We prefer the quasi global to the fully global setup since many OGCMs solve the problem of meridians converging at the North Pole by relocating coordinate poles to continents, and these OGCMs would be unable to run the fully global simulation.

There is no external forcing, the only "forcing" in this test being the nonzero initial conditions.

Tidal tests (TIDa, TIDb)

The initial conditions in TIDa and TIDb are homogeneous, i.e., velocities and SSH are zero at time $t = 0$ s. The meridional boundaries are the same as in the TSU test. The initial positions of the Moon and Sun are given by their positions on January 1, 2015, 00:00:00 UTC, i.e., the initial right ascension, declination and geocentric distance from the Earth are equal to $\alpha^{Moon} = 0.854807$ rad, $\delta^{Moon} = 0.263626$ rad and $l^{Moon} = 2.564 \times 10^{-3}$ AU for the Moon and $\alpha^{Sun} = 4.906612$ rad, $\delta^{Sun} = -0.402134$ rad and $l^{Sun} = 0.983311$ AU for the Sun, respectively. We apply space and time dependent tidal forcing to the initially resting ocean in the successive time steps. In order to verify this implementation, the time evolution of the tidal force at five points along the prime meridian is provided in Fig. 6.2.

The tidal tests differ in their bathymetry and land-mask:

- TIDa: The ocean bottom undulates with four Gaussian-shape ridges,

$$H(\lambda, \phi) = H_{max} - A_r \sum_{k=1}^{4} \exp\left[-\frac{(\lambda_r^k - \lambda)^2}{2\sigma_r^2}\right], \tag{6.3}$$

  where $\lambda_r^k = [45 + 90(k-1)]°$, the maximum height of the ridge is $A_r = 1\ 290$ m, and its standard deviation is $\sigma_r = 10°$. The maximum depth of the ocean bottom is $H_{max} = 3\ 790$ m. The bathymetry is depicted in the right panel of Fig. 6.1.

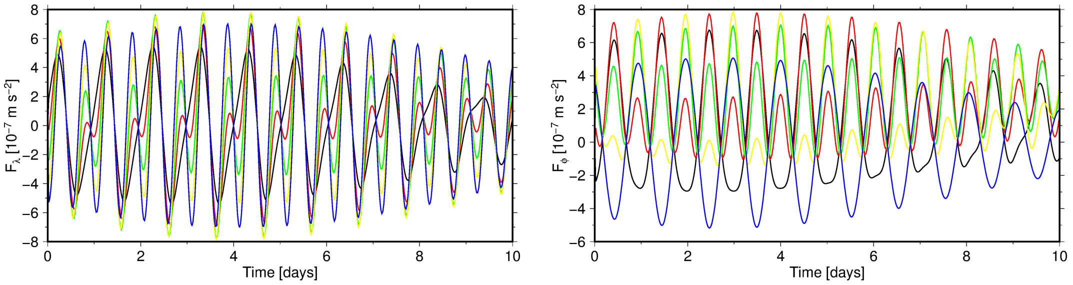

Figure 6.2: Time evolution of zonal (left panel) and meridional (right panel) components of tidal force at five points along the prime meridian with latitudes −79.5° (black), −60° (red), −40.5° (green), −19.5° (yellow) and 0° (blue).

- TIDb: The ocean bottom is flat with a uniform depth of 3 790 m and we prescribe a realistic land mask.

Ocean-model settings

The spatial resolution of Arakawa grids B and C is chosen to be 0.5° for all numerical tests. The choice was motivated by accuracy and computational demands. The 0.5° resolution is sufficient for testing, the results do not change much when finer resolutions (1/3°, 1/4°) are used (not shown). At the same time, 0.5° resolution is not extremely computationally demanding. The E-grid resolution is chosen to be $\Delta\lambda_E = \frac{3}{2}\Delta\lambda_C = 0.75°$. The total number of SSH points on Arakawa grids B/C and E are therefore $N_C = (360/\Delta\lambda_C)(180/\Delta\lambda_C)$ and $N_E = (360/\Delta\lambda_E)[180/(\Delta\lambda_E/2)] = (8/9)N_C$, respectively, since $\Delta\phi_C = \Delta\lambda_C$, $\Delta\phi_E = \Delta\lambda_E/2$. Both values are similar, which makes a comparison of results computed using different grids meaningful. Besides that, each grid has one SSH point at $(0°, 0°)$ and thus every 3rd B/C-grid SSH point in both zonal and meridional directions is common with an E-grid SSH point.

The time step is chosen to be slightly below the Courant-number criterion in order to keep simulations stable for explicit schemes. We use the time step $\Delta t = 15$ s in all tests.

The values of the Earth's radius, gravity acceleration and angular velocity of the Earth's rotation are given in Table 6.2.

Parameter	Value
Earth's radius	6.371×10^6 m
gravitational acceleration	9.80665 m/s^2
angular velocity of the Earth's rotation	7.292115×10^{-5} rad/s

Table 6.2: The Earth's parameters used in the numerical tests.

6.1.3 Assessment methods

We discuss and compare the different model outputs using the following diagnostics and methods.

Invariants

Consider the following integral quantities:

$$V_0 = \int\limits_A \eta dA, \tag{6.4}$$

$$E_k = \frac{1}{2}\int\limits_A h\mathbf{u}^2 dA, \qquad E_p = \frac{1}{2}\int\limits_A g\eta^2 dA, \qquad E = \frac{1}{2}\int\limits_A \left(h\mathbf{u}^2 + g\eta^2\right) dA \tag{6.5}$$

$$Q_n = \int\limits_A hq^n dA, \qquad n \in N, \tag{6.6}$$

where A is the surface of ocean, dA its element, n is a natural number, q is the potential vorticity,

$$q = \frac{f+\zeta}{h}. \tag{6.7}$$

and ζ is the relative vorticity given by Eq. (5.17). The meanings of V_0, E_k, E_p and E are the total volume of ocean water above the reference level $\eta = 0$, kinetic, potential and total energy, respectively. Together with Q_n, they are computed at each time step as diagnostics. The definition of Q_1 can be further simplified in all numerical tests because there is a symmetry in the meridional direction of the prescribed bathymetry and boundaries. Indeed, the Coriolis parameter is an odd function of latitude and an integral of an odd function over a symmetric interval is equal to zero. We thus redefine Q_1 as

$$Q_1 = \int\limits_A \zeta dA. \tag{6.8}$$

Moreover, we emphasize that the quantities V_0, E and Q_n are time-invariant, provided no external force is acting [McWilliams, 2006]. This is the case with the TSU numerical test. Additionally, $Q_1(t) = 0$ for $t > 0$ since $Q_1(0) = 0$ due to $u(0) = v(0) = 0$ in TSU. Note that the time invariance of E and Q_n only holds for a model with the full momentum equation containing the advection and nonlinear terms depending on both SSH and velocities.

If the external force $\mathbf{F}$ is applied, E and Q_n are not time-invariant since $\mathbf{F}$ produces source terms violating the balances. As a consequence, we introduce the new time invariants E^g and Q^g_n,

$$E^g := E - \int\limits_0^t \int\limits_A h\mathbf{F}\cdot\mathbf{u} dA dt = E - E^s, \tag{6.9}$$

$$Q^g_n := Q_n - \int\limits_0^t \int\limits_A nq^{n-1}(\nabla\times\mathbf{F})_r dA dt = Q_n - Q^s_n, \tag{6.10}$$

which are generalized forms of E and Q_n (see Appendices C.1 and C.2 for the derivation). The terms arising due to the external force in Eqs. (6.9) and (6.10) will be denoted by E^s and Q^s_n, respectively, to shorten the notations. In the tidal numerical tests TIDa and TIDb, $V_0(t) = E^g(t) = Q^g_1(t) = 0$ for $t > 0$ since $V_0(0) = E(0) = Q_1(0) = 0$, due to zero initial velocities and SSH. The discrete forms of the invariants are given in Appendix C.3.

Time curves

The main purpose of this method is to effectively check the model's behaviour over time. We choose nine check points on a sphere and compute the time evolution of the SSH at these points.

In the TSU test, we place check points in the vicinity of the island and along the direction from the initial position of the Gaussian depression towards the island. The coordinates (λ, ϕ) of the check points are $(-51°, 0°)$, $(-30°, 0°)$, $(0°, 0°)$, $(30°, 0°)$, $(-60°, 30°)$, $(-60°, 10°)$, $(-60°, -10°)$, $(-60°, -30°)$ and $(-81°, 0°)$ (see the white crosses in the left panel of Fig. 6.1).

In the TIDa test, the check points are located in the bottom of the valley along the prime meridian with latitudes $-79.5°$, $-60°$, $-40.5°$, $-19.5°$, $0°$, $19.5°$, $40.5°$, $60°$ and $79.5°$ (see the white crosses in the right panel of Fig. 6.1). The angular distance of approximately $20°$ between two neighbouring check points is sufficiently small with respect to a large scale pattern of the resulting SSH (see Fig. 6.8 (a)).

Note that check-point positions are deliberately selected to be common on all the computational grids used. No interpolation is thus needed as it was mentioned in Sec. 6.1.2. However, for other models with, e.g., triangular, hexahedral or cubed sphere grids, interpolation will still be needed.

The method of time curves is not used in the TIDb test (see Sec. 6.1.6 for further details).

Spatial patterns

The method of spatial patterns is complementary to the method of time curves. We choose a particular time instant and examine the global spatial distribution of the SSH. The SSH computed using the model configuration C–FB, see Table 6.1, is taken as a reference. The reference SSH is thus discretized on the Arakawa grid C. The SSH computed on the Arakawa grids B or C and the reference SSH are easy to compare value by value. This is not possible if the SSH is computed on the Arakawa grid E. We thus interpolate the C-grid values to the Arakawa grid E using a bilinear interpolation. Its accuracy was tested by comparing the original and interpolated initial SSH and also by a comparison with the inverse-distance-weighting interpolation (see Appendix E for further discussion).

Spherical harmonic expansion coefficients

A real function f which is square-integrable in space on a unit sphere can be written as a series of surface spherical harmonics $Y_l^m(\lambda, \phi)$ of degree l and order m [Varshalovich et al., 1988],

$$f(\lambda, \phi, t) = \sum_{l=0}^{\infty} \sum_{m=-l}^{l} f_l^m(t) Y_l^m(\lambda, \phi), \tag{6.11}$$

where the complex time-dependent expansion coefficients f_l^m are given by the surface integral,

$$f_l^m(t) = \int_{-\pi}^{\pi} \left(\int_{-\pi/2}^{\pi/2} f(\lambda, \phi, t) P_l^m(\sin\phi) e^{-im\lambda} \cos\phi \, d\phi \right) d\lambda. \tag{6.12}$$

where P_l^m is the associated Legendre function. The SSH is a real bounded function on a sphere, hence it is square integrable and Eq. (6.12) can be used to compute the expansion coefficients of the SSH. Additionally, the coefficients with $m < 0$ are fully determined by coefficients with $m \geq 0$, $\eta_l^{-m} = (-1)^m (\eta_l^m)^*$ since SSH is a real function.

The comparison of expansion coefficients is an advantageous assessment method if the space-time distribution of SSH is predominantly represented by a few expansion coefficients. This is the case of TIDa. On the contrary, the method is not suitable for TSU because most of the coefficients are of similar magnitudes.

6.1.4 Results of tsunami numerical test TSU

As already indicated in Sec. 4.5, the additional smoothing term is added into the SSH equation in the B–FB and E–FB model configurations in the TSU test. The equatorial diffusivity is equal to 2×10^6 m^{2}s$^{-1/2}$ and 4.5×10^6 m^{2}s$^{-1/2}$ in the B–FB and E–FB model configurations, respectively. These values have been chosen by trial and error to obtain a SSH that is acceptably smooth. In fact, the solution is not completely free of the grid-scale noise, as small patchy areas still exist, especially in the vicinity of the island (not shown). It is possible to enlarge the diffusivity and make the solution smoother, but larger smoothing has certain negative effects on the solution, as we will see later on.

Invariants

All solutions conserve total volume very well, and there are no significant oscillations or trends in any of the solutions. If the y-scale is chosen to be 1% of the initial value, the individual volume curves are straight lines in time and they overlay each other (not shown). It is a desired behaviour which is enforced by the flux form of Eqs. 4.2 or 4.4 for the SSH used by all model configurations. Note that the biharmonic smoothing operators 4.51 and 4.52 do not violate the total-volume balance since they are also written in the flux form. In principle, we might expect some discrepancies in the CNmod scheme because a system of linear equations is solved for the SSH. But if some discrepancies are present in the solution, they are negligibly small.

Fig. 6.3 (left panel) depicts the time evolution of Q_1 for all model configurations, except for the C–CNmod. The time evolution of Q_1 is a highly oscillating function in time, but in fact it is only white noise on the level of the rounding errors. Indeed, invariant Q_1 defined by Eq. (6.8) does not contain the contribution from the Coriolis parameter due to the symmetry presented in the discussion above. However, if we focused on a particular area on one hemisphere, e.g., the North Atlantic, the Coriolis parameter would give a constant offset in time. This means that we are missing the reference value.

We have decided to take the surface integral of the absolute value of the Coriolis parameter over the whole ocean surface as a reference value. Its value, $a^2 \int_{-\pi}^{\pi} \left(\int_{-\phi_{max}}^{\phi_{max}} |f| \cos \phi d\phi \right) d\lambda = \pi a^2 \Omega [1 - \cos(2\phi_{max})] \approx 1.85 \times 10^{10}$m^2/s, exceeds the amplitudes of oscillations in Fig. 6.3 (left panel) by several orders of magnitude. The Q_1 in the C–CN is also highly oscillating over time, but the amplitudes of the oscillations are approximately two orders of magnitude larger than in the other schemes, and so we do not plot it in Fig. 6.3 (left panel). Nonetheless, even these discrepancies are small with respect to our reference value.

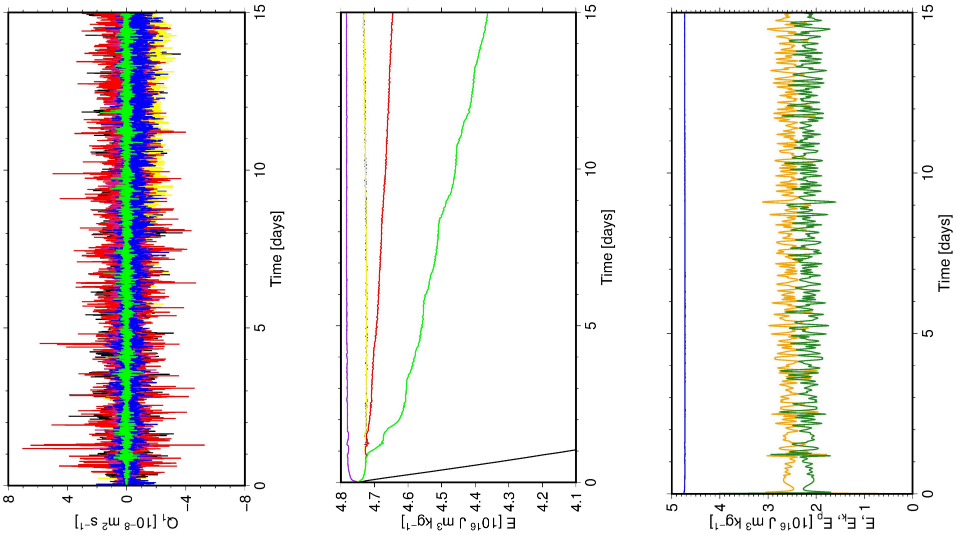

Figure 6.3: Invariants in the TSU numerical test. Left panel: Time evolution of Q_1 using model configurations C–FB (blue), C–FBgen (yellow), B–FB (red), E–FB (green) and E–IMP (black). Middle panel: Time evolution of total energy E using the same model configurations plus C–CN (purple). Right panel: Total energy (blue), kinetic energy (orange) and potential energy (forest green) in C–FB.

Fig. 6.3 (middle panel) depicts the time evolution of the total energy. The energy decays rapidly in the C–IMP solution (black). The total energy after 15 days of the numerical test is equal to 1.42×10^{16} J m^3 kg^{-1}, which means that more than 70% of the energy were dissipated, which is unacceptable. Mesinger and Arakawa [1976] showed that the Euler backward scheme slightly damps long-period waves, but it highly damps short-period oscillations associated with small spatial scales. Our tsunami propagation is a rather fast process, thus the energy leakage can be associated with this damping. Note that the dedicated tsunami codes use either explicit (NAMI DANCE, GeoClaw, Tsunami-HySEA, TSUNAMI3D, etc.) or semi-implicit (SCHISM, NEOWAVE, pCOULWAVE, etc.) time-stepping schemes [Lynett et al., 2017].

The total energy in the B–FB and E–FB model configurations does not decay as rapidly as in the E–IMP model configuration, but energy leakage is also present. However, it has a different origin since the FB scheme itself does not cause the energy leakage, it is caused by the biharmonic smoothing term. The total energy is equal to approximately 4.65×10^{16} J m^3 kg^{-1} in the B–FB, and 4.36×10^{16} J m^3 kg^{-1} in E–FB solutions after 15 days of the numerical test. The energy leakage is thus approximately 2.1% and 8.2% in the B–FB and E–FB solutions, respectively, which might be considerable with regards to the particular application. The length of computation may also be decisive, since the energy diffusion will most likely continue.

The total energy in the C–FB, C–FBgen and C–CNmod solutions is equal to approximately 4.732×10^{16} J m^3 kg^{-1}, 4.732×10^{16} J m^3 kg^{-1} and $4.784 \times$

10^{16} J m^3 kg^{-1}, respectively. The energy conservation is violated by approximately 0.43%, 0.44% and 0.66%. Contrary to other schemes, there is an excessive generation rather than leakage of energy in the C–CNmod solution. In our opinion, all C-grid values are safely acceptable. Besides that, the energy conservation is mainly violated at the beginning of the numerical test, when a huge 100 m depression starts to oscillate. We tested that the energy conservation would improve if we decreased the initial amplitude of the SSH depression. Finally, the individual constituents of total energy, the kinetic energy E_k, and potential energy E_p, in the C–FB solution are shown in Fig. 6.3 (right panel). They oscillate in time in such a way that one energy is almost mirrored in the other one.

Spatial patterns

Fig. 6.4 depicts SSHs computed with the C–FB model configuration after 12, 24, 36 and 48 hours. We deliberately restrict ourselves to the first two days of computations since the SSH evolution can be illustrated better. The initial SSH anomaly is forced by the surface pressure gradient at the beginning of the the numerical test. The amplitude of the Gaussian depression decreases in order to reach the equilibrium. However, there is no damping mechanism and thus the SSH overshoots the equilibrium point instead and it changes the sign from negative to positive. The process is similar to the harmonic oscillator. At the same time, the depression is expanding and it propagates in the form of a gravity wave (see panel (a)). Note that the expansion is direction-dependent and the SSH is not symmetric in the zonal direction (with respect to the $\lambda = 60°$ meridian). This is due to the presence of the Coriolis force. If we performed the same numerical test on a non-rotating Earth, the wave propagation would be the same in all directions and the SSH pattern would be perfectly symmetric. The waves propagate further and at approximately time $t = 12.5$ h some of them reach the meridional boundaries of the computational domain and they are reflected there. Approximately at $t = 18$ h, the direct wave hits the island and it is also partly reflected (see panel (b)). The dark blue SSH feature at $\lambda = -150°$ is the direct wave which propagated in the eastern direction from the initial position. The direct waves from both directions collide and interfere with the reflected waves. The second expansion, similar to the one in panel (a), starts afterwards (see panel (c)). The SSH feature has a more complex shape now due to all the processes that have occurred since the beginning of the numerical test. Finally, the waves are propagating back to the eastern hemisphere to collide approximately at $(60°, 0°)$ where the center of the SSH depression was initially located (see panel (d)).

Fig. 6.5 depicts SSH differences between C–FB and other solutions. All model configurations considered in the numerical tests are able to capture the main characteristics and features of the tsunami propagation as it has been described. The C–FB and C–FBgen solutions are almost identical, the differences being barely visible. The differences in the C–CN solution are somewhat larger. We noticed a small shift and distortion of the C–CN time curves at particular check points. The B–FB, E–FB and E–IMP solutions are, however, more different than any of the solutions discussed so far. Some differences in the E–FB and E–IMP solutions are caused by the different shape of the island and meridional boundaries on the Arakawa grid E, although this is not the only reason since

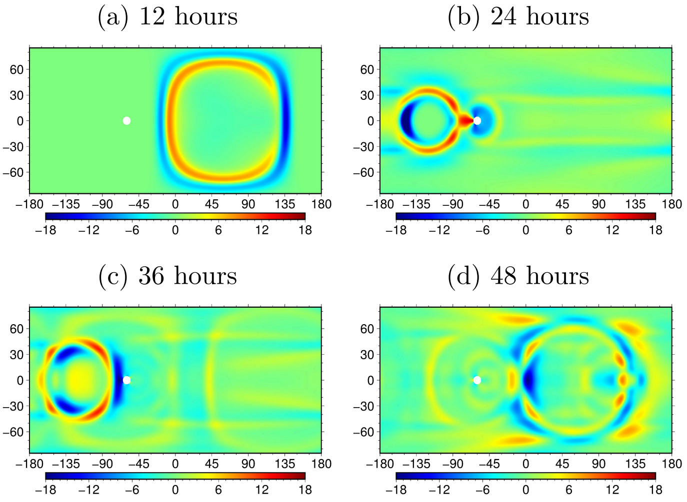
(a) 12 hours
(b) 24 hours
(c) 36 hours
(d) 48 hours

Figure 6.4: SSHs [m] computed in the TSU numerical test using the C–FB model configuration after 12, 24, 36 and 48 hours of experiment.

the same pattern is also visible in the B–FB solution and island and meridional boundaries are the same on both Arakawa grids B and C. We argue that the B–FB, E–FB and E–IMP solutions differ from the C–FB and C–FBgen solutions because the Arakawa grids B and E use no-slip boundary conditions (see Eq. (4.7)) whereas the Arakawa grid C uses free-slip boundary conditions (Eq. (4.6)). It also explains the discrepancies in the vicinity of meridional boundaries.

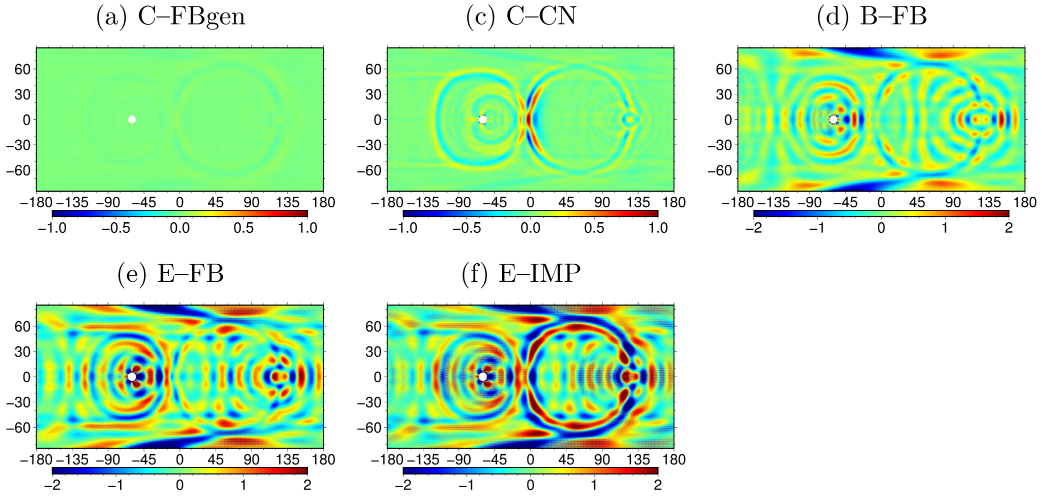
(a) C–FBgen
(c) C–CN
(d) B–FB
(e) E–FB
(f) E–IMP

Figure 6.5: Differences [m] between the SSH computed using the C–FB model configuration and the other model configurations after 48 hours of experiment.

We point out that the initial configuration and bathymetry are symmetric in the meridional direction with respect to the equator. Consequently, the computed SSH must conserve this symmetry. We recommend that this feature be examined further.

Time curves

The amplitudes of time curves are zero after the onset of the SSH displacement for certain times and then they change rapidly. The rapid changes occur at different times with amplitudes decaying from $(30°, 0°)$ to $(0°, 0°)$ and $(-30°, 0°)$ (not shown), i.e., from east to west. This behaviour corresponds to the direct wave coming from the initial position at $(60°, 0°)$. Fig. 6.6 shows results from the two equatorial check-points at (30°, 0°) and (−51°, 0°) and the check point at (30°, −60°). The second check point is close to the island, where we expect larger differences between the computed curves. We also depict only the C–FB, B–FB, E–FB and E–IMP solutions, since the other curves would either overlap the reference curve or would be close to it. Fig. 6.6 confirms certain findings from the previous sections. The shape of E–FB (green) and E–IMP (black) curves are very similar, and the amplitudes of E–IMP curves are smaller due to the energy leakage discussed in Sec. 6.1.4. Depending on the check point and time, the B–FB solution is closer to the E–FB and E–IMP solutions or to the C–FB solution.

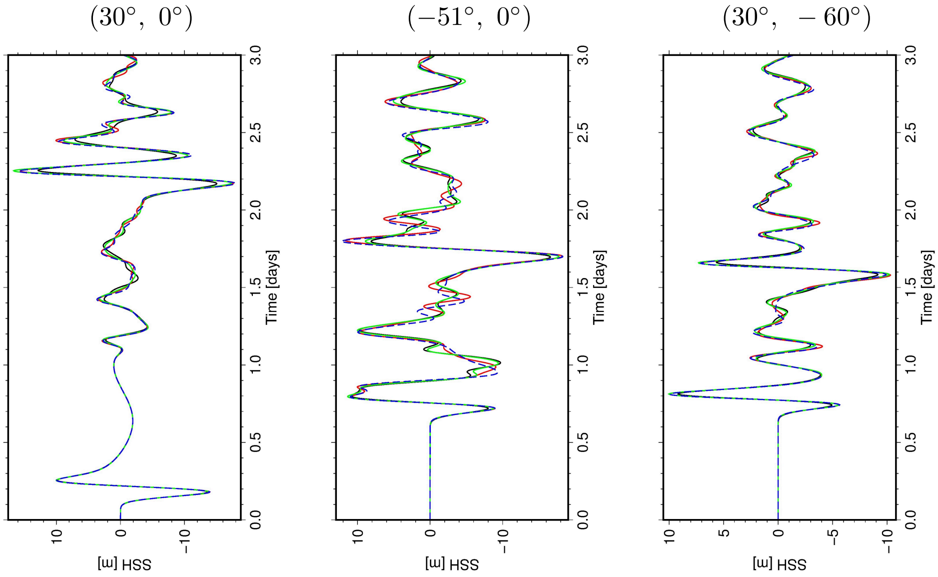

Figure 6.6: Time evolution of SSH at the chosen check points, see (λ, ϕ) above each panel, in the TSU numerical test computed using model configurations C–FB (dashed blue), B–FB (red), E–FB (green) and E–IMP (black).

6.1.5 Results of tidal numerical test TIDa

We compare only the C–FB, B–FB, E–FB and E–IMP solutions in this section because the C–FBgen and C–CNmod solutions are virtually identical to the C–FB solution. The biharmonic smoothing is not applied in the B–FB and E–FB model configurations in TIDa since there is no disturbing noise in the computed SSH.

Invariants

The time evolution of the total volume is shown in Fig. 6.7 (left panel). If we consider that the ocean surface A in TIDa is equal to $A = 4\pi a^2 \sin\phi_{max} \approx$

5×10^{14} m^2, the change of total volume of the order of 10^{-1} m^3 corresponds to the global SSH change of the order of 10^{-15} m, which is negligible.

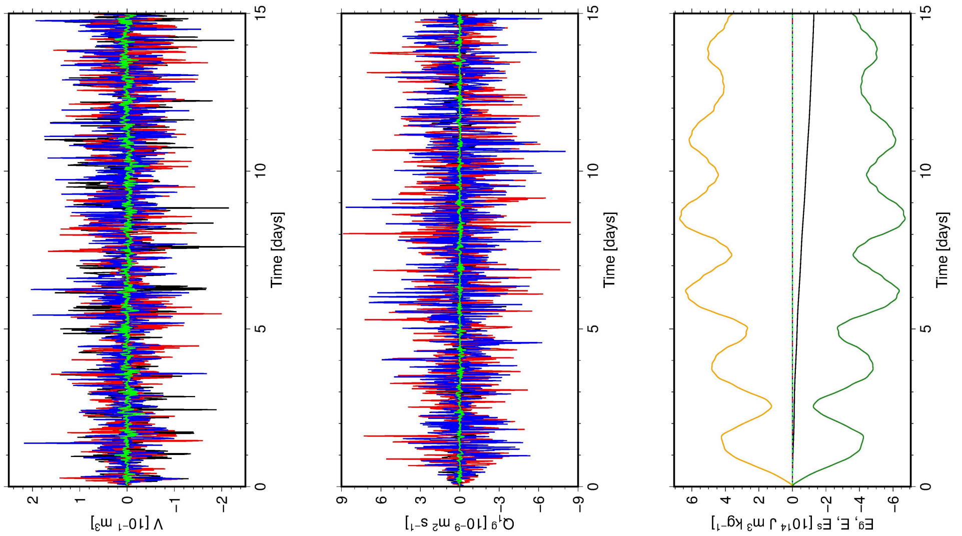

Figure 6.7: Time evolution of total volume (left panel), Q_1^g (middle panel) and E^g (right panel) in the TIDa numerical test computed using model configurations C–FB (blue), B–FB (red), E–FB (green) and E–IMP (black). In the right panel, E (orange) and $-E^s$ (forest green) computed using the C–FB model configuration are also depicted.

Fig. 6.7 (middle panel) depicts the time evolution of Q_1^g. All the curves look qualitatively similar to the Q_1 curves from the TSU, in that they are highly oscillating over time. The amplitudes of the Q_1^g oscillations are about one order of magnitude smaller than the amplitudes of the Q_1 oscillations in the TSU numerical test. The reference value is the same as in the TSU test and thus there is no problem with the conservation of Q_1^g. Note that the contribution of the external force to the overall balance is small (not shown).

Fig. 6.7 (right panel) depicts the time evolution of E^g for the considered model configurations and time evolution of E and $-E^s$ in the C–FB solution. The model configurations C–FB, B–FB and E–FB conserve E^g very well, the results overlap each other and the curves are basically straight lines. Recall, however, that we do not apply the biharmonic smoothing in the B–FB and E–FB configurations in the TIDa test contrary to the TSU test. There is a decrease of E^g in the E–IMP solution. Its origin is the same as the energy leakage in the TSU test, where inherent damping is draining energy from certain waves. The leakage of E^g after 15 days of the numerical test is approximately 1.2×10^{14} J m^3 kg^{-1}, which corresponds to around 18% of the maximum value of E. We regard such an energy leakage as considerable for the dynamics of the system, even though it is less severe than in the TSU test.

Note that $E^g = 0$ means that all the work done by the tidal force has been converted to the total energy. If we did not stop the numerical test after 15 days, the total energy would further grow since the tidal force is pumping energy into the system and there is no dissipation.

Spatial patterns

We examine spatial patterns at 1-day intervals after a 10-day spin up which is a period after which the flow is “reasonably developed”. The SSH pattern is usually dominated by 12 tidal bulges that are arranged in a checker-board pattern (see Fig. 6.8 (a) which shows results after 13 days of the numerical test). Nevertheless, other configurations may also occur. For example, after 14 days of the numerical test, the amplitudes of four low-latitude tidal bulges decrease substantially and the SSH pattern is dominated by eight mid-latitude tidal bulges (not shown). Note that if the bathymetry were flat, the SSH pattern would be dominated by only four large-scale bulges predominantly located in the latitudinal interval $\langle -40°, 40° \rangle$ (not shown).

(a) SSH, C–FB

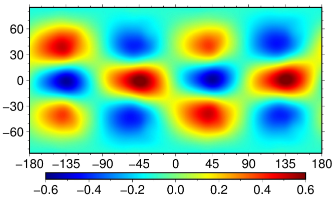

(b) SSH differences, B–FB (c) SSH differences, E–FB (d) SSH differences, E–IMP

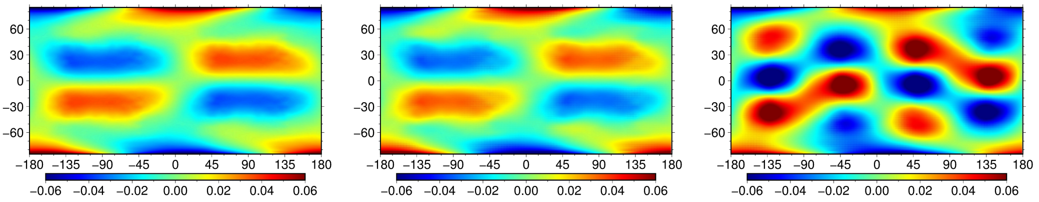

Figure 6.8: Panel (a) shows SSH [m] computed in the TIDa numerical test using the C–FB model configuration at day 13. The other panels show differences [m] between the SSH at panel (a) and the SSH computed using model configurations B–FB (b), E–FB (c) and E–IMP (d).

Qualitatively, all solutions are the same with tidal SSH bulges located roughly at the same positions. However, SSH patterns in the B–FB, E–FB and E–IMP solutions are slightly shifted and distorted with respect to the reference C–FB solution (not shown). The differences between the C–FB solution and the B–FB, E–FB and E–IMP solutions are depicted in panels (b), (c) and (d) of Fig. 6.8, respectively. The B–FB and E–FB solutions are very similar, their SSH-difference patterns are virtually identical, with slightly different amplitudes. The E–IMP solution differ from the B–FB and E–FB solutions, however, all three solutions display similar discrepancies near the meridional boundaries. The magnitude of the discrepancies depend on the model configuration and position in space and time, but they may reach 10% of maximum SSH amplitudes. The spatial discretization of the governing equations and boundary conditions applied thus have a non-negligible effect on both tsunami propagation and tidally-driven circulation.

Time curves

Time curves at points $(0°, 0°)$, $(0°, -20°)$, $(0°, -60°)$ and $(0°, -80°)$ are depicted in Fig. 6.9. We do not show time curves at other check points since they display similar information. Most importantly, time curves give us confidence that our findings in the previous section are not limited to chosen time instants. Indeed, all time curves are the same at $(0°, 0°)$, with the exception of the E–IMP curve, which mostly underestimates SSH amplitudes. Time curves at $(0°, -20°)$ and $(0°, -60°)$ already show certain differences. The B–FB and E–FB curves are much the same, but they overshoot the C–FB amplitudes. The shape of the E–IMP curve is similar to the B–FB and E–FB curves, but the E–IMP amplitudes are lower. This sometimes makes the E–IMP curve be closer to the C–FB curve than to the B–FB and E–FB curves. It may also clarify the specific pattern of the SSH differences mentioned previously. The southernmost check point at $(0°, -80°)$ reveals the most striking differences between the computed time curves. There are phase shifts, amplitude overshoots and also distortions of the curves due to the vicinity of boundary.

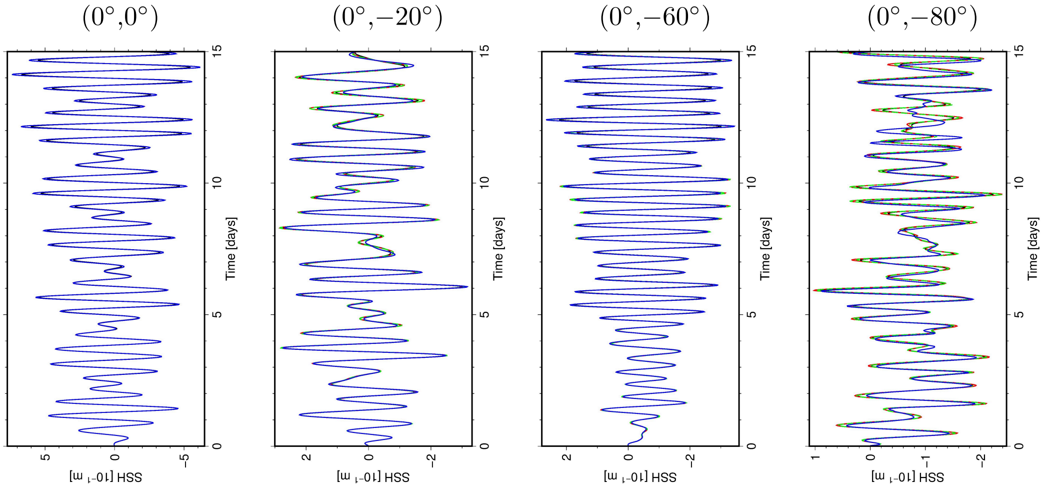

Figure 6.9: Time evolution of SSH at the chosen check points, see (λ, ϕ) above each panel, in the TIDa numerical test computed using model configurations C–FB (blue), B–FB (red), E–FB (green) and E–IMP (black)

Spherical harmonic expansion coefficients

We compute spherical harmonic expansion coefficients from degree 0 up to degree 10. We examine only the real parts of the coefficients with $m \geq 0$. There are 66 coefficients, although, only a few are dominant. We measure the maximum amplitudes of the real parts of coefficients over 15 days of the numerical test. The coefficients with the largest maximum amplitudes are η_4^2 and η_2^2. The coefficients with maximum amplitudes of at least 10% of this value are summarized in Table 6.3. Note that there are only even-degree coefficients due to the second-degree tidal potential forcing. The ocean's dynamics is responsible for the energy transport from the second-degree forcing to other than degree-two response coefficients. If the bathymetry was flat, there would be only coefficients with orders

0, 1 and 2, which accounts for long-period, diurnal and semi-diurnal tides. This is not true in the presence of undulated bathymetry. For example, the η_6^6 coefficient is one of the major coefficients.

l	2	2	**2**	4	4	**4**	6	6
m	0	1	**2**	0	1	**2**	2	6
$max(\lvert\eta_l^m\rvert)[10^{-1}m/s]$	2.2	1.5	3.8	0.9	0.9	6.5	1.7	0.8
$100\,\frac{max(\lvert\eta_l^m\rvert)}{max(\lvert\eta_4^2\rvert)}$ [%]	34	23	58	14	14	100	26	12

Table 6.3: Degrees l and orders m of spherical harmonic expansion coefficients η_l^m with maximum amplitudes $max(|\eta_l^m|) \geq 0.1max(|\eta_4^2|)$ in the TIDa numerical test.

Fig. 6.10 depicts the time evolution of the two largest coefficients, η_2^2, η_4^2, and coefficients η_2^1 and η_4^1. The E–IMP coefficients are smaller than the reference C–FB coefficients. The B–FB and E–FB coefficients are almost identical to the C–FB coefficients with the exception of the η_2^1 and η_4^1 coefficients, which show certain discrepancies. The integral property of spherical harmonic coefficients guarantee that global scale characteristics of the solutions are preserved. The results may, however, differ locally as we have seen in Secs. 6.1.5 and 6.1.5.

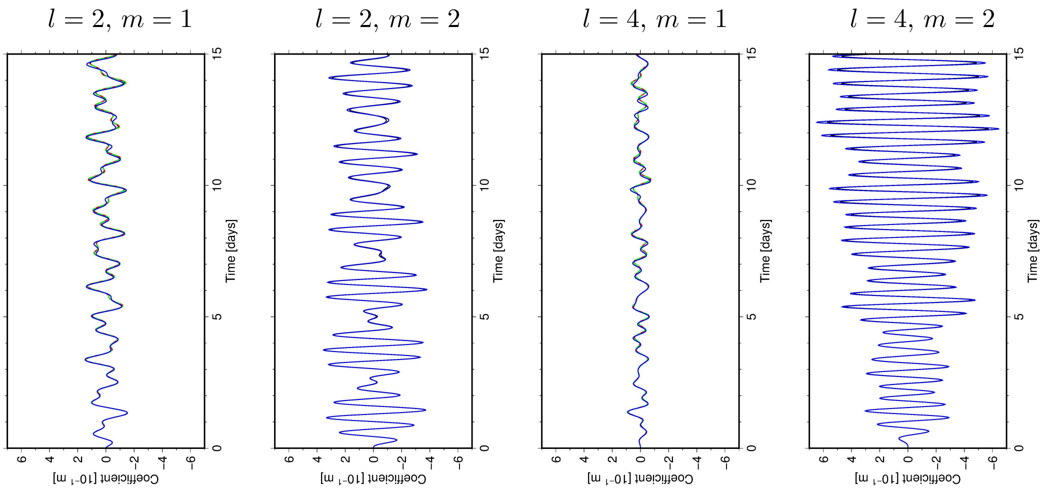

Figure 6.10: Time evolution of SSH spherical harmonic expansion coefficients η_2^1, η_2^2, η_4^1 and η_4^2 in the TIDa numerical test computed using model configurations C–FB (blue), B–FB (red), E–FB (green) and E–IMP (black)

6.1.6 Results of tidal numerical test TIDb

The performance of model configuration E–IMP was not satisfactory in the TSU and TIDa tests. We thus do not include E–IMP in the last experiment.

Spatial patterns

In contrast to previous sections, we start with a comparison of the resulting spatial patterns. Fig. 6.11 shows the spatial patterns of individual solutions after

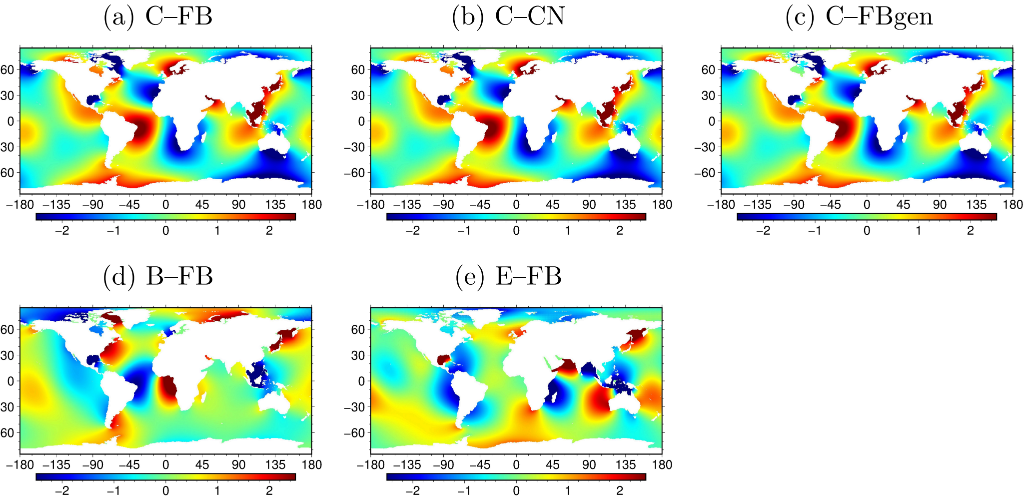
(a) C–FB

(b) C–CN

(c) C–FBgen

(d) B–FB

(e) E–FB

Figure 6.11: SSH [m] after 15 days of computations in the TIDb numerical test computed using different model configurations.

15 days of the numerical test. The C–FB and C–CN solutions are in excellent agreement, while the C–FBgen solution is slightly different. Detailed inspection reveals some differences with respect to the reference C–FB solution, which are most pronounced in the Hudson Bay. However, generally speaking, all examined C-grid solutions are in good agreement. This is, however, hardly true if we compare any of C-grid solutions to the B–FB or E–FB solutions. There are many places where the SSH has opposite signs and the solutions differ significantly even after two days of computations (not shown), which is shortly after the model's start. In order to reduce the effect of the boundary conditions, we added realistic bathymetry and repeated the computations. The agreement between the C–FB, B–FB and E–FB solutions improved, with the match acceptable after five days of computations (not shown). Nevertheless, the solutions differ significantly again after 15 days of integration. We checked that the discrepancies are not caused by the short spin-up period. The differences persist if we perform the comparison after 30 days of the numerical test.

Our explanation is that boundary effects influence the solution considerably more than in previous numerical tests due to the realistic ocean-land mask, where the extent of the coastlines and complexity of their shape has significantly increased. The previous numerical tests have shown that solutions on Arakawa grids C and B/E differ in the vicinity of solid boundaries as a consequence of different boundary conditions. Additionally, the shape of the land areas and ocean-land boundaries differ on Arakawa grid E as a consequence of the different shapes of the E-grid and B/C-grid elementary grid cells.

This might have an important impact, since barotropic tidal models are usually discretized on the Arakawa grid C with free-slip boundary conditions, while OGCMs have frequently used Arakawa grid B in the past, especially the Bryan-Cox-Semtner type models. The successors in this lineage, such as the POP, MOM (up to version 5), COCO, INMIO or CLIO (ocean component of the LOVECLIM Earth system model) models are still using the B-grid spatial discretization. Nonetheless, friction terms that we neglected in our numerical tests may also come into play. The momentum equation should include Reynold's stresses

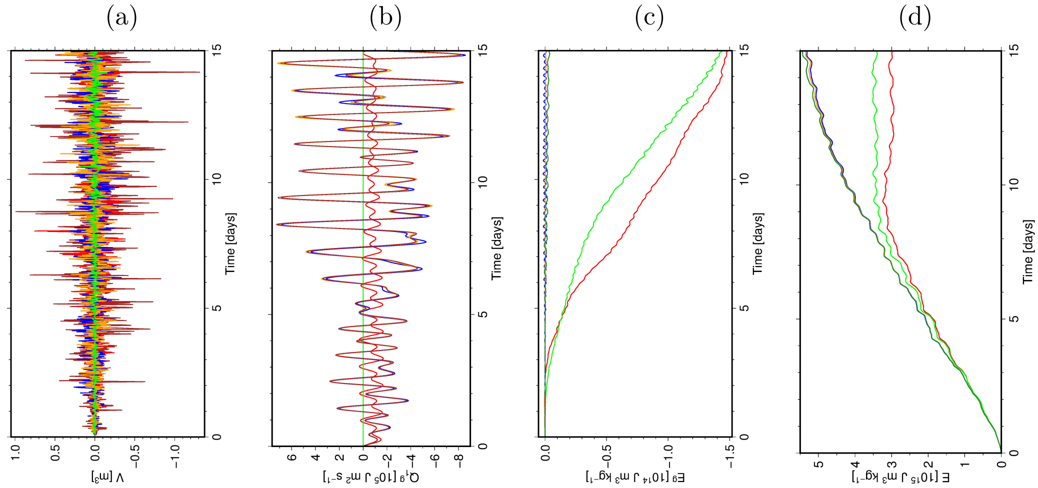

Figure 6.12: Time evolution of total volume (a), Q_1^g (b), E^g (c) and total mechanical energy (d) in the TIDb numerical test computed using model configurations C–FB (blue), C–FBgen (orange), B–FB (red) and E–FB (green).

via the divergence of a stress tensor and the bottom friction. Models that aim to accurately resolve tides need to include also the IWD term. The three missing friction terms will most likely restrict the flow especially in shallow areas, i.e., in the vicinity of boundaries, and the spread in the solutions will be reduced. Nevertheless, it is beyond the scope of this paper to compare the performance of fully tuned tidal models discretized on different Arakawa grids in realistic settings.

Invariants

We will show neither time-curves nor time evolution of the spherical harmonic expansion coefficients from the TIDb test due to massive differences between the model configurations on different grids. However, we have checked the invariants to verify that the solutions are self-consistent. Note that the C–CN solution is not shown since it is very similar to the C–FB solution as we have already seen.

The total volume is conserved well in all solutions (see Fig. 6.12 (a)). The oscillatory behaviour of the solutions is the same as in the TIDa test. The maximum amplitudes of discrepancies are approximately one order larger than in the TIDa results, which is still negligible as discussed previously.

The time evolution of Q_1^g is different from that in the TIDa. It is not a highly oscillating but rather a smooth function (see Fig. 6.12 (b)). Its time evolution is also markedly different in the B-grid, C-grid and E-grid solutions. In any case, the maximum computed amplitudes of Q_1^g do not exceed 10^6 m^2 s^{-1}, which is at least four orders of magnitude smaller than the reference value used previously. We thus consider Q_1^g to be a well-conserved quantity in all solutions.

The evolution of E^g is shown in Fig. 6.12 (c). The energy conservation is satisfied in the C-grid solutions C–FB and C–FBgen. A detailed inspection reveals that there are small ripples in the C–FB solution, nonetheless, we consider them as being negligible due to their magnitude. Both the B–FB and E–FB solutions suffer from an energy leakage as a consequence of the applied biharmonic smoothing. Time evolutions of E^g are not the same, but quite similar in both solutions. The energy leakages after 15 days of the numerical test are also very similar, 1.48×10^{14} J m^3 kg^{-1} and 1.45×10^{14} J m^3 kg^{-1} for B–FB and E–FB, respectively, which corresponds to approximately 4.6% and 4.1% of the respective energy values of 3.24×10^{15} J m^3 kg^{-1} and 3.54×10^{15} J m^3 kg^{-1}. The energy leakage is thus non-negligible, although not critical, similar to the TSU numerical test. Fig. 6.12 (d) depicts the evolution of total energy. The C-grid solutions are very much the same, where the energies in the C–FB and C–FBgen solutions differ by less than 1% after 15 days of computations. However, there is a clear separation between C-grid and B/E-grid solutions. It is distinct after 10 days, but it is noticeable as early as after four days of computations.

6.1.7 Concluding remarks

The total volume of ocean water and potential-vorticity invariant are well conserved in all tested schemes and numerical tests. The energy conservation is violated in several model configurations. The implicit time-stepping scheme used in one model configuration suffers from the energy leakage. The leakage reaches 70% and 18% of energy in the TSU and TIDa numerical tests, respectively. We recommend not to use the implicit time-stepping scheme for tidally driven models, although the energy conservation is violated much less in the tidal numerical test than in the tsunami numerical test. The B-grid and E-grid model configurations do not conserve energy either if biharmonic smoothing of SSH is applied. The energy leakage reaches 2.1% and 8.2% in TSU and 4.6% and 4.1% in TIDb in B-grid and E-grid model configurations, respectively. It is probably an acceptable energy leakage for a global tidal model since its realistic configuration contains internal wave drag and bottom drag terms which are tuned to obtain realistic results. All C-grid schemes conserve energy successfully. Regarding the spherical harmonic expansion coefficients, the largest coefficients in the TIDa solutions have degree l and order m equal to $l = 2$, $m = 2$ and $l = 4$, $m = 2$. The other significant coefficients have even degrees, which is a plausible result for a tidally driven numerical test.

There are differences between C-grid and B/E-grid solutions in all numerical tests. Comparisons of spatial patterns and time curves show that discrepancies are more pronounced in the vicinity of domain boundaries as a consequence of different boundary conditions (free-slip and no-slip) and shapes of rigid boundaries on different Arakawa grids. The most distinct discrepancies are present in the TIDb numerical test in which boundary effects have a much stronger impact on the solution due to the significantly larger extent of land areas. Both free-slip and no-slip boundary conditions are approximations of the real-world boundary conditions, which are a combination of these two options. The choice of boundary conditions could be important, but it is beyond the scope of this paper to test which one is closer to reality.

6.2 Numerical tests of Yin-Yang and reduced spherical coordinate grids

We test the YY and RSC grids in modified versions of the tests that we introduced in Sec. 6.1.2. We call these tests TSU0, TID0 and mTIDa. All three tests are fully global, there are no artificial continents at poles as in TSU, TIDa and TIDb. The absence of artificial continents is the only difference between mTIDa and TIDa. TSU0 and TID0 are simplified versions of TSU and TIDa (mTIDa). The bathymetry if flat at the depth of 3790 m in both TSU0 and TID0. Additionally, the initial amplitude of the Gaussian depression is reduced from -100 m to -1 m and the Earth's rotation is set equal to zero, $\Omega = 0$, in TSU0.

In the YY simulations, we use 0,5° resolution in TSU0 and 1° resolution in TID0 and mTIDa. The grid in all RSC simulations has 512 grid points along the Equator which corresponds to approximately 0.7° resolution.

Results of the TSU0 test

It was noted in Sec. 6.1.4 that the propagation of the initial depression is not symmetric in all directions in the TSU test due to the presence of the Coriolis force. The Coriolis term is absent in the TSU0 test and thus the propagation should be perfectly symmetric. Indeed, the SSH is symmetric in both YY and RSC simulations, see panels (a) and (b) of Fig. 6.13. The gravity waves propagate over the globe meet at the antipodal point and return back to the initial point, see panels (c) and (d) of Fig. 6.13, and the entire process repeats. The SSH is symmetric even after 105 hours of experiment, see panels (e) and (f) of Fig. 6.13.

Note that we apply a linear interpolation in the zonal direction in the post processing phase of the RSC simulation. We interpolate values to the grid points that are missing in the RSC grid but are present in the SC grid to make the visual inspection more convenient.

Fig. 6.14 shows the same propagation viewed from the North Pole. It demonstrates that the gravity-waves smoothly pass the North Pole in both YY and RSC simulations. Both simulations are in a very good agreement.

Results of the TID0 test

Fig. 6.15 depicts SSHs computed in the YY and RSC simulations in the TID0 test after 20 days. The agreement is very good, again. We use the time step $\Delta t = 30$ s in the YY simulation. In comparison, the time step used in the RSC simulation is four times larger, $\Delta t = 120$, and the simulation is still numerically stable.

Results of the mTIDa test

The mTIDa test is significantly more demanding than TSU0 and TID0 tests. We start with the YY grid. We examine several configurations in the YY simulations, see Table 6.4. Configuration I represents the most straightforward implementation of the YY grid. It uses the non-optimized YY grid and the bilinear interpolation to couple the Yin and Yang parts. It is a sufficient configuration for

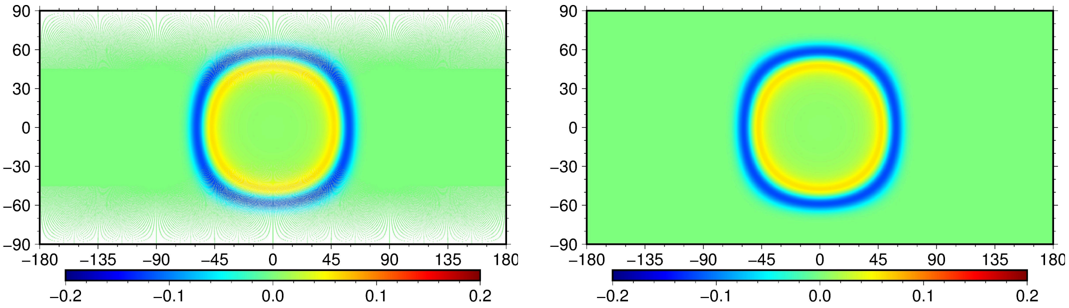

(a) 9 h, YY grid

(b) 9 h, RSC grid

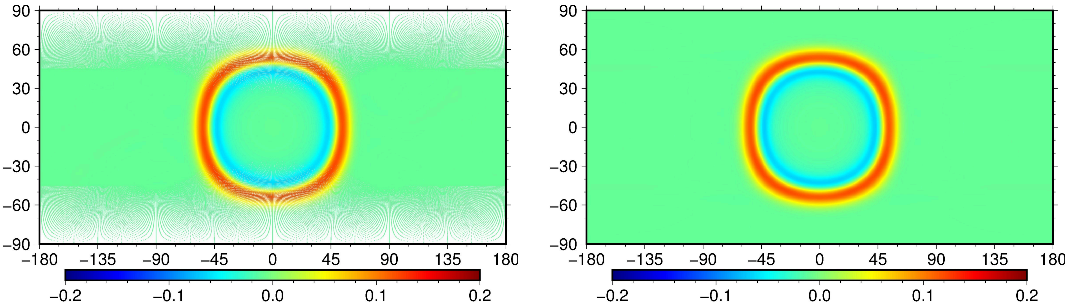

(c) 64 h, YY grid

(d) 64 h, RSC grid

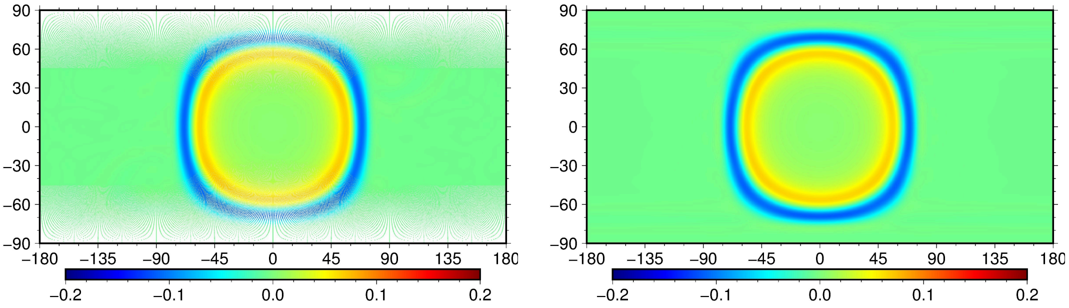

(e) 105 h, YY grid

(f) 105 h, RSC grid

Figure 6.13: SSHs [m] computed in the TSU0 test using the Yin-Yang grid (left column) and the reduced spherical coordinate grid (right column) after 9, 64 and 105 hours.

both TSU0 and TID0 tests but it fails completely in mTIDa. The SSH after 20 days computed using configuration I is depicted in Fig. 6.16 (a). The tidal SSH is completely overlaid by noise in panel (a).

It is not presented but we checked that the bilinear interpolation is implemented correctly: We prescribed an initial SSH and velocities in the form of sine and cosine functions. The initial distribution was set at all inner grid points and the values were interpolated to the halo regions. We inspected Yin and Yang grids with their respective halo regions separately. The visual inspection did not reveal any problems, there was a smooth transition from the inner domain to the halo region in all fields.

We replace the bilinear interpolation with the IDW interpolation in configuration II. Both interpolations use four points and thus we expected them to perform similarly. In fact, the bilinear interpolation was superior to the IDW interpolation in the comparison presented in Appendix E. The opposite is true in the YY simulations. The SSH computed using the configuration II is depicted in

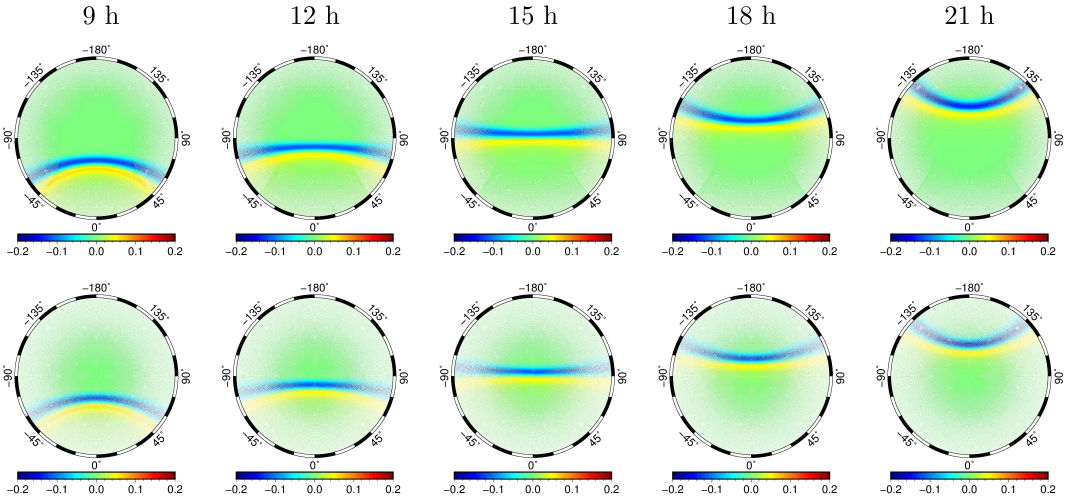

Figure 6.14: SSHs [m] on the Northern hemisphere computed in the TSU0 test using the Yin-Yang grid (upper row) and the reduced spherical coordinate grid (lower row) after 9, 12, 15, 18 and 21 hours viewed from the North Pole.

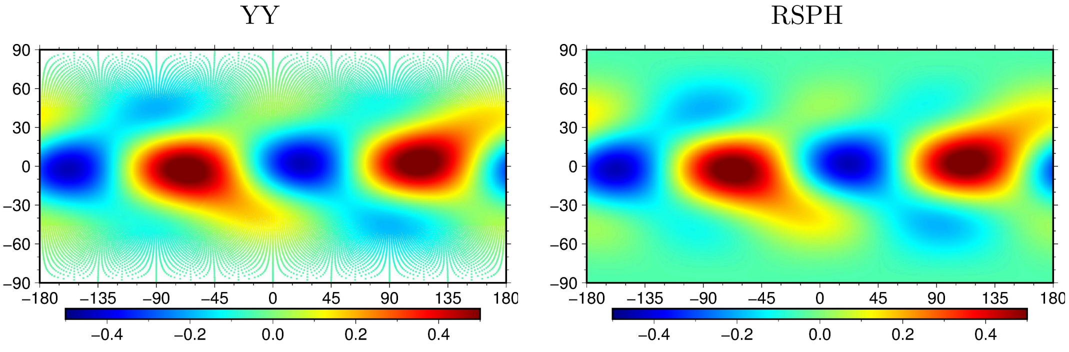

Figure 6.15: SSHs [m] computed using the Yin-Yang grid (left panel) and the reduced spherical coordinate grid (right panel) in the TID0 test after 20 days.

Fig. 6.16 (b). The noise is still extremely strong but the tidal SSH can already be recognized.

Similar to the simulations in Sec. 6.1.5, we do not apply friction in the presented YY simulations with the exception of configuration III. In configuration III, we return to the non-optimized YY grid with the bilinear interpolation but we apply friction. We expected a friction force with our default value of eddy viscosity, $A_H = 2 \times 10^4$ m^2/s, to be sufficient to get rid of the grid-scale noise. Fig. 6.16 (c) shows the resulting SSH. It is significantly better than the SSH in Fig. 6.16 (a) but it is hardly noise-free.

According to Kageyama and Sato [2004], the overlapping areas in the non-optimized YY grid "might be slight (6%) waste of computational time, but the double solution causes no problem in actual calculations. The difference between the two solutions is within the discretization error that is omnipresent all over the sphere any way." Our experience is much different. We retain the bilinear interpolation but replace the non-optimized grid by the optimized grid in configuration IV. The SSH computed using the configuration IV is shown in Fig. 6.16 (d). The SSH is not completely free of the grid-scale noise, see the region around

Configuration	Yin-Yang grid	Interpolation	A_H [$m^2\ s^{-1}$]	Smoothing
I	non-optimized	bilinear	0	no
II	non-optimized	IDW	0	no
III	non-optimized	bilinear	2×10^4	no
IV	optimized	bilinear	0	no
V	non-optimized	bilinear	0	DFP, $s = 0.01$

Table 6.4: Yin-Yang configurations used in the mTIDa test.

(a) Configuration I

(b) Configuration II

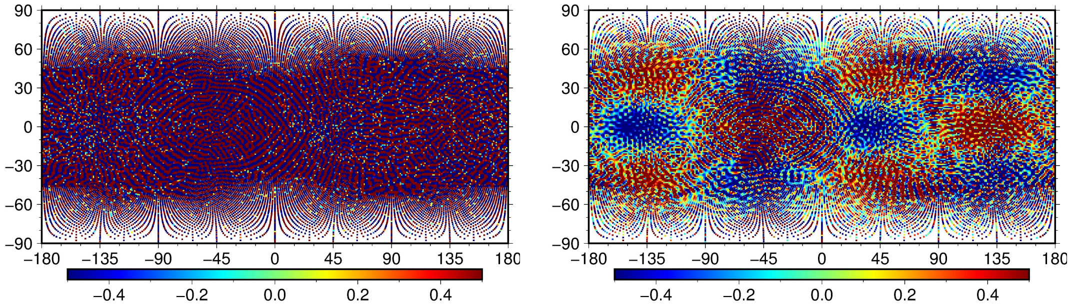

(c) Configuration III

(d) Configuration IV

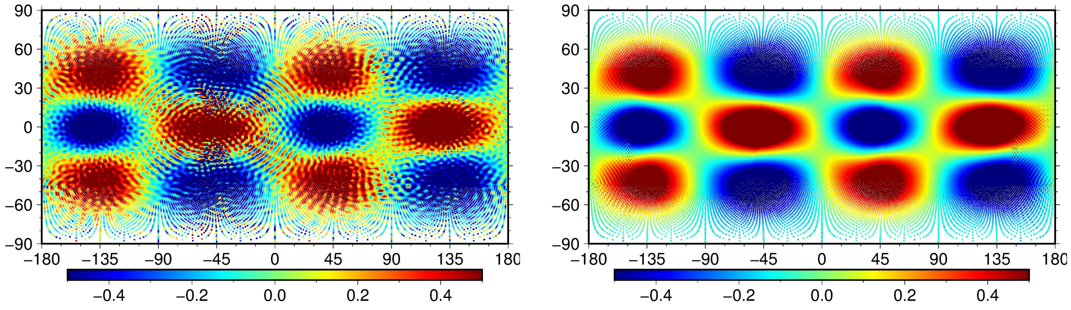

Figure 6.16: SSHs [m] computed using different Yin-Yang configurations in the mTIDa test after 20 days. The configuration used is written above each panel.

the 180th meridian, but the grid-scale noise is significantly reduced in comparison to the SSH from configuration I shown in Fig. 6.16 (a).

Baba et al. [2010] also experienced a grid-scale noise in their simulations. They did not provide details about it in the paper but they applied Shapiro filter to solve the problem. We use another technique in configuration V, it is the DFP smoother given by Eqs. (5.127) and (5.128). We set the parameter s in the DFP smoother to $s = 0.01$. The resulting SSH in Fig. 6.17 (c) is completely noise-free.

Let us move our focus to the RSC grid. The SSH computed using the RSC grid in mTIDa after six days is depicted in Fig. 6.17 (b). Similar to the TSU0 and TID0 tests, there is again a very good agreement between the SSHs computed in the YY and RSC simulations after six days, compare panels (a) and (b) of Fig. 6.17. Unfortunately, the grid-scale noise that was present in the YY simulations is generated also in the RSC simulations. The SSH in the RSC simulation is seriously affected by the grid-scale noise generated in the polar regions after 20 days, see Fig. 6.17 (d). Nevertheless, the SSH in mid-latitudes corresponds very well to the SSH calculated in the YY simulation. We tried to apply the

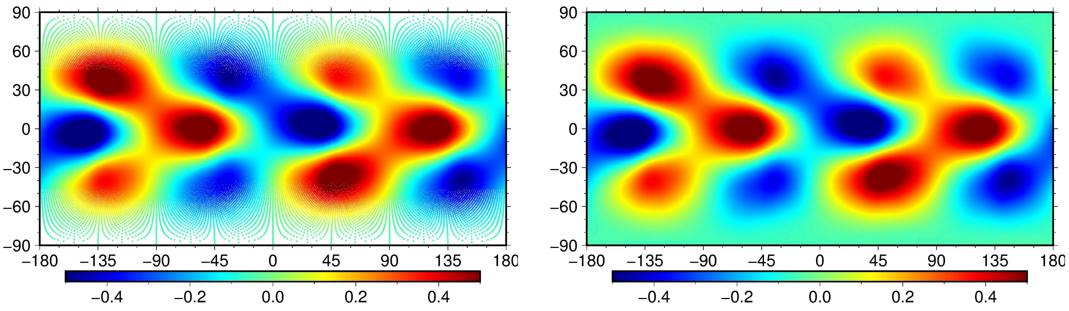
(a) YY, configuration V, day 6

(b) RSPH , day 6

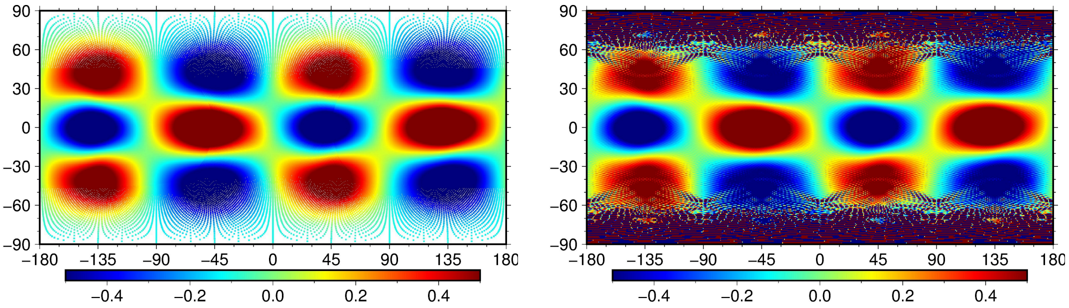
(c) YY, configuration V, day 20

(d) RSPH , day 20

Figure 6.17: SSHs [m] computed using the Yin-Yang and reduced spherical coordinate grids in the mTIDa test after 6 and 20 days.

DFP smoother. Its implementation was more complicated due to missing grid points in the RSC grid and its performance was worse than in the YY grid. The DFP smoother managed to decrease the amplitudes of the grid-scale noise but the noise was still present (not shown).

Starius [2014] suggested to use the so-called Pole Tangent Derivative (PTD) method on the three northernmost and three southernmost parallels. The PTD method approximates the zonal derivative using the derivative along the great circle that is tangent to the parallel at the particular point. The derivative along the great circle is approximated by the twelve-point centered non-equidistant finite difference formula. The values at the twelve points are determined by interpolation in either zonal or meridional direction. Additionally, an interpolation in the zonal direction using trigonometric polynomials is applied prior to the PTD method in order to have 32 points in each of the 3+3 polar parallels. We have not implemented the PTD method into the LSOMG model. The number of interpolations needed seems to be rather excessive.

To sum it up. The RSC simulations helped to validate the YY simulations. Unfortunately, unresolved issues remain in the RSC simulations. The PTD method might resolve them. Nevertheless, the high-order interpolation schemes used on the RSC grid could hardly be used in the presence of realistic land mask. The RSC grid could be used only in aqua-planet simulations not in paleo simulations or in a realistic present-day seamless coupled model. The YY grid could be used for these purposes if the grid-scale noise is kept under control.

6.3 Munk problem

In the so-called Munk problem, the motion of a homogeneous fluid in a rectangular basin is to be found. The problem is described by barotropic geostrophic equations with the harmonic friction,

$$f\mathbf{e}_3 \times \mathbf{U} + gh\nabla_h\eta = A_H\Delta_h\mathbf{U} + \frac{\boldsymbol{\tau}_w}{\rho_0}, \tag{6.13}$$

$$\nabla_h \cdot \mathbf{U} = 0. \tag{6.14}$$

The nonlinearities are neglected and the ocean bottom is supposed to be flat.

Note that if the linear drag was considered instead of the harmonic friction, the equations would constitute the so-called Stommel problem instead of the Munk problem. Finally, if the friction (or drag) was neglected completely, we would obtain the original Sverdrup problem.

Under these assumptions, the barotropic stream function ψ_b (the concept of the barotropic stream function is explained in Appendix F) can be found analytically. The stream function is composed from three terms,

$$\psi_b = \frac{\mathbf{e}_3 \cdot (\nabla \times \boldsymbol{\tau}_w)}{\beta\rho_0}(\psi_I + \psi_E + \psi_W), \tag{6.15}$$

where ψ_I is the interior solution inside the ocean basin away from boundaries, ψ_E is the solution that arise due to the presence of eastern boundary and, similarly, ψ_W is the western-boundary layer solution. The form of the individual terms can be found in Vallis [2006],

$$\psi_I = d_B - d_W, \tag{6.16}$$

$$\psi_E = d_M e^{\frac{d_W - d_B}{d_M}}, \tag{6.17}$$

$$\psi_W = -d_B e^{-\frac{d}{2d_M}}\left[\cos\left(\frac{\sqrt{3}d_W}{2d_M}\right) + \frac{1}{\sqrt{3}}\sin\left(\frac{\sqrt{3}d_W}{2d_M}\right)\right], \tag{6.18}$$

where d_B stands for the width of the whole basin, d_W is the distance from the western boundary and $d_M = (A_H/\beta)^{1/3}$.

In our numerical test, we use the settings of Frisius et al. [2009], in which the basin covers almost half of the Earth and the wind is purely zonal:

- Idealized basin: $\lambda \in \langle -90°, 90° \rangle$, $\phi \in \langle -85°, 85° \rangle$.
- Depth of flat bottom: $H = 5000$ m.
- Wind stress: $\boldsymbol{\tau}_w = -0.1\cos(3\phi)\mathbf{e}_\lambda$ Nm^{-2}.

Moreover, the reference density is set equal to the LSOMG default value $\rho_0 = 1020$ kg/m^3 and the horizontal viscosity is chosen to be $A_H = 2 \times 10^5$ m^2/s.

The barotropic stream function computed according to Eqs. (6.15), (6.16), (6.17) and (6.18) and the stream function computed in the LSOMG-BT model are depicted in Fig. 6.18. The both solutions agree well in the basin's interior and close to the eastern boundary. A clear discrepancy is present close to the poles. However, as noted by Frisius et al. [2009], the discrepancy can be expected

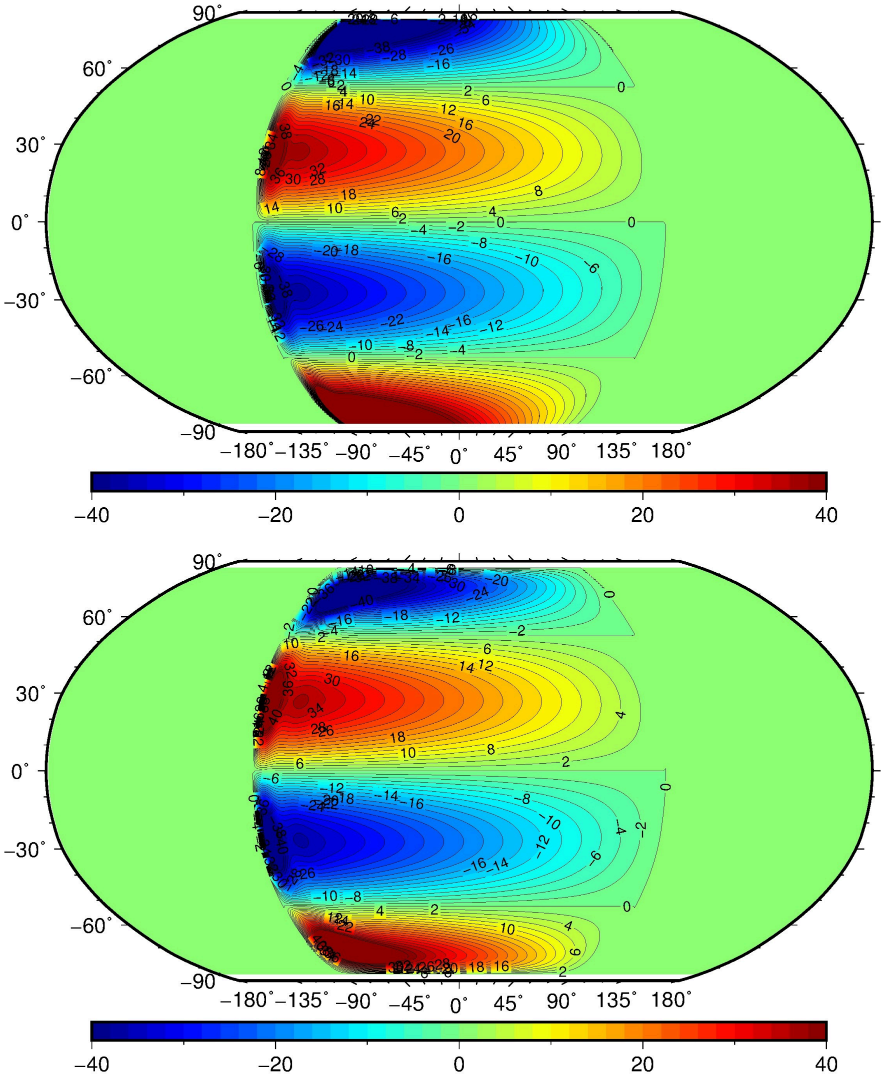

Figure 6.18: Barotropic stream functions [Sv] in the Munk problem. Upper panel: Theoretically predicted barotropic stream function. Lower panel: Barotropic stream function computed in the LSOMG-BT model.

because the analytic solution is derived under the condition $d_M \ll d_B$ which is not valid close to the poles.

Besides that, both solutions show a well developed western boundary currents, the isolines are intensified in the neighbourhood of western boundary. This feature is missing in the Sverdrup solution but it is present in the Stommel and Munk solutions. However, the Stommel and Munk solutions differ at first sight in one aspect. The isolines form bodies that are convex in the Stommel solution but concave in the Munk solution. The Munk solution contains a particular "dent" east of the western-boundary region, see fig. 14.5 in Vallis [2006]. This feature is clearly present in the analytic solution as well as in the numerical solution.

There is some discrepancy in the western-boundary region between the two solution. We argue that it might be caused by the fact that the analytic solution satisfies the no-slip boundary condition whereas the numerical solution satisfies the free-slip boundary condition on the Arakawa C-grid.

6.4 Numerical test of the Ekman layer

The purpose of this numerical test is to check the implementation of vertical shears of horizontal velocities in the momentum equation. The so-called Ekman problem is described by the simplified governing equations,

$$fv + A_V \frac{\partial^2 u}{\partial z^2} = 0, \tag{6.19}$$

$$-fu + A_V \frac{\partial^2 v}{\partial z^2} = 0, \tag{6.20}$$

where the vertical viscosity A_V is taken to be constant. We prescribe a steady wind that is blowing from the South to the North in the northern hemisphere. The surface boundary condition 5.2 has the form,

$$A_V \frac{\partial u}{\partial z} = 0, \tag{6.21}$$

$$A_V \frac{\partial v}{\partial z} = \frac{\tau_w}{\rho_0}. \tag{6.22}$$

The problem is solved analytically in Stewart [2008],

$$u = v_0 e^{a_e z} \sin\left(\frac{\pi}{4} - a_e z\right), \tag{6.23}$$

$$v = v_0 e^{a_e z} \cos\left(\frac{\pi}{4} - a_e z\right), \tag{6.24}$$

where

$$a_e = \sqrt{\frac{f}{2A_V}}. \tag{6.25}$$

The Eqs. (6.23), (6.24) describe the well-known Ekman spiral. The velocity components at the surface, for $z = 0$, are equal to

$$u = v_0 \sin\left(\frac{\pi}{4}\right), \tag{6.26}$$

$$v = v_0 \cos\left(\frac{\pi}{4}\right). \tag{6.27}$$

The velocity vector at the surface is thus pointing in the north-east direction, the angle between the wind vector and velocity vector is 45°. Deeper below the surface, the velocity vector starts to rotate and its amplitude is decreasing. The depth in which the velocity vector is rotated by 180° and it is pointing in the south-west direction, is the base of the Ekman layer. The thickness of the Ekman layer is thus equal to

$$D_e = \frac{\pi}{a_e} = \pi\sqrt{\frac{2A_V}{f}}. \tag{6.28}$$

Our target is to validate the functionality of the LSOMG model using these theoretical predictions. We set up the model as follows:

- Depth of ocean bottom: $H = 200$ m.
- Computational domain: $15° \leq \phi \leq 60°$, no boundaries in the zonal direction.

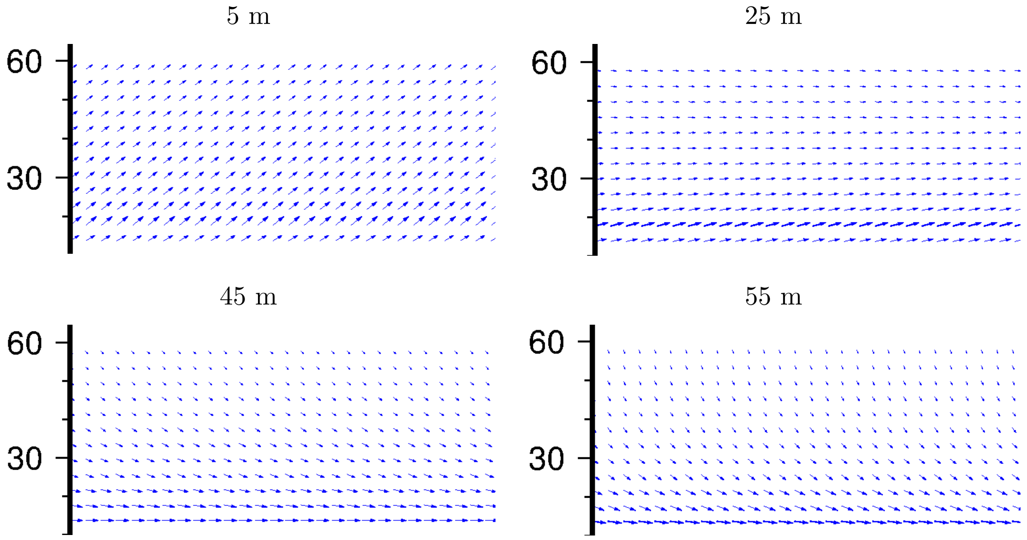

Figure 6.19: The velocities in the Ekman layer computed in the LSOMG model.

- Vertical resolution: 20 layers, each layer is 10 m thick.
- Vertical viscosity: $A_V = 0.05$ m^2/s.

The governing equations in the LSOMG model do not, however, fully correspond to Eqs. 6.19 and 6.20. The momentum equation in the model contains the time derivative, the model is not designed to compute the steady state directly. Consequently, we run the model for 15 days to reach the (quasi) steady state. The results are depicted in Fig. 6.19.

The computed velocity field is in accordance with the analytic solution (6.23) and (6.24). In the surface layer (5 m deep), all velocity vectors are pointing in the north-east direction. The velocity vectors rotate in the clockwise direction with the increasing depth. The rotation of velocity vectors and their size do not depend on the longitude, only on the latitude. The vectors rotate faster in high latitudes than in low latitudes. The Ekman layer in high latitudes is thus shallower than in low latitudes. The analytic formula (6.28) does predict this behaviour. The Coriolis parameter f is proportional to the sine of latitude, $1/f$ is thus smaller in high latitudes than in low latitudes and so also the Ekman layer is shallower in high latitudes than in low latitudes.

The computed velocity vectors at $\phi = 45°$ are rotated by approximately 90° in 55 m depth. The Ekman layer should be twice as deep, which gives us 110 m. The predicted thickness of the Ekman layer is, according to Eq. (6.28), $D_e \approx 98$ m at $\phi = 45°$ which corresponds to our estimate.

6.5 Numerical test of tracer advection

The purpose of this numerical test is to check the performance of advection schemes that advect active tracers (temperature and salinity) in the LSOMG model. We test both the horizontal and vertical advection.

6.5.1 Horizontal advection

The idea of the numerical test is simple. We disable the physically motivated diffusive processes in the model. We prescribe a particular initial tracer field. We then advect this tracer field with a constant zonal velocity. The tracer field should be transported without any distortions or amplitude drops caused by inherent deficiencies of the scheme such as the artificial diffusivity. The development of artificial extrema is undesirable either. After one period, the actual tracer field should be identical to the initial tracer field.

We test three advection schemes, the original QUICK scheme, the newly implemented Lax-Wendroff scheme of Smith et al. [2010] (LW–Smith) and the Lax-Wendroff scheme with the Superbee flux limiter (LW–Superbee) in the following numerical setup:

- Initial tracer field: Gaussian bell and box in the zonal direction, see the pink curve in Fig. 6.20. The field is constant in the meridional direction
- Resolution: 1°
- Horizontal velocity: $u = 1.1 \cos\phi$ m/s, $v = 0$ m/s
- Vertical velocity: $w = 0$ m/s
- Time step: 1800 s
- Length of simulation: 420 days which corresponds to one period

Fig. 6.20 shows initial and advected tracer fields along the equator. The Gaussian bell is advected without any significant deficiencies by all tested advection schemes. A detailed inspection reveals that the LW–Superbee scheme tends to make a box out of the Gaussian bell and the LW–Smith scheme somewhat distorts the Gaussian bell and decreases its amplitude. The best performance shows the original QUICK scheme which is probably due to the quadratic interpolation used.

However, the situations is much different if we focus on the advection of a simple box. The QUICK scheme fails in this test since it produces artificial extrema with significant amplitudes, see the wiggles on the edges of the box. In fact, this behaviour was expected. Gaussian bell represents smooth variations in the tracer field while the box represents a sudden change. The QUICK scheme does not contain flux limiters and the scheme is thus unable to model the box correctly. The other two schemes are using flux limiters which make their results much better. Neither the LW–Smith solution nor the LW–Superbee solution shows the artificial extrema that are present in the QUICK solution. We consider the performance of both schemes to be satisfactory for our purposes. The LW–Superbee scheme seems to advect the box better than the LW–Smith scheme. However, it is probably natural for the LW–Smith scheme to capture the box since it has a tendency to create boxes out of smooth distributions as we have seen in the advection of the Gaussian bell. We thus hesitate to call the LW–Superbee scheme an overall winner and we consider the LW–Superbee and LW–Smith schemes equally useful.

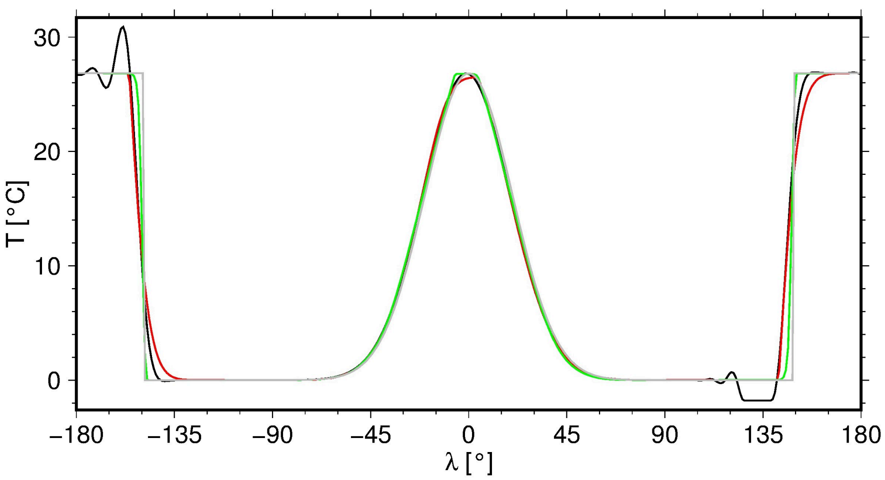

Figure 6.20: Initial tracer field (pink) and tracer fields advected by the QUICK scheme (black), the Lax-Wendroff scheme of Smith et al. [2010] (red) and the Lax-Wendroff scheme with the Superbee flux limiter (green).

6.5.2 Vertical advection

The vertical-advection numerical test is very similar to the horizontal-advection test. We again advect the initial tracer field with the constant velocity field. The main difference is that the grid is equidistant in the horizontal-advection test while it is non-equidistant in the vertical-advection test.

We test the QUICK scheme, the LW–Smith scheme, the Lax-Wendroff scheme with the van Leer flux limiter (LW–vanLeer) and the Lax-Wendroff scheme with the Koren flux limiter (LW–Koren) in the following model setup:

- Initial tracer field: Gaussian bell, see the left panel of Fig. 6.21
- Resolution: 22 layers
- Horizontal velocity: $\mathbf{u} = 0$
- Vertical velocity: $w = 2 \times 10^{-3}$ m/s
- Time step: 1800 s
- Length of simulation: 10 days

The right panel of Fig. 6.21 shows the tracer field after the advection. The overall picture is similar to the horizontal-advection numerical test. The QUICK scheme does not contain flux limiters and so it creates artificial extrema. We do not recommended to use the QUICK scheme. The other schemes use flux limiters and consequently no artificial extrema are present in their solutions. The performances of LW–Smith, LW–vanLeer and LW–Koren schemes are similar. We prefer the LW–Smith scheme which seems to preserve the initial Gaussian bell somewhat better. Nevertheless, it is more a personal preference than objectively justified decision.

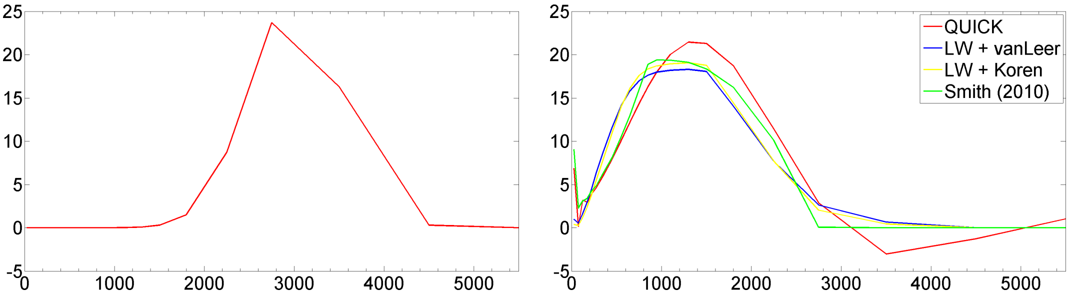

Figure 6.21: Left panel: Vertical profile of the initial tracer field from the surface down to 5500 m. Right panel: Vertical profiles of tracer fields advected by the QUICK scheme (black), the Lax-Wendroff scheme with the van Leer flux limiter (blue), the Lax-Wendroff scheme with the Koren flux limiter (yellow) and the Lax-Wendroff scheme of Smith et al. [2010] (green).

7. Realistic runs of the LSOMG model

7.1 Tidal barotropic circulation

In order to validate the tidally driven circulation from the LSOMG-BT model, we compared our results with a commonly used and respected tidal model. There are quite a few tidal models available. We start with the assimilative models that are constrained by data. Stammer et al. [2014] divided the assimilative models into two groups: empirically adjusted hydrodynamic models and hydrodynamic models constrained by assimilation. GOT4.8, OSU12, DTU10 and EOT11a are representatives of the first group, while HAMTIDE, FES2014 and TPXO8 belong to the second group. The methodologies used include empirical harmonic analysis of satellite altimetry, response method or spectral ensemble optimal interpolation. We refer the interested user to Stammer et al. [2014] for a discussion about the numerical methods and a comparison of individual models.

There also exist purely hydrodynamic models that are not constrained by data such as HIM, STORMTIDE or HYCOM. The models employ the IWD and SAL parameterizations similar to the LSOMG-BT model. Except for these two parameterizations, the modelling approaches differ. HIM is an isopycnal OGCM but it is commonly used in a 2-D barotropic version in tidal studies. In comparison, STORMTIDE and HYCOM models are 3-D baroclinic models. A further aspect is the computational domain. The STORMTIDE and HYCOM are global models while HIM is only quasi-global since it has the North-Pole cap from 82° N is entirely covered by land. Finally, it is the resolution. HIM has the lowest resolution, 1/8°, while HYCOM has the highest resolution, 1/12.5°. The HYCOM resolution is thus higher by a factor of approximately 1.5. The key differences are summarized in Table 7.1. The modelling efforts with purely hydrodynamic models are very appealing. Unfortunately, the accuracy of purely hydrodynamic models is still significantly lower than the accuracy of constrained models. The discrepancies can be one order of magnitude larger in the unconstrained models than in the models constrained by data [Stammer et al., 2014].

In light of these facts, any assimilative model would probably be a good reference for us. We decided to take TPXO8-1 as the reference model. Nevertheless, before we proceed to the validation of LSOMG-BT model results, we present a quick check-up of TPXO8-1 model skills. We downloaded not only the TPXO8-1 model but also the DTU10, FES2012 and EOT11ag tidal models and used them to compute the SSH on 1.1 2015 at 00:00:00. The results are depicted in Fig. 7.1.

Model	BT/BC	Vertical coordinate	Domain	Resolution
HIM	BT	none	86° S-82° N	1/8°
STORMTIDE	BC	z	global	1/10°
HYCOM	BC	hybrid ($\rho + z$)	global	1/12.5°

Table 7.1: Comparison of main characteristics of three hydrodynamic tidal models; BT=barotropic, BC=baroclinic.

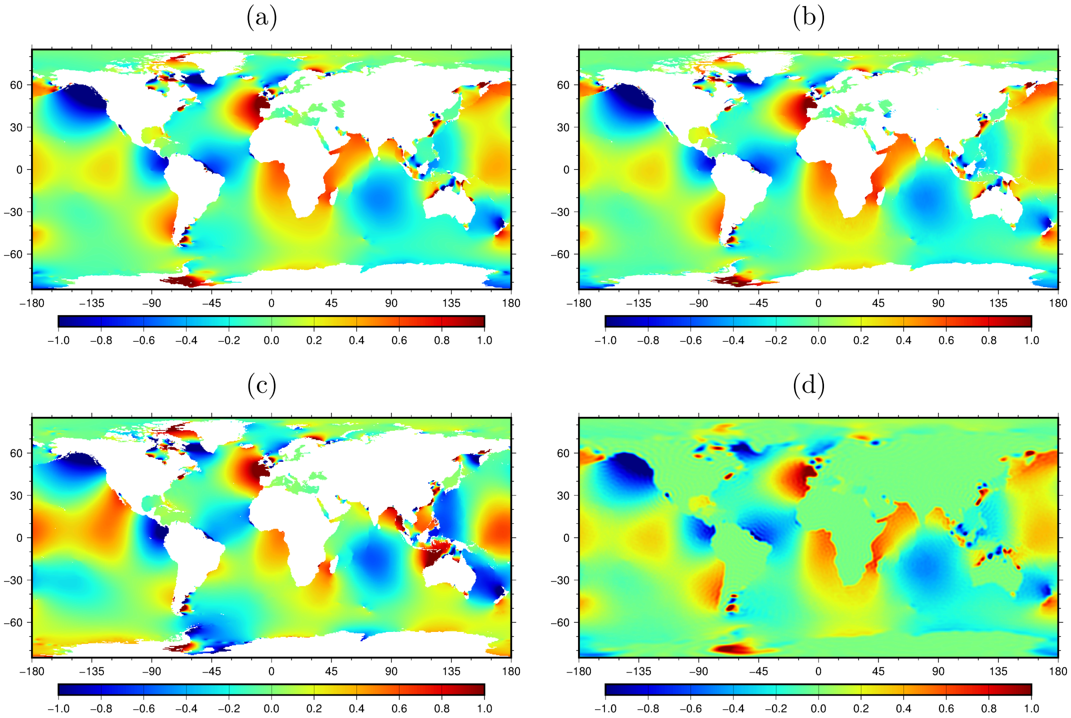

Figure 7.1: Tidal SSH [m] on 1.1 2015 at 00:00:00 according to TPXO8-1 (a), DTU10 (b), FES2012 (c) and EOT11ag (d) tidal models.

Note that we used Matlab version of EOT11ag model. It is a light-weight version of the EOT11ag model in which the tidal SSH is represented by spherical harmonics. The Gibbs phenomenon is thus clearly visible in the EOT11ag SSH in Fig. 7.1 (d). However, it is sufficient for a qualitative visual comparison with other solutions. A brief comparison does not show much differences between TPXO8-1 and DTU10 solutions in panels (a) and (b) of Fig. 7.1, respectively . A more thorough inspection reveals that tidal bulges are slightly shifted with respect to each other. The EOT11ag solution in Fig. 7.1 (d) is qualitatively in excellent agreement with the DTU10 solution and so it is also in a good agreement with the TPXO8-1 solution. The most different solution is the FES2012 solution in Fig. 7.1 (c). The phases of tides around Antarctica are shifted. For example, the SSH is negative in FES2012 in the Weddell sea while the other three tidal models predict positive SSH in this region. The tides in low and mid latitudes are in much better agreement. Nevertheless, the discrepancies are present in Atlantic, Pacific as well as Indian Oceans.

Our validation experiment is similar to the one performed by Buijsman et al. [2015b]. We run the LSOMG-BT model for 19 days. The first 16 days serve as a spin up. According to our experience, it is a sufficiently long period to spin up a barotropic tidal model. The last three days are used to compare the SSHs from the LSOMG-BT and TPXO8-1 models. In our comparison, we consider only grid points where ocean is deeper than 1000 m. Additionally, the tides in high latitudes are not considered. The presence of sea ice makes the prediction of high-latitude tides complicated. Consequently, we restrict ourselves to $-66° < \phi < 66°$. Our

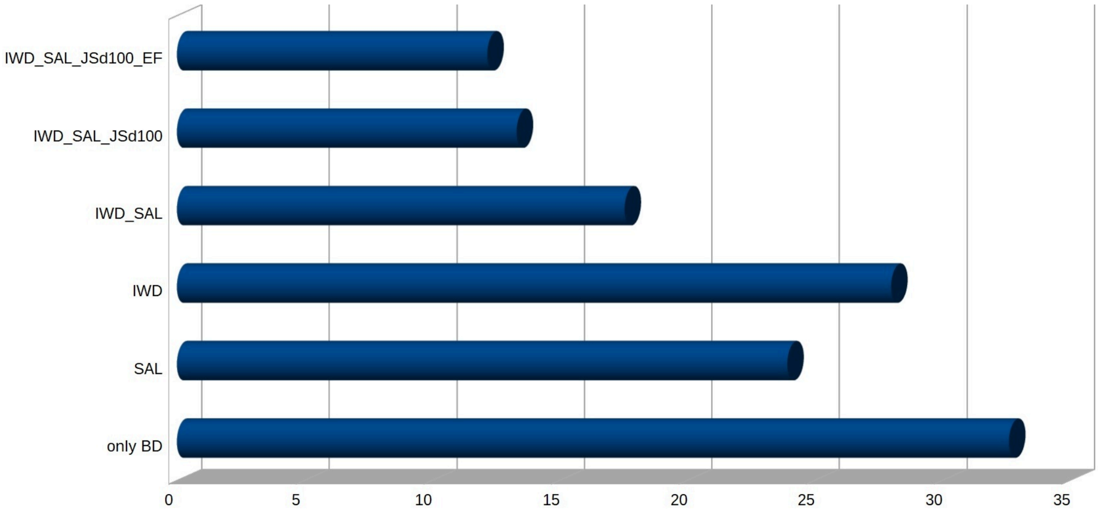

Figure 7.2: RSS [m] from the barotropic LSOMG-BT model in the validation experiment. Several model configuration are tested. The model is run with the bottom-drag (BD), internal wave drag (IWD), self-attraction and loading (SAL), nonlinear free surface (EF). Internal wave drag is applied if $H > 1000$ m (without JSd100) or if $H > 100$ m (with JSd100).

metric is the so-called root-sum-square (RSS),

$$RSS = \sqrt{\frac{\left\langle \int\limits_S \left(\eta_{LSOMG} - \eta_{TPXO}\right)^2 dS \right\rangle}{S}}, \tag{7.1}$$

where the bracket denotes the time averaging. We choose the sampling frequency of tidal SSH to be 30 minutes and we average all samples stored during the last three days of our experiment.

The LSOMG-BT model is run in the 0.25° resolution with the time step $\Delta t = 7.5$ s. The coefficient of bottom friction is set to $C_b = 2.5 \times 10^{-3}$ and the horizontal viscosity is equal to $A_H = 1.25 \times 10^3$ m^2/s

The results of our experiment are depicted in Fig. 7.2. If only bottom drag is included and no tidal parameterizations are used, the RSS is rather large, $RSS =$ 32.62 cm. The inclusion of IWD or SAL improves the accuracy significantly which is in agreement with the conclusions of other authors. The RSS reduces down to 28.0 cm and 23.93 cm if we include IWD or SAL, respectively. Thus, the parameterization of SAL affects the SSH more than the parameterization of IWD in our experiment. Jayne and St. Laurent [2001] applied the IWD only in waters deeper than 1000 m. We also used this setting but we also tried to relax this condition to waters deeper than 100 m. Our results suggest that the condition $H > 100$ m for the application of IWD is better than the condition $H > 1000$ m, the RSS has improved from 17.55 cm to 13.32 cm. This finding is in agreement with Arbic et al. [2004] but it is in disagreement with Buijsman et al. [2015b] who strongly supported the condition $H > 1000$ m. Finally, the nonlinear free surface outperforms linear free surface, although the improvement of RSS is only modest, from 13.32 cm to 12.17 cm. However, it is expected that the improvement would be larger if we focused on shallow regions.

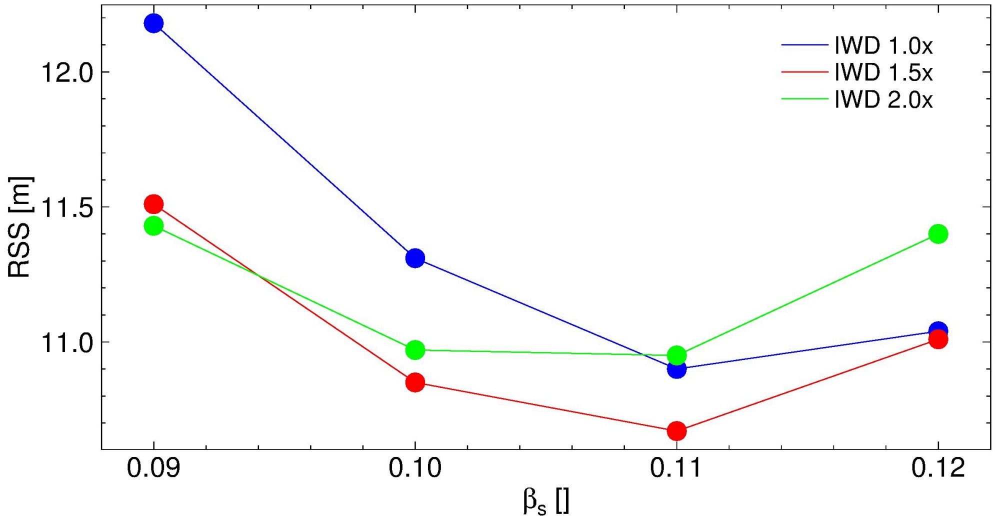

Figure 7.3: Sensitivity of RSS in the tidal validation experiment on the values of IWD and SAL.

We further study sensitivity of the RSS to the strength of IWD and SAL. We test three IWD setups: The default setup with $L = 10$ km, the setup with IWD increased 1.5× which corresponds to $L \approx 6.67$ km and the setup with IWD increased 2× which corresponds to $L = 5$ km. And four values of β_s coefficient in the SAL parameterization: 0.09 (default value), 0.10, 0.11 and 0.12. In total, we computed RSS for 12 setups. The results are depicted in Fig. 7.3. The computed RSS indicates that increased IWD strength and larger β_s are favourable. On the other hand, $\beta_s = 0.12$ is obviously too large value since the RSS increases for all three IWD setups if β_s is increased from $\beta_s = 0.11$ to $\beta_s = 0.12$. Similarly, 2× increased IWD is too strong since the RSS computed with 1.5× increased IWD is smaller for all tested values of β_s, except for the default $\beta_s = 0.09$ where it is slightly larger. The best $RSS = 10.67$ cm is achieved with 1.5× increased IWD and $\beta_s = 0.11$. Similar but slightly larger $RSS = 10.85$ cm is achieved with 1.5× increased IWD and $\beta_s = 0.10$ and $RSS = 10.90$ cm is achieved with the default IWD and $\beta_s = 0.11$.

Einšpigel and Martinec [2016] conducted a similar but more detailed sensitivity study. They compared the results of simulations with tide gauge data in four regions: deep ocean, European shelf, other shallow-water regions and along continental coastlines. They also tested broader ranges of coefficients in the IWD and SAL parameterizations. They used two successive 1-D minimizations of RSS in order to find the best configuration. They found optimal IWD strength for $\beta_s = 0.10$ and then they optimized β_s using the optimal IWD strength from the first step. In fact, Fig. 7.3 shows that this approach may fail to reach the best setup with the minimum RSS. If we start with $\beta_s = 0.09$ fixed, the best RSS is achieved with 2× increased IWD. The second minimization leads to $\beta_s = 0.11$ with $RSS = 10.95$ cm which is not the best RSS that can be achieved. Despite that, Einšpigel and Martinec [2016] suggested to use 1.4× increased IWD and $\beta_s = 0.10$ which is in agreement with our results.

The RSS is a single number. On one hand it makes the comparison extremely simple and effective, on the other hand it can also be misleading. We thus proceed similarly as in Sec. 6.1 and inspect spatial patterns and time curves.

We start with the spatial patterns. Fig. 7.4 (a) depicts the SSH computed using the default IWD and SAL setup on 20.1. 2015 at 00:00:00. The other panels show SSH differences for our tested setups except for the $\beta_s = 0.12$ setups. The best setup is depicted in panel (f), the other two recommendable setups are shown in panels (c) and (e) of Fig. 7.4. The SSH differences caused by IWD and SAL are of similar magnitude but their spatial pattern is different. The maximum amplitudes of SSH differences are around 20 cm which is significant if we consider that the maximum SSH amplitudes are around 1 m.

(a) η, IWD 1.0x, $\beta_s = 0.09$ (b) $\Delta\eta$, IWD 1.0x, $\beta_s = 0.10$ (c) $\Delta\eta$, IWD 1.0x, $\beta_s = 0.11$

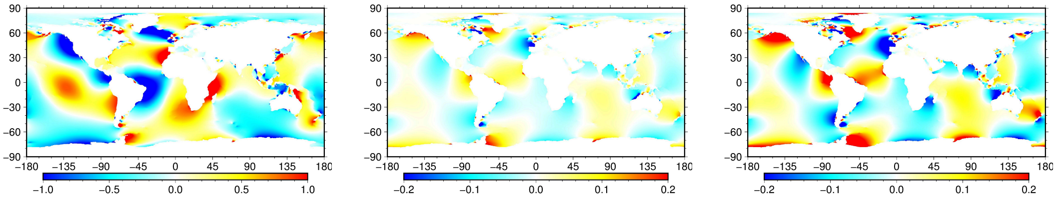

(d) $\Delta\eta$, IWD 1.5x, $\beta_s = 0.09$ (e) $\Delta\eta$, IWD 1.5x, $\beta_s = 0.10$ (f) $\Delta\eta$, IWD 1.5x, $\beta_s = 0.11$

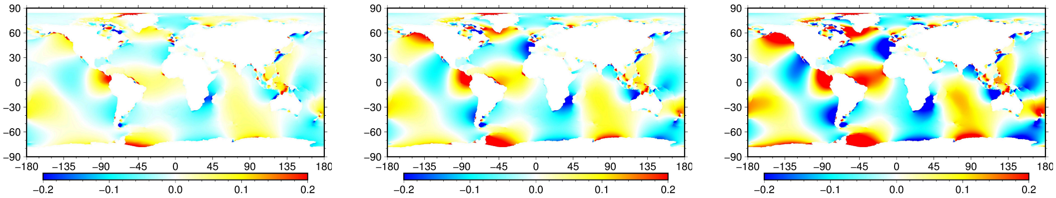

(g) $\Delta\eta$, IWD 2.0x, $\beta_s = 0.09$ (h) $\Delta\eta$, IWD 2.0x, $\beta_s = 0.10$ (i) $\Delta\eta$, IWD 2.0x, $\beta_s = 0.11$

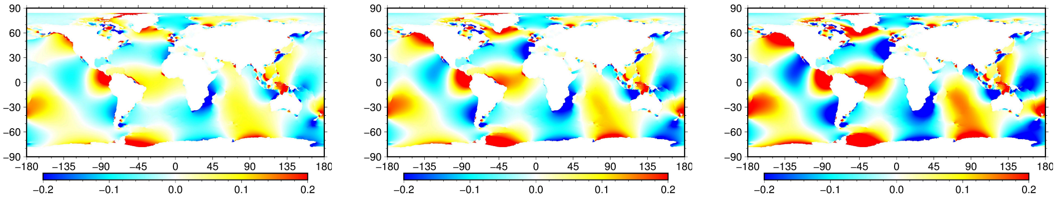

Figure 7.4: Panel (a) shows the tidal SSH [m] on 20.1. 2015 computed using the default SAL ($\beta_s = 0.09$ in Eq. (4.43)) and IWD (L=10 km in Eq. (4.45)). The other panels show differences [m] between the SSH computed using other model configurations and the SSH at panel (a).

The SSH time curves are shown in Fig. 7.6. In particular, we depict time curves which correspond to the default (black curve), "increased IWD" (red), "increased SAL" (green) and "best RSS" setups (blue) (the corresponding panels in Fig. 7.4 are (a) , (c), (g) and (f), respectively). We consider 11 check points which are located in Atlantic, Pacific and Indian Oceans, see Fig. 7.5. The effect of both IWD and SAL is relatively small at points 2, 3, and 9. On the other hand, the differences between the results from the default and modified setups are significant at points 4 and 8 although the SSH amplitudes at these points are smaller. The IWD has a form of linear drag, which could lead to the opinion that IWD is simply damping the SSH amplitude without any phase shifts. It may happen, see time curves at points 1, 7 and 10, but in the general behaviour is more complicated. IWD damps the signal but it also introduces phase shifts at points 4, 5 and 11. In fact, it may locally increase rather than decrease the SSH amplitude, see points 6 and 8. These local effects are probably caused by the dependence of IWD on the ocean depth and coefficient C_{iwd} that are both spatially varying quantities. It is also interesting that the effects of IWD and SAL may partly counteract each other, see points 1, 3, 4 and 10.

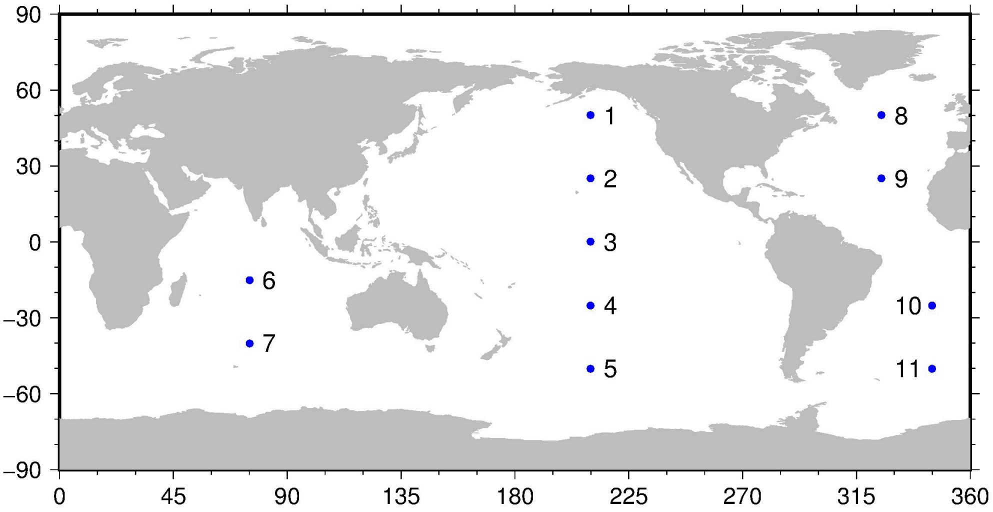

Figure 7.5: Points where SSH time curves depicted in Fig. 7.6 are computed

To sum it up, the inclusion of IWD and SAL terms into the LSOMG-BT model improved the agreement with the TPXO8-1 solution significantly; the RSS has decreased to approximately one third of its starting value. Nevertheless, neither RSS = 12.17 cm (default IWD and SAL setup) nor RSS = 10.67 cm (best RSS; IWD increased 1.5×, $\beta_s = 0.11$) are perfect results. However, it is a standard performance of a barotropic tidal ocean model, see Arbic et al. [2004] and Einšpigel and Martinec [2016]. The results could be improved if we allowed L in the IWD parameterization to be spatially varying and found its optimal values as it was done by Buijsman et al. [2015a]. The quality of simulation can also be further improved using data assimilation [Einšpigel and Martinec, 2016]. We have not inspected these possibilities.

(a) Point 1, (-150.125°, 50.125°)

(b) Point 2, (-150.125°, 25.125°)

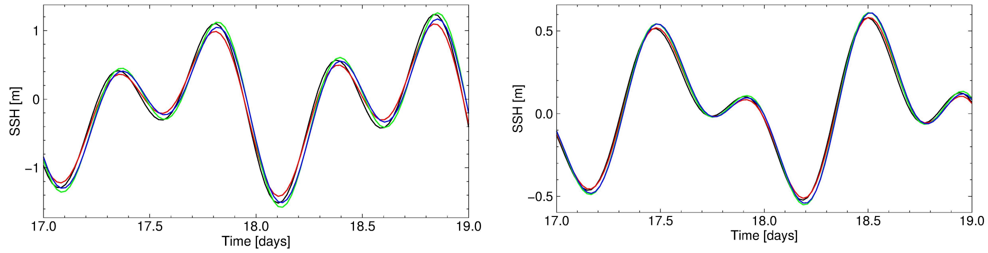

(c) Point 3, (-150.125°, 0.125°)

(d) Point 4, (-150.125°, -25.125°)

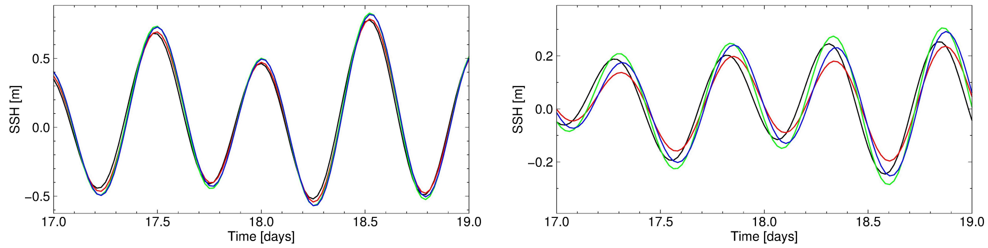

(e) Point 5, (-150.125°, -50.125°)

(f) Point 6, (-35.125°, 50.125°)

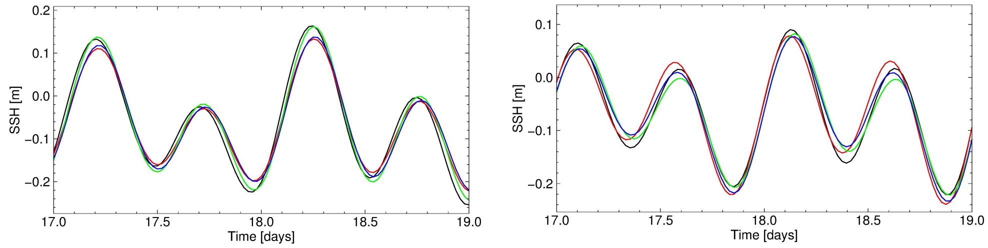

(g) Point 7, (-35.125°, 25.125°)

(h) Point 8, (-15.125°, -25.125°)

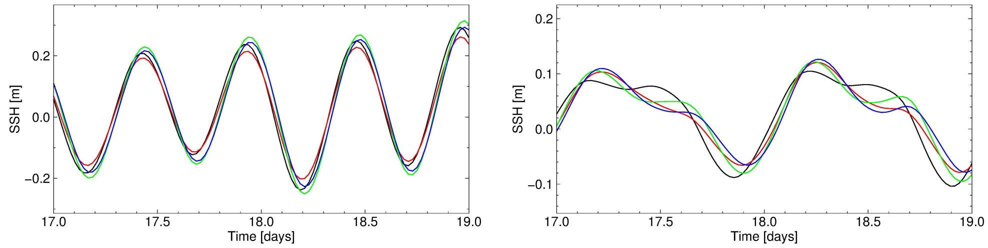

(i) Point 9, (-15.125°, -50.125°)

(j) Point 10, (75.125°, -15.125°)

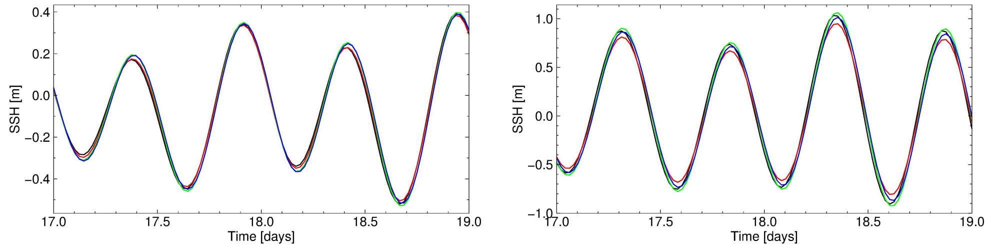

(k) Point 11, (75.125°, -40.125°)

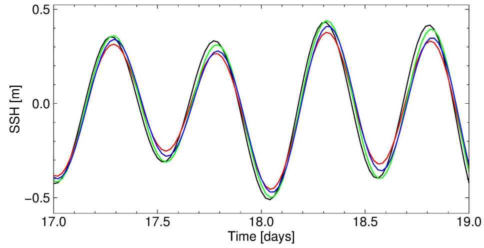

Figure 7.6: Tidal SSH from 18.1. 2015 to 19.1. 2015 computed using IWD 1.0x, $\beta_s = 0.09$ (black), IWD 2.0x, $\beta_s = 0.09$ (red), IWD 1.0x, $\beta_s = 0.11$ (green), IWD 1.5x, $\beta_s = 0.11$ (blue) at points depicted in Fig. 7.5

7.2 Steady wind-driven barotropic circulation

We have shown in Sec. 7.1 that a hydrodynamic barotropic tidal model such as LSOMG-BT needs additional parameterizations (SAL and IWD) and its accuracy is limited. On the other hand, it is a light-weight tool in comparison to the full baroclinic model and its accuracy could be sufficient for certain (geophysical) applications such as the modelling of tidally-driven OIMF. If we consider these facts, a barotropic model is not flawless but it is certainly a useful tool for the modelling of tidal circulation. What about the wind-driven circulation? Could a barotropic model perform equally well also with this type of circulation?

Certain limits are obvious. The circulation in the barotropic model is 2-D. The model determines neither the vertical structure of the flow nor vertical velocities. If these flow features are important for the particular application such as the modelling of ocean-generated toroidal magnetic field, the barotropic model is useless. Similarly, the barotropic model does not solve the evolution equations for temperature and salinity which means that it can not be used to calculate the heat transport in the ocean. Unfortunately, we will demonstrate that there are also other drawbacks.

We follow Frisius et al. [2009] and perform barotropic simulations forced by the annual-mean wind stress. Frisius et al. [2009] used the SOM model forced by wind stresses of Hellerman and Rosenstein [1983], see Fig. 7.7 (a). We do not have this data and therefore we use ERA-Interim data [Dee et al., 2011]. The annual means of zonal and meridional wind velocities are not available in the ERA-Interim archives. We compute the annual means by averaging the monthly means from the year 2013, see Fig. 7.7 (b). We perform two experiments in accordance with Frisius et al. [2009]. The experiments differ in the bathymetry used. The bathymetry is realistic in the first experiment and there is a flat bottom in depth of 5000 m in the second experiment. We run the simulations for 90 days in accordance with Frisius et al. [2009]. We checked out that it is a sufficiently long spin up. In fact, the spin-up could be shorter in the experiment with the realistic bathymetry.

The results are depicted in Fig. 7.8. Panels (a,c,e) correspond to the experiment with the realistic bathymetry, panels (b,d,f) correspond to the experiment with the flat bathymetry. The LSOMG-BT results are depicted in panels (a-d), the SOM results are depicted in panels (e,f). We test two viscosity values. The smaller value $A_H = 2 \times 10^4$ m/s^2 is used in panels (a,b) while one-order larger value $A_H = 2 \times 10^5$ m/s^2 is used in panels (c,d). The GECCO reanalysis is shown in panel (g).

An important finding, which does not depend on the viscosity used and it is in agreement with the SOM results, is that the barotropic modelling of the ACC current is inaccurate. If the bathymetry is realistic, the ACC current virtually disappears. In contrast, if the bathymetry is flat, the ACC current is about five times stronger than it actually is. It is known that the baroclinic processes are important for the ACC current [Olbers and Lettmann, 2007, Cunningham et al., 2003]. The barotropic model does not contain baroclinic pressure gradients and thus an important part of the ACC dynamics is missing in the barotropic model.

The absence of strong ACC current in the experiment with realistic bathymetry affects currents in the Southern hemisphere. The stream functions of these cur-

(a) Hellerman and Rosenstein [1983]

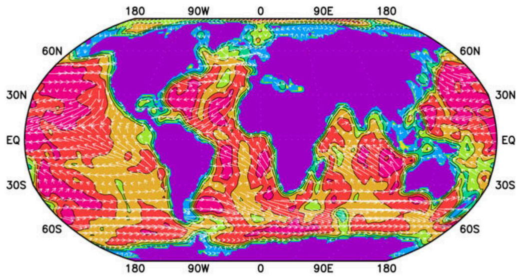

(b) ERA-Interim

(c) CORE-II

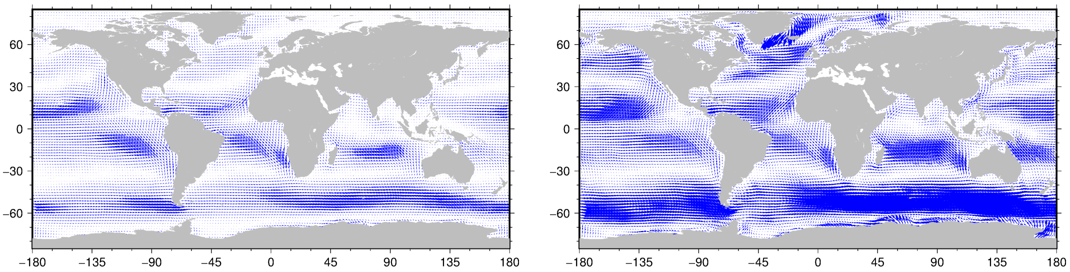

Figure 7.7: Annual-mean wind stress from Hellerman and Rosenstein [1983] (a), ERA-Interim (b) and CORE-II (c) databases.

rents computed in the LSOMG-BT and SOM models do not match the GECCO stream functions. The situation is different in the Northern hemisphere where the computed stream functions are in much better agreement with the GECCO stream functions. The stream functions are similar in both experiments, but they are notably smoother in the flat-bottom experiment. In fact, it seems that they are overly smooth if we compare them with GECCO.

In terms of viscosity, the LSOMG-BT stream functions are smoother and the flow is weaker if higher viscosity is used. The LSOMG-BT high-viscosity results are in better agreement with the SOM results despite the fact that viscosity $A_H = 2 \times 10^5$ m/s^2 is rather large for a 1° model. However, the GECCO results indicate that the low-viscosity setup is more correct.

The LSOMG-BT and SOM stream functions have similar shapes but the flow is stronger in the SOM model. As already mentioned, the forcing is not identical in both models. In order to assess the influence of a different forcing data set, we repeat all LSOMG-BT simulations with the CORE-II forcing, see Fig. 7.7 (c). The flow is noticeably more vigorous in the CORE-II simulations. We assess that the transports are larger in the CORE-II simulations by 10-15 Sv than in the ERA-Interim simulations.

(a) LSOMG-BT, H real, $A_H = 2 \times 10^4$ m/s^2 (b) LSOMG-BT, H const, $A_H = 2{\times}10^4$ m/s^2

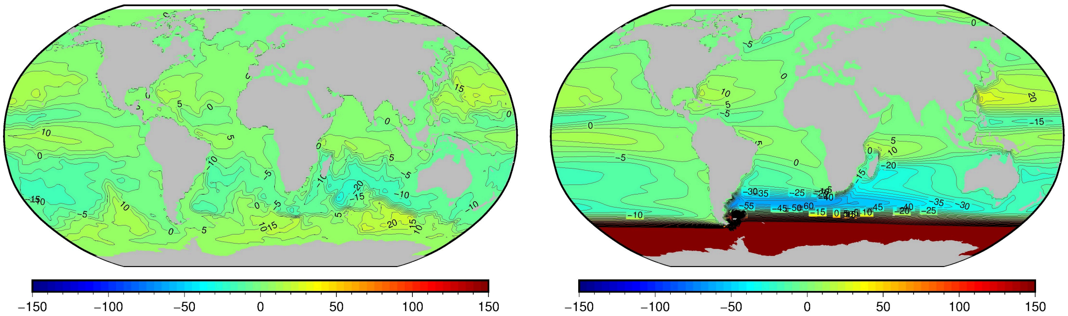

(c) LSOMG-BT, H real, $A_H = 2 \times 10^5$ m/s^2 (d) LSOMG-BT, H const, $A_H = 2{\times}10^5$ m/s^2

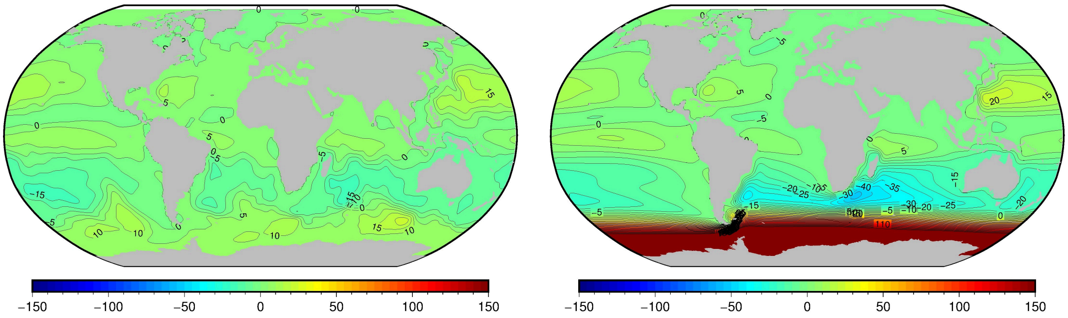

(e) SOM, H real (f) SOM, H const

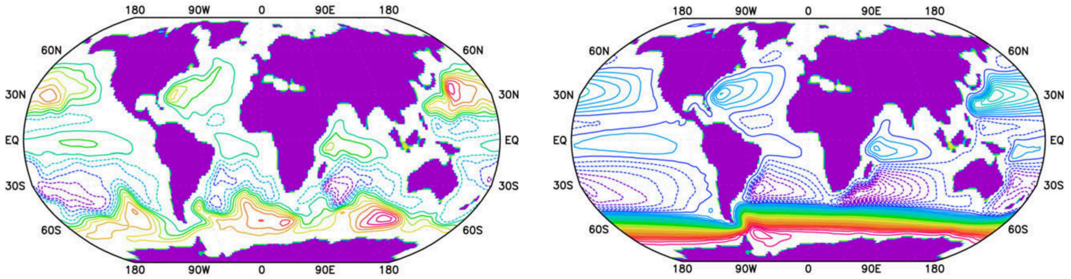

(g) GECCO reanalysis

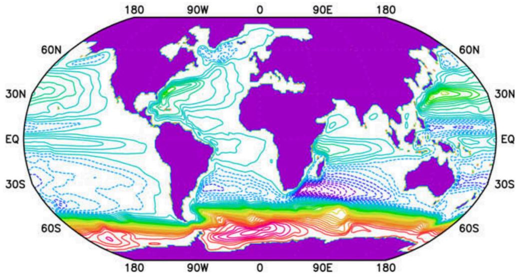

Figure 7.8: Barotropic stream function [Sv] from the wind-driven barotropic simulations from the LSOMG-BT (a-d) and SOM (e,f) models and the GECCO reanalysis (g). Stream lines are depicted in 5 Sv intervals, negative stream lines in panels (e-g) are dashed. Bathymetry used in simulations is either realistic (a,c,e) or constant (b,d,f), $H = 5000$ m. The viscosity used in the LSOMG-BT simulations is either $A_H = 2 \times 10^4$ m/s^2 (a,b) or $A_H = 2 \times 10^5$ m/s^2 (c,d). The viscosity used in the SOM model is unknown.

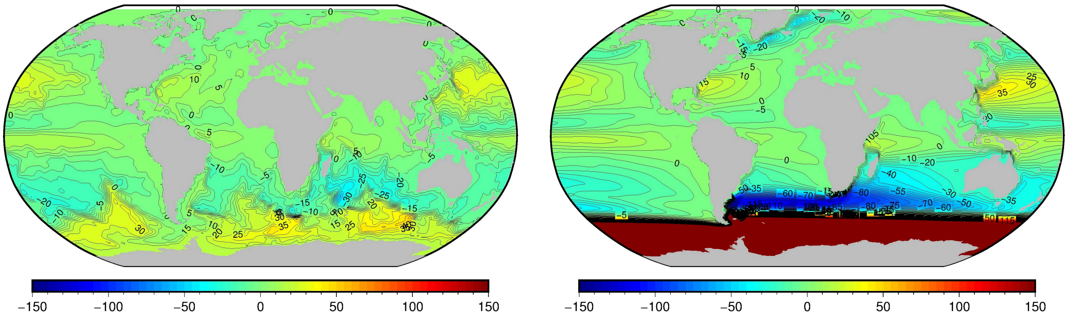

(a) LSOMG-BT, H real, $A_H = 2 \times 10^4$ m/s^2 (b) LSOMG-BT, H const, $A_H = 2{\times}10^4$ m/s^2

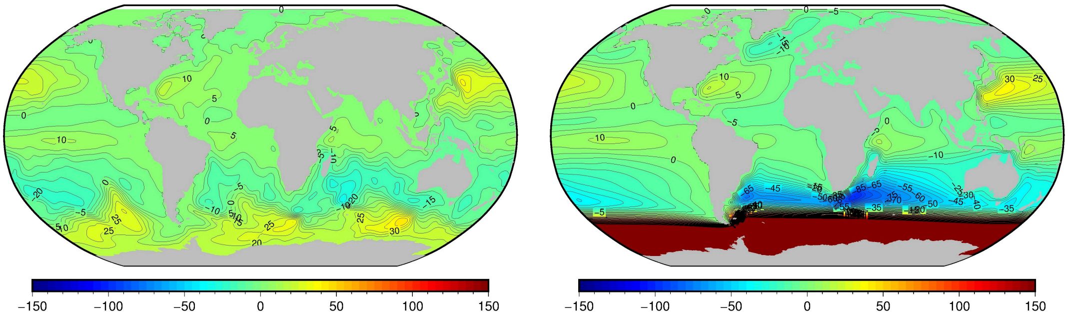

(c) LSOMG-BT, H real, $A_H = 2 \times 10^5$ m/s^2 (d) LSOMG-BT, H const, $A_H = 2{\times}10^5$ m/s^2

Figure 7.9: The same as panels (a-d) in Fig. 7.8 but the simulations are forced by the CORE-II instead of ERA-Interim wind stresses.

7.3 Wind driven baroclinic circulation

In Sec. 7.2, we demonstrated that the barotropic model can reasonably model the wind-driven driven gyres on the northern hemisphere but it completely fails to model the ACC current which significantly affects the circulation on the southern hemisphere. Consequently, we switch to the baroclinic LSOMG model in this section. We shall inspect the model SSH, barotropic transports, barotropic stream function and average temperature and salinity.

In all the presented simulations, we use the horizontal Smagorinsky viscosity [Smagorinsky, 1963, 1993] with $k_H = 4$ and $U_R = 4$ in the minimum viscosity based on the grid Reynolds number. The vertical viscosity is constant $A_V = 1 \times 10^{-3}$ m^2/s. The nonlinear bottom friction with $C_b = 2.5 \times 10^{-3}$ is used. The depth-dependent horizontal (epineutral) and vertical (dianeutral) diffusivities are set according to Eq. (5.64) and (5.57). We use the Lax-Wendroff scheme with flux limiters according to Smith et al. [2010] for the advection of tracers. The energy conserving scheme ENE [Madec, 2012] is used for the discretization of the Coriolis term together with the divergence damping of the second-order with $A_d = 1.3 \times 10^4$. The convective adjustment scheme of Rahmstorf [1993] is applied. The predictor-corrector time stepping scheme is used in the barotropic system. We refer to previous sections for further details about the implemented numerical schemes. The horizontal model resolution is 1° and we use either 11 or 22 layers in the vertical (see Fig. 5.4). The model time step is 30 minutes for the baroclinic system and 30 s for the barotropic system. The simulations are 21 years long.

The first 20 years serve as a spin-up. The annual means are computed from the last year of the simulation.

We start with the simulations from the 11-layer LSOMG model forced by climatological ERA-Interim wind stresses and surface fluxes prescribed in the form of strong 30-day relaxation towards the surface temperature and salinity. Despite the simplified surface forcing and somewhat coarse resolution in the vertical, the model can produce reasonable results.

Fig. 7.10 (a) shows the SSH computed in the LSOMG model. For comparison, the SSHs from the ECCO and POP models are depicted in Fig. 7.10 (b) and (c), respectively, and the SSH estimate of Maximenko et al. [2009] derived from satellite and marine data is depicted in Fig. 7.10 (c). Note that the ECCO product combines the 1° MITgcm model with the data to obtain the best SSH estimate. The POP model used much higher horizontal resolution of 1° but it was a purely hydrodynamic simulation as in our case.

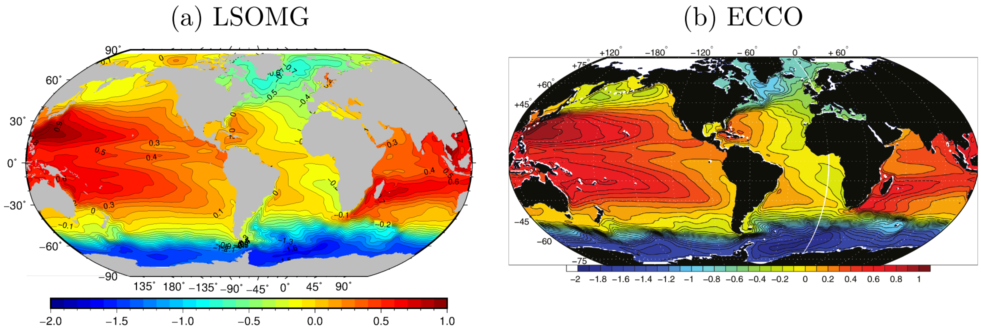
(a) LSOMG

(b) ECCO

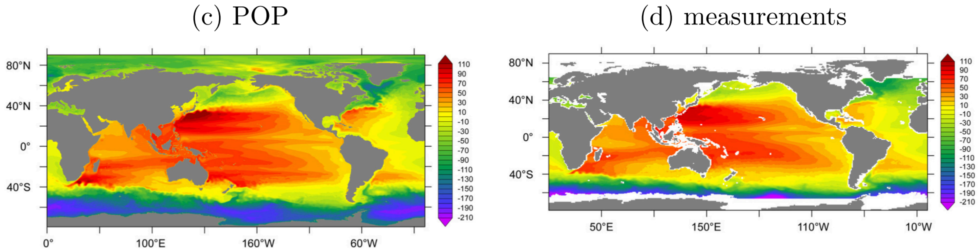
(c) POP

(d) measurements

Figure 7.10: SSHs [m] computed using the LSOMG (a), ECCO (b), and POP (c) models and the SSH determined from satellite and marine data (d). Panel (b) is taken from Wunsch [2011], panels (c,d) are taken from McClean et al. [2011].

Overall, the SSH from the LSOMG model matches the other solutions very well. The SSH has its typical pattern with large-scale lobes in the ocean basins especially in the Pacific Ocean. The SSH is positive in the Pacific and Indian Oceans and negative in the ACC region and in the Atlantic sub-polar gyre. The SSH in the Atlantic Ocean is both positive and negative and the SSH amplitudes are slightly smaller than in the Atlantic and Pacific Oceans. In details, the SSH from the LSOMG model displays certain deficiencies. If we compare it with the ECCO product, the iso lines are too much inclined in the zonal direction in the North Atlantic and the SSH is underdeveloped in the South Atlantic. Certain distortion is present also in the North and South Pacific where the SSH lobes should be more prolonged. Nevertheless, the SSH from the POP model also displays deviations from the ECCO estimate and data-derived SSH of Maximenko et al. [2009]. We thus consider the LSOMG result as satisfactory.

We further inspect the vertically integrated currents. Fig. 7.11 (a) shows the LSOMG velocity vertically integrated from the surface down to approximately 1000 m. The same quantity computed in the OMCT model is shown in Fig. 7.11 (b). The LSOMG model is in a good agreement with the OMCT model. Both simulations show the ACC current, the equatorial currents and the boundary currents in the ocean basins. The OMCT currents seems to be weaker than the LSOMG currents. This is notable on the ACC current and the western-boundary current in the South Atlantic which is pronounced in the LSOMG simulation it is hardly visible in the OMCT simulation. We argue that the weaker flow in the OMCT simulation could be caused by its resolution. The OMCT used 13 layers in the vertical which is similar to the LSOMG simulation but the horizontal resolution was only 1.875°.

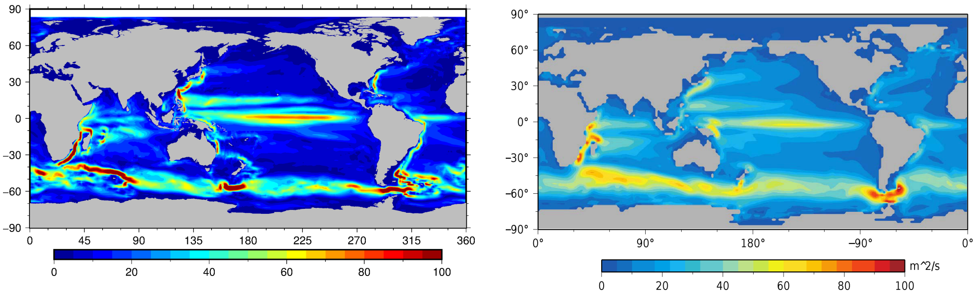
(a) LSOMG

(b) OMCT

Figure 7.11: Vertically integrated velocity [10^3 m^2/s] computed using the LSOMG (a) and OMCT [Irrgang et al., 2016a] (b) models.

The comparison with the OMCT could lead us to conclusion that the flow in the 11-layer LSOMG simulation with simplified forcing is overly strong. This not true. We will show that it is weaker than it should be.

Fig. 7.12 shows barotropic stream functions from the MASNUM [Lei, 2014] and CNRM-CM5.1 [Voldoire et al., 2013] models. The MASNUM model was used in the ocean-only 0.5° configuration with 21 layers in the vertical. The CNRM-CM5.1 is a coupled atmosphere-ocean model with the nominal horizontal resolution of 1° which is refined in the tropics to 1/3° and 42 vertical levels. The CNRM-CM5.1 is significantly smoother than the MASNUM stream function which could be a consequence of a coarser resolution or some kind of smoothing applied in the postprocessing. The MASNUM stream function looks more realistic but the key features of the global ocean circulation are better depicted in the CNRM-CM5.1 stream function.

Fig. 7.13 (a) depicts the barotropic stream function from the 11-layer LSOMG simulation with the simplified forcing. The LSOMG stream function is comparable with the MASNUM and CNRM-CM5.1 stream functions in terms of shape, however, it is globally weaker. It is well pronounced in the ACC region, where the MASNUM simulation is notably stronger. The ACC strength in this LSOMG configuration and the CNRM-CM5.1 model are comparable but the ACC current is underestimated in the CNRM-CM5.1 model [Voldoire et al., 2013].

In order to improve the simulation quality, we increase the vertical resolution from 11 to 22 layers, see Fig. 7.13 (b). The ACC strength has increased by approximately 10 Sv. The stream function has also increased in the North Pacific

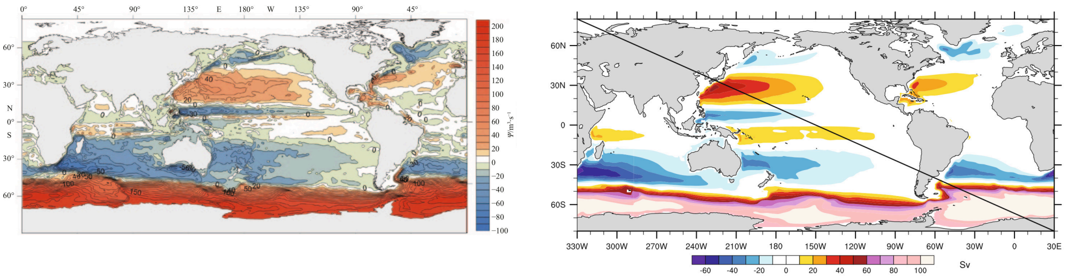

(a) MASNUM

(b) CNRM-CM5.1

Figure 7.12: Barotropic stream functions [Sv] from the MASNUM [Lei, 2014] (a) and CNRM-CM5.1 [Voldoire et al., 2013] (b) models.

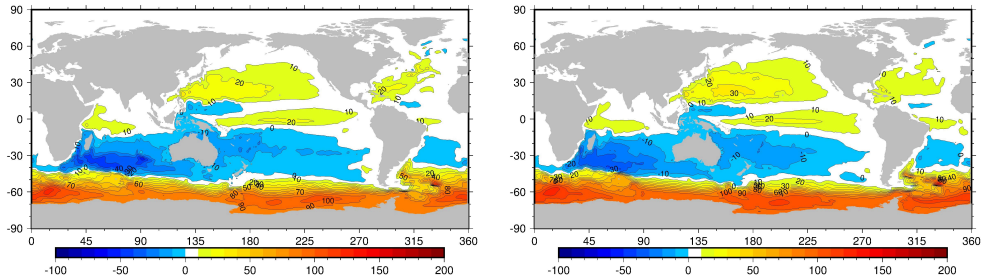

(a) 11 layers, ERA simple forcing

(b) 22 layers, ERA simple forcing

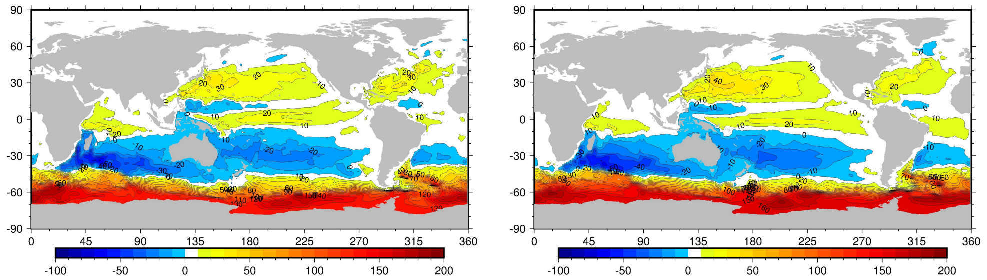

(c) 11 layers, ERA full forcing

(d) 22 layers, ERA full forcing

Figure 7.13: Barotropic stream functions [Sv] from the LSOMG simulations forced by ERA-Interim data.

but also decreased in the North Atlantic and in the Indian Ocean. Overall, the stream function in the 22-layer simulation is not significantly better than in the 11-layer simulation.

In the next step, we improve the model forcing. We replace the simplified forcing by the full forcing. The major improvement is that the full forcing contains the proper heat fluxes computed using the bulk formulas (see Sec. 5.14.6). Additionally, the full forcing varies more rapidly in time since it is represented by daily values rather than monthly values in the simplified forcing. Fig. 7.13 (c) depicts the barotropic stream function from the 11-layer simulation with the full forcing. The improved forcing has a favourable impact on the stream function, all gyres are stronger. The major change is the strengthening of the ACC current. The stream-function maximum has increased from 126 Sv with the simplified forcing to 182 Sv with the full forcing. If we further increase the vertical resolution to 22 layers, the stream-function maximum is virtually the same with 184 Sv but the ACC current has further strengthened in most regions, see Fig. 7.13 (d). The stream function has also increased in the Pacific Ocean. This is favourable in terms of comparison with the MASNUM, CNRM-CM5.1 and GECCO stream (see Fig. 7.8 (g)) functions but also with the altimeter estimate of 42 Sv of Imawaki et al. [2001]. The steam function in the Atlantic Ocean is well shaped but it remains to be slightly underdeveloped. For example, the strength of the Florida current should be around 30 Sv according to Schott et al. [1988].

We also test the sensitivity of presented stream functions on the particular forcing data set. We replace the ERA-Interim forcing with the CORE-II forcing and repeat the simulations. The corresponding stream functions are depicted in Fig. 7.14 (a-d). The CORE-II stream functions in the simulations with the simplified forcing in Fig. 7.14 (a,b) are stronger than the corresponding ERA-Interim stream functions in Fig. 7.13 (a,b). The differences over 10 Sv are present in the North Pacific and Indian Oceans. The stream-function maximum has increased from 126 Sv to 155 Sv in the 11-layer simulations and from 134 Sv to 160 Sv in the 22-layer simulations. This corresponds to the wind-driven barotropic simulations presented in Sec. 7.2. However, in contrast to the ERA-Interim simulations, the CORE-II simulations with the full forcing in Fig. 7.14 (c,d) are not that much different to the CORE-II simulations with the simplified forcing. The major differences are the strengthening of the ACC current. The CORE-II simulations with the full forcing match the corresponding ERA-Interim simulations well. The ERA-Interim stream functions are in slightly better agreement with the MASNUM, CNRM-CM5.1 and GECCO stream functions but the differences are relatively small.

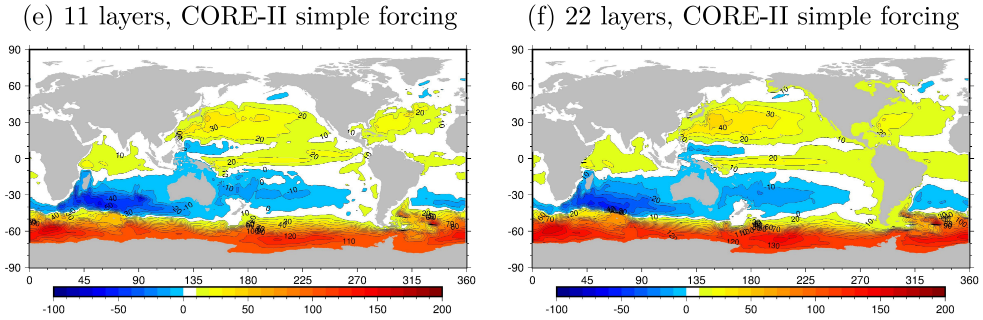
(e) 11 layers, CORE-II simple forcing

(f) 22 layers, CORE-II simple forcing

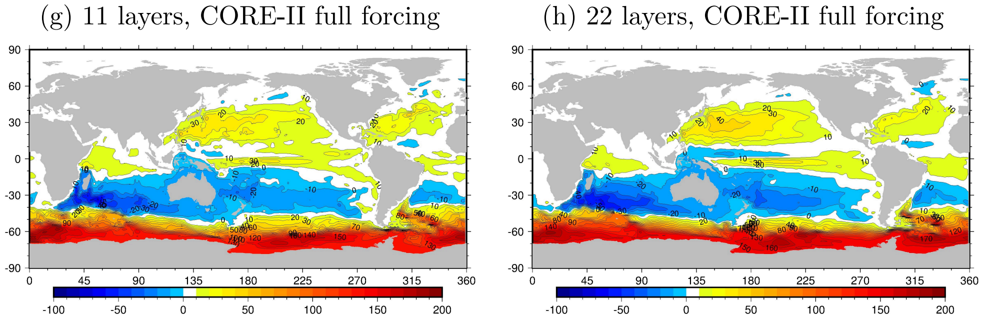
(g) 11 layers, CORE-II full forcing

(h) 22 layers, CORE-II full forcing

Figure 7.14: Barotropic stream functions [Sv] from the LSOMG simulations forced by CORE-II data.

Finally, we inspect the globally averaged temperature and salinity in the presented simulations. Fig. 7.15 (a,c) show the globally averaged temperature in the ERA-Interim and CORE-II simulations, respectively. Fig. 7.15 (b,d) show the globally averaged salinity in the ERA-Interim and CORE-II simulations, respectively. In all panels, the red curves correspond to the simulations with the simplified forcing and the blue curves correspond to the simulations with the full forcing. The solid curves correspond to the 11-layer simulations and the dashed curves correspond to the 22-layer simulations. Overall, there are certain trends in the globally averaged fields. It is probably a model deficiency rather than a real phenomenon. The global temperature is better conserved in the 22-layer simulations than in the 11-layer simulations. Similarly, the simulations with the full forcing conserve temperature better than the simulations with the simplified forcing. The temperature increased by 0.42° and 0.52° in the 11-layer simulations with the simplified ERA-Interim and CORE-II forcings, respectively. That is a relatively large change. On the other hand, the temperature increased by 0.14° and 0.16° in the 22-layer simulations with the full ERA-Interim and CORE-II forcings, respectively. A comparable drifts were present in the simulations from the comparison study of Griffies et al. [2009]. The salinity trends are smaller than the temperature trends which is in accordance with the simulations in Griffies et al. [2009]. The figures are slightly misleading since there is a sharp decrease in salinity at the beginning of each simulation. The decrease is larger in the simulations with the simplified forcing. Consequently, the difference between the final and initial salinity is actually smaller in simulations with simplified forcing. It is almost zero in the ERA-Interim simulation and 0.003 PSU in the CORE-II simulation. There is a decrease in salinity of about 0.025 PSU in both 22-layer simulations with the full forcing. All values are acceptable.

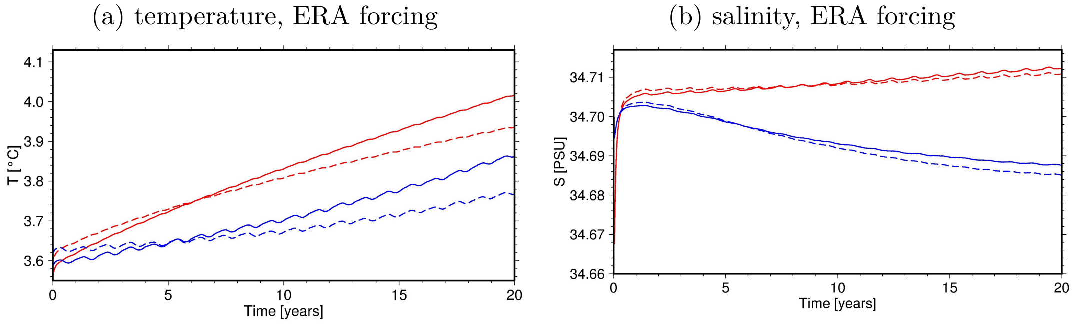
(a) temperature, ERA forcing

(b) salinity, ERA forcing

(c) temperature, CORE-II forcing

(d) salinity, CORE-II forcing

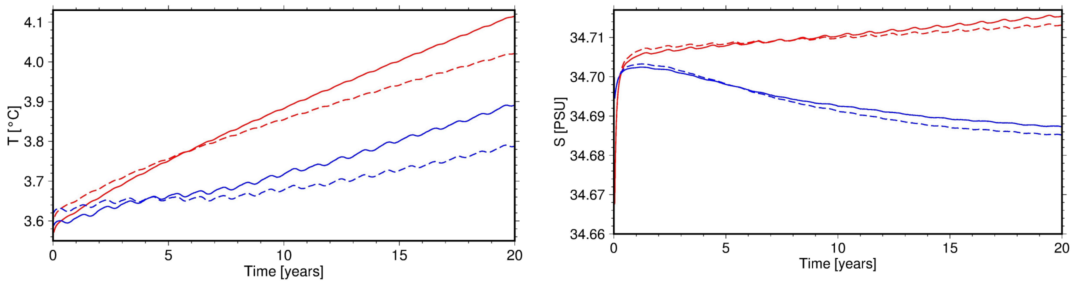

Figure 7.15: Mean temperature and salinity. Results from the 11-layer (solid curves) and 22-layer (dashed curves) simulations with the simplified (red curves) or full (blue curves) forcing.

7.4 Combined wind and tidally driven baroclinic circulation

In this section, we present the results from the concurrent simulations of wind-driven and tidal circulations. We start with the spatial patterns of SSHs and barotropic transports from 1° and 0.25° baroclinic simulations and then we continue with the modeling of tidal dissipation in the 0.25° baroclinic model.

Our simulations are composed of two steps. In the first step, we run the LSOMG model with the ERA-Interim climatological forcing for 20 years. The first step serves as a spin up for the baroclinic model. In the second step, we apply the tidal forcing and run the model for the next 20 days. Tides are included via the linear tidal model with the full lunisolar tidal forcing and both IWD and SAL parameterizations (in the default setup $L = 10$ km, $\beta_s = 0.09$) that improve the quality of tidal simulations, see Secs. 4.4 and 5.10. The simulation is much shorter in the second step than in the first step since the tidal circulation needs a much shorter spin up than the wind-driven circulation; 10 days are sufficient.

Panels (a,c) of Fig. 7.16 depict the wind-driven SSH at the beginning of combined simulations in 1° and 0.25° configurations, respectively. Both SSH amplitudes and SSH pattern are very similar in both solutions. Panels (b) and (d) of Fig. 7.16 depict the SSHs after 20 days in 1° and 0.25° combined simulations, respectively. The SSH pattern is still very similar in both solutions but the differences are more apparent since the 1° is too coarse for the modelling of tides.

(a) 1°, day 0 (b) 1°, day 20

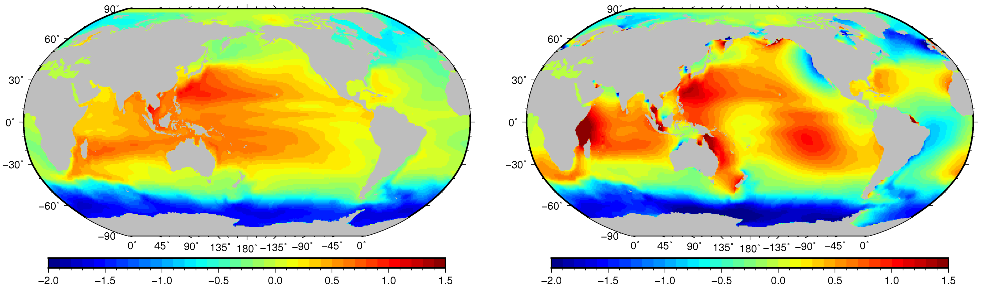

(c) 0.25°, day 0 (d) 0.25°, day 20

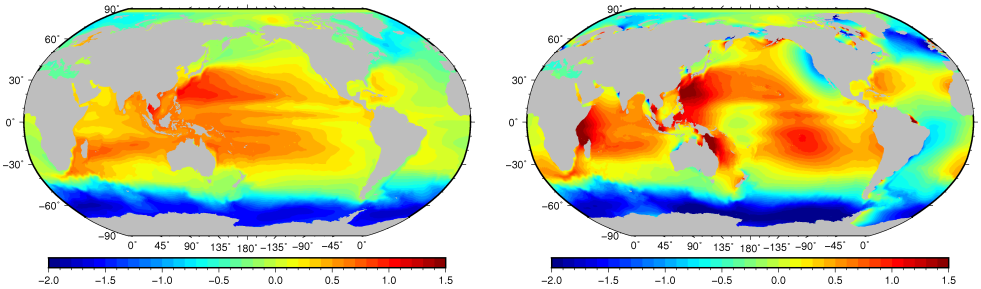

Figure 7.16: SSHs [m] in the combined 1° (a,b) and 0.25° (c,d) LSOMG simulations. Panels (a,c) depict the pure wind-driven SSH at the beginning of combined simulation. Panels (b,d) depict the combined SSH after 20 days of simulations.

The differences between the pure wind-driven and the combined simulations are even more apparent in the barotropic transports, see the zonal barotropic transports in Fig. 7.17. Panels (a,b) and (c,d) correspond to the 1° and 0.25° simulations, respectively. The wind-driven transports at the beginning of the combined simulation are depicted in panels (a,c), the combined transports after 20 days of simulation are shown in panels (b,d). The transports are much stronger and their pattern is significantly altered in the presence of tides. At the same time, the eddy-permitting 0.25° simulation is clearly distinguishable from the eddy-parameterized 1° simulation due to the increased mesoscale activity.

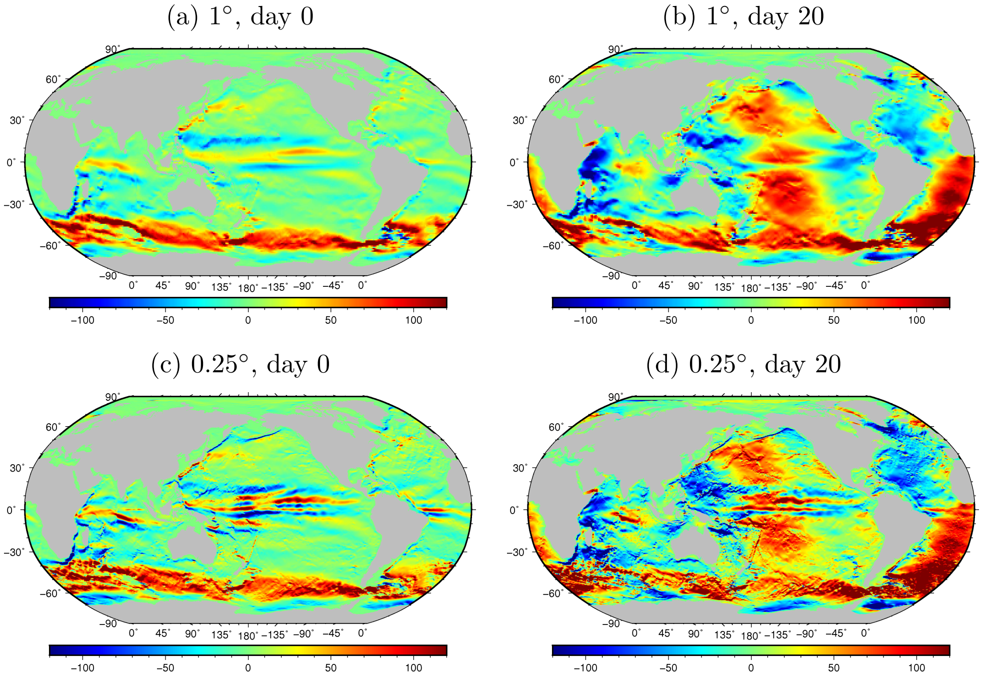
(a) 1°, day 0

(b) 1°, day 20

(c) 0.25°, day 0

(d) 0.25°, day 20

Figure 7.17: Zonal barotropic transports [10^3 m^2/s] in the combined 1° (a,b) and 0.25° (c,d) LSOMG simulations. Panels (a,c) depict the pure wind-driven SSH at the beginning of simulation. Panels (b,d) depict the combined SSH after 20 days of simulations.

The IWD parameterization is needed for a barotropic tidal model since the process is missing there, see Secs. 4.4 and 7.1. In contrast, tidal forcing in the baroclinic model generates the internal waves and their breaking on topography drains energy from barotropic tides. We attempted to model the modification of tidal SSH due to the tidal dissipation. We used the LSOMG model with the 0.25° horizontal resolution and 11 vertical layers. As it was noted in Sec. 5.10, the present-day global high-resolution OGCMs resolve only the low baroclinic modes in spite of using the resolution around 0.1°. We expected to roughly cover the first baroclinic mode in our simulations which means that we can hardly model the entire effect. The purpose of our simulations is to prove the concept of energy loss of barotropic tides in the baroclinic model via tidal dissipation rather than the accurate modelling of internal tides.

Fig. 7.18 shows SSH time curves at the check points 1-5 from Fig. 7.5 in the Pacific Ocean. The red curve is the tidal SSH from the barotropic LSOMG model, the dashed red curve is the TPXO prediction, the blue curve is the total SSH from the baroclinic LSOMG model and the black curve is the total baroclinic SSH minus the tidal barotropic SSH (blue curve minus red curve). If there was no interaction between the tidal and non-tidal flows, the black curve would correspond to the non-tidal SSH. The black curve would be an almost straight line since the non-tidal (wind-driven) SSH changes slowly. This is not the case since there are wiggles on the black curve. The amplitudes of wiggles are small at points 1, 2 and 4 but they are larger at point 5 and they are significant at point 2. The wiggles and barotropic tides are in roughly opposite phases which means that tidal amplitudes are reduced in the baroclinic simulation. We think that this is a correct behaviour which corresponds to the concept of tidal dissipation.

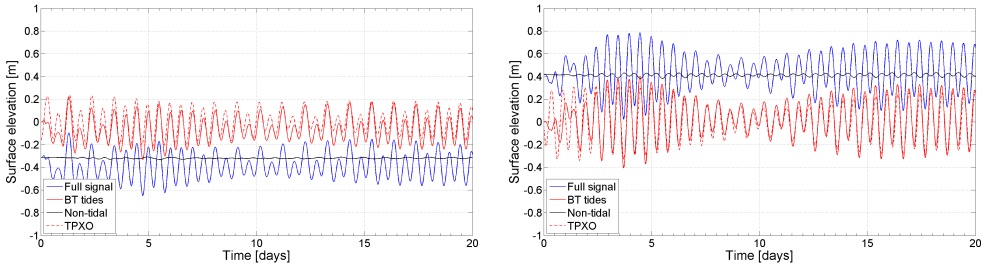

(a) Point 1, (-150.125°, 50.125°)

(b) Point 2, (-150.125°, 25.125°)

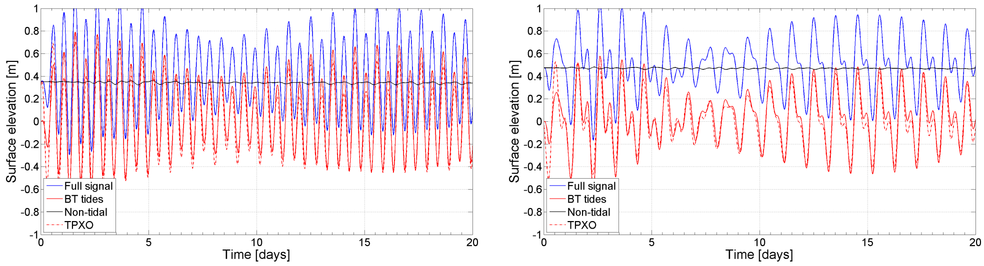

(c) Point 3, (-150.125°, 0.125°)

(d) Point 4, (-150.125°, -25.125°)

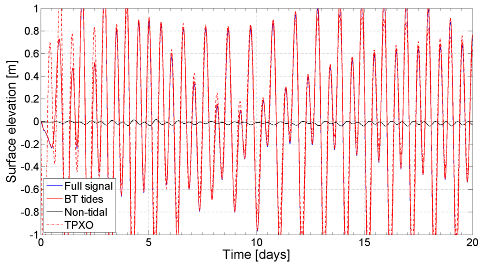

(e) Point 5, (-150.125°, -50.125°)

Figure 7.18: Tidal SSH [m] computed with the barotropic LSOMG model (red) and the TPXO7.2 model (dashed red) together with the SSH [m] computed with the baroclinic LSOMG model forced by wind and tides (blue) at points 1-5 depicted in Fig. 7.5. The “non-tidal” signal (black) is the baroclinic signal minus barotropic tides.

8. Modelling of OIMF: Physical approximations and numerical issues

The following study is a result of cooperation with our colleagues from GFZ, DIAS, Freie Universität Berlin and CIRES. We are concerned with modelling the OIMF due to the wind- and buoyancy-driven ocean circulation. Originally, the paper summarized our results of a benchmark study which compared the performance of different magnetic induction solvers. However, the submitted paper was rejected. One of major reviewers' objections was insufficient diversity of participating solvers. We thus modified our study and focused more on the methods used rather than the comparison of solvers. In particular, we inspected how various commonly used approximations affect the accuracy of modelled OIMF. The modified study was published as a paper [Šachl et al., 2019]. The tidally-driven OIMF is considered separately in a companion paper of Velímský et al. [2018].

In [Šachl et al., 2019], we present the results from the UTSM solver that was operated by the GFZ group. The performance of our UTSM solver is equal. It was simply not meaningful to present the results from both solvers since the paper's focus has changed and it was not a benchmark study any longer. Similarly, we used the ocean circulation calculated by the OMCT model that was operated by the GFZ group. We could have used the LSOMG model instead. The decision was made to prefer OMCT since the model has already been used for the OIMF studies and so it is known in the community.

8.1 Introduction

Interest in OIMF has been raised by the pioneering works of Cox et al. [1970], Sanford [1971], Sanford [1982] and Larsen and Sanford [1985]. The first attempts to numerically model the OIMF were by Stephenson and Bryan [1992] and Flosadóttir et al. [1997], who used ocean currents from the Geophysical Fluid Dynamics Laboratory (GFDL) ocean model, and Tyler et al. [1997], who used The Ocean and isoPYCnal coordinates [OPYC, Oberhuber, 1993b,c] ocean currents. Vivier et al. [2004] attempted quantifying the magnitude of the OIMF forced by electric currents from the Océan PArallélisé [OPA, Madec et al., 1998], Hamburg Ocean Primitive Equation [HOPE, Marsland et al., 2003] and Estimating the Circulation and Climate of the Ocean [ECCO, Marshall et al., 1997] models at the CHAMP satellite altitude of 400 km. Manoj et al. [2006] studied the magnetic field induced by ocean electric currents from the ECCO and Ocean Circulation and Climate Advanced Modelling project [OCCAM, Webb et al., 1998] models both at the sea level and the Swarm lower satellite-pair altitude of 430 km. All studies found a small (≈ 1 nT) signal at satellite height with the Antarctic Circumpolar Current (ACC) producing the largest signal because of its substantial water transport (it is the largest ocean current on Earth) and proximity to the geomagnetic pole.

The most consistent approach for calculating the OIMF is based on full 3-D electromagnetic (EM) modelling where electric conductivity and ocean electric currents vary with lateral coordinates as well as with depth. However, the above mentioned papers follow an alternative approach which relies on vertically integrating the ocean electric conductivity and electric currents. The effect of both quantities' vertical stratification is thus lost. The ocean model is forced by fluxes of momentum due to wind stress, heat, and fresh water [Large and Yeager, 2004, 2009]. All of these fluxes enter the ocean via its surface. The transport and diffusive processes are then responsible for the distribution of surface fluxes into the whole ocean volume. Consequently, ocean circulation is not 2-D, it has a complex vertical structure. This is in contrast to tidal circulation which is predominantly barotropic due to low variations of the tidal force in the vertical direction within the ocean. Velímský et al. [2019] demonstrated the importance of the toroidal magnetic field generated by vertically stratified flows, as well as the galvanic coupling between the ocean and mantle.

A commonly used modelling simplification is the neglect of both EM self-induction in the ocean and mutual induction with the underlying mantle. This effect can be safely neglected when the horizontal spatial scale is much smaller than the penetration depth. In the case of seasonal variations, the penetration depth is in the range of thousands of kilometers, and hence, OIMF variations on comparable scales will be affected. Additionally, global ocean circulation is a nonlinear dynamic system with turbulent features such as eddies and jets. Self-induction in the oceans will be important for the mesoscale induced OIMF (i.e., spatial scales below 10 km, and time scales from days to weeks), provided both the ocean model and magnetic field model have sufficient spatio-temporal resolution to resolve these features.

Practical motivation for our study comes from the ongoing geomagnetic field measuring satellite mission, Swarm. Swarm has provided new knowledge about Earth and its electromagnetic environment [Olsen et al., 2016], however, one of the declared objectives of the mission – detecting magnetic signatures due to ocean circulation [Friis-Christensen et al., 2006] – has not yet been achieved. Such an accomplishment is a challenging task. Firstly, the OIMF is rather small, up to 2 nT at the satellite height, and it is overlaid by larger contributions ($\approx 50,000$ nT) from the main magnetic field and the magnetic fields of ionosphere and magnetosphere origin. Secondly, unlike the tidal magnetic signature, there is no single dominant frequency for ocean circulation and the process is instead relatively slow with a typical time scale of weeks. The ocean-induced magnetic field may thus be erroneously attributed to the lithospheric field which is stationary in time and has comparable magnitudes. Nonetheless, if the ocean-induced contribution is one day reliably isolated from satellite magnetic data, such satellite measurements could constrain ocean dynamics by coupling models of ocean circulation and ocean-induced magnetic fields [Irrgang et al., 2017]. Accurate and efficient forward (and inverse) modelling is necessary for this breakthrough.

This study aims to fill the gap in literature by inspecting the impact of galvanic coupling using unimodal and bimodal solutions, vertical stratification of ocean flow and electrical conductivity, self-induction and horizontal resolution on the numerically predicted OIMF. The unimodal solution considers only the poloidal magnetic field mode and there is no galvanic coupling between the ocean and the underlying mantle. The bimodal solution contains both the toroidal and poloidal magnetic field modes. The toroidal magnetic mode is generated by poloidal electric currents which galvanically couple the ocean with the mantle.

8.2 Modelling of OIMF

The OIMF $\mathbf{B}(\mathbf{r},t)$ obeys the quasi-static Maxwell equations supplemented by Ohm's law,

$$\nabla \cdot \mathbf{B} = 0, \tag{8.1}$$

$$\nabla \times \mathbf{B} = \mu_0 \left(\mathbf{j} + \mathbf{j}^{\mathrm{imp}}\right), \tag{8.2}$$

$$\nabla \times \mathbf{E} = -\frac{\partial \mathbf{B}}{\partial t}, \tag{8.3}$$

$$\mathbf{j} = \sigma \mathbf{E}, \tag{8.4}$$

where $\mathbf{E}(\mathbf{r},t)$ is the electric field, $\mathbf{j}(\mathbf{r},t)$ is the electric current density, $\mathbf{j}^{\mathrm{imp}}(\mathbf{r},t)$ is the imposed electric current density, $\sigma(\mathbf{r})$ is the electric conductivity, μ_0 is the permeability of vacuum, $\mathbf{r}$ is the radius vector and t is time.

Alternatively, we can combine Eqs. (8.2)-(8.4) into the second-order EM induction equation for the OIMF,

$$\nabla \times \left(\frac{1}{\sigma} \nabla \times \mathbf{B}\right) + \mu_0 \frac{\partial \mathbf{B}}{\partial t} = \mu_0 \nabla \times \mathbf{E}^{\mathrm{imp}}, \tag{8.5}$$

where $\mathbf{E}^{\mathrm{imp}}(\mathbf{r},t)$ is the imposed electric field that is linked to the imposed electric current density through Ohm's law.

Note that Eqs. (8.1), (8.2) and (8.5) implicitly assume that the main geomagnetic field $\mathbf{B}_M(\mathbf{r},t)$ is a potential field and its temporal variations are much slower than the temporal variations of the OIMF.

We compute the imposed electric field or electric currents from the ocean velocity $\mathbf{u}(\mathbf{r},t)$ and the main geomagnetic field, following:

$$\mathbf{E}^{\mathrm{imp}} = \mathbf{j}^{\mathrm{imp}}/\sigma = \mathbf{u} \times \mathbf{B}_M, \tag{8.6}$$

where we assume that the main geomagnetic field is much stronger than the OIMF.

In this paper, we use three EM induction solvers: the ElmgTD, X3DG and UTSM. All of them were thoroughly tested; ElmgTD and X3DG took part in the benchmark study of Kelbert et al. [2014], and were used to model OIMF in the past [Manoj et al., 2006, Irrgang et al., 2016a, Velímský et al., 2019]. The main characteristics of individual solvers are summarized in Table 8.1. Each solver uses a different modelling technique – including different spatial discretizations and different ways to propagate dependent variables in time. Additionally, each solver was developed independently; the authors' teams do not overlap. Thus, we believe that our conclusions are not biased by choices specific to one particular solver. In the following text we briefly describe the ElmgTD, X3DG and UTSM solvers.

	ElmgTD	X3DG	UTSM
Physics	full	full	UTSA
Ocean layer	3-D	3-D	2-D thin sheet
Sub-ocean layer	cond/insul	cond/insul	insul
Domain	time	freq	time
Lateral discretization	SH	PWC	FD+SH
Radial discretization	FE	PWC	-

Table 8.1: Quick comparison of the EM induction solvers used in the study. UTSA = unimodal thin-sheet approximation of Tyler et al. [1997] and Vivier et al. [2004] with insulating mantle and core, SH = spherical harmonics, FE = finite elements, PWC = piece-wise constant representation, FD = finite differences.

8.2.1 ElmgTD solver

ElmgTD [Velímský and Martinec, 2005, Velímský, 2013] solves the EM induction equation (8.5) using a time-domain, spherical harmonic-finite element approach.

The recent version of ElmgTD employs the Crank-Nicolson time integration scheme, enforces the divergence-free condition on the magnetic field by means of Lagrange-multiplier constraint [Martinec, 1999], and allows for the presence of internal forcing as specified by the right-hand side of equation (8.5). The magnetic field is parameterized by vector spherical harmonic functions in the angular directions. This approach inherently separates the poloidal and toroidal magnetic field modes, and thus can include or suppress energy exchange between the two modes through lateral conductivity variations, as needed. The disadvantage of spherical harmonic functions is that they are susceptible to the Gibbs phenomenon if the expanded function contains discontinuities. The high contrast of electrical conductivity between oceans and continents may thus cause ringing in the computed OIMF. The spatial extension of ringing can be reduced by increasing the spatial resolution. The solver can also solve the stationary problem by simply setting the reciprocal time step to zero. 3-D functions are used for the electrical conductivity and the internal forcing. The 2-D approach can be simulated by specifying a layer of small but finite thickness. However, full 3-D spatial operators are preserved even in this case.

Both ocean velocities and electrical conductivity values are located at the same grid points. For fast and accurate transformations between the spatial and spherical-harmonic domains, we utilize Gauss-Legendre quadrature nodes in colatitude; however, this can introduce small differences due to grid interpolation. The numerical resolution of the method is controlled by the choice of spherical harmonic truncation degree $j_{\max}$ and the number of layers. The implicit formulation in time leads to a large, block-tridiagonal matrix that needs to be solved at each time step. For lateral resolution up to $j_{\max} \approx 80$ a direct solver based on the factorization of individual blocks is employed. For larger resolutions, the memory requirements do not allow storage of the full matrix, and an iterative matrix-free solver must be used in each time step employing a sparse preconditioner based on an a-priori 1-D conductivity model.

8.2.2 X3DG solver

X3DG [Kuvshinov, 2008] solves the Maxwell equations (8.1)-(8.3) in the frequency domain using the integral equation (IE) approach. Within this approach, the electric/magnetic fields are expressed as a sum of electric/magnetic fields within a background media that has 1-D conductivity and the volume integral of the conductivity anomaly with respect to the background media multiplied by the Green's tensor and the electric field. This system of integral equations is solved iteratively. The construction and calculation of Green's tensors are discussed in detail in Kuvshinov and Semenov [2012]. Note that the actual implementation of the IE approach in X3DG is based on the so-called contracting integral equation [CIE, Pankratov et al., 1995, Singer, 1995]. The advantage of using the CIE is that the condition number of the CIE system matrix depends only on the square root of maximum lateral conductivity contrast in the model [Pankratov and Kuvshinov, 2016], and thus does not require preconditioning the matrix.

The X3DG solver computes frequency-domain electric and magnetic fields in spherical Earth models that have 3-D electrical conductivity distribution. Alternatively, infinitesimal sheets with prescribed 2-D conductance can also be used, leading to reduced dimensionality of the corresponding Green tensors. The model allows for excitation in the form of spatially distributed extraneous electric currents either above or within the Earth. The fields can be computed at any point of physical space. The excitation electric current's frequency can be small but must be non-zero. The stationary regime is mimicked with a sufficiently small frequency; in this study, we use 10^{-6} years^{-1}. The solver can account for complex-valued (i.e., for modeling displacement currents and polarization effects), and tensor-valued (i.e., for modeling the effect of anisotropy) electrical conductivities. The X3DG solution contains both the poloidal and the toroidal modes but their separation is not as straightforward as in ElmgTD.

All electromagnetic fields and 3-D electric conductivity distributions are parameterized within X3DG by piece-wise constant functions in both the angular and radial directions. The grid is assumed to be longitudinally equidistant. Ocean velocities and electrical conductivity values are located at the same grid points. X3DG's computational load (i.e., memory and time of execution) depends linearly on the longitudinal dimension, and quadratically on the latitudinal dimension and on the number of 3-D layers in the model.

8.2.3 UTSM solver

The UTSM solver is based on the unimodal thin-sheet approximation of Tyler et al. [1997] and Vivier et al. [2004]. In this approximation, the 3-D EM induction equation is simplified. The self-induction term is neglected and the equations are vertically integrated. The 3-D problem is thus reduced into a 2-D problem for a thin sheet. Moreover the thin sheet is assumed to be surrounded by an insulator on the top and bottom, i.e., both outer space and also the Earth's mantle and core are treated as insulators.

Technically, the 3-D EM induction equation is replaced by the simplified 2-D equation for the stream function $\Psi(\vartheta, \lambda, t)$ at colatitude ϑ, longitude λ and time

t,

$$\frac{1}{a^2}\nabla_\Omega \cdot \left(\frac{1}{\Sigma}\nabla_\Omega \Psi\right) = -\left[\nabla \times \left(\frac{\mathbf{J}^{\mathrm{imp}}}{\Sigma}\right)\right] \cdot \mathbf{e}_r, \tag{8.7}$$

where a is the Earth's radius, ∇_Ω is the angular part of the nabla operator, $\mathbf{e}_r$ is the unit radius vector, $\Sigma(\vartheta, \lambda)$ is the vertically integrated conductivity and $\mathbf{J}^{\mathrm{imp}}(\vartheta, \lambda, t)$ is the vertically integrated imposed electric current density,

$$\Sigma(\vartheta, \lambda) = \int_{-D}^{\eta(\vartheta,\lambda)} \sigma(\mathbf{r}) dr, \tag{8.8}$$

$$\mathbf{J}^{\mathrm{imp}}(\vartheta, \lambda) = \int_{-D}^{\eta(\vartheta,\lambda)} \mathbf{j}^{\mathrm{imp}}(\mathbf{r}, t) dr, \tag{8.9}$$

in which $\eta(\vartheta, \lambda)$ is the sea surface height and D is the thickness of the ocean layer. Notice that the radial diffusion term is missing in the stream-function equation. The term on the left-hand side of Eq. (8.7) resembles the first term on the left-hand side of Eq. (8.5). However, the term in Eq. (8.5) contains 3-D spatial operators while the operators in Eq. (8.7) are only 2-D.

Equation (8.7) is discretized by the finite-difference method on a C-grid [Arakawa and Lamb, 1977] and its solution is expanded into spherical harmonics. The spherical-harmonic coefficients of Ψ are converted to the internal-field coefficients of the magnetic field using a simple scaling relation.

8.3 Modelling framework

We consider four test cases labeled A-D. We describe our electrical conductivity and ocean circulation models first, discuss how forcing is applied to our EM induction solvers, and finally present the considered test cases.

8.3.1 Conductivity model

We consider the 3-D conductivity, σ, from the sea surface down to the bottom of the ocean layer. Conductivity is determined using the bathymetry $H(\vartheta, \lambda)$,

$$\sigma(r, \vartheta, \lambda) = \begin{cases} \sigma_{\mathrm{ocean}} & \text{for } r \geq a - H(\vartheta, \lambda), \\ \sigma_{\mathrm{crust}} & \text{for } a - D \leq r < a - H(\vartheta, \lambda), \end{cases} \tag{8.10}$$

where σ_{ocean} and σ_{crust} are the nominal conductivities of sea water and crust. In this study, we use the values,

$$\sigma_{\mathrm{ocean}} = 3.2 \text{ S/m}, \qquad a = 6371 \text{ km}, \tag{8.11}$$

$$\sigma_{\mathrm{crust}} = 10^{-3} \text{ S/m}, \qquad h = 6 \text{ km}. \tag{8.12}$$

The bathymetry is reused from the ocean circulation model OMCT, as introduced below. This simplified conductivity model is easy to implement in all used approaches, and preserves the dominant effect of laterally varying bathymetry. Note that Velímský et al. [2019] used a salinity and temperature-dependent conductivity with the ElmgTD solver, and the implementation of the recent WOA

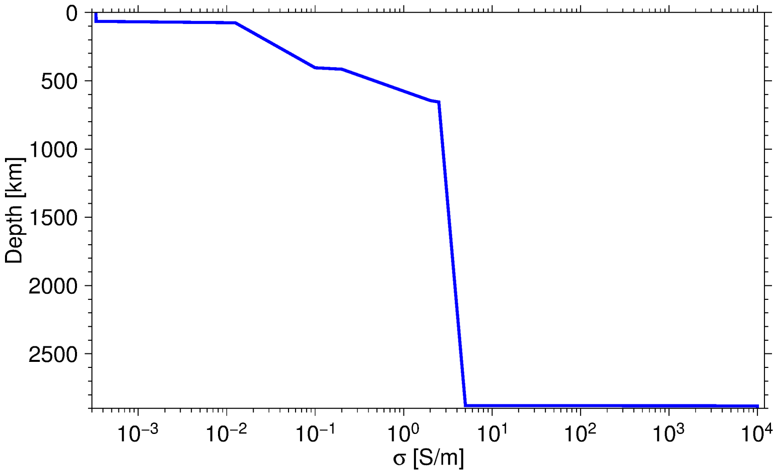

Figure 8.1: 1-D electrical conductivity profile from the Earth's surface down to the core-mantle boundary (2880 km depth) based on the study by Grayver et al. [2017].

conductivity from collocated measurements [Tyler et al., 2017] is underway for future studies. In Case A, we consider both the mantle and the core to be perfect insulators. In the other cases, the mantle conductivity is given by a 1-D profile from Grayver et al. [2017], and the core is considered to be highly conductive (10^4 S/m). The mantle conductivity profile is shown in Fig. 8.1.

8.3.2 Ocean circulation model

We simulate the general ocean circulation using the Ocean Model for Circulation and Tides [OMCT, Thomas et al., 2001]. This model depicts the major ocean currents [Dobslaw et al., 2013], and has already been used for several studies on EM induction in the ocean [Irrgang et al., 2016a,b, Saynisch et al., 2016]. The corresponding ocean velocities $\mathbf{u}$ build the source for ocean circulation's electric currents and the motional induction.

The OMCT is a baroclinic general ocean circulation model that incorporates non-linear balance equations for momentum, conservation equations for heat and salinity, and the continuity equation. The hydrostatic and the Boussinesq approximations are applied. Artificial mass changes due to the Boussinesq approximation are corrected as proposed by Greatbatch [1994].

We use the configuration in which OMCT is set up on a C-grid [Arakawa and Lamb, 1977] with a horizontal resolution of 1°, 20 layers in the vertical, and a time step of 20 minutes [Dobslaw et al., 2013]. Ocean tides are not considered. OMCT's bathymetry is based on ETOPO1 [Amante, 2009] with local adjustments to keep the natural bathymetric current barriers. We force the ocean model with 3-hourly reanalysis products from the European Centre for Medium-Range Weather Forecasts [ECMWF, Dee et al., 2011], which encompass wind stress, precipitation, evaporation, and surface pressure. As an example, we show the OMCT barotropic transports on 2007/01/01 in Fig. 8.2.

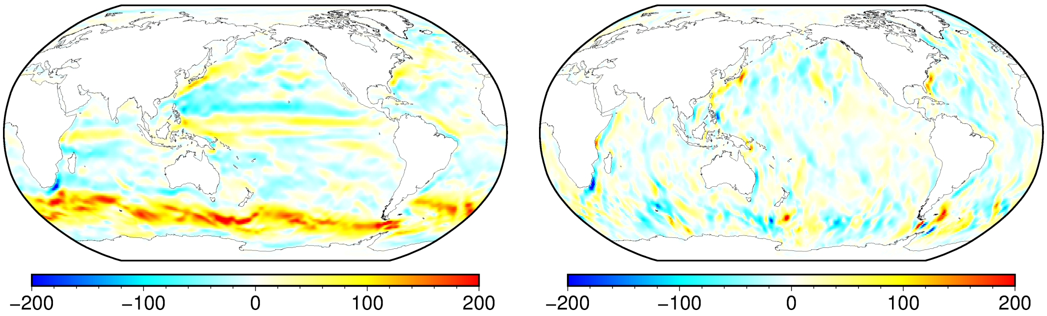

Figure 8.2: Zonal (left) and meridional (right) components of barotropic transports [10^3 m^2/s] on 2007/01/01 from the OMCT model. Zonal and meridional components are positive eastwards and northwards, respectively.

8.3.3 Forcing

We compute the forcing using the OMCT velocities $\mathbf{u}$ and the 12th generation of the International Geomagnetic Reference Field [IGRF–12, Thébault et al., 2015] $\mathbf{B}_M$. OMCT velocities are bilinearly interpolated from the staggered Arakawa C-grid to the grids required respectively by ElmgTD and X3DG. Since the velocity field is primarily large scale, this interpolation is not critical for our study. The UTSM solver is build on the same grid as OMCT and thus no interpolation is needed.

The OMCT velocities are provided in 20 layers using partial bottom cells. This method allows the thickness of bottom grid cells to differ from the respective global layer thickness which leads to better representation of bathymetry. For EM induction modelling, we reduce the vertical resolution by merging the OMCT layers into a single layer in Cases A-B, and into five layers in Cases C-D. We use a thickness-weighted averaging scheme that preserves the total transports.

For stationary Cases A-C, we prescribe the forcing using the OMCT velocities on 2007/01/01. For Case D, we use a time series of forcing spanning the years 2004-2007, with a temporal discretization step of one day. The first three years are a spin-up period to suppress the transient effect of initial conditions on the time-domain ElmgTD. Based on our experience, the spin-up is sufficiently long if initial conditions are taken in the form of the static solution.

8.3.4 Test cases

Our study's four test cases are summarized in Table 8.2. Complexity increases from Case A to Case D. In the simplest Case A, the underlying mantle is treated as a perfect insulator and the ocean has no vertical structure. In ElmgTD and X3DG, we use a single oceanic layer of finite thickness. The UTSM solver uses the equivalent thin-sheet setup. The test case is stationary and calculates a single snapshot corresponding to 2007/01/01. The solution is also unimodal, containing only the poloidal magnetic field.

In Case B, we include the 1-D mantle conductivity model and consider a bimodal solution, the toroidal magnetic field is included. Thus, the ocean and mantle are galvanically coupled through vertical electric currents. The UTSM is not used anymore, as the physical model is beyond its approximation. The

	A	B	C	D
Mantle + core	insulator	1-D	1-D	1-D
Galvanic coupling	no	yes	yes	yes
Ocean layers	1	1	5	5
Self-induction	no	no	no	yes
EM solvers used	ElmgTD, X3DG, UTSM	ElmgTD, X3DG	ElmgTD, X3DG	ElmgTD

Table 8.2: Test cases considered in the study.

inclusion of galvanic coupling is very cheap for both the ElmgTD and X3DG solvers. The additional cost results in extension of runtime by a few percents.

In Case C, we add the vertical stratification of imposed currents and ocean conductivity, using five layers with lower boundaries at depths of 87.5 m, 187.5 m, 500 m, 1700 m and 6000 m. Runtimes of both the X3DG and ElmgTD solvers scale up from approximately one hour for Cases A and B to about one day for Case C.

Finally, Case D implements self-induction and we calculate the full time series throughout the year 2007. X3DG could theoretically solve this case by using a Fourier-transformed excitation in the frequency domain, but this is beyond the scope of our study since the OIMF's spectrum is wide ranged and the X3DG computation would be expensive. Given the cross validation of ElmgTD and X3DG on the static cases, we find it sufficient to use only ElmgTD to evaluate the effect of self-induction.

Our EM solvers are based on different numerical techniques and thus the resolution used is not exactly the same. We use 1° resolution in X3DG and UTSM. In ElmgTD, we set up the maximum spherical-harmonic degree to $j_{\max} = 480$ in Cases A-C in order to minimize the effect of ringing. In Case D, the solution evolves in time which forced us to decrease the resolution to $j_{\max} = 80$ in order to enable the use of the ElmgTD direct solver.

8.3.5 Comparison methods

We assess the performance of individual solutions by three methods. The first one is comparing the X, Y and Z components of the OIMF at the Earth's surface and at the depth of 6 km. The purpose is to visually inspect the key spatial features of the OIMF.

The second method is to compare the power spectrum of OIMF, computed according to eq. (21) in Maus [2008]. We calculate the power spectra at the Earth's surface and at a typical satellite altitude of 400 km.

Finally, for Case D we inspect the time evolution of power P_j on the first four spherical-harmonic degrees.

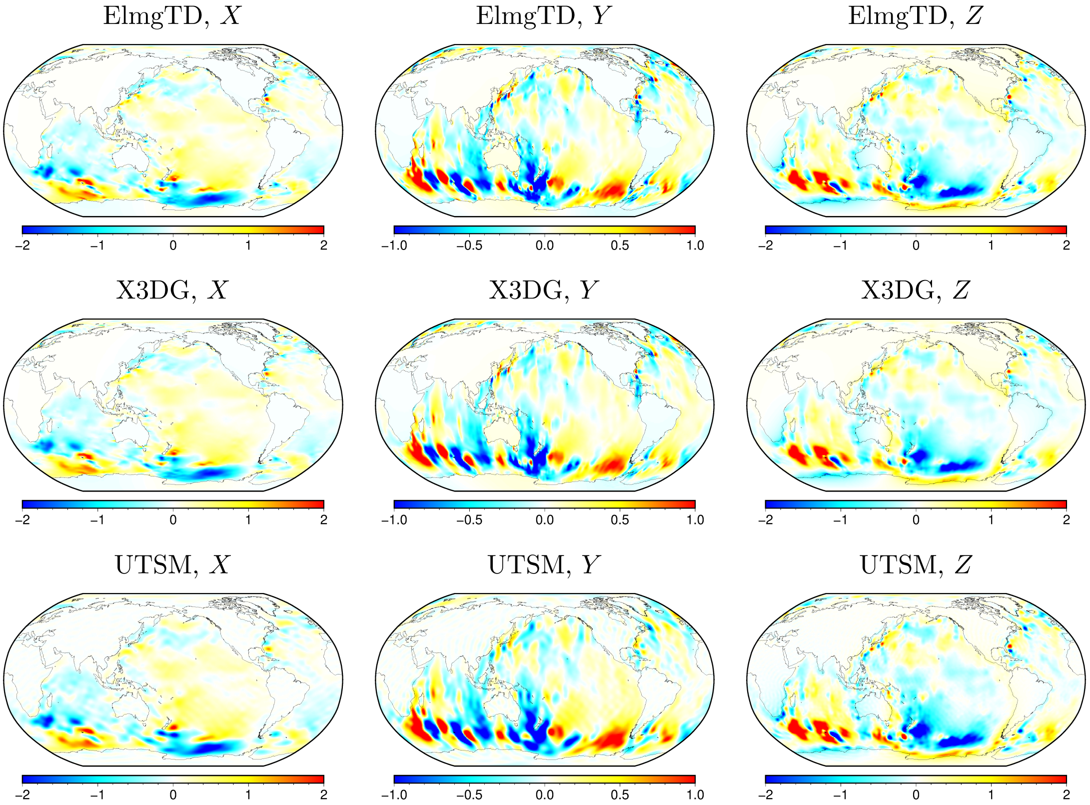

Figure 8.3: Comparison of ElmgTD, X3DG, and UTSM solvers. The X, Y and Z components of the ocean-induced magnetic fields [nT] in Case A at the Earth's surface on 2007/01/01 computed using the ElmgTD, X3DG, and UTSM solvers.

8.4 Results

8.4.1 Case A

We depict the computed OIMFs at the Earth's surface in Fig. 8.3. Regardless of the solver used, the largest amplitudes of the OIMF are located in the region of the Antarctic Circumpolar Current (ACC), which agrees with other studies [e.g. Manoj et al., 2006]. The Z component is somewhat stronger than the X and Y components, although it does not dominate the other two. The minimum values of the X, Y, and Z components in the ElmgTD solution are -2.14 nT, -4.13 nT and -5.87 nT, respectively. The maximum values of the X, Y, and Z components in the ElmgTD solution are 2.68 nT, 2.28 nT and 4.56 nT, respectively. Considering the structure of the OIMF, the Y component is the most complex. Its minima and maxima frequently alternate, especially in the ACC region of the Indian Ocean between Africa and Australia. The Z component is less complicated; it is predominantly positive in the Indian Ocean and predominantly negative in the South Pacific.

There is a good agreement between the ElmgTD and X3DG solutions. The large-scale patterns agree well, however, some discrepancies exist in the smaller scale structures. In accordance, the power spectra depicted in Fig. 8.4 match for the lower degrees but disagree for the higher degrees. The level of discrepancy also depends on the lateral resolution since ElmgTD and X3DG solvers have different

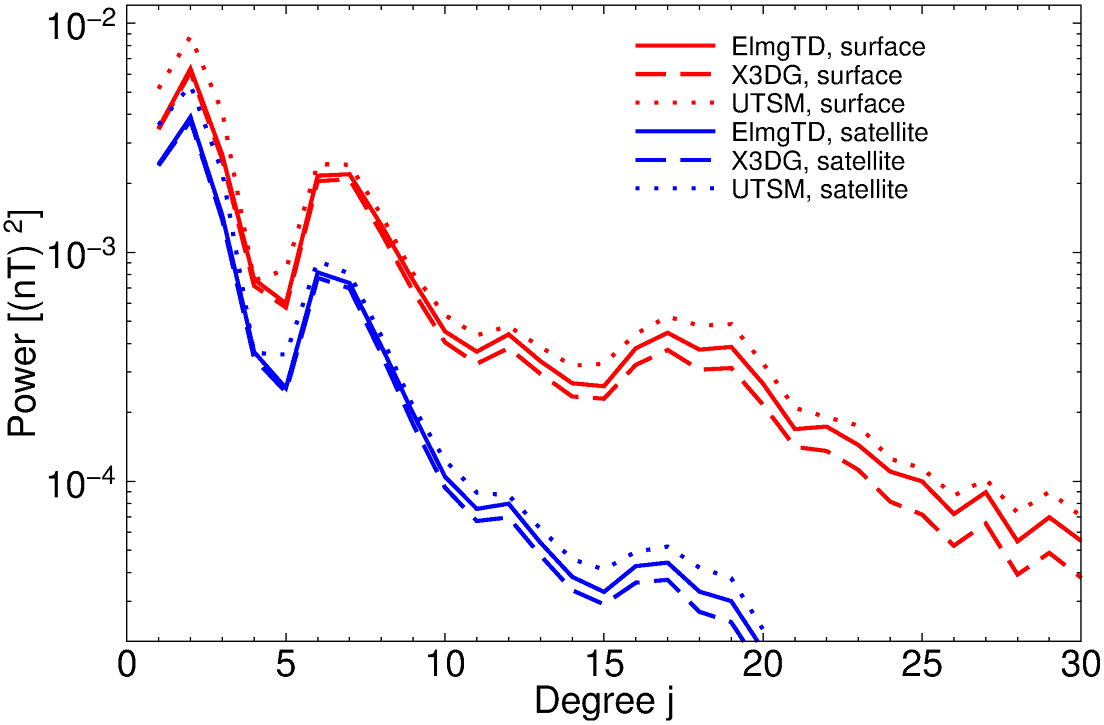

Figure 8.4: Power spectra of ocean-induced magnetic fields at the Earth's surface and at satellite height (400 km altitude) computed using the ElmgTD, X3DG, and UTSM solvers in Case A.

sensitivity to the resolution. If we decrease the lateral resolution from 1° to 2° in X3DG and from $j_{\max} = 480$ to $j_{\max} = 80$ in ElmgTD, the ElmgTD power spectrum slightly changes but the X3DG power spectrum drops significantly – only the lowest degrees are minimally unaffected (see Fig. 8.5). We attribute the discrepancies and the varying sensitivity to the different numerical methods used. The CIE method used in the X3DG solver allows for a more local representation of the magnetic field than does the spherical harmonics used in the ElmgTD solver. However, the spherical harmonics' behavior is not necessarily a disadvantage as long as the main modelling task is to compute the global solution with its large-scale features. Spherical harmonics are well suited for global studies but if fine-scale features are of paramount importance, the X3DG solver would be the better choice.

The UTSM solution agrees qualitatively with the ElmgTD and X3DG solutions. Nonetheless, a more detailed inspection reveals differences in the spatial patterns of its OIMF: its amplitudes are larger and the UTSM spectrum (shown in Fig. 8.4) is above the ElmgTD and X3DG spectra for all the considered degrees. These differences are likely due to the unimodal thin-sheet approximation's assumption that each of the OIMF's X and Y components have equal magnitude, but opposite sign, just above and below the thin ocean layer. This assumption is correct for an infinitely thin sheet surrounded by an insulator, but it is incorrect for a thin spherical shell. One can show that the spherical harmonic coefficients of the horizontal magnetic field in the insulators just above and under the thin spherical shell are related by a $-j/(j+1)$ ratio. Hence, substantial errors are introduced for the large scale magnetic fields, while the small-scale features are well represented by the UTSM. Currently, this problem can be addressed by an

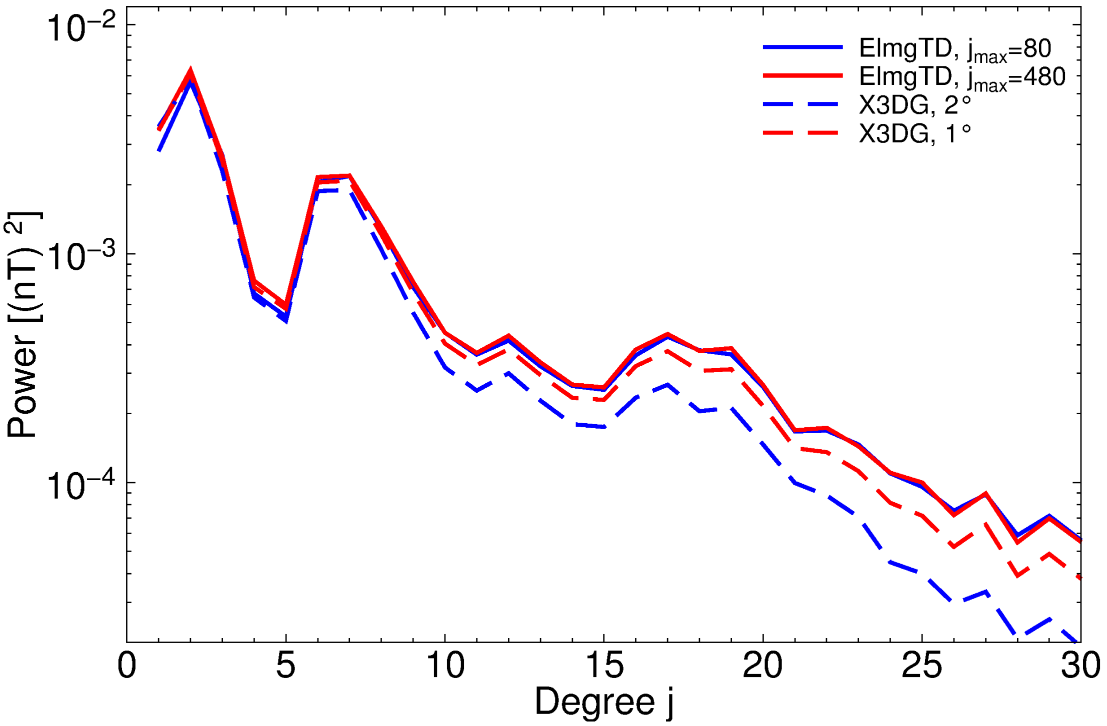

Figure 8.5: Effect of lateral resolution. Power spectra of ocean-induced magnetic fields at the Earth's surface in Case A computed with the ElmgTD solver using $j_{\max} = 80$ and $j_{\max} = 480$ and X3DG solver using 1° and 2° lateral resolutions.

improved method, such as that given in eq. (2.42) of Tyler et al. [2017].

In order to complete our analysis of Case A, we depict the power spectra and spatial patterns of the OIMF at the satellite level in Figs. 8.4 and 8.6, respectively. The OIMF in the atmosphere decreases with r according to $r^{-(j+2)}$ and the power for degree j decreases as $r^{-(2j+4)}$. Thus, short wavelengths are damped more rapidly than long wavelengths. Consequently, the spectrum of OIMF at satellite altitude decays faster and its spatial patterns are much smoother than spatial patterns computed at the Earth's surface (compare Figs. 8.3 and 8.6).

In the remaining test cases, we only discuss the OIMF computed by the ElmgTD solver. Nonetheless, we still compare the ElmgTD and X3DG spectra to ensure that both solvers respond similarly.

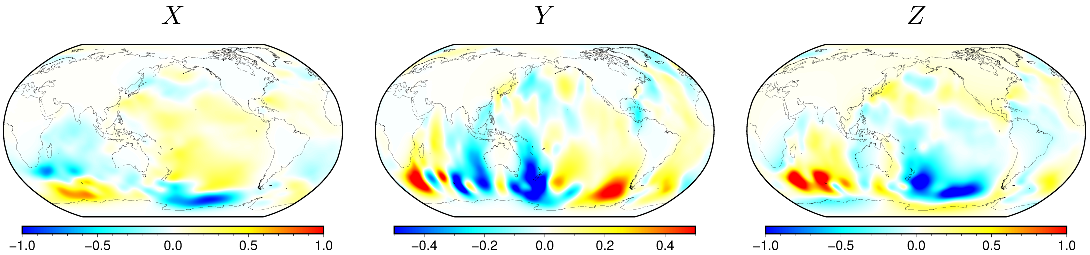

Figure 8.6: The X, Y, and Z components of the ocean-induced magnetic field [nT] in Case A computed using the ElmgTD solver at satellite height (400 km altitude).

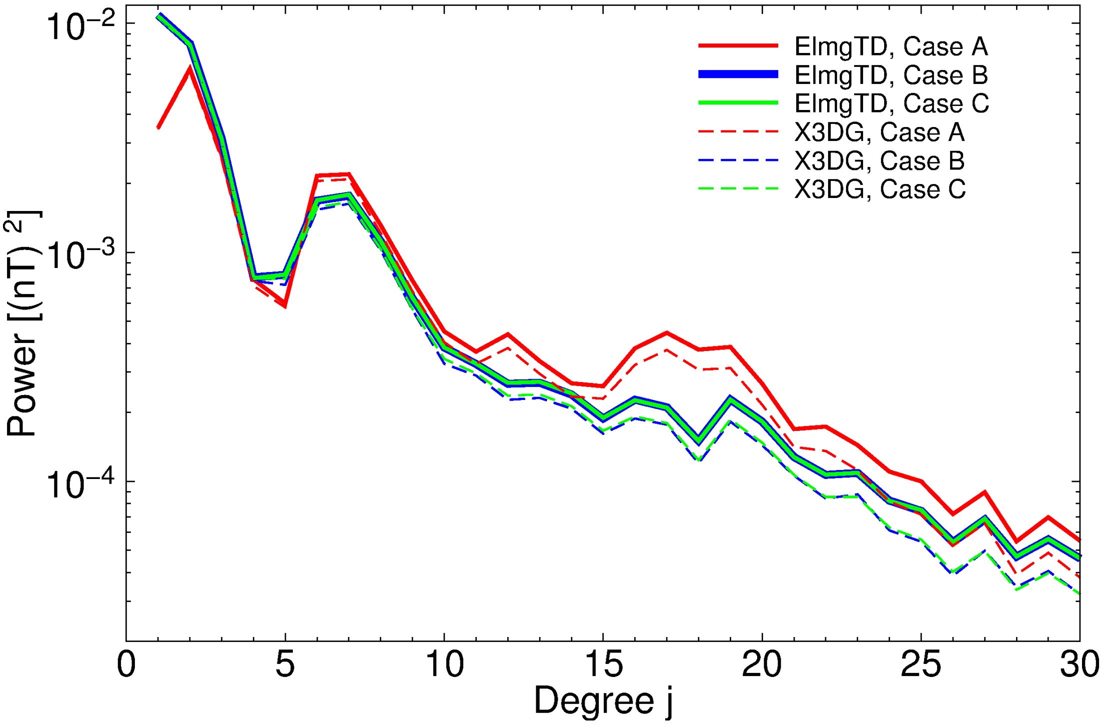

Figure 8.7: Power spectra of the ocean-induced magnetic fields computed using the ElmgTD solver (solid line) and the X3DG solver (dashed line) in Cases A-C at the Earth's surface.

8.4.2 Case B

Figure 8.8 depicts the differences between Case B's and Case A's OIMFs computed at the Earth's surface using the ElmgTD solver. There are significant changes in the OIMF due to the added effect of galvanic coupling. Although the toroidal mode's amplitude is equal to zero at the Earth's surface, it is nonzero inside the Earth [Velímský et al., 2019] and there is coupling between the toroidal and poloidal field components. The toroidal mode is converted to the poloidal mode by the lateral electrical conductivity variations. Consequently, the toroidal mode affects the poloidal mode at the Earth's surface even though the toroidal mode itself has zero amplitude there.

Based on Figure 8.8, the OIMF in Case B is stronger in some regions than the OIMF in Case A, but the opposite is the case in other regions. The power spectra (compared in Fig. 8.7) are more instructive. Indeed, Case B's OIMF has less power for degrees higher than five, but it has more power for degrees one to five. Degree one is especially stronger; its power has increased from 1.8 $\times 10^{-2}$ $(\mathrm{nT})^2$ to 1.1 $\times 10^{-1}$ $(\mathrm{nT})^2$. The shift of the power spectra is consistent in both ElmgTD and X3DG solutions (compare the full and dashed red lines with the full and dashed blue lines in Fig. 8.7). A similar power spectra shift was theoretically predicted by Tyler [2017] and reported by Velímský et al. [2018] for the magnetic field driven by ocean tides. These studies predicted the critical cross-over degree would be six rather than five.

Figure 8.9 shows the differences between OIMFs from the same cases as in Fig. 8.8 but at the bottom of the surface layer (i.e., 6 km deep) rather than at the Earth's surface. The sensitivity of individual OIMF components to galvanic

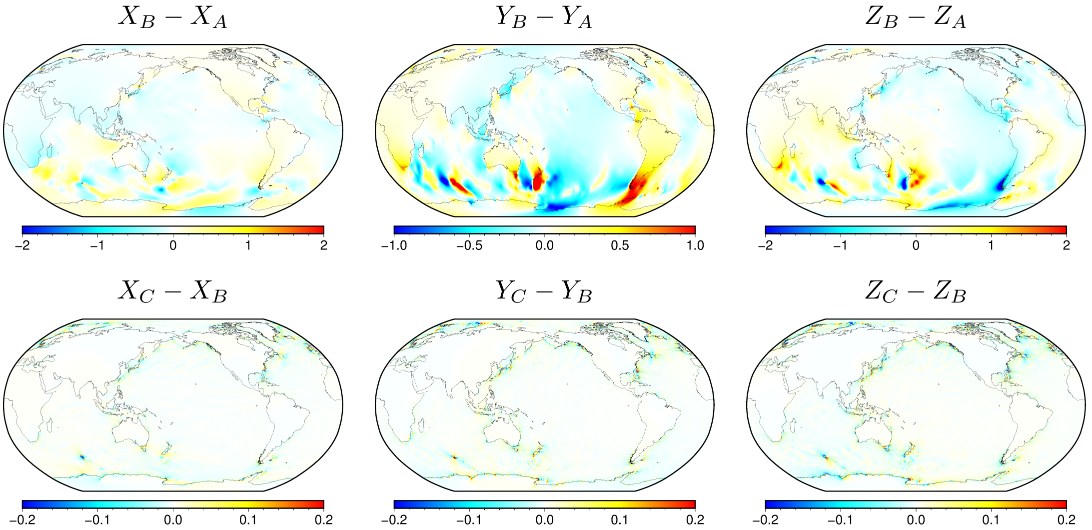

Figure 8.8: Effect of galvanic coupling (Case B) and vertical stratification (Case C) on the OIMF at the Earth's surface. The top row shows the differences [nT] between Cases B and A in the X, Y, and Z components of the ocean-induced magnetic fields computed using the ElmgTD solver. The bottom row shows the differences between the OIMFs in Cases C and B.

coupling differs – the Z component is the least sensitive, whereas the Y component is the most sensitive. Indeed, the Y component's amplitudes have significantly increased due to the toroidal mode; the Y component plot's color scale maximum value is now 10x larger. Besides changing the magnitude of the Y component, the spatial pattern has also changed. At this depth, Case B's Y component is positive for the entire ACC region – Case A's spatially alternating positive and negative amplitude regions are no longer visible.

8.4.3 Case C

The vertical stratification of flow and conductivity has much less impact on the OIMF than the inclusion of galvanic coupling. Case B's and Case C's power spectra are virtually identical for both ElmgTD and X3DG solutions (see Fig. 8.7). In fact, the effect of vertical stratification is negligible for most of the globe, however, there are certain regions where vertical stratification matters – for example, coastal areas around New Zealand, north of the Bahama islands, and south of Japan, see Figs 8.8 and 8.9. These areas have differences in the surface Z component up to 1.1 nT. Thus, for comparing modelled OIMF to measurement from coastal stations, using the full 3-D approach should provide a more accurate comparison.

8.4.4 Case D

Figure 8.10 shows the effect of self-induction on the spectral power of low degrees (1-4). The red curve represents the time evolution of spectral power computed without the self-induction term (which corresponds to Case C's configuration), while the blue curve represents the time evolution of spectral power with the

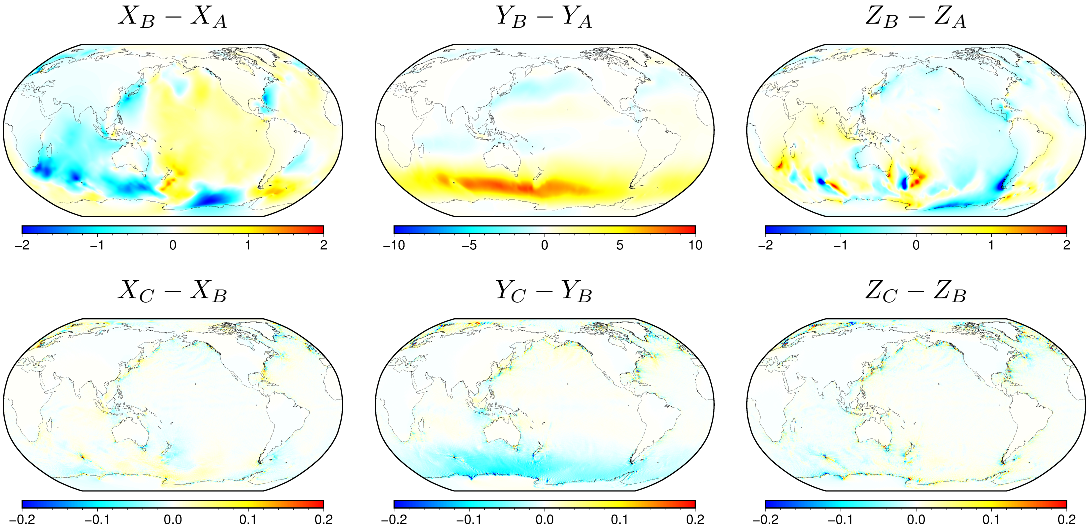

Figure 8.9: Effect of galvanic coupling (Case B) and vertical stratification (Case C) on the OIMF at 6 km depth. The top row shows the differences [nT] between Cases B and A in the X, Y, and Z components of the ocean-induced magnetic fields computed using the ElmgTD solver. The bottom row shows the differences between OIMFs in Cases C and B.

self-induction term included. The red curve is obviously oscillating more rapidly than the blue curve. The difference between the two spectra is largest for the lowest degree $j = 1$; the difference is much weaker for $j = 4$ and it further diminishes for higher degrees (not shown). Otherwise the mean evolution trajectories of both solutions are similar, suggesting that the self-induction term damps the solution's fast temporal oscillations, smoothing the time evolution. Additionally, the solution computed without the self-induction term follows the forcing instantly, while the solution that contains the self-induction term is delayed in time. Cross-correlating the spherical harmonic coefficients from the two solutions, we determined that the time delay is not the same for all coefficients. Coefficients $(j = 1, m = -1)$, $(2, -2)$, $(2, 2)$, $(3, -3)$, $(3, 0)$, $(3, 1)$ and $(5, -3)$ show the largest delay of 5 hours. The general tendency is that the delay decreases with the increasing spherical harmonic coefficient degree, e.g., the largest delay among the $j = 10$ coefficients is 2 hours.

The error caused by the neglection of the self-induction term is evidently time-dependent. We compare the OIMFs computed with and without the self-induction term for time t=1 day and t=128 days. The latter time instant corresponds to the largest difference in spectral power on degree one, i.e., $\Delta P_1 = |(P_1)_D - (P_1)_C| = 4.5 \times 10^{-3}$ $(\mathrm{nT})^2$. Figure 8.11 shows the OIMF differences between the Case D and Case C solutions both using $j_{\max} = 80$. Their spatial pattern is predominantly large-scale which corresponds to the above mentioned fact that the spectral powers most differ for the lowest degrees. The amplitudes of the differences do not exceed 10 % of the signal strengths and there are no specific regions in which the differences are more pronounced.

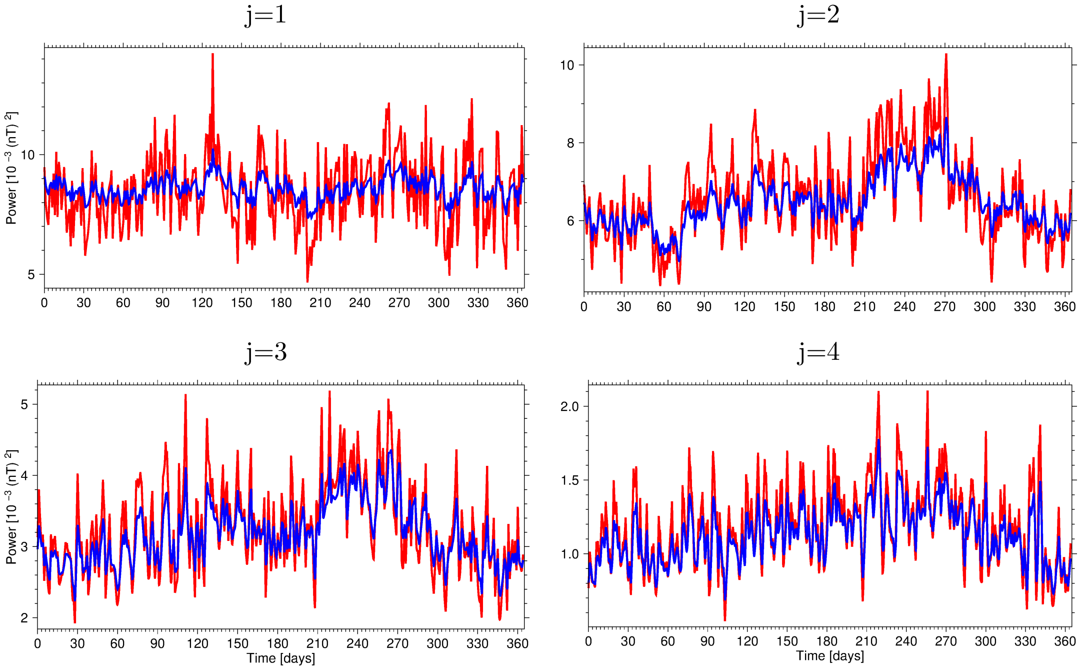

Figure 8.10: Effect of self-induction on the OIMF power spectrum. Time evolution of the ocean-induced magnetic field's power spectra computed using the ElmgTD solver with (blue) and without (red) self-induction throughout the year 2007.

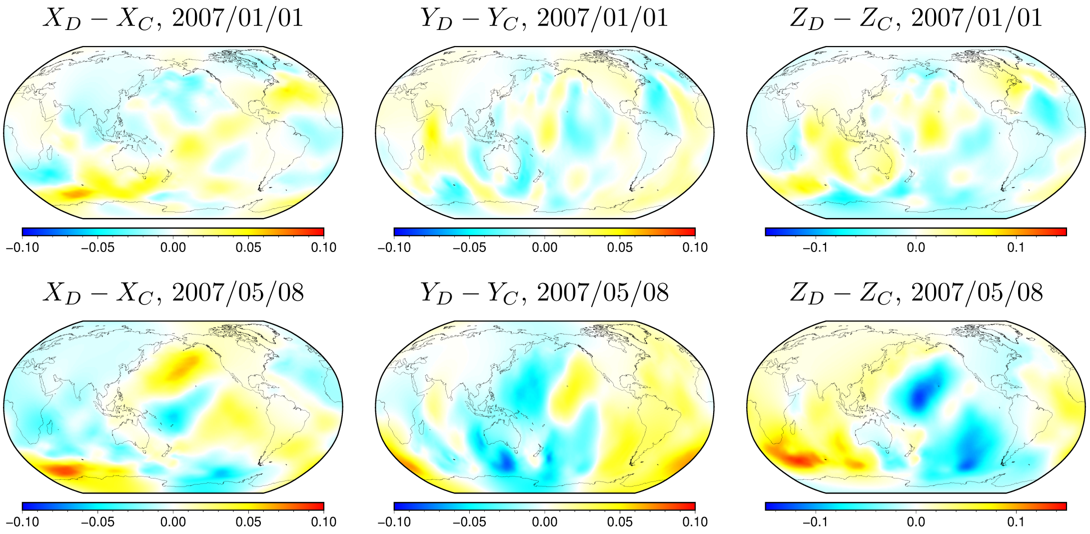

Figure 8.11: Effect of self-induction on the OIMF at the Earth's surface. Differences [nT] between the ocean-induced magnetic fields at the Earth's surface computed using the ElmgTD solver with (Case D) and without (Case C) self-induction on 2007/01/01 and 2007/05/08.

Conclusion

This thesis combines two different scientific fields: the oceanography and magnetohydrodynamics. The first one was a real challenge for us. The numerical modelling of ocean circulation is a well established in many seaside countries around the world. There exist whole oceanographic centers around the world: Alfred Wegener Institute (AWI) in Bremerhaven in Germany, GEOMAR Helmholtz Centre for Ocean Research Kiel in Germany, European Centre for Medium Range Weather Forecasts (ECMWF) in Reading in UK, National Oceanography Centre Southampton (NOCS) in UK, Laboratoire d'Océanographie et du Climate (LOCEAN) in Paris in France, Laboratoire de Physique des Océans (LPO) in Brest in France and Royal Netherlands Institute of Sea Research (NIOZ) in Netherlands are several examples of European centres. There is no such center in the Czech Republic and there is no senior scientist working in oceanography either. Of course, not every oceanographer works in physical oceanography; many oceanographers perform measurements or they work in different branches of oceanography such as marine biogeochemistry or marine ecology. Additionally, according to our experience, the majority of ocean modellers simply use OGCMs as tools to study certain physical processes in the ocean rather than actively develop these models. Nevertheless, OGCMs remain to be results of colaborative work of research teams rather than individuals (which is more common in geophysics), see the coauthors listed in the manuals of NEMO [Madec, 2012], POP [Smith et al., 2010] or MITgcm [Adcroft et al., 2014] models. It is complicated if not impossible to compete these scientific teams and their OGCMs. Despite that, we have developed our OGCM rather than used an already existing one. We call it LSOMG. The LSOMG model is not revolutionary, it is a z-coordinate baroclinic model based on Boussinesq and hydrostatic approximations, but it is a decent work horse for the modelling of OIMF, which is the second part of this PhD. Moreover, the possibility to build the model from scratch was a valuable experience. It was a chance for us to study the numerical cores of state-of-art OGCMs and also to implement the numerical schemes on our own rather than take the model as a black box. The truth is that we have learned a lot during the development of LSOMG.

Part I of the thesis serves as an introduction for a reader who is new to the topic. Parts II and III refer to the project itself. Part II describes the LSOMG model. It is not a manual since we neither explain parameters in the control module and CPP switches in the shell scripts nor give examples how to run the model. It is meant to be a detailed description of the LSOMG numerical core. We build the model according to our requirements specified in Sec. 3.1. The base for the LSOMG model was the LSG model but they have almost nothing in common at present, see Table 3.1.

The LSOMG model is 3-D baroclinic model but it can also be used as a simplified 2-D barotropic model LSOMG-BT, see Chapter 4. The shallow water equation are discretized using the finite difference method. The LSOMG-BT model supports the forward-backward (or its modification predictor-corrector scheme), generalized forward-backward, modified Crank-Nicolson and Euler implicit time stepping schemes and Arakawa grids B, C and E. However, not every combination of a time stepping scheme and a computational grid is available, see Table 6.1. The tidal parameterizations for the realistic tidal simulations are provided only for the forward-backward and generalized forward-backward schemes on the C-grid. The LSOMG-BT model can be used for tidal simulations since it is equiped with the tidal forcing and the parameterizations of SAL and IWD according to Eqs. (4.34), (4.43) and (4.44), respectively. LSOMG-BT can also be forced by surface wind stress (4.24) although baroclinic LSOMG is better suited for the wind-driven simulations.

The baroclinic part of the LSOMG model is addressed in Chapter 5 . As already mentioned, LSOMG is a z-coordinate model. The primitive equations in hydrostatic and Boussinesq approximations are expressed in orthogonal cuvilinear coordinates using metric coefficients according to Sec. 5.1. The LSOMG model uses the split-explicit time stepping scheme which is depicted in Fig. 5.2. The barotropic part of the model uses exactly the same time step as the LSOMG-BT model while the time step of the baroclinic part is much (typically 60 times) longer. The extension of baroclinic time step decreases the computational demands of the model and the small barotropic time step provides fine resolution in time for tidal simulations. The state equation (5.43) of McDougall et al. [2003] with the values of coefficients from Jackett et al. [2006] is implemented. It is accurate, it benefits from the representation in potential temperature (no conversions from potential to in-situ temperature) and it is not overly complicated (25 coefficients). The friction force for the incompressible fluid, transversely isotropic with respect to the vertical coordinate is used. It is expressed in curvilinear coordinates according to Murray and Reason [2001] in LSOMG and Einšpigel and Martinec [2015] in LSOMG-BT, see Sec. 5.6 and the discussion in Appendix B. The horizontal friction is discretized explicitly in time. The recommended temporal discretization for the vertical friction is implicit to ensure numerical stability but the explicit discretization is also available. The horizontal viscosity is the Smagorinsky viscosity [Smagorinsky, 1963, 1993, Griffies and Hallberg, 2000] under CFL, grid-Reynolds and Munk-layer criteria with a prescribed minimum viscosity, see Sec. 5.6.2. The advantage of the Smagorinsky viscosity is that it is flow dependent. It keeps low if the flow is weak and it increases if the flow becomes vigorous. The vertical viscosity is either constant or it is set according to the Richardson-number based parameterization of Pacanowski and Philander [1981] given by Eq. (5.59). The LSOMG model offers three advection schemes with flux limiters that are explained in Sec. 5.7. We prefer the Lax-Wendroff scheme of Smith et al. [2010] but the Lax-Wendroff scheme with Superbee and Koren/van Leer/MC flux limiters and the third order direct space time scheme are also available. All schemes use multidimensional splitting method of Adcroft et al. [2014] which enables to use 1-D flux limiters in the 3-D model. The primitive equations are discretized on the Arakawa grid C. We discussed in Sec. 2.1 that C-grid has certain favourable properties such as good representation of gravity waves or placement of variables for advection schemes. On the other hand, the Coriolis is a C-grid weak spot and it needs special treatment which is explained in Sec. 5.8. LSOMG offers four spatial-discretization schemes that conserve energy, vorticity or both. The Adams-Bashforth extrapolation of the third-order is used in the temporal discretization. The grid-scale noise is suppressed using the divergence-damping method. Tidal parameterizations are the same as in the

LSOMG-BT model. There is, however, a problem with the separation of tidal and non-tidal flows since tidal parameterizations are acting on tidal not total flow. We follow Sakamoto et al. [2013] and use two (rather than one) barotropic systems: the wind-driven and tidally-driven systems. The scheme is illustrated in Fig. 5.8. We discussed the problem of standard spherical-coordinate grid in the North Pole region in Sec. 2.2. Sec. 5.11 provides technical details about dipolar and tripolar grids which solve the Pole problem and their implementation in LSOMG. Sec. 5.12 explains a simple model of melting and freezing which is used to model sea ice. The LSOMG model is parallelized using the MPI standard. A standard regular domain decomposition is used. We discuss more sophisticated algorithms in Sec. 5.13 but their benefit is uncertain. Finally, we discuss input data for our simulations in Sec. 5.14. The bathymetry is taken from GEBCO or ETOPO1 data, temperature and salinity data are taken from the World Ocean Atlas 2013 and climatological data such as wind speed are mainly from the ERA-Interim database. We discuss how data are processed to get them on the LSOMG computational grid. We implemented and tested four different methods to compute net heat flux. The coldest to the warmest fluxes are the fluxes of Brunnabend [2010], Kondo [1975], Large and Yeager [2009] and Kara et al. [2002]. We do not recommend the method of Brunnabend [2010] since it produces too cold climatological net heat flux. The methods differ in the bulk transfer coefficients but we demonstrated on latent heat fluxes that smaller but non-negligible amount of differences is caused by different data formulas.

Part III presents our modelling results. In Chapter 6, we performed several numerical tests to check the model performance. We designed one tsunami and two tidal numerical tests for ocean tidal models. We calculated six solutions using different time stepping schemes and/or computational grids and compared them. We recommend not to use the Euler implicit time stepping scheme for tidal simulations. The choice of computational grid matters. B/E-grid configurations suffer from small (several percents) energy leakage due to the biharmonic smoothing of SSH. C-grid configurations do not have these problems. Different boundary conditions on grids B/E and C can have strong impact on the solution especially in the realistic configurations with extensive coastlines. See Sec. 6.1.7 for more details.

We calculated the flow in the Munk problem. It is an idealized wind-driven simulation in which the flow is not stratified, the wind-stress is purely zonal with a smooth meridional cosine profile and the basin is large with a simple rectangular shape. We compare the numerical solution with the analytic solution of Munk. Both solutions are in good agreement in mid latitudes where the analytic solution is valid. The western boundary currents are well developed.

We tested the implementation of the vertical friction force, in particular its implementation using the implicit time stepping scheme. We modeled the Ekman spiral in the Ekman layer using simplified model equations. The numerical solution is uniform in the zonal direction, the angle between the direction of wind and surface current is 45° and the Ekman layer is shallower in higher latitudes which is all in agreement with the analytic solution.

The last numerical test evaluates the performance of advection schemes. The initial tracer distribution is advected with a given constant velocity. Both horizontal and vertical advections are tested. The computational grid is equidistant in the horizontal advection but non-equidistant in the vertical advection. As expected, the Quick advection scheme nicely advects the smooth Gaussian bell but it produces artificial oscillations in the vicinity of jump in the box function due to the absence of flux limiters. All other schemes are free of artificial oscillations. In contrast to the Quick advection scheme, the Lax-Wendroff scheme with the Superbee flux limiter accurately advects the box function but it somewhat distorts the Gaussian function, it is making a box out of it. The Lax-Wendroff scheme of Smith et al. [2010] has average performance. The advected box function is not as sharp as it should be and the Gaussian function is smooth but also slightly distorted.

The results from realistic simulations are presented in Chapter 7. We show results from tidal barotropic simulations in Sec. 7.1, wind-driven barotropic simulations Sec. 7.2, wind-driven baroclinic simulations in Sec. 7.3 and combined wind- and tidally-driven simulations Sec. 7.4.

Fig. 7.2 demonstrates the importance of IWD and SAL parameterizations for tidal simulations. The RSS computed by the comparison with the TPXO8-1 solution according to Eq. (7.1) decreased from 32.62 cm to 13.32 cm (linear free surface) and 12.17 cm (nonlinear free surface) if IWD and SAL were used. We have chosen the default IWD and SAL setups according to the values used by other authors but both can be tuned to decrease RSS. Fig. 7.3 shows the sensitivity of RSS on the strength of IWD and SAL. The best setup with IWD increased by factor 1.5 and $\beta_s = 0.11$ has RSS= 10.67 cm which corresponds to the improvement of RSS by 12%. Figs. 7.4 and 7.6 complement the sensitivity study by showing how spatial SSH patterns and SSH time curves at particular points respond to increased IWD and SAL.

LSOMG-BT can be forced not only by tides but also by atmospheric winds. Figs. 7.8 and 7.9 depict barotropic stream functions from eight LSOMG-BT simulations forced by the steady wind-driven stress. The simulations differ in the bathymetry (realistic or flat) and horizontal viscosity (2×10^4 m/s^2 or 2×10^5 m/s^2). Simulations are forced by ERA-Interim data in Fig. 7.8 and by CORE-II data in Fig. 7.9. The simulations with the realistic bathymetry suffer from a serious problem, the ACC current is virtually missing and the other currents in the Southern hemisphere are also affected. On the other hand, if bathymetry is flat, the barotropic stream function in the Southern hemisphere improves but the ACC current is overly strong. The same issues were reported by [Frisius et al., 2009] using the barotropic SOM model. The LSOMG-BT simulations with higher viscosity are in better agreement with the SOM simulations but the simulations with lower viscosity are in better agreement with the GECCO reanalysis. LSOMG-BT stream functions are stronger if we use the CORE-II instead of ERA-Interim forcing. The stronger stream function matches both SOM simulations and GECCO reanalysis better.

The barotropic stream functions from the baroclinic LSOMG simulations forced by ERA-Interim data are shown in Fig. 7.13. The model configurations used in the simulations differ in the vertical resolution and the forcing. The vertical resolution is either 11 or 22 layers. The forcing is either simplified or full. The simplified forcing contains the climatological data and the heat fluxes are represented by the strong relaxation towards the prescribed surface teperature distribution. The full forcing contains daily data and the heat fluxes are computed from the bulk formulas discussed in Sec. 5.14.6. If the simplified forcing is used, the stream function is globally weaker than it should be. If the full forcing is used, the stream function becomes globally stronger. This is especially pronounced in the ACC regions where the stream-function maximum has increased from 126 Sv to 182 Sv. The increase in the vertical resolution has a favourable effect on the circulation in the Pacific Ocean and it also further strengthens the ACC current. We also run the simulations under the CORE-II forcing. First, we came to the same conclusion as in Sec. 7.2, the CORE-II simulations with the simplified forcing are notably stronger than the corresponding ERA-Interim simulations. Second, both data sets produce comparable circulations if the full forcing is applied. We prefer the ERA-Interim stream function over the CORE-II stream function. It matches the stream functions from other models and the GECCO reanalysis slightly better. We further demonstrated that the LSOMG model with the full forcing conserves both temperature and salinity within the range which is comparable with other OGCMs. We also presented the SSH and velocities vertically integrated over the upper 1000 m in Figs. 7.10 and 7.11, respectively. The comparison with other models and data products was favourable.

Finally, Figs. 7.16 and 7.17 depict SSHs and zonal barotropic transports from the combined wind- and tidally-driven baroclinic simulations, respectively. The results from 1° eddy-parameterized and 0.25° eddy-permitting simulations are shown. Both figures demonstrate that LSOMG is capable of simulations with the combined forcing. For example, the barotropic transports from the combined simulations contain the wind-driven ACC current mixed together with the large-scale tidal signal. Both 0.25° and 1° simulations are generally in agreement, although there is a significantly larger mesoscale activity in the 0.25° simulation which was expected. Fig. 7.18 shows that tidal dissipation is working in the 0.25° combined LSOMG simulations as it decreases amplitudes of tidal SSH, see the wiggles on the black curve. However, the effect is relatively small which is probably caused by the 0.25° resolution which is insufficient for the modelling of internal tides.

In the last Sec. 8, we demonstrated the importance of galvanic coupling for the modelling of wind-driven OIMF. Its omission affects power spectrum in Fig. 8.7 (compare Cases A and B), OIMF at the surface in Fig. 8.8 and OIMF at 6 km depth in Fig. 8.9 where especially Y component is affected. The self-induction is less important but it also matters. Fig. 8.10 shows that it affects lower spherical harmonic degrees (up to 40% of the spectral power on degree one) by damping sudden changes in the OIMF which results in a smoother evolution in time. Locally, the OIMF differences around 0.1 nT in the X and Y components and 0.15 nT in the Z component may appear. One layer in the vertical is sufficient for global studies of OIMF at the surface or at satellite height but the local studies should consider a higher vertical resolution. We do not recommend to use unimodal thin sheet approximation of Tyler et al. [1997] and Vivier et al. [2004] since it neglects both galvanic coupling and self-induction. We recommend to use the horizontal resolution of at least 1°.

The attached paper Velímský et al. [2019] further focuses on the toroidal magnetic field. We used a more realistic ocean electrical conductivity which was computed from the temperature and salinity and thus it was spatially variable rather than constant. We also used a higher vertical resolution; 11 instead of

5 layers. We found the maximum of 15 nT in the Y component of the OIMF in approximately 1800 m depth. At the surface, the toroidal field is zero but it affects the poloidal field through coupling. The observable poloidal field is smaller and its spatial and temporal variability is reduced if there is no couling between the toroidal and poloidal fields.

To sum it up, we have developed a new baroclinic model called LSOMG and studied the OIMF. We answered some questions but there still remain open issues. It is tempting to complete our efforts to detect the wind-driven OIMF in the Swarm data. We might have all necessary components: An OGCM, a magnetic solver and a magnetospheric model. It can however be a tidious work with a possibility that additional pitfalls may apper. A further development of the LSOMG model would also be interesting, we would benefit from knowledge gained during this PhD and the fact that the code is familiar to us. For example, we could further improve barotropic tides by local tuning of IWD and SAL. We inspected several global setups in Sec. 7.1 but it we could also use different IWD and SAL values in different regions. If we found regional sensitivity, we could even constuct an inverse problem that would locally tune IWD and SAL. A study related to the internal tides in the baroclinic LSOMG could also be perspecitve altough it would require large computational resources on a supercomputer.

Bibliography

C. D. Aakjær, N. Olsen, and Ch. C Finlay. Determining polar ionospheric electrojet currents from Swarm satellite constellation magnetic data. *Earth Planets Space*, 68(1):140, 2016.

M. Abramowitz and I. (Eds.) Stegun. *Handbook of Mathematical Functions with Formulas, Graphs, and Mathematical Tables.* Dover Publications Inc., NewYork, 1968.

Y. Accad and C. L. Pekeris. Solution of the tidal equations for the M$_2$ and S$_2$ tides in the world oceans from a knowledge of the tidal potential alone. *Phil. Trans. R. Soc. London*, 290(1368):235–266, 1978.

A. Adcroft, W. Anderson, V. Balaji, C. Blanton, M. Bushuk, C. O. Dufour, J. P. Dunne, S. M. Griffies, R. W. Hallberg, M. J. Harrison, et al. The GFDL global ocean and sea ice model OM4.0: Model description and simulation features. *J. Adv. Model. Earth Sy.*

A. Adcroft, C. Hill, and J. Marshall. Representation of topography by shaved cells in a height coordinate ocean model. *Mon. Weather Rev.*, 125:2293–2315, 1997. doi: 10.1175/1520-0493(1997)125$\langle$2293:ROTBSC$\rangle$2.0.CO;2.

A. Adcroft, J.-M. Campin, S. Dutkiewicz, C. Evangelinos, D. Ferreira, G. Forget, B. Fox-Kemper, P. Heimbach, Ch. Hill, E. Hill, H. Hill, O. Jahn, M. Losch, J. Marshall, G. Maze, D. Menemenlis, and A. Molod. MITgcm user manual. Technical report, MIT Department of EAPS, 2014. URL `http://mitgcm.org/public/r2_manual/latest/`.

A. J. Adcroft. Numerical algorithms for use in a dynamical model of the ocean. Master's thesis, University of London, London, 1995. URL `http://gfdl.noaa.gov/~aja/papers/adcroft_PhD_1995.pdf`.

A. J. Adcroft, C. N. Hill, and J. C. Marshall. A new treatment of the Coriolis terms in C-grid models at both high and low resolutions. *Mon. Weather Rev.*, 8:1928–1936, 1999.

C. Amante. ETOPO1 1 arc-minute global relief model: procedures, data sources and analysis. NOAA Technical Memorandum NESDIS NGDC-24, National Geophysical Data Center, NOAA, Boulder, Colorado, 2009. URL `http://www.ngdc.noaa.gov/mgg/global/global.html`.

A. Arakawa and V. R. Lamb. Computational design of the basic dynamical processes of the UCLA general circulation model. *Methods Computat. Phys.*, 17:173–265, 1977.

B. K. Arbic, T. G. Stephen, W. H. Robert, and H. L. Simmons. The accuracy of surface elevations in forward global barotropic and baroclinic tide models. *Deep-Sea Res. II*, 51:3069–3101, 2004.

B. K. Arbic, A. J. Wallcraft, and E. J. Metzger. Concurrent simulation of the eddying general circulation and tides in a global ocean model. *Ocean model.*, 32:175–187, 2010.

Y. Baba, K. Takahashi, T. Sugimura, and K. Goto. general circulation model on a yin–yang grid. *Mon. Weather. Rev.*, 138(10):3988–4005, 2010.

J. O. Backhaus. A semi-implicit scheme for the shallow water equations for application to shelf sea modelling. *Cont. Shelf Res.*, 2(4):243–254, 1983.

P. G Baines. On internal tide generation models. *Deep-Sea Res. Pt. I*, 29(3): 307–338, 1982.

T. Barth and D. Jespersen. The design and application of upwind schemes on unstructured meshes. In *27th Aerospace sciences meeting*, page 366, 1989.

M. L. Batteen and Y.-J. Han. On the computational noise of finite–difference schemes used in ocean models. *Tellus*, 33(4):387–396, 1981. doi: 10.1111/j.2153-3490.1981.tb01761.x.

J. Beckers and E. Deleersnijder. Stability of a FBTCS scheme applied to the propagation of shallow-water inertia-gravity waves on various space grids. *J. Comput. Phys.*, 108:95–104, 1993. doi: 10.1006/jcph.1993.1166.

A. Beckmann and R. Döscher. A method for improved representation of dense water spreading over topography in geopotential–coordinate models. *J. Phys. Oceanogr.*, 27:581–591, 1997. doi: 10.1175/1520-0485(1997)027⟨0581:AMFIRO⟩2.0.CO;2.

M. Berger, M. Aftosmis, and S. Muman. Analysis of slope limiters on irregular grids. In *43rd AIAA Aerospace Sciences Meeting and Exhibit*, page 490, 2005.

H. Berntsen, Z. Kowalik, S. Sælid, and K. Sørli. Efficient numerical simulation of ocean hydrodynamics by a splitting procedure. *Model. ident. control*, 2(4): 181–199, 1981.

J. Berntsen. Internal pressure errors in sigma–coordinate ocean models. *J. Atmos. Oceanic Technol.*, 19:1403–1414, 2002. doi: 10.1175/1520-0426(2002)019⟨1403:IPEISC⟩2.0.CO;2.

R. Bleck, C. Rooth, D. Hu, and T. S. Smith. Salinity–driven thermocline transients in a wind– and thermohaline–forced isopycnic coordinate model of the North Atlantic. *J. Phys. Oceanogr.*, 22:1486–1505, 1992. doi: 10.1175/1520-0485(1992)022⟨1486:SDTTIA⟩2.0.CO;2.

A. F. Blumberg and G. L. Mellor. A description of a three–dimensional coastal ocean circulation model. In N. Heaps, editor, *Three–Dimensional Coastal Ocean Models*, volume 4 of *Coastal and Estuarine Series*, pages 1–16. American Geophysical Union, 1987.

A. S. Bower, M. S. Lozier, S. F. Gary, and C. W. Böning. Interior pathways of the north atlantic meridional overturning circulation. *Nature*, 459(7244):243, 2009.

W. S. Broecker et al. The great ocean conveyor. *Oceanography*, 4(2):79–89, 1991.

S. A. Brunnabend. Sea level variations derived from mass conserving finite element sea-ice ocean model. Master's thesis, Universität Bremen, Bremen, 2010. URL `http://gfdl.noaa.gov/~aja/papers/adcroft_PhD_1995.pdf`.

K. Bryan. A numerical method for the study of the circulation of the world ocean. *J. Comput. Phys.*, 4:347–376, 1969. doi: 10.1016/0021-9991(69)90004-7.

K. Bryan and M. D. Cox. An approximate equation of state for numerical models of ocean circulation. *J. Phys. Oceanogr.*, 2:510–514, 1972. doi: 10.1175/1520-0485(1972)002⟨0510:AAEOSF⟩2.0.CO;2.

K. Bryan and L. J. Lewis. A water mass model of the world ocean. *J. Geophys. Res.-Oceans*, 84(C5):2503–2517, 1979.

K. Bryan, S. Manabe, and R. C. Pacanowski. A global ocean-atmosphere climate model. Part II. The oceanic circulation. *J. Phys. Oceanogr.*, 5(1):30–46, 1975.

H. L. Bryden. New polynomials for thermal expansion, adiabatic temperature gradient, and potential temperature of sea water. *Deep–Sea Res.*, 20:401–408, 1973.

M. C. Buijsman, B. K. Arbic, J. A. M. Green, R. W. Helber, J. G. Richman, J. F. Shriver, P. G. Timko, and A. Wallcraft. Optimizing internal wave drag in a forward barotropic model with semidiurnal tides. *Ocean model.*, 85:42–55, 2015a.

M. C. Buijsman, B. K. Arbic, J. A. M. Green, R. W. Helber, J. G. Richman, J. F. Shriver, P. G. Timko, and A. Wallcraft. Optimizing internal wave drag in a forward barotropic model with semidiurnal tides. *Ocean Model.*, 85:42–55, 2015b.

D. R. Caldwell. The maximum density points of pure and saline water. *Deep–Sea Res.*, 25:175–181, 1978. doi: 10.1016/0146-6291(78)90005-X.

J.-M. Campin and H. Goosse. Parameterization of density-driven downsloping flow for a coarse-resolution ocean model in z-coordinate. *Tellus A*, 51(3):412–430, 1999.

J. M. Campin, A. Adcroft, C. Hill, and J. Marshall. Conservation of properties in a free-surface model. *Ocean Model.*, 6:221–244, 2004. doi: 10.1016/S1463-5003(03)00009-X.

L. Carrère, F. Lyard, M. Cancet, A. Guillot, and L. Roblou. FES2012: A new global tidal model taking advantage of nearly 20 years of altimetry. In *Proceedings of meeting*, volume 20, 2012.

E. P. Chassignet and Z. Garraffo. Viscosity parameterization and the Gulf Stream separation. In P. Müller and D. Henderson, editors, *From Stirring to Mixing in a Stratified Ocean, Proceedings of the 12th Hawaiian Winter Workshop*, pages 37–41. University of Hawaii at Manoa, 2001.

C. Chen, H. Liu, and R. C. Beardsley. An unstructured grid, finite-volume, three-dimensional, primitive equations ocean model: application to coastal ocean and estuaries. *J. Atmos. Ocean. Tech.*, 20(1):159–186, 2003.

A. Chulliat, P. Vigneron, and G. Hulot. First results from the Swarm dedicated ionospheric field inversion chain. *Earth Planets Space*, 68(1):104, 2016.

CLIMAP Project. *Seasonal reconstructions of the Earth's surface at the last glacial maximum.* Geological Society of America, 1981.

C. A. Collins and R. H. Heinmiller. The polymode program. 1989.

A. Coward, P. Killworth, and J. Blundell. Tests of a two–grid world ocean model. *J. Geophys. Res.*, 99:22725–22735, 1994. doi: 10.1029/94JC01893.

M. D. Cox. A primitive equation, 3–dimensional model of the ocean. GFDL ocean group technical report no. 1, Geophysical Fluid Dynamics Laboratory, Princeton, New Jersey, 1984.

R. A. Cox, M. J. McCartney, and F. Culkin. The specific gravity/salinity/temperature relationship in natural seawater. *Deep–Sea Res.*, 17: 679–689, 1970. doi: 10.1016/0011-7471(70)90034-3.

S. A. Cunningham, S. G. Alderson, B. A. King, and M. A. Brandon. Transport and variability of the Antarctic Circumpolar Current in Drake Passage. *J. Geophys. Res.-Oceans*, 108(C5), 2003.

G. Danabasoglu, J. C. McWilliams, and P. R. Gent. The role of mesoscale tracer transports in the global ocean circulation. *Science*, 264(5162):1123–1126, 1994.

S. Danilov, G. Kivman, and J. Schröter. A finite-element ocean model: principles and evaluation. *Ocean Model.*, 6(2):125–150, 2004.

S. Danilov, D. Sidorenko, Q. Wang, and T. Jung. The finite-volume sea ice–ocean model (FESOM2). *Geosci. Model Dev.*, 10:765–789, 2017.

D. P. Dee, S. M. Uppala, A. J. Simmons, P. Berrisford, P. Poli, S. Kobayashi, U. Andrae, M. a. Balmaseda, G. Balsamo, P. Bauer, et al. The ERA-Interim reanalysis: Configuration and performance of the data assimilation system. *Q. J. Roy. Meteor. Soc.*, 137(656):553–597, 2011. doi: 10.1002/qj.828.

V. A. Del Grosso. New equation for the speed of sound in natural waters (with comparisons to other equations). *J. Acoust. Soc. Amer.*, 56:1084–1091, 1974. doi: 10.1121/1.1903388.

E. Deleersnijder, J.-P. Van Ypersele, and J.-M. Campin. An orthogonal, curvilinear coordinate system for a world ocean model. *Ocean Model.*, 100:7–10, 1993.

H. Dobslaw, F. Flechtner, I. Bergmann-Wolf, C. Dahle, R. Dill, S. Esselborn, I. Sasgen, and M. Thomas. Simulating high-frequency atmosphere-ocean mass variability for dealiasing of satellite gravity observations: AOD1B RL05. *J. Geophys. Res.*, 118(7):3704–3711, 2013. doi: 10.1002/jgrc.20271. URL `http://doi.wiley.com/10.1002/jgrc.20271`.

J. K. Dukowicz. Mesh effects for Rossby waves. *J. Comput. Phys.*, 119:188–194, 1995. doi: 10.1006/jcph.1995.1126.

D. R. Durran. *Numerical Methods for Wave Equations in Geophysical Fluid Dynamics*. Springer Verlag, 1999.

M. Eby and G. Holloway. Grid transformation for incorporating the Arctic in a global ocean model. *Clim. Dynam.*, 10:241–247, 1994.

G. D. Egbert and S. Y. Erofeeva. Efficient inverse modeling of barotropic ocean tides. *J. Atmos. Ocean. Tech.*, 19(2):183–204, 2002.

G. D. Egbert and R. D. Ray. Significant dissipation of tidal energy in the deep ocean inferred from satellite altimeter data. *Nature*, 405(6788):775, 2000.

D. Einšpigel and Z. Martinec. A new derivation of the shallow water equations in geographical coordinates and their application to the global barotropic ocean model (the DEBOT model). *Ocean Model.*, 92:85–100, 2015. doi: 10.1016/j.ocemod.2015.05.006.

D. Einšpigel and Z. Martinec. Time-domain modeling of global ocean tides generated by the full lunisolar potential. *Ocean Dynam.*, 67:165–189, 2016. doi: 10.1007/s10236-016-1016-1.

V. W. Ekman. Die zusammendruckbarkeit des meerwassers nebst einigen werten fur wasser und quecksilber. *Publications de Circonst.*, 43:1–47, 1908.

T. Ezer and G. L Mellor. Diagnostic and prognostic calculations of the North Atlantic circulation and sea level using a sigma coordinate ocean model. *J. Geophys. Res.–Oceans*, 99:14159–14171, 1994. doi: 10.1029/94JC00859.

D. E. Farrow and D. P. Stevens. A new tracer advection scheme for Bryan and Cox type ocean general circulation models. *J. Phys. Oceanogr.*, 25:1731–1741, 1995. doi: 10.1175/1520-0485(1995)025⟨1731:ANTASF⟩2.0.CO;2.

I. Federico, N. Pinardi, G. Coppini, P. Oddo, R. Lecci, and M. Mossa. Coastal ocean forecasting with an unstructured grid model in the southern adriatic and northern ionian seas. *Nat. Hazard. Earth Sys.*, 2017.

R. Feistel. Equilibrium thermodynamics of seawater revisited. *Prog. Oceanogr.*, 31:101–179, 1993. doi: 10.1016/0079-6611(93)90024-8.

R. Feistel. A new extended Gibbs thermodynamic potential of seawater. *Prog. Oceanogr.*, 58:43–114, 2003. doi: 10.1016/S0079-6611(03)00088-0.

R. Feistel and E. Hagen. On the GIBBS thermodynamic potential of seawater. *Prog. Oceanogr.*, 36:249–327, 1995. doi: 10.1016/0079-6611(96)00001-8.

C. C. Finlay, N. Olsen, S. Kotsiaros, N. Gillet, and L. Tøffner-Clausen. Recent geomagnetic secular variation from Swarm and ground observatories as estimated in the CHAOS-6 geomagnetic field model. *Earth Planets Space*, 68(1): 112, 2016.

G. J. Fix. Finite element models for ocean circulation problems. *SIAM J. Appl. Math.*, 29(3):371–387, 1975.

Á. H. Flosadóttir, J. C. Larsen, and J. T. Smith. Motional induction in North Atlantic circulation models. *J. Geophys. Res.: Oceans*, 102(C5):10353–10372, 1997.

N. P. Fofonoff. Physical properties of seawater: A new salinity scale and equation of state for seawater. *J. Geophys. Res.–Oceans*, 20:3332–3342, 1985.

C. Forch, M. Knudsen, and S. P. L. Sorensen. *Berichte über die Konstantenbestimmungen zur Aufstellung der hydrographischen Tabellen.* D. Kgl., Danske Vidensk., Selsk. Skifter, Raekker 6 Naturv. og math. afd. XII, 1902.

E. Friis-Christensen, H. Lühr, and G. Hulot. Swarm: A constellation to study the Earth's magnetic field. *Earth Planets Space*, 58(4):351–358, 2006.

T. Frisius, K. Fraedrich, X. Zhu, and W. Wang. A spectral barotropic model of the wind-driven world ocean. *Ocean Model.*, 30(4):310–322, 2009.

L.-L. Fu and A. (Eds.) Cazenave. *Satellite Altimetry and Earth Sciences: A Handbook of Techniques and Applications.* Academic Press, San Diego, Calif., 2001.

A. J. Gadd. An economical explicit integration scheme. Meteor. office tech. note 44, 1974.

W. L. Gates and Ch. A Riegel. A study of numerical errors in the integration of barotropic flow on a spherical grid. *J. Geophys. Res.*, 67(2):773–784, 1962.

P. R. Gent and J. C. McWilliams. Isopycnal mixing in ocean circulation models. *J. Phys. Oceanogr.*, 20:150–155, 1990.

P. R. Gent, J. Willebrand, T. J. McDougall, and J. C. McWilliams. Parameterizing eddy–induced tracer transports in ocean circulation models. *J. Phys. Oceanogr.*, 25:463–474, 1995.

P. R. Gent, F. O. Bryan, G. Danabasoglu, S. C. Doney, W. R. Holland, W. G. Large, and J. C. McWilliams. The NCAR climate system model global ocean component. *J. Climate*, 11:1287–1306, 1998. doi: 10.1175/1520-0442(1998)011⟨1287:TNCSMG⟩2.0.CO;2.

D. L. George. *Finite volume methods and adaptive refinement for tsunami propagation and inundation.* Citeseer, 2006.

R. Gerdes, C. Koberle, and J. Willebrand. The influence of numerical advection schemes on the results of ocean general circulation models. *Clim. Dynam.*, 5: 211–226, 1991.

A. E. Gill. *Atmosphere–Ocean Dynamics.* Academic Press, 1982.

S. K. Godunov. A difference scheme for numerical solution of discontinuous solution of hydrodynamic equations. *Math. Sbornik*, 47:271–306, 1959.

H. Goosse, E. Deleersnijder, T. Fichefet, and M. H. England. Sensitivity of a global coupled ocean-sea ice model to the parameterization of vertical mixing. *J. Geophys. Res.-Oceans*, 104(C6):13681–13695, 1999.

A. L. Gordon and F. W. G. Baker. *Oceanography: Annals of The International Geophysical Year*, volume 46. Elsevier, 2013.

A. V. Grayver, F. D. Munch, A. V. Kuvshinov, A. Khan, T. J. Sabaka, and L. Tøffner-Clausen. Joint inversion of satellite-detected tidal and magnetospheric signals constrains electrical conductivity and water content of the upper mantle and transition zone. *Geophys. Res. Lett.*, 44:6074–6081, 2017.

R. J. Greatbatch. A note on the representation of steric sea level in models that conserve volume rather than mass. *J. Geophys. Res.*, 99(C6):12767, 1994. doi: 10.1029/94JC00847.

J. A. M. Green and J. Nycander. A comparison of tidal conversion parameterizations for tidal models. *Ocean model.*, 43:104–119, 2013.

M. C. Gregg. Variations in the intensity of small-scale mixing in the main thermocline. *J. Phys. Oceanogr.*, 7(3):436–454, 1977.

S. Griffies, A. Gnanadesikan, R. Pacanowski, V. Larichev, J. Dukowicz, and R. Smith. Isoneutral diffusion in a z-coordinate ocean model. *J. Phys. Oceanogr.*, 28:805–830, 1998.

S. M. Griffies. The Gent–McWilliams skew–flux. *J. Phys. Oceanogr.*, 28:831–841, 1998.

S. M. Griffies. *Fundamentals of Ocean Climate Models.* Princeton University Press, 2004.

S. M. Griffies. Elements of the Modular Ocean Model (MOM) (2012 release). GFDL ocean group technical report no. 7, NOAA/Geophysical Fluid Dynamics Laboratory, 2012. URL `http://mom-ocean.org/web/docs/project/MOM5_elements.pdf`.

S. M. Griffies and R. W. Hallberg. Biharmonic friction with a Smagorinsky–like viscosity for use in large–scale eddy–permitting ocean models. *Mon. Wea. Rev.*, 128:2935–2946, 2000. doi: 10.1175/1520-0493(2000)128⟨2935:BFWASL⟩2.0.CO;2.

S. M. Griffies, C. Böning, F. O. Bryan, E. P. Chassignet, R. Gerdes, H. Hasumi, A. Hirst, A.-M. Treguier, and D. Webb. Developments in ocean climate modelling. *Ocean. Model.*, 2:123–192, 2000. doi: 10.1016/S1463-5003(00)00014-7.

S. M. Griffies, A. W. D. K. Gnanadesikan, K. W. Dixon, J. P. Dunne, R. Gerdes, M. J. Harrison, A. Rosati, J. L. Russell, B. L. Samuels, M. J. Spelman, et al. Formulation of an ocean model for global climate simulations. *Ocean Sci.*, 1 (1):45–79, 2005.

S. M. Griffies, A. Biastoch, C. Böning, F. Bryan, G. Danabasoglu, E. P. Chassignet, M. H. England, R. Gerdes, H. Haak, R. W. Hallberg, et al. Coordinated ocean-ice reference experiments (COREs). *Ocean model.*, 26(1-2):1–46, 2009.

Y. Guan and D. Zhang. Finite difference TVD scheme for modeling two-dimensional advection-dispersion. In *Environmental hydraulics and sustainable water management, Proceedings of the 4th International Symposium on Environmental Hydraulics and the 14th Congress of Asia and Pacific Division, International Association of Hydraulic Engineering and Research, Hong Kong*, pages 15–18, 2004.

S. K. Gulev, B. Barnier, H. Knochel, J.-M. Molines, and M. Cottet. Water mass transformation in the north atlantic and its impact on the meridional circulation: Insights from an ocean model forced by NCEP–NCAR reanalysis surface fluxes. *J. Climate*, 16(19):3085–3110, 2003.

A. V. Gusev and N. A. Diansky. Numerical simulation of the world ocean circulation and its climatic variability for 1948–2007 using the inmom. *Iz. Atmos. Ocean. Phy+*, 50(1):1–12, 2014.

D. B. Haidvogel, H. G. Arango, K. Hedstrom, A. Beckmann, and A. F. Malanotte-Rizzoli, P. Shchepetkin. Model evaluation experiments in the North Atlantic basin: simulations in nonlinear terrain–following coordinates. *Dynam. Atmos. Oceans*, 32:239–281, 2000. doi: 10.1016/S0377-0265(00)00049-X.

L. Han. A two-time-level split-explicit ocean circulation model (MASNUM) and its validation. *Acta Oceanol. Sin.*, 33(11):11–35, 2014. doi: 10.1007/s13131-014-0553-z.

R. L. Haney. On the pressure gradient force over steep topography in sigma coordinate ocean models. *J. Phys. Oceanogr.*, 21:610–619, 1991. doi: 10.1175/1520-0485(1991)021⟨0610:OTPGFO⟩2.0.CO;2.

S. Hellerman and M. Rosenstein. Normal monthly wind stress over the world ocean with error estimates. *J. Phys. Oceanogr.*, 13(7):1093–1104, 1983.

M. C. Hendershott. The effects of solid earth deformation on global ocean tides. *Geophys. J. Int.*, 29(4):389–402, 1972.

W. D. Hibler III and K. Bryan. A diagnostic ice–ocean model. *J. Phys. Oceanogr.*, 17:987–1015, 1987. doi: 10.1175/1520-0485(1987)017⟨0987:ADIM⟩2.0.CO;2.

W. R. Holland, J. C. Chow, and F. O. Bryan. Application of a third-order upwind scheme in the ncar ocean model. *J. Climate*, 11(6):1487–1493, 1998.

W. W. Hsieh, M. K. Davey, and R. C. Wajsowicz. The free Kelvin Wave in finite–difference numerical models. *J. Phys. Oceanogr.*, 13:1383–1397, 1983. doi: 10.1175/1520-0485(1983)013⟨1383:TFKWIF⟩2.0.CO;2.

S. Imawaki, H. Uchida, H. Ichikawa, M. Fukasawa, S. Umatani, and ASUKA Group. Satellite altimeter monitoring the Kuroshio transport south of Japan. *Geophys. Res. Lett.*, 28(1):17–20, 2001.

Intergovernmental Oceanographic Commission. *The International Decade of Ocean Exploration, IDOE, 1971-1980*, volume 13. UNESCO, 1974.

IOC, IHO and BODC. Centenary edition of the gebco digital atlas, published on cd-rom on behalf of the intergovernmental oceanographic commission and the international hydrographic organization as part of the general bathymetric chart of the oceans. 2003.

C. Irrgang, J. Saynisch, and M. Thomas. Impact of variable seawater conductivity on motional induction simulated with an ocean general circulation model. *Ocean Sci.*, 12(4):129–136, 2016a. doi: 10.5194/os-12-129-2016.

C. Irrgang, J. Saynisch, and M. Thomas. Ensemble simulations of the magnetic field induced by global ocean circulation: Estimating the uncertainty. *J. Geophys. Res. Oceans*, 121(3):1866–1880, 2016b. doi: 10.1002/2016JC011633.

Ch. Irrgang, J. Saynisch, and M. Thomas. Utilizing oceanic electromagnetic induction to constrain an ocean general circulation model: A data assimilation twin experiment. *J. Adv. Model. Earth Sy.*, 2017. doi: 10.1002/201simu7MS000951.

Ch. Jablonowski and D. L. Williamson. The pros and cons of diffusion, filters and fixers in atmospheric general circulation models. In P. Lauritzen, Ch. Jablonowski, M. Taylor, and N. Ramachandran, editors, *Numerical techniques for global atmospheric models*. Springer Berlin Heidelberg, Berlin, 2011.

D. R. Jackett and T. J. McDougall. Minimal adjustment of hydrographic profiles to achieve static stability. *J. Atmos. Oceanic Technol.*, 12:381–389, 1995. doi: 10.1175/1520-0426(1995)012⟨0381:MAOHPT⟩2.0.CO;2.

D. R. Jackett, T. J. McDougall, R. Feistel, D. G. Wright, and S. M. Griffies. Algorithms for density, potential temperature, conservative temperature, and the freezing temperature of seawater. *J. Atmos. Oceanic Technol.*, 23:1709–1728, 2006. doi: 10.1175/JTECH1946.1.

B. M. Jamart and J. Ozer. Numerical boundary layers and spurious residual flows. *J. Geophys. Res.*, 91:10621–10631, 1986.

I. J. Janjic. A stable centered difference scheme free of two-grid-interval noise. *Mon. Weather Rev.*, 102:319–323, 1974.

S. R. Jayne. The impact of abyssal mixing parameterizations in an ocean general circulation model. *J. Phys. Oceanogr.*, 39(7):1756–1775, 2009.

S.R. Jayne and L.C. St. Laurent. Parameterizing tidal dissipation over rough topography. *Geophys. Res. Let.*, 28:811–814, 2001.

T. C. Johns, C. F. Durman, H. T. Banks, M. J. Roberts, A. J. McLaren, J. K. Ridley, C. A. Senior, K. D. Williams, A. Jones, G. J. Rickard, et al. The new Hadley Centre climate model (HadGEM1): Evaluation of coupled simulations. *J. Climate*, 19(7):1327–1353, 2006.

B. A. Kagan and A. A. Timofeev. Spatial variability in the drag coefficient and its role in tidal dynamics and energetics, a case study: The surface M_2 tide in the subsystem of the Barents and Kara Seas. *Izv. Atmos. Ocean. Phy+*, 51(1): 98–111, 2015.

A. Kageyama and T. Sato. “yin-yang grid”: An overset grid in spherical geometry. *Geochem. Geophy. Geosy.*, 5(9), 2004.

E. Kalnay, M. Kanamitsu, R. Kistler, W. Collins, D. Deaven, L. Gandin, M. Iredell, S. Saha, G. White, J. Woollen, et al. The ncep/ncar 40-year reanalysis project. *B. Am. Meteorol. Soc.*, 77(3):437–472, 1996.

G. Kaplan, J. Bartlett, A. Monet, J. Bangert, and W. Puatua. User’s guide to NOVAS version F3.1. Technical report, Washington, DC: USNO, 2011. URL `http://aa.usno.navy.mil/software/novas/novas_f/NOVAS_F3.1_Guide.pdf`.

A. B. Kara, P. A. Rochford, and H. E. Hurlburt. Air–sea flux estimates and the 1997–1998 ENSO event. *Bound.-Lay. Meteorol.*, 103(3):439–458, 2002.

A. Kelbert, A. Kuvshinov, J. Velímský, T. Koyama, J. Ribaudo, J. Sun, Z Martinec, and C. J. Weiss. Global 3-d electromagnetic forward modelling: a benchmark study. *Geophys. J. Int.*, 197(2):785–814, 2014.

P. D. Killworth, D. J. Webb, D. Stainforth, and S. M. Paterson. The development of a free-surface Bryan–Cox–Semtner ocean model. *J. Phys. Oceanogr.*, 21(9): 1333–1348, 1991.

M. Knudsen. *Hydrographische Tabellen.* G.E.C. Gad, Copenhagen, and Williams Norgate, London, 1901.

J. Kondo. Air-sea bulk transfer coefficients in diabatic conditions. *Bound.-Lay. Meteorol.*, 9(1):91–112, 1975.

P. Korn. Formulation of an unstructured grid model for global ocean dynamics. *J. Comput. Phys.*, 339:525–552, 2017.

S. Kotsiaros. Toward more complete magnetic gradiometry with the Swarm mission. *Earth Planets Space*, 68(1):130, 2016.

K. Kremling. Comparison of specific gravity in natural seawater from hydrographic tables and measurements by a new density instrument. *Deep–Sea Res.*, 19:377–383, 1972.

Y. Kurihara. Numerical integration of the primitive equations on a spherical grid. *Mon. Wea. Rev*, 93(7):399–415, 1965.

A. Kuvshinov. 3-D global induction in the oceans and solid Earth: recent progress in modeling magnetic and electric fields from sources of magnetospheric, ionospheric and oceanic origin. *Surv. Geophys.*, 29:139–186, 2008.

A. V. Kuvshinov and A. A. Semenov. Global 3-D imaging of mantle electrical conductivity based on inversion of observatory C-responses – I. An approach and its verification. *Geophys. J. Int.*, 189:1335–1352, 2012.

Z. Lai, C. Chen, G. W. Cowles, and R. C. Beardsley. A nonhydrostatic version of fvcom: 1. validation experiments. *J. Geophys. Res.-Oceans*, 115(C11), 2010.

W. B. Large. Surface fluxes for practitioners of global ocean data assimilation. In *Ocean Weather Forecasting*, pages 229–270. Springer, 2006.

W. G. Large and S. G. Yeager. Diurnal to decadal global forcing for ocean and sea-ice models: the data sets and flux climatologies. NCAR technical note: Ncar/tn-460+str, CGD Division of the National Center for Atmospheric Research, 2004.

W. G. Large and S. G. Yeager. The global climatology of an interannually varying air–sea flux data set. *Clim. dynam.*, 33(2-3):341–364, 2009.

W. G. Large, G. Danabasoglu, J. C. McWilliams, P. R. Gent, and F. O. Bryan. Equatorial circulation of a global ocean climate model with anisotropic horizontal viscosity. *J. Phys. Oceanogr.*, 31:518–536, 2001. doi: 10.1175/1520-0485(2001)031⟨0518:ECOAGO⟩2.0.CO;2.

J. C. Larsen and T. B. Sanford. Florida current volume transports from voltage measurements. *Science*, 227(4684):302–304, 1985.

K. M. Laundal, C. C. Finlay, and N. Olsen. Sunlight effects on the 3D polar current system determined from low Earth orbit measurements. *Earth Planets Space*, 68(1):142, 2016.

L. S. Laurent, H. L. Simmons, and S. R. Jayne. Estimates of tidally driven enhanced mixing in the deep ocean. *Geophys. Res. Lett.*, 29:21–1–21–4, 2002. doi: 10.1029/2002GL015633.

C. Le Provost. On the use of finite element methods for ocean modelling. In *Advanced Physical Oceanographic Numerical Modelling*, pages 557–580. Springer, 1986.

S. Legg, R. W. Hallberg, and J. B. Girton. Internal pressure errors in sigma–coordinate ocean models. *Ocean model.*, 11:69–97, 2006. doi: 10.1016/j.ocemod.2004.11.006.

H. Lei. A two-time-level split-explicit ocean circulation model (MASNUM) and its validation. *Acta Oceanol. Sin.*, 33:11–35, 2014. doi: 10.1007/s13131-014-0553-z.

C. E. Leith. Diffusion approximation for two–dimensional turbulence. *Phys. Fluids*, 10:1409–1416, 1968. doi: 10.1063/1.1691968.

C. E. Leith. Stochastic models of chaotic systems. *Physica D.*, 98:481–491, 1996. doi: 10.1016/0167-2789(96)00107-8.

B. P. Leonard. A stable and accurate convective modelling procedure based on quadratic upstream interpolation. *Comput. Method. Appl. M.*, 19:59–98, 1979. doi: 10.1016/0045-7825(79)90034-3.

B. P. Leonard. The ULTIMATE conservative difference scheme applied to unsteady one-dimensional advection. *Comput. Method. Appl. M.*, 88(1):17–74, 1991.

P. F. J. Lermusiaux. Evolving the subspace of the three-dimensional multiscale ocean variability: Massachusetts Bay. *J. Marine Syst.*, 29(1-4):385–422, 2001.

R. A. Locarnini, A. V. Mishonov, J. I. Antonov, T. P. Boyer, H. E. Garcia, O. K. Baranova, M. M. Zweng, C. R. Paver, J. R. Reagan, D. R. Johnson, M. Hamilton, and D. Seidov. World ocean atlas 2013, volume 1: Temperature. In S. Levitus, editor, *NOAA Atlas NESDIS 73*, page 40. 2013.

P. J. Lynett, K. Gately, R. Wilson, L. Montoya, D. Arcas, B. Aytore, Y. Bai, J. D. Bricker, M. J. Castro, K. F. Cheung, et al. Inter-model analysis of tsunami-induced coastal currents. *Ocean Model.*, 114:14–32, 2017.

R. V. Madala and S. A. Piacseki. A semi-implicit numerical model for baroclinic oceans. *J. Comput. Phys.*, 23(2):167–178, 1977.

G. Madec. NEMO ocean engine (version 3.4). Technical report, Laboratoire d'Océanographie et du Climat: Expérimentation et Approches Numériques, 2012. URL `http://www.nemo-ocean.eu/About-NEMO/Reference-manuals`.

G. Madec, P. Delecluse, M. Imbard, and C. Le'vy. OPA 8.1 ocean general circulation model reference manual. Note du pôle de modélisation, Inst. Pierre-Simon Laplace, Paris, France, 1998.

E. Maier-Reimer and U. Mikolajewicz. The hamburg large scale geostrophic ocean general circulation model (cycle 1). DKRZ report 2, Max–Planck–Institut für Meteorologie, Hamburg, Germany, 1992. URL `http://mud.dkrz.de/fileadmin/extern/documents/reports/ReportNo.02.pdf`.

E. Maier-Reimer, U. Mikolajewicz, and K. Hasselmann. Mean circulation of the hamburg LSG OGCM and its sensitivity to the thermohaline surface forcing. *J. Phys. Oceanogr.*, 23(4):731–757, 1993.

C. Manoj, A. Kuvshinov, S. Maus, and H. Lühr. Ocean circulation generated magnetic signals. *Earth Planets Space*, 58(4):429–437, 2006.

J. Marshall, A. Adcroft, C. Hill, L. Perelman, and C. Heisey. A finite-volume, incompressible Navier Stokes model for studies of the ocean on parallel computers. *J. Geophys. Res.: Oceans*, 102(C3):5753–5766, 1997.

S. J. Marsland, H. Haak, J. H. Jungclaus, M. Latif, and F. Röske. The Max-Planck-Institute global ocean/sea ice model with orthogonal curvilinear coordinates. *Ocean Model.*, 5(2):91–127, 2003.

Z. Martinec. Spectral-finite element approach to three-dimensional electromagnetic induction in a spherical Earth. *Geophys. J. Int.*, 136:229–250, 1999.

Z. Martinec. Continuum mechanics (lecture notes), 2011. URL `http://geo.mff.cuni.cz/teachingcz.htm`.

Z. Martinec. *Principles of Continuum Mechanics: A Basic Course for Physicists.* Springer, 2019.

Z. Martinec, J. Velímský, R. Haagmans, and L. Šachl. A two-step along-track spectral analysis for estimating the magnetic signals of magnetospheric ring current from Swarm data. *Geophys. J. Int.*, 212(2):1201–1217, 2017.

M. F. Maury. *The physical geography of the sea, and its meteorology.* Sampson Low, Marston, Low and Searle, 1874.

S. Maus. The geomagnetic power spectrum. *Geophys. J. Int.*, 174(1):135–142, 2008.

N. Maximenko, P. Niiler, L. Centurioni, M.-H. Rio, O. Melnichenko, D. Chambers, V. Zlotnicki, and B. Galperin. Mean dynamic topography of the ocean derived from satellite and drifting buoy data using three different techniques. *J. Atmos. Ocean. Tech.*, 26(9):1910–1919, 2009.

J. L. McClean, D. C. Bader, F. O. Bryan, M. E. Maltrud, J. M. Dennis, A. A. Mirin, P. W. Jones, Y. Y. Kim, D. P. Ivanova, M. Vertenstein, et al. A prototype two-decade fully-coupled fine-resolution CCSM simulation. *Ocean Model.*, 39 (1-2):10–30, 2011.

T. J. McDougall, D. R. Jackett, D. G. Wright, and R. Feistel. Accurate and computationally efficient algorithms for potential temperature and density of seawater. *J. Atmos. Oceanic Technol.*, 20:730–741, 2003. doi: 10.1175/1520-0426(2003)20⟨730:AACEAF⟩2.0.CO;2.

J. C. McWilliams. *Fundamentals of Geophysical Fluid Dynamics.* Cambridge University Press, 2006.

P. J. Melchior. *The tides of the planet Earth, 2nd edition.* Pergamon Press, Oxford, 1983.

G. L. Mellor. An equation of state for numerical models of oceans and estuaries. *J. Atmos. Oceanic Technol.*, 8:609–611, 1991. doi: 10.1175/1520-0426(1991)008⟨0609:AEOSFN⟩2.0.CO;2.

G. L. Mellor and L. Kantha. An ice–ocean coupled model. *J. Geophys. Res.*, 94: 10937–10954, 1989.

F. Mesinger. An economical explicit scheme which inherently prevents the false two-grid-interval wave in the forecast fields. In *Proc. Symp. "Difference and spectral methods for atmosphere and ocean dynamics problems", Academy of Sciences, Novosibirsk*, pages 17–22, 1973.

F. Mesinger. Forward-backward scheme, and its use in a limited area model. *Contrib. Atmos. Phys.*, 50:200–210, 1977.

F. Mesinger and A. Arakawa. *Numerical methods used in atmospheric models (Volume 1)*, volume 17 of *GARP Publ. ser.* World Meteorological Organization, International Council of Scientific Unions, 1976.

F. Mesinger and J. Popovic. Forward-backward scheme on the B/E grid modified to suppress lattice separation: the two versions, and any impact of the choice made? *Meteorol. Atmos. Phys.*, 108:1–8, 2010. doi: 10.1007/s00703-010-0080-1.

F. J. Millero and A. Poisson. International one–atmosphere equation of state of seawater. *Deep–Sea Res.*, 28:625–629, 1981a. doi: 10.1016/0198-0149(81)90122-9.

F. J. Millero and A. Poisson. Summary of data treatment for the international one atmosphere equation of state for seawater. *UNESCO Technical Papers in Marine Science*, 38:19–85, 1981b.

F. J. Millero, A. Gonzalez, and G. K. Ward. The density of seawater solutions at one atmosphere as a function of temperature and salinity. *J. Mar. Res.*, 34: 61–93, 1976.

F. J. Millero, C.-T. Chen., A. Bradshaw, and K. Schleicher. A new high pressure equation of state for seawater. *Deep–Sea Res.*, 27:255–264, 1980. doi: 10.1016/0198-0149(80)90016-3.

F. J. Millero, C.-T. Chen, A. Bradshaw, and K. Schleicher. Summary of data treatment for the international high pressure equation of state of seawater. *UNESCO Technical Papers in Marine Science*, 38:99–188, 1981.

Mode Group and others. The Mid-Ocean Dynamics Experiment. *Deep-Sea Res.*, 25(10):859–910, 1978.

M. Montoya, A. Griesel, A. Levermann, J. Mignot, M. Hofmann, A. Ganopolski, and S. Rahmstorf. The earth system model of intermediate complexity CLIMBER-3α. Part I: description and performance for present-day conditions. *Clim. Dynam.*, 25(2-3):237–263, 2005.

M. Müller, H. Haak, J. H. Jungclaus, J. Sundermann, and M. Thomas. The effect of ocean tides on a climate model simulation. *Ocean Model.*, 35:304–313, 2010. doi: 10.1016/j.ocemod.2010.09.001.

M. Müller, J. Y. Cherniawsky, M. G. G. Foreman, and J.-S. von Storch. Global M2 internal tide and its seasonal variability from high resolution ocean circulation and tide modeling. *Geophys. Res. Let.*, 39:304–313, 2012. doi: 10.1029/2012GL053320.

W. Munk and C. Wunsch. Abyssal recipes II: Energetics of tidal and wind mixing. *Deep-Sea Res. Pt. I*, 45(12):1977–2010, 1998.

W. H. Munk. On the wind–driven ocean circulation. *J. Meteorol.*, 7:3–29, 1950. doi: 10.1175/1520-0469(1950)007⟨0080:OTWDOC⟩2.0.CO;2.

W. H. Munk. Abyssal recipes. In *Deep Sea Research and Oceanographic Abstracts*, volume 13, pages 707–730. Elsevier, 1966.

R. J. Murray. Explicit generation of orthogonal grids for ocean models. *J. Comput. Phys.*, 126:251–273, 1996. doi: 10.1006/jcph.1996.0136.

R. J. Murray and C. J. C. Reason. A curvilinear version of the Bryan-Cox-Semtner ocean model and its representation of the Arctic circulation. *J. Comput. Phys.*, 171:1–46, 2001. doi: 10.1006/jcph.2001.6761.

R. J. Murray and C. J. C. Reason. Fourier filtering and coefficient tapering at the North Pole in OGCMs. *Ocean model.*, 4:1–25, 2002. doi: 10.1016/S1463-5003(01)00009-9.

Y. Niwa and T. Hibiya. Estimation of baroclinic tide energy available for deep ocean mixing based on three-dimensional global numerical simulations. *J. Oceanogr.*, 67:493–502, 2011. doi: 10.1007/s10872-011-0052-1.

J. Nycander. Generation of internal waves in the deep ocean by tides. *J. Geophys. Res.: Oceans*, 110(C10), 2005.

J. M. Oberhuber. The OPYC Ocean General Circulation Model. Report no. 7, Deutsches Klimarechenzentrum GmbH, Hamburg, 1993a. URL `http://mud.dkrz.de/fileadmin/extern/documents/reports/ReportNo.0.pdf`.

J. M. Oberhuber. The OPYC ocean general circulation mode. Tech. Rep. 7, Dtsh. Klimarechenzentrum GmbH, Hamburg, Germany, 1993b.

J. M. Oberhuber. Simulation of the atlantic circulation with a coupled sea ice-mixed layer-isopycnal general circulation model. part I: Model description. *J. Phys. Oceanogr.*, 23(5):808–829, 1993c.

D. Olbers and K. Lettmann. Barotropic and baroclinic processes in the transport variability of the Antarctic Circumpolar Current. *Ocean Dynam.*, 57(6):559–578, 2007.

N. Olsen, C. C. Finlay, S. Kotsiaros, and L. Tøffner-Clausen. A model of Earth's magnetic field derived from 2 years of Swarm satellite constellation data. *Earth Planets Space*, 68(1):124, 2016.

R. Pacanowski and S. M. Griffies. MOM 3.0 manual. GFDL ocean group technical report, NOAA/Geophysical Fluid Dynamics Laboratory, 2000. URL `http://mom-ocean.org/web/docs/project/MOM5_elements.pdf`.

R. C. Pacanowski. Effect of equatorial currents on surface stress. *J. Phys. Oceanogr.*, 17:833–838, 1987. doi: 10.1175/1520-0485(1987)017⟨0833:EOECOS⟩2.0.CO;2.

R. C. Pacanowski and A. Gnanadesikan. Transient response in a z–level ocean model that resolves topography with partial–cells. *Mon. Weather Rev.*, 126:3248–3270, 1998. doi: 10.1175/1520-0493(1998)126⟨3248:TRIAZL⟩2.0.CO;2.

R. C. Pacanowski and S. G. H. Philander. Parameterization of vertical mixing in numerical models of tropical oceans. *J. Phys. Oceanogr.*, 11(11):1443–1451, 1981.

O. Pankratov and A. Kuvshinov. Applied mathematics in EM studies with special emphasis on an uncertainty quantification and 3-D IE modelling. *Surv. Geophys.*, 37:109–147, 2016.

O. Pankratov, D. Avdeev, and A. Kuvshinov. Electromagnetic field scattering in a homogeneous Earth: a solution to the forward problem. *Phys. Solid. Earth*, 31:201–209, 1995.

J. Pedlosky. *Geophysical fluid dynamics (second edition).* Springer–Verlag, New York, 1987.

N. A. Phillips. A coordinate system having some special advantages for numerical forecasting. *J. Meteor.*, 14:184–185, 1957. doi: 10.1175/1520-0469(1957)014⟨0184:ACSHSS⟩2.0.CO;2.

M. Prange, G. Lohmann, and A. Paul. Influence of vertical mixing on the thermohaline hysteresis: Analyses of an OGCM. *J. Phys. Oceanogr.*, 33:1707–1721, 2003. doi: 10.1175/2389.1.

S. Rahmstorf. A fast and complete convection scheme for ocean models. *Ocean model.*, 101(9.11), 1993.

D. A. Randall. Geostrophic adjustment and the finite–difference shallow–water equations. *Mon. Weather Rev.*, 122:1371–1377, 1994. doi: 10.1175/1520-0493(1994)122⟨1371:GAATFD⟩2.0.CO;2.

M. H. Redi. Oceanic isopycnal mixing by coordinate rotation. *J. Phys. Oceanogr.*, 12:1154–1158, 1982. doi: 10.1175/1520-0485(1982)012⟨1154:OIMBCR⟩2.0.CO;2.

P. Rivière, A. M. Treguier, and P. Klein. Effects of bottom friction on nonlinear equilibration of an oceanic baroclinic jet. *J. Phys. Oceanogr.*, 34:416–432, 2004. doi: 10.1175/1520-0485(2004)034⟨0416:EOBFON⟩2.0.CO;2.

J. L. Roberts, P. Heil, R. J. Murray, D. S. Holloway, and N. L. Bindoff. Pole relocation for an orthogonal grid: An analytic method. *Ocean model.*, 12:16–31, 2006. doi: 10.1016/j.ocemod.2005.03.004.

P. L. Roe. Characteristic-based schemes for the Euler equations. *Annu. Rev. Fluid Mech.*, 18(1):337–365, 1986.

C. G. Rooth and G. Östlund. Penetration of tritium into the atlantic thermocline. In *Deep Sea Research and Oceanographic Abstracts*, volume 19, pages 481–492. Elsevier, 1972.

H. A. Ruhl, M. André, L. Beranzoli, M. N. Çağatay, A. Colaço, M. Cannat, J. J. Dañobeitia, P. Favali, L. Géli, M. Gillooly, et al. Societal need for improved understanding of climate change, anthropogenic impacts, and geo-hazard warning drive development of ocean observatories in european seas. *Prog. Oceanogr.*, 91(1):1–33, 2011.

Y. Saad and M. H. Schultz. GMRES: A generalized minimal residual algorithm for solving nonsymmetric linear systems. *SIAM J. Sci. Statist. Comput.*, 7:856–869, 1986. doi: 10.1137/0907058.

l. Šachl, Z. Martinec, J. Velímský, C. Irrgang, J. Petereit, J. Saynisch, D. Einšpigel, and N. R. Schnepf. Modelling of electromagnetic signatures of global ocean circulation: physical approximations and numerical issues. *Earth Planets Space*, 71(1):58, 2019.

K. Sakamoto, H. Tsujino, H. Nakano, M. Hirabara, and G. Yamanaka. A practical scheme to introduce explicit tidal forcing into an OGCM. *Ocean Sci.*, 9(6):1089, 2013.

T. B. Sanford. Motionally induced electric and magnetic fields in the sea. *J. Geophys. Res.*, 76(15):3476–3492, 1971.

T. B. Sanford. Temperature transport and motional induction in the Florida current. *J. Mar. Res.*, 40:621–639, 1982.

J. Saynisch, J. Petereit, C. Irrgang, A. Kuvshinov, and M. Thomas. Impact of climate variability on the tidal oceanic magnetic signal-A model-based sensitivity study. *J. Geophys. Res. Oceans*, 121(8):5931–5941, 2016. doi: 10.1002/2016JC012027.

A. Schiller and R. Fiedler. Explicit tidal forcing in an ocean general circulation model. *Geophys. Res. Lett.*, 34:L03611, 2007. doi: 10.1029/2006GL028363.

W. J. Schmitz Jr. On the world ocean circulation: Volume 2 the pacific and indian oceans/a global update. Technical report, WOODS HOLE OCEANOGRAPHIC INSTITUTION MA, 1996.

Friedrich A Schott, Thomas N Lee, and Rainer Zantopp. Variability of structure and transport of the Florida Current in the period range of days to seasonal. *J. Phys. Oceanogr.*, 18(9):1209–1230, 1988.

G. Seeber. *Satellite Geodesy.* Walter de Gruyter, Berlin, Germany, 2003.

A. J. Semtner. An oceanic general circulation model with bottom topography. Technical report no. 9, UCLA Department of Meteorology, 1974.

A. J. Semtner. Numerical simulation of the Arctic ocean circulation. *J. Phys. Oceanogr.*, 6:409–425, 1976. doi: 10.1175/1520-0485(1976)006⟨0409:NSOTAO⟩2.0.CO;2.

A. J. Semtner. A numerical study of sea ice and ocean circulation in the Arctic. *J. Phys. Oceanogr.*, 17:1077–1099, 1987. doi: 10.1175/1520-0485(1987)017⟨1077:ANSOSL⟩2.0.CO;2.

A. F. Shchepetkin and J. C. McWilliams. The regional oceanic modeling system (ROMS): a split-explicit, free-surface, topography-following-coordinate oceanic model. *Ocean Model.*, 9:347–404, 2005.

A. F. Shchepetkin and J. C. McWilliams. Computational kernel algorithms for fine-scale, multi-process, long-time oceanic simulations. In R. Temam and J. Tribbia, editors, *Handbook of Numerical Analysis: Computational Methods for the Ocean and the Atmosphere*, pages 121–183. Elsevier Science, 2008. ISBN: 978-0-444-51893-4.

J. Sheng, Wright D. G., Greatbatch R. J., and Dietrich D. E. CANDIE: A new version of the DieCAST ocean circulation model. *J. Atmos. Oceanic Technol.*, 15: 1414–1432, 1998. doi: 10.1175/1520-0426(1998)015⟨1414:CANVOT⟩2.0.CO;2.

G. Siedler, S. M. Griffies, J. Gould, and J. A. Church. *Ocean circulation and climate: A 21st century perspective*, volume 103. Academic Press, 2013.

A. Sielecki. An energy conserving difference scheme for the storm surge equations. *Mon. Weather Rev.*, 96:150–156, 1968. doi: 10.1175/1520-0493(1968)096⟨0150:AECDSF⟩2.0.CO;2.

H. L. Simmons, R. W. Hallberg, and B. K. Arbic. Internal wave generation in a global baroclinic tide model. *Deep-sea Res. Pt. II*, 51:3043–3068, 2004. doi: 10.1016/j.dsr2.2004.09.015.

B. S. Singer. Method for solution of Maxwell's equations in non-uniform media. *Geophys. J. Int.*, 120(3):590–598, 1995.

J. Smagorinsky. General circulation experiments with the primitive equations: I. the basic experiment. *Mon. Weather Rev.*, 91:99–164, 1963. doi: 10.1175/1520-0493(1963)091⟨0099:GCEWTP⟩2.3.CO;2.

J. Smagorinsky. Some historical remarks on the use of nonlinear viscosities. In B. Galperin and S.A. Orszag, editors, *Large Eddy Simulation of Complex Engineering and Geophysical Flows*, pages 3–36. Cambridge University Press, Cambridge, 1993.

R. Smith, P. Jones, B. Briegleb, F. Bryan, G. Danabasoglu, J. Dennis, J. Dukowicz, C. Eden, B. Fox-Kemper, P. Gent, M. Hecht, S. Jayne, M. Jochum, W. Large, K. Lindsay, M. Maltrud, N. Norton, S. Peacock, M. Vertenstein, and S. Yeager. The Parallel Ocean Program (POP) reference manual ocean component of the Community Climate System Model (CCSM) and Community Earth System Model (CESM). Technical report, Technical Report LAUR-10-01853, Los Alamos National Laboratory, Los Alamos, 2010. URL `http://www.cesm.ucar.edu/models/cesm1.0/pop2/doc/sci/POPRefManual.pdf`.

R. D. Smith and J. C. McWilliams. Anisotropic horizontal viscosity for ocean models. *Ocean model.*, 5(2):129–156, 2003.

Y. Song and D. Haidvogel. A semi–implicit ocean circulation model using a generalized topography–following coordinate system. *J. Comput. Phys.*, 15: 228–244, 1994. doi: 10.1006/jcph.1994.1189.

D. Stammer, R. D. Ray, O. B. Andersen, B. K. Arbic, W. Bosch, L. Carrère, Y. Cheng, D. S. Chinn, B. D. Dushaw, G. D. Egbert, et al. Accuracy assessment of global barotropic ocean tide models. *Rev. Geophys.*, 52(3):243–282, 2014.

A. Staniforth and J. Thuburn. Horizontal grids for global weather and climate prediction models: a review. *Q. J. Roy. Meteor. Soc.*, 138(662):1–26, 2012.

G. Starius. A solution to the pole problem for the shallow water equations on a sphere. *TWMS JPAM*, 5:152–170, 2014.

D. Stephenson and K. Bryan. Large-scale electric and magnetic fields generated by the oceans. *J. Geophys. Res.: Oceans*, 97(C10):15467–15480, 1992.

R. H. Stewart. *Introduction To Physical Oceanography.* World Scientific, 2008. URL `https://open.umn.edu/opentextbooks/textbooks/introduction-to-physical-oceanography`.

P. K. Sweby. High resolution schemes using flux limiters for hyperbolic conservation laws. *SIAM J. Numer. Anal.*, 21(5):995–1011, 1984.

E. Taguchi, D. Stammer, and W. Zahel. Inferring deep ocean tidal energy dissipation from the global high-resolution data-assimilative HAMTIDE model. *J. Geophys. Res.: Oceans*, 119(7):4573–4592, 2014.

E. Thébault, C. C. Finlay, C. D. Beggan, P. Alken, J. Aubert, O. Barrois, F. Bertrand, T. Bondar, A. Boness, L. Brocco, et al. International geomagnetic reference field: the 12th generation. *Earth Planets Space*, 67(1):1–19, 2015.

M. Thomas, J. Sündermann, and E. Maier-Reimer. Consideration of ocean tides in an OGCM and impacts on subseasonal to decadal polar motion excitation. *Geophys. Res. Lett.*, 28(12):2457–2460, 2001. doi: 10.1029/2000GL012234.

T. G. Thompson and H. E. Wirth. The specific gravity of seawater at zero degrees in relation to chlorinity. *J. Cons. int. Explor. Mer*, 6:232–240, 1931. doi: 10.1093/icesjms/6.2.232.

R. Timmermann, S. Danilov, J. Schröter, C. Böning, D. Sidorenko, and K. Rollenhagen. Ocean circulation and sea ice distribution in a finite element global sea ice-ocean model. *Ocean Dyn.*, 27:114–129, 2009. doi: 10.1016/j.ocemod.2008.10.009.

A. Treguier. Kinetic energy analysis of an eddy resolving, primitive equation North Atlantic model. *J. Geophys. Res.*, 97:687–701, 1992. doi: 10.1029/91JC02350.

K. E. Trenberth, W. G. Large, and J. G. Olson. The mean annual cycle in global ocean wind stress. *J. Phys. Oceanogr.*, 20:1742–1760, 1990. doi: 10.1175/1520-0485(1990)020⟨1742:TMACIG⟩2.0.CO;2.

H. Tsujino, T. Motoi, I. Ishikawa, M. Hirabara, H. Nakano, G. Yamanaka, T. Yasuda, and H. Ishizaki. Reference manual for the meteorological research institute community ocean model (MRI.com) version 3. Technical reports of the meteorological research institute no.59, Ocenographic research department, Meteorological Research Institute, Japan, Tsukuba, Japan, 2010. URL `http://www.mri-jma.go.jp/Publish/Technical/DATA/VOL_59/tec_rep_mri_59.pdf`.

R. H. Tyler. Mathematical modeling of electrodynamics near the surface of earth and planetary water worlds. In *Technical report TM-2017-219022, NASA*, 2017. URL `https://ntrs.nasa.gov/archive/nasa/casi.ntrs.nasa.gov/20170011279.pdf`.

R. H. Tyler, L. A. Mysak, and J. M. Oberhuber. Electromagnetic fields generated by a three dimensional global ocean circulation. *J. Geophys. Res.: Oceans*, 102 (C3):5531–5551, 1997.

R. H. Tyler, T. P. Boyer, T. Minami, M. M. Zweng, and J. R. Reagan. Electrical conductivity of the global ocean. *Earth Planets Space*, 69:156, 2017.

UNESCO. Background papers and supporting data on the international equation of state of seawater 1980. *UNESCO technical papers in marine sci.*, 36, 1981.

G. K. Vallis. *Atmospheric and Oceanic Fluid Dynamics, Fundamentals and Large–Scale Circulation*. Cambridge University Press, 2006.

G. D. Van Albada, B. Van Leer, and W. W. Roberts. A comparative study of computational methods in cosmic gas dynamics. In *Upwind and High-Resolution Schemes*, pages 95–103. Springer, 1997.

B. Van Leer. Towards the ultimate conservative difference scheme. ii. Monotonicity and conservation combined in a second-order scheme. *J. Comput. Phys.*, 14 (4):361–370, 1974.

D. A. Varshalovich, A. N. Moskalev, and V. K. Khersonskii. *Quantum theory of angular momentum*. World Scientific, 1988.

J. Velímský. Determination of three-dimensional distribution of electrical conductivity in the Earth's mantle from Swarm satellite data: Time-domain approach. *Earth Planets Space*, 65:1239–1246, 2013.

J. Velímský and Z. Martinec. Time-domain, spherical harmonic-finite element approach to transient three-dimensional geomagnetic induction in a spherical heterogeneous Earth. *Geophys. J. Int.*, 160:81–101, 2005.

J. Velímský, A. Grayver, A. Kuvshinov, and L. Šachl. On the modelling of M_2 tidal magnetic signatures: Effects of physical approximations and numerical resolution. *Earth Planets Space*, 70(1):70–192, 2018.

J. Velímský, L. Šachl, and Z. Martinec. The global toroidal magnetic field generated in the Earth's oceans. *Earth Planet. Sc. Lett.*, 509:47–54, 2019.

P. N. A. M. Visser, N. Sneeuw, T. Reubelt, M. Losch, and T. van Dam. Spaceborne gravimetric satellite constellation and ocean tides: Aliasing effects. *Geophys. J. Int.*, 181:789–805, 2010.

F. Vivier, E. Maier-Reimer, and R. H. Tyler. Simulations of magnetic fields generated by the Antarctic Circumpolar Current at satellite altitude: Can geomagnetic measurements be used to monitor the flow? *Geophys. Res. Lett.*, 31(10), 2004.

A. Voldoire, E. Sanchez-Gomez, D. S. Mélia, B. Decharme, Ch. Cassou, S. Sénési, S. Valcke, I. Beau, A. Alias, M. Chevallier, et al. The CNRM-CM5.1 global climate model: description and basic evaluation. *Clim. Dynam.*, 40(9-10): 2091–2121, 2013.

L. Šachl, D. Einšpigel, and Z. Martinec. Simple numerical tests for ocean tidal models. *Accepted to Stud. Geophys. Geod.*, 2020.

R. C. Wajsowicz. Free planetary waves in finite–difference numerical models. *J. Phys. Oceanogr.*, 16:773–789, 1986. doi: 10.1175/1520-0485(1986)016⟨0773:FPWIFD⟩2.0.CO;2.

R. C. Wajsowicz. A consistent formulation of the anisotropic stress tensor for use in models of the large–scale ocean circulation. *J. Comp. Phys.*, 105:333–338, 1993. doi: 10.1006/jcph.1993.1079.

D. Wang, Q. Liu, and X. Lv. A study on bottom friction coefficient in the Bohai, Yellow, and East China Sea. *Math. Probl. Eng.*, 2014, 2014.

G. L. Weatherly. An estimate of bottom frictional dissipation by gulf stream fluctuations. *J. Mar. Res.*, 42:289–301, 1984. doi: 10.1357/002224084788502729.

A. J. Weaver, M. Eby, E. C. Wiebe, C. M. Bitz, P. B. Duffy, T. L. Ewen, A. F. Fanning, M. M. Holland, A. MacFadyen, H. D. Matthews, et al. The UVic Earth System Climate Model: Model description, climatology, and applications to past, present and future climates. *Atmos. Ocean*, 39(4):361–428, 2001.

D. J. Webb, B. A. De Cuevas, and A. C. Coward. The first main run of the OCCAM global ocean model. *Internal document*, 34, 1998.

W. Weijer, W. P. M. De Ruijter, A. Sterl, and S. S. Drijfhout. Response of the Atlantic overturning circulation to South Atlantic sources of buoyancy. *Global Planet. Change*, 34(3-4):293–311, 2002.

J. Willebrand, B. Barnier, C. Böning, C. Dieterich, P. D. Killworth, C. Le Provost, Y. Jia, J. M. Molines, and A New. Circulation characteristics in three eddy–permitting models of the North Atlantic. *Prog. Oceanogr.*, 48:123–161, 2001. doi: 10.1016/S0079-6611(01)00003-9.

G. P. Williams. Friction term formulation and convective instability in a shallow atmosphere. *J. Atmos. Sci.*, 29(5):870–876, 1972.

D. L. Williamson, J. B. Drake, J. J. Hack, J. Rüdiger, and P. N. Swarztrauber. A standard test set for numerical approximations to the shallow water equations in spherical geometry. *J. Comput. Phys.*, 102(1):211–224, 1992. doi: 10.1016/S0021-9991(05)80016-6.

D. G. Wright. An equation of state for use in ocean models: Eckart's formula revisited. *J. Atmos. Oceanic Technol.*, 14:735–740, 1997. doi: 10.1175/1520-0426(1997)014⟨0735:AEOSFU⟩2.0.CO;2.

D. G. Wright and T. F. Stocker. A zonally averaged ocean model for the thermohaline circulation. Part I: Model development and flow dynamics. *J. Phys. Oceanogr.*, 21:1713–1724, 1991. doi: 10.1175/1520-0485(1991)021⟨1713:AZAOMF⟩2.0.CO;2.

C. Wunsch. The decadal mean ocean circulation and Sverdrup balance. *J. Marine Res.*, 69:417–434, 2011.

M. Yelland and P. K. Taylor. Wind stress measurements from the open ocean. *J. Phys. Oceanogr.*, 26:541–558, 1996. doi: 10.1175/1520-0485(1996)026⟨0541:WSMFTO⟩2.0.CO;2.

M. J. Yelland, B. I. Moat, P. K. Taylor, R. W. Pascal, J. Hutchings, and V. C. Cornell. Wind stress measurements from the open ocean corrected for airflow distortion by the ship. *J. Phys. Oceanogr.*, 28:1511–1526, 1998. doi: 10.1175/1520-0485(1998)028⟨1511:WSMFTO⟩2.0.CO;2.

E. D. Zaron and G. D. Egbert. Estimating open-ocean barotropic tidal dissipation: The Hawaiian Ridge. *J. Phys. Oceanogr.*, 36:1019–1035, 2006.

M. M. Zweng, J. R. Reagan, J. I. Antonov, R. A. Locarnini, A. V. Mishonov, T. P. Boyer, H. E. Garcia, O. K. Baranova, D. R. Johnson, D. Seidov, and M. M. Biddle. World ocean atlas 2013, volume 2: Salinity. In S. Levitus, editor, *NOAA Atlas NESDIS 74*, page 39. 2013.

A. Numerics used in IMP and CNmod schemes

The overbars in the symbols for barotropic velocities are dropped out in this section in order to simplify the notation. The spherical instead of generalized coordinates are considered. The numbering of grid points is the same as in Fig. 2.1.

A.1 IMP scheme

The discrete form of Eq. (4.10) on the Arakawa grid E is

$$\begin{aligned}
&A_1 v_{i+\frac{1}{2},j} + A_2 u_{i+\frac{3}{2},j} + (1+A_3) u_{i+\frac{1}{2},j} + A_4 u_{i-\frac{1}{2},j} \\
&+A_5 v_{i+\frac{1}{2},j+1} + A_6 v_{i-\frac{1}{2},j+1} + A_7 v_{i+\frac{3}{2},j-1} + A_8 v_{i+\frac{1}{2},j-1} = RHS_\lambda^n, \qquad \text{(A.1)}\\
&B_1 u_{i+\frac{1}{2},j} + B_2 v_{i-\frac{1}{2},j+2} + (1+B_3) v_{i+\frac{1}{2},j} + B_4 v_{i+\frac{3}{2},j-2} \\
&+B_5 u_{i+\frac{1}{2},j+1} + B_6 u_{i-\frac{1}{2},j+1} + B_7 u_{i+\frac{1}{2},j-1} + B_8 u_{i+\frac{3}{2},j-1} = RHS_\phi^n, \qquad \text{(A.2)}
\end{aligned}$$

where

$$A_1 = -f\Delta t, \tag{A.3}$$

$$[A_2, A_3, A_4] = K_1 \left[-\overline{h^n}^{i+\frac{3}{2},j}, 2\overline{h^n}^{i+\frac{1}{2},j}, -\overline{h^n}^{i-\frac{1}{2},j} \right], \tag{A.4}$$

$$\begin{aligned}
[A_5, A_6, A_7, A_8] = K_2 \Big[&-\Delta x_{j-1} \overline{h^n}^{i+\frac{1}{2},j+1}, \Delta x_{j-1} \overline{h^n}^{i-\frac{1}{2},j+1}, \\
&\Delta x_{j+1} \overline{h^n}^{i+\frac{3}{2},j-1}, -\Delta x_{j+1} \overline{h^n}^{i+\frac{1}{2},j-1} \Big],
\end{aligned} \tag{A.5}$$

$$B_1 = -f\Delta t, \tag{A.6}$$

$$\begin{aligned}
[B_2, B_3, B_4] = K_3 \Big[&-\frac{\Delta x_{j+2}}{\Delta x_{j+1}} \overline{h^n}^{i-\frac{1}{2},j+2}, \left(\frac{\Delta x_j}{\Delta x_{j+1}} + \frac{\Delta x_j}{\Delta x_{j-1}} \right) \overline{h^n}^{i+\frac{1}{2},j}, \\
&-\frac{\Delta x_{j-2}}{\Delta x_{j-1}} \overline{h^n}^{i+\frac{3}{2},j-2} \Big],
\end{aligned} \tag{A.7}$$

$$[B_5, B_6, B_7, B_8] = K_2 \left[-\frac{\overline{h^n}^{i+\frac{1}{2},j+1}}{\Delta x_{j+1}}, \frac{\overline{h^n}^{i-\frac{1}{2},j+1}}{\Delta x_{j+1}}, -\frac{\overline{h^n}^{i+\frac{3}{2},j-1}}{\Delta x_{j-1}}, \frac{\overline{h^n}^{i+\frac{1}{2},j-1}}{\Delta x_{j-1}} \right], \tag{A.8}$$

$$K_1 = \frac{g(\Delta t)^2}{(\Delta x_j)^2}, \quad K_2 = \frac{g(\Delta t)^2}{(\Delta x_j)^2 \Delta y}, \quad K_3 = \frac{g(\Delta t)^2}{(\Delta y)^2}, \tag{A.9}$$

$$RHS_\lambda^n = u_{i+\frac{1}{2},j}^n + g\Delta t \frac{\delta_{i+\frac{1}{2}}\eta}{\Delta x_j} + F_\lambda^n \Delta t, \tag{A.10}$$

$$RHS_\phi^n = v_{i+\frac{1}{2},j}^n + g\Delta t \frac{\delta_j \eta}{\Delta y} + F_\phi^n \Delta t, \tag{A.11}$$

where Δx and Δy denote the zonal and meridional grid spacings in the geographic coordinates, respectively.

A.2 CNmod scheme

The discrete form of Eq. (4.13) on the Arakawa grid C is

$$-\eta_{i+1,j}k_1 - \eta_{i-1,j}k_2 + \eta_{i,j}(1 + k_1 + k_2 + k_3 + k_4) - \eta_{i,j+1}k_3 - \eta_{i,j-1}k_4 = RHS, \quad \text{(A.12)}$$

where

$$RHS = (h_{i,j} - H_{i,j}) - \beta_c \Delta t \left[\frac{\delta_i \left(\overline{h}^{i+\frac{1}{2}} u^*_{i+\frac{1}{2},j} \right)}{\Delta x_j} + \frac{\delta_j \left(\overline{h}^{j+\frac{1}{2}} v_{i,j+\frac{1}{2}} \Delta x_{j+\frac{1}{2}} \right)}{\Delta x_j \Delta y} \right], \quad \text{(A.13)}$$

$$\begin{aligned} k_1 &= K_c \frac{\overline{h}^{i+\frac{1}{2}}}{(\Delta x_j)^2}, & k_3 &= K_c \frac{\overline{h}^{j+\frac{1}{2}} \Delta x_{j+\frac{1}{2}}}{(\Delta y)^2 \Delta x_j}, \\ k_2 &= K_c \frac{\overline{h}^{i-\frac{1}{2}}}{(\Delta x_j)^2}, & k_4 &= K_c \frac{\overline{h}^{j-\frac{1}{2}} \Delta x_{j-\frac{1}{2}}}{(\Delta y)^2 \Delta x_j}, \end{aligned} \quad \text{(A.14)}$$

and $K_c = \beta_c \gamma_c g (\Delta t)^2$.

B. Form of the friction force

B.1 Friction force for a baroclinic ocean model with partial bottom cells

The friction force in general horizontal coordinates was derived and discussed by Murray and Reason [2001]. However, Murray and Reason [2001] did not allow partial bottom cells since they assumed that the third metric coefficient is independent of horizontal coordinates,

$$\frac{\partial h_3}{\partial \xi_1} = \frac{\partial h_3}{\partial \xi_2} = 0. \tag{B.1}$$

The LSOMG is using partial bottom cells, it is thus necessary to generalize the formulas for the case without conditions B.1. We calculate the divergence of Cauchy stress tensor $\boldsymbol{\sigma}$,

$$\begin{aligned}\mathbf{F}^{(\mathbf{u})} \cdot \mathbf{e}_1 = (\nabla \cdot \boldsymbol{\sigma}) \cdot \mathbf{e}_1 = \frac{1}{h_1 h_2 h_3} \left[\frac{\partial}{\partial \xi_1}(h_2 h_3 \sigma_{11}) + \frac{\partial}{\partial \xi_2}(h_3 h_1 \sigma_{21}) + \frac{\partial}{\partial \xi_3}(h_1 h_2 \sigma_{31}) \right] \\ + \frac{1}{h_2 h_1} \left(\frac{\partial h_1}{\partial \xi_2} \sigma_{12} - \frac{\partial h_2}{\partial \xi_1} \sigma_{22} \right) + \frac{1}{h_3 h_1} \left(\frac{\partial h_1}{\partial \xi_3} \sigma_{13} - \frac{\partial h_3}{\partial \xi_1} \sigma_{33} \right)\end{aligned} \tag{B.2}$$

and apply condition 5.15 by which we assume that the horizontal metric coefficients are independent of ξ_3, and we consider that σ_{33} is negligible, see Murray and Reason [2001] for the discussion. Consequently,

$$\frac{1}{h_3 h_1} \frac{\partial h_1}{\partial \xi_3} \sigma_{13} = 0, \qquad \frac{\partial}{\partial \xi_3}(h_1 h_2 \sigma_{31}) = h_1 h_2 \frac{\partial \sigma_{31}}{\partial \xi_3}, \qquad \frac{1}{h_3 h_1} \frac{\partial h_3}{\partial \xi_1} \sigma_{33} = 0, \tag{B.3}$$

and Eq. (B.2) simplifies,

$$\begin{aligned}\mathbf{F}^{(\mathbf{u})} \cdot \mathbf{e}_1 = \frac{1}{h_1 h_2} \left[\frac{1}{h_3} \frac{\partial}{\partial \xi_1}(h_2 h_3 \sigma_{11}) + \frac{1}{h_3} \frac{\partial}{\partial \xi_2}(h_3 h_1 \sigma_{21}) + \sigma_{21} \frac{\partial h_1}{\partial \xi_2} - \sigma_{22} \frac{\partial h_2}{\partial \xi_1} \right] \\ + \frac{1}{h_3} \frac{\partial \sigma_{31}}{\partial \xi_3}.\end{aligned} \tag{B.4}$$

According to Murray and Reason [2001], we rearrange the terms in the square bracket,

$$\begin{aligned}\mathbf{F}^{(\mathbf{u})} \cdot \mathbf{e}_1 = \frac{1}{h_1 h_2} \Bigg\{ \frac{1}{h_3} \frac{\partial}{\partial \xi_1} \left[h_2 h_3 \left(\frac{\sigma_{11} - \sigma_{22}}{2} + \frac{\sigma_{11} + \sigma_{22}}{2} \right) \right] + \frac{1}{h_3} \frac{\partial}{\partial \xi_2}(h_3 h_1 \sigma_{21}) \\ + \sigma_{21} \frac{\partial h_1}{\partial \xi_2} + \left(\frac{\sigma_{11} - \sigma_{22}}{2} - \frac{\sigma_{11} + \sigma_{22}}{2} \right) \frac{\partial h_2}{\partial \xi_1} \Bigg\} + \frac{1}{h_3} \frac{\partial \sigma_{31}}{\partial \xi_3}.\end{aligned} \tag{B.5}$$

Terms that contain $\sigma_{11} + \sigma_{22}$ can be neglected because they are proportional to σ_{33} due to the zero trace of $\boldsymbol{\sigma}$, see Eq. 1.47. We insert Eq. (20) from Murray and Reason [2001],

$$\frac{\sigma_{11} - \sigma_{22}}{2} = A_H D_T, \tag{B.6}$$

$$\sigma_{12} = A_H D_S, \tag{B.7}$$

$$\sigma_{31} = \sigma_{13} = 2 A_V e_{13}, \tag{B.8}$$

into Eq. (B.5),

$$\begin{aligned}
\mathbf{F}^{(\mathbf{u})} \cdot \mathbf{e}_1 &= \frac{1}{h_1 h_2}\left[\frac{1}{h_3}\frac{\partial}{\partial \xi_1}\left(h_2 h_3 A_H D_T\right) + \frac{1}{h_3}\frac{\partial}{\partial \xi_2}\left(h_1 h_3 A_H D_S\right)\right. \\
&\quad \left. + A_H D_S \frac{\partial h_1}{\partial \xi_2} + A_H D_T \frac{\partial h_2}{\partial \xi_1}\right] + \frac{1}{h_3}\frac{\partial}{\partial \xi_3}\left(2 A_V e_{13}\right), \\
&= \frac{1}{h_1 h_2}\left[\frac{1}{h_2 h_3}\frac{\partial}{\partial \xi_1}\left(h_2^2 h_3 A_H D_T\right) + \frac{1}{h_1 h_3}\frac{\partial}{\partial \xi_2}\left(h_1^2 h_3 A_H D_S\right)\right] \\
&\quad + \frac{1}{h_3}\frac{\partial}{\partial \xi_3}\left(2 A_V e_{13}\right). \qquad \text{(B.9)}
\end{aligned}$$

Finally, we obtain Eq. 5.67 if we use the expression for e_{13},

$$e_{13} = \frac{1}{2h_3}\frac{\partial u}{\partial \xi_3} + \frac{1}{2h_1}\frac{\partial w}{\partial \xi_1}, \qquad \text{(B.10)}$$

where the second term can be neglected according to Murray and Reason [2001]. We apply a similar procedure to the meridional component to obtain Eq. 5.68.

B.2 Friction force for a barotropic ocean model

Einšpigel and Martinec [2015] derived a physically consistent friction force for a barotropic ocean model. They considered a 3-D physically consistent stress tensor derived by Wajsowicz [1993] and calculated the friction force from the stress tensor using Eq. (1.46). The barotropic friction force was then calculated by vertically integrating the friction force under the assumption that the horizontal flow is only weakly dependent on the depth. Mathematically expressed,

$$\mathbf{u} = \bar{\mathbf{u}} + O(\epsilon),\ \ \overline{u^2} = \bar{u}^2 + O(\epsilon),\ \ \overline{v^2} = \bar{v}^2 + O(\epsilon),\ \ \overline{uv} = \bar{u}\bar{v} + O(\epsilon), \qquad \text{(B.11)}$$

where ϵ is a small quantity. The resulting barotropic friction force is

$$\mathbf{F}^{(\mathbf{u})} \cdot \mathbf{e}_1 = \frac{A_H}{ah}\left\{\frac{1}{\cos\phi}\frac{\partial}{\partial \lambda}\left[h\left(\widehat{e_{11}} - \widehat{e_{22}}\right)\right] + 2\frac{\partial}{\partial \phi}\left(h\widehat{e_{12}}\right) - 4h\widehat{e_{12}}\tan\phi\right\} \qquad \text{(B.12)}$$

$$\mathbf{F}^{(\mathbf{u})} \cdot \mathbf{e}_2 = \frac{A_H}{ah}\left\{\frac{2}{\cos\phi}\frac{\partial}{\partial \lambda}\left(h\widehat{e_{12}}\right) - \frac{\partial}{\partial \phi}\left[h\left(\widehat{e_{11}} - \widehat{e_{22}}\right)\right] + 2h\left(\widehat{e_{11}} - \widehat{e_{22}}\right)\tan\phi\right\} \qquad \text{(B.13)}$$

where $\widehat{e_{11}}$, $\widehat{e_{22}}$ and $\widehat{e_{12}}$ are components of barotropic strain-rate tensor,

$$\hat{\mathbf{e}} = \frac{1}{2}\left[\nabla_h \bar{\mathbf{u}} + \left(\nabla_h \bar{\mathbf{u}}\right)^T\right]. \qquad \text{(B.14)}$$

We mentioned in Sec. 5.6.1 that the friction force given by Eqs. (B.12) and (B.13) can be viewed as a special case of Eqs. (5.67) and (5.68). Indeed, take the horizontal friction from Eqs. (5.67) and (5.68), replace the third metric coefficient by the water-column height, use spherical-coordinate metric coefficients $h_1 = a\cos\phi$,

$h_2 = a$ and calculate the horizontal tension $\widehat{D_T}$ and shearing strain $\widehat{D_S}$ using the barotropic velocities,

$$\mathbf{F}^{(\mathbf{u})} \cdot \mathbf{e}_1 = \frac{1}{a^2 h \cos\phi} \left[\frac{1}{a} \frac{\partial}{\partial \lambda} \left(a^2 h A_H \widehat{D_T} \right) + \frac{1}{a \cos\phi} \frac{\partial}{\partial \phi} \left(a^2 \cos^2 \phi h A_H \widehat{D_S} \right) \right], \tag{B.15}$$

$$\mathbf{F}^{(\mathbf{u})} \cdot \mathbf{e}_2 = \frac{1}{a^2 h \cos\phi} \left[\frac{1}{a} \frac{\partial}{\partial \lambda} \left(a^2 h A_H \widehat{D_S} \right) - \frac{1}{a \cos\phi} \frac{\partial}{\partial \phi} \left(a^2 \cos^2 \phi h A_H \widehat{D_T} \right) \right]. \tag{B.16}$$

If we further assume that A_H is constant and rewrite the second term on the right-hand side of Eqs. (B.15) and (B.16),

$$\mathbf{F}^{(\mathbf{u})} \cdot \mathbf{e}_1 = \frac{A_H}{ah} \left[\frac{1}{\cos\phi} \frac{\partial}{\partial \lambda} \left(h\widehat{D_T} \right) + \frac{\partial}{\partial \phi} \left(h\widehat{D_S} \right) - 2h\widehat{D_S} \tan\phi \right], \tag{B.17}$$

$$\mathbf{F}^{(\mathbf{u})} \cdot \mathbf{e}_2 = \frac{A_H}{ah} \left[\frac{1}{\cos\phi} \frac{\partial}{\partial \lambda} \left(h\widehat{D_S} \right) - \frac{\partial}{\partial \phi} \left(h\widehat{D_T} \right) + 2h\widehat{D_T} \tan\phi \right]. \tag{B.18}$$

Eqs. (B.17) and (B.18) turn to Eqs. (B.12) and (B.13) if we consider Eqs. (1.56) and (1.57)

C. Invariants in the shallow water equations

The overbars in the symbols for barotropic velocities are dropped out in this chapter in order to simplify the notation.

C.1 Energy in the shallow water equations

The purpose of Appendices C.1 and C.2 is to generalize the derivation of McWilliams [2006] and make it more clear. We consider SWE in the advective form, see Eqs. (4.1) and (4.2). We next follow McWilliams [2006], Eq. (4.16), and write down the following integral identity,

$$\begin{aligned}0 = \int\limits_A \Bigg\{ & h\mathbf{u} \cdot \left(\frac{\partial \mathbf{u}}{\partial t} + \mathbf{u} \cdot \nabla \mathbf{u} + f\mathbf{k} \times \mathbf{u} + g\nabla\eta - \mathbf{F} \right) \\ & + \left(g\eta + \frac{1}{2}\mathbf{u}^2 \right) \left[\frac{\partial h}{\partial t} + \nabla \cdot (h\mathbf{u}) \right] \Bigg\} dA, \end{aligned} \tag{C.1}$$

where A stands for the whole ocean surface and dA is its infinitesimal element. The identity is valid because of Eqs. (4.1) and (4.2). The individual terms can be rewritten as

$$h\mathbf{u} \cdot (f\mathbf{k} \times \mathbf{u}) = 0 \tag{C.2}$$

$$h\mathbf{u} \cdot \left(\frac{\partial \mathbf{u}}{\partial t} + \mathbf{u} \cdot \nabla \mathbf{u} \right) = \frac{1}{2} h \frac{\partial \mathbf{u}^2}{\partial t} + \frac{1}{2} h\mathbf{u} \cdot \nabla \mathbf{u}^2 \tag{C.3}$$

$$\begin{aligned}\left(g\eta + \frac{1}{2}\mathbf{u}^2 \right) \left[\frac{\partial h}{\partial t} + \nabla \cdot (h\mathbf{u}) \right] &= g\eta \frac{\partial h}{\partial t} + g\eta\nabla \cdot (h\mathbf{u}) + \frac{1}{2}\mathbf{u}^2 \frac{\partial h}{\partial t} + \frac{1}{2}\mathbf{u}^2 \nabla \cdot (h\mathbf{u}) \\ &= \frac{\partial}{\partial t}\left(\frac{1}{2} g\eta^2 \right) + \nabla \cdot (g\eta h\mathbf{u}) - gh\mathbf{u} \cdot \nabla\eta \\ &+ \frac{1}{2}\mathbf{u}^2 \frac{\partial h}{\partial t} + \frac{1}{2}\mathbf{u}^2 \nabla \cdot (h\mathbf{u}), \end{aligned} \tag{C.4}$$

We insert Eqs. (C.2), (C.3) and (C.4) into (C.1) and combine certain terms to obtain

$$\begin{aligned}0 = \int\limits_A \Bigg\{ & \left[\frac{1}{2} h \frac{\partial \mathbf{u}^2}{\partial t} + \frac{1}{2} h\mathbf{u} \cdot \nabla \mathbf{u}^2 \right] + gh\mathbf{u} \cdot \nabla\eta - h\mathbf{F} \cdot \mathbf{u} \\ & + \Bigg[\frac{\partial}{\partial t}\left(\frac{1}{2} g\eta^2 \right) + \nabla \cdot (g\eta h\mathbf{u}) - gh\mathbf{u} \cdot \nabla\eta \\ & + \frac{1}{2}\mathbf{u}^2 \frac{\partial h}{\partial t} + \frac{1}{2}\mathbf{u}^2 \nabla \cdot (h\mathbf{u}) \Bigg] \Bigg\} dA =, \\ = & \int\limits_A \left[\frac{\partial}{\partial t}\left(\frac{1}{2} h\mathbf{u}^2 + \frac{1}{2} g\eta^2 \right) \right] dA - \int\limits_A h\mathbf{F} \cdot \mathbf{u} dA \\ + & \int\limits_A \left[\frac{1}{2} \nabla \cdot \left(h\mathbf{u}^2 \mathbf{u} \right) + \nabla \cdot (g\eta h\mathbf{u}) \right] dA, \end{aligned} \tag{C.5}$$

where the last term is equal to zero if we apply the Gauss theorem and the boundary conditions (4.6) or (4.7). Hence, we obtain the evolution equation

$$\frac{dE}{dt} - \int\limits_A h\mathbf{F} \cdot \mathbf{u} dA = 0 \tag{C.6}$$

for the total mechanical energy (defined by Eq. (6.5)). In the special case of no external force being applied, the total mechanical energy is time invariant. If external force is applied, the quantity E^g defined by Eq. (6.9) is a time invariant.

C.2 Potential vorticity in the shallow water equations

Similarly as in Appendix C.1, we build the derivation on the integral identity,

$$0 = \int\limits_A \left(nhq^{n-1} \left[\frac{\partial q}{\partial t} + \mathbf{u} \cdot \nabla q - \frac{\nabla \times \mathbf{F}}{h} \right] + q^n \left[\frac{\partial h}{\partial t} + \nabla \cdot (h\mathbf{u}) \right] \right) dA, \tag{C.7}$$

which is valid due to Eqs. (4.2) and (4.24) in McWilliams [2006]. We apply the identity

$$nhq^{n-1}\mathbf{u} \cdot \nabla q = \nabla \cdot (h\mathbf{u}q^n) - q^n \nabla \cdot (h\mathbf{u}), \tag{C.8}$$

the Gauss theorem and boundary conditions (4.6) or (4.7) to obtain

$$0 = \frac{d}{dt} \int\limits_A hq^n dA - \int\limits_A nq^{n-1} (\nabla \times \mathbf{F}) dA. \tag{C.9}$$

In the special case of no external force being applied, the quantity Q_n, defined by Eq. (6.6), is time-invariant. If external force is applied, quantity Q_n^g, defined by Eq. (6.10) is time invariant.

C.3 Discrete forms of invariants

We use the C-grid differencing and 2-point spatial averaging operators in the discrete forms of equations as introduced by Eqs. (2.8) and (2.9), respectively. The equivalent operators on Arakawa grids B/E are constructed analogously. On Arakawa grids B/E, we also introduce a 4-point averaging operator,

$$\overline{A}^{i,j} = \frac{A_{i+\frac{1}{2},j+\frac{1}{2}} + A_{i-\frac{1}{2},j+\frac{1}{2}} + A_{i+\frac{1}{2},j-\frac{1}{2}} + A_{i-\frac{1}{2},j-\frac{1}{2}}}{4} \tag{C.10}$$

on Arakawa grid B and analogously on Arakawa grid E.

The potential energy is naturally discretized as

$$E_p = \frac{g}{2} \sum_{i,j} \eta_{i,j}^2 \Delta x_j \Delta y, \tag{C.11}$$

and no averaging is needed. On the contrary, the averaging has to be applied to compute the kinetic energy since Arakawa grids B, C and E are staggered.

We prefer the averaging of the squared velocity components over the averaging of SSH,

$$E_k = \frac{1}{2}\sum_{i,j} h_{i,j}^2 \left(\overline{u^2}^i + \overline{v^2}^j\right) \Delta x_j \Delta y \quad \text{on Arakawa grid C,} \tag{C.12}$$

$$E_k = \frac{1}{2}\sum_{i,j} h_{i,j}^2 \left(\overline{u^2 + v^2}^{i,j}\right) \Delta x_j \Delta y \quad \text{on Arakawa grids B and E.} \tag{C.13}$$

The reason is that both potential and kinetic energy are discretized at SSH points. Nevertheless, the latter choice gives nearly identical results since

$$\sum_i A_i \overline{B}^i = \sum_i \overline{A}^{i+\frac{1}{2}} B_{i+\frac{1}{2}}. \tag{C.14}$$

The relative vorticity and invariant Q_n^g require the computation of a rotation operator. In the spherical coordinates, this is given by

$$\nabla \times \mathbf{F} = \frac{1}{R\cos\phi}\left[F^{\phi}_{,\lambda} + (F^{\lambda}\cos\phi)_{,\phi}\right]. \tag{C.15}$$

Its discrete form depends on the type of the Arakawa grid,

$$(\nabla \times \mathbf{F})_{i+\frac{1}{2},j+\frac{1}{2}} = \frac{1}{\Delta x_{j+\frac{1}{2}}}\left[\delta_i F^{\phi}_{i,j+\frac{1}{2}} + \frac{\delta_{j+\frac{1}{2}}\left(\Delta x_j F^{\lambda}_{i+\frac{1}{2},j}\right)}{\Delta y}\right] \quad \text{on Arakawa grid C,} \tag{C.16}$$

$$(\nabla \times \mathbf{F})_{i,j} = \frac{1}{\Delta x_j}\left[\delta_i F^{\phi}_{i+\frac{1}{2},j} + \frac{\delta_j\left(\Delta x_{j+1} F^{\lambda}_{i-\frac{1}{2},j+1}\right)}{\Delta y}\right] \quad \text{on Arakawa grid E,} \tag{C.17}$$

$$(\nabla \times \mathbf{F})_{i,j} = \frac{1}{\Delta x_j}\left[\delta_i \overline{F^{\phi}}^j + \frac{\delta_j\left(\overline{\Delta x F^{\lambda}}^i\right)}{\Delta y}\right] \quad \text{on Arakawa grid B.} \tag{C.18}$$

Note that there is no averaging on Arakawa grids C/E, but it is present on Arakawa grid B.

The source term in Eq. C.6 representing the work done by tidal forcing needs special attention. Its spatial discretization is simple, the difficult part is the discretization in time since the dot product between vectors of tidal force and velocity is integrated in time over the duration of experiment. If the velocity is discretized incorrectly in time, the induced phase shifts generate errors that add up during the computation via the integration process. Consider a simplified case in which the water-column height h is approximated by the depth H of the ocean bottom and repeat the first step of the derivation given in Appendix C.1,

$$0 = \int_A \left[H\hat{\mathbf{u}} \cdot \left(\frac{\mathbf{u} - \mathbf{u}^n}{\Delta t} - \mathbf{F}^n + \dots\right) + \dots\right] dA, \tag{C.19}$$

where dots stand for other terms that are not important for this discussion. The task is to determine the velocity $\widehat{\mathbf{u}}$ to obtain the discrete form of the time derivative of kinetic energy. If we choose

$$\widehat{\mathbf{u}} = \frac{\mathbf{u} + \mathbf{u}^n}{2}, \tag{C.20}$$

and plug it into Eq. C.19, we obtain

$$0 = \int\limits_A \left(\frac{H\mathbf{u}^2/2 - H(\mathbf{u}^n)^2/2}{\Delta t} \right) dA - \int\limits_A \left[\left(H\mathbf{F}^n \cdot \frac{\mathbf{u} + \mathbf{u}^n}{2} + \ldots \right) + \ldots \right] dA, \tag{C.21}$$

which finally leads to the discrete form of Eq. C.6.

D. Implementation details of Yin-Yang and reduced spherical coordinate grids

D.1 Bilinear and inverse-distance-weighting interpolations on the Yin-Yang grid

We interpolate both SSH and velocities. Consider, for example, the SSH interpolation. We use either the bilinear or the inverse-distance-weighting (IDW) interpolation. Both interpolation techniques calculate the interpolated SSH $\widehat{\eta}$ at $(\lambda,\ \phi)$ from the four nearest grid points,

$$\widehat{\eta}(\lambda, \phi) = \left(\sum_{ij=1}^{2} w_{i,j}\eta_{ij} \right) / \left(\sum_{i,j=1}^{2} w_{ij} \right), \tag{D.1}$$

where η_{ij} are SSHs at the nearest grid points with the geographic coordinates (λ_i, ϕ_j) and w_{ij} are weights.

In the bilinear interpolation, the weights are given by

$$\begin{aligned} w_{11} &= Z_2 M_2, \qquad & w_{21} &= Z_1 M_2, \\ w_{12} &= Z_2 M_1, \qquad & w_{22} &= Z_1 M_1, \end{aligned} \tag{D.2}$$

where

$$Z_1 = \min(|\lambda_1 - \lambda|, 360 - |\lambda_1 - \lambda|), \tag{D.3}$$

$$Z_2 = \min(|\lambda_2 - \lambda|, 360 - |\lambda_2 - \lambda|), \tag{D.4}$$

$$M_1 = |\phi_1 - \phi|, \tag{D.5}$$

$$M_2 = |\phi_2 - \phi|. \tag{D.6}$$

In the IDW interpolation, the weights are given by

$$w_{ij} = d_{ij}^{-1}, \tag{D.7}$$

where d_{ij} is the spherical distance between the points (λ, ϕ) and $(\lambda_{ij}, \phi_{ij})$,

$$d_{ij} = \arccos\left[\sin\phi \sin\phi_{ij} + \cos\phi \cos\phi_{ij} \cos(\lambda - \lambda_{ij})\right]. \tag{D.8}$$

Note that the bilinear and IDW interpolations are equivalent in one dimension.

D.2 Coriolis term on the Yin-Yang grid

It can be proved that the Coriolis force on the Yin-Yang grid has the same form as on the standard spherical-coordinate grid. It is sufficient to prove it for the Yang part. The components of the Coriolis force on the Yang part are equal to

$$\mathbf{F}_c^a = R\mathbf{F}_c^i = RC \begin{pmatrix} u^i \\ v^i \end{pmatrix} = RCR^{-1} \begin{pmatrix} u^a \\ v^a \end{pmatrix}, \tag{D.9}$$

where $\mathbf{F}_c$ is the vector containing components of the Coriolis force, C is the Coriolis-force matrix,

$$C = \begin{pmatrix} 0 & -f \\ f & 0 \end{pmatrix}, \tag{D.10}$$

f is the Coriolis parameter and R is the rotation matrix from Yin to Yang coordinate system given by Eq. (4.58). If the Yang coordinate system is rotated by the angle α with respect to the Yin coordinate system then

$$R(\alpha) = \begin{pmatrix} \cos\alpha & -\sin\alpha \\ \sin\alpha & \cos\alpha \end{pmatrix}, \tag{D.11}$$

where α is positive if the Yang coordinate system is rotated counter-clockwise with respect to the Yin coordinate system.

It holds that $R^{-1} = R(-\alpha) = R^T$ since R is the rotation matrix. It is thus sufficient to prove that either R or R^T commute with C,

$$RC = CR, \tag{D.12}$$

$$CR^T = R^T C. \tag{D.13}$$

The both equalities are valid which can be proved by simply evaluating the left-hand and right-hand sides.

An alternative and more elegant proof of Eqs. (D.12) and (D.13) uses the fact that matrix C is also a rotation matrix,

$$C = f \begin{pmatrix} 0 & -1 \\ 1 & 0 \end{pmatrix} = fR(90^\circ) \tag{D.14}$$

and thus

$$RC = R(\alpha) f R(90^\circ) = fR(\alpha + 90^\circ) = fR(90^\circ)R(\alpha) = CR, \tag{D.15}$$

where we used the fact that rotations around one common axis can be applied in an arbitrary order.

Using commutators (D.12) and (D.13), we can rewrite Eq. (D.9) to the well-known form,

$$\mathbf{F}_c^a = RCR^T \begin{pmatrix} u^a \\ v^a \end{pmatrix} = CRR^T \begin{pmatrix} u^a \\ v^a \end{pmatrix} = C \begin{pmatrix} u^a \\ v^a \end{pmatrix}. \tag{D.16}$$

D.3 Interpolations on the reduced spherical coordinate grid

Consider a 1-D space where we have a grid with the regular grid spacing d and a smooth function f. Taylor expansion can used to express the function values at the grid points x_{j-1} and x_{j+1} using the function value and its derivative at the grid point x_j.

$$f(x_j) + f'(x_j)d + O(d^2) = f(x_{j+1}) \tag{D.17}$$

$$f(x_j) - f'(x_j)d + O(d^2) = f(x_{j-1}) \tag{D.18}$$

Eqs. (D.17) and (D.18) can be used to derive an approximate formula for $f(x_j)$ and $f'(x_j)$ using $f(x_{j-1})$ and $f(x_{j+1})$,

$$\begin{pmatrix} f(x_j) \\ f'(x_j) \end{pmatrix} = A^{-1} \begin{pmatrix} f(x_{j+1}) \\ f(x_{j-1}) \end{pmatrix}, \tag{D.19}$$

where

$$A = \begin{pmatrix} 1 & d \\ 1 & -d \end{pmatrix}. \tag{D.20}$$

The solution of Eq. (D.19) are the well-known two-point formulas for the centered interpolation and derivative,

$$f(x_j) = \frac{f(x_{j-1}) + f(x_{j+1})}{2}, \tag{D.21}$$

$$f'(x_j) = \frac{f(x_{j+1}) - f(x_{j-1})}{2d}. \tag{D.22}$$

We use the same procedure to derive the eight-point interpolation formulas,

$$\begin{aligned} f_{j+\frac{1}{2}} &= \frac{1225}{2048}\left(f_j + f_{j+1}\right) - \frac{245}{2048}\left(f_{j-1} + f_{j+2}\right) + \frac{49}{2048}\left(f_{j-2} + f_{j+3}\right) \\ &\quad - \frac{5}{2048}\left(f_{j-3} + f_{j+4}\right), \end{aligned} \tag{D.23}$$

$$\begin{aligned} f_{j+\frac{1}{4}} &= \frac{225225}{262144} f_j + \frac{75075}{262144} f_{j+1} - \frac{27027}{262144} f_{j-1} - \frac{19305}{262144} f_{j+2} \\ &\quad + \frac{5005}{262144} f_{j-2} + \frac{4095}{262144} f_{j+3} - \frac{495}{262144} f_{j-3} - \frac{429}{262144} f_{j+4}, \end{aligned} \tag{D.24}$$

and ten-point interpolation formulas,

$$\begin{aligned} f_j &= \frac{5}{6}\left(f_{j+1} + f_{j-1}\right) - \frac{10}{21}\left(f_{j+2} + f_{j-2}\right) + \frac{5}{28}\left(f_{j+3} + f_{j-3}\right) \\ &\quad - \frac{5}{126}\left(f_{j+4} + f_{j-4}\right) + \frac{1}{252}\left(f_{j+5} + f_{j-5}\right), \end{aligned} \tag{D.25}$$

$$\begin{aligned} f_{j+\frac{1}{2}} &= \frac{39690}{65536}\left(f_j + f_{j+1}\right) - \frac{8820}{65536}\left(f_{j-1} + f_{j+2}\right) + \frac{2268}{65536}\left(f_{j-2} + f_{j+3}\right) \\ &\quad - \frac{405}{65536}\left(f_{j-3} + f_{j+4}\right) + \frac{35}{65536}\left(f_{j-4} + f_{j+5}\right) \end{aligned} \tag{D.26}$$

where we used $f_j = f(x_j)$, $f_{j+\frac{1}{2}} = f\left(\frac{x_j + x_{j+1}}{2}\right)$ and $f_{j+\frac{1}{4}} = f\left(\frac{x_j + 3x_{j+1}}{4}\right)$ to shorten the formulas.

Note that the systems of eight and ten linear equations have to be solved to derive the eight- and ten-point interpolation formulas. We used the Mathematica software since the problem is already too complex to solve it in hand.

E. Interpolation error of the bilinear interpolation

The error of bilinear interpolation used in the method of spatial patterns in Sec. 6.1 could be, in principle, of the same order or even larger than the inspected differences between the model configurations. One may argue that either a higher-order method or even a completely different interpolation technique should be used. We provide two tests that clearly show that this is not the case:

1. We apply the bilinear interpolation to the initial SSH of the TSU test and compare the interpolated C-grid SSH with the untouched E-grid SSH. The differences are depicted in the left panel of Fig. E.1. The differences are not zero (except for the grid points which are common for both grids) but they do not exceed 0.24 m which corresponds to 0.24% of the maximum SSH.

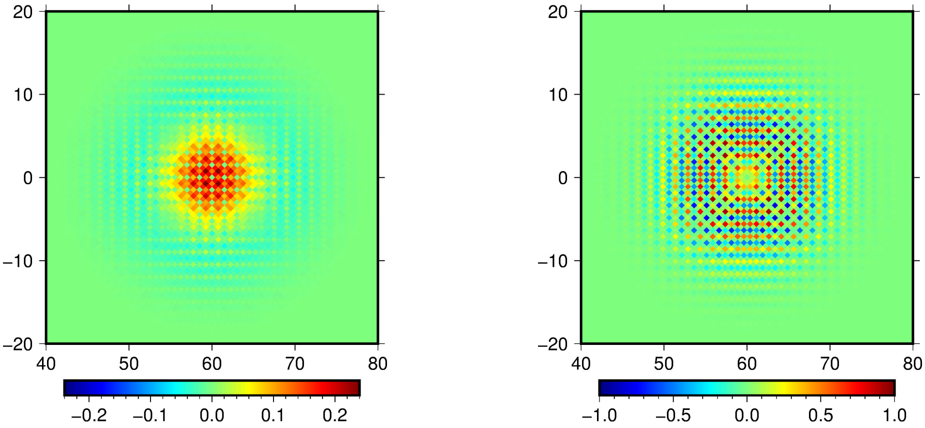

Figure E.1: Differences [m] between the interpolated (to the grid E) C-grid SSH and E-grid SSH at $t = 0$ s in the TSU test. The bilinear (left panel) and inverse-distance-weighting interpolations (right panel) are used.

2. We change the interpolation scheme. The bilinear interpolation is replaced by the IDW (see Appendix D.1) interpolation. The differences between E-grid solutions and C-grid solutions interpolated using bilinear and IDW interpolations are very similar. It means that the choice of interpolation technique does not affect our results and conclusions significantly.

   We also repeat the first test with the IDW interpolation. The differences are larger, they reaching up to 0.92 m, see the right panel of Fig. E.1. The IDW interpolation could be used, as the discrepancy is still below 1%, but the bilinear interpolation performed better.

F. Barotropic stream function

Consider for simplicity a divergence-free flow in the Cartesian coordinates,

$$\frac{\partial u}{\partial x} + \frac{\partial v}{\partial y} = 0. \tag{F.1}$$

As the flow is divergence-free, we can introduce a scalar function ψ with the following properties

$$u = \frac{\partial \psi}{\partial y}, \quad v = -\frac{\partial \psi}{\partial x}. \tag{F.2}$$

If we compute the velocity using Eq. (F.2), the incompressibility condition is fulfilled automatically. Additionally, the velocity vector is perpendicular to the gradient of ψ since

$$\mathbf{u} \cdot \nabla \psi = 0, \tag{F.3}$$

which can be easily proved using Eq. (F.2). The gradient of ψ is a vector that is perpendicular to the isolines of ψ. The velocity vector is thus parallel to the isolines of ψ.

To sum it up, if we plot the isolines of ψ we immediately see the flow patterns and if isolines are close to each other in one direction the velocities are increased in the other direction.

In the generalized coordinates, the function ψ for the divergence-free flow can be introduced as follows. We first introduce a 3D vector function $\boldsymbol{\psi}$,

$$\mathbf{u} = \nabla \times \boldsymbol{\psi}, \tag{F.4}$$

where $\mathbf{u}$ is considered to be a 3D vector with the third component equal to zero. The divergence-free condition is fulfilled due to the vector differential identity $\nabla \cdot (\nabla \times \mathbf{A})$, where $\mathbf{A}$ is an arbitrary vector function. Note that the vector function $\boldsymbol{\psi}$ that suits Eq. (F.4) is not unique. The vector function $\boldsymbol{\psi}'$,

$$\boldsymbol{\psi}' = \boldsymbol{\psi} + \nabla \Phi, \tag{F.5}$$

where Φ is an arbitrary scalar function, generates the same velocity field. We choose $\boldsymbol{\psi} = \psi \mathbf{e}_3$ to ensure that the third component of $\mathbf{u}$ is equal to zero,

$$\mathbf{u} = \nabla \times (\psi \mathbf{e}_3). \tag{F.6}$$

In the Cartesian coordinates, Eq. (F.6) is identical to Eq. (F.2).

In the realistic Boussinesq ocean model, the barotropic transports are approximately divergence free,

$$\nabla_h \cdot \mathbf{U} \approx 0. \tag{F.7}$$

Indeed, consider Eq. (1.12) where we neglected the surface water flux and the SSH time derivative since the SSH varies slowly in time.

We introduce the so-called barotropic stream function ψ_b according to Eq. (F.6),

$$\mathbf{U} = \nabla \times (\psi_b \mathbf{e}_3). \tag{F.8}$$

The value of stream function ψ_b at the particular point $(\xi_1 = x_2, \xi_2 = y_2, \xi_3 = a)$ on the Earth's surface for the given velocity distribution is then equal to

$$\psi_b(x_2, y_2, a) = \psi_b(x_1, y_1, a) + \int\limits_{x_1}^{x_2} U h_2 d\xi_2 - \int\limits_{y_1}^{y_2} V h_1 d\xi_1, \qquad \text{(F.9)}$$

where point (x_1, y_1, a) is usually in the corner of the computational domain and $\psi(x_1, y_1, a)$ is set equal to zero.

Note that Eq. (F.9) is written vaguely. We integrate over the rectangular path in $\xi_1 - \xi_2$ plane from point (x_1, y_1) to point (x_2, y_2). However, we may either integrate over ξ_1 with $\xi_2 = y_1$ fixed and then integrate over ξ_2 with $\xi_1 = x_2$ fixed, or integrate over ξ_2 with $\xi_1 = x_1$ fixed and then integrate over ξ_1 with $\xi_2 = y_2$ fixed. If **U** was a divergence-free field, both integrations would give the same result since the integral of a divergence-free field over the closed trajectory is equal to zero. However, the barotropic transport is only approximately divergence-free. The choice of integration path thus matters but the results should only differ in details. It is also a useful numerical test that both integration paths give approximately the same result.

G. UTSM magnetic induction solver

Our UTSM solver was originally coded by my colleague David Einšpigel. The theoretical aspects of the UTSM solver are briefly described in Sec. 8.2.3. We made two important modifications in the code:

- The computational domain was enlarged. In the original version, the computational domain covered only the ocean and the stream function Ψ was equal to zero on continents. This is not correct. The sources are nonzero only in the oceans (nonzero velocities), however, the induced magnetic field diffuses into continents and thus it is nonzero there. Consequently, the computational domain must cover the whole sphere.
- The discretization of the left-hand side of Eq. (8.7) was changed. We discretize the stream-function equation on the Arakawa C-grid and solve it numerically using the finite difference method. The discretized stream-function equation transforms into a system of linear equations for the grid-point values of the stream function. The discretization directly affects the matrix of the system. The matrix structure is the same in both discretizations but values of nonzero elements are different. The old discretization suffered from numerical instabilities if conductivity values 10^{-2} S/m or lower were prescribed on land. The new discretization allows us to compute the induced magnetic field even for the land conductivity 10^{-3} S/m. The details about the old and new discretizations are given in the following text.

G.1 Discretization of the stream-function equation in the UTSM solver

We express the stream-function equation (8.7) in the spherical coordinates,

$$\begin{aligned}\frac{1}{a^2\cos^2\phi}\frac{\partial}{\partial\lambda}\left(R\frac{\partial\Psi}{\partial\lambda}\right)+\frac{1}{a^2\cos\phi}\frac{\partial}{\partial\phi}\left(R\cos\phi\frac{\partial\Psi}{\partial\phi}\right)=&\\-\frac{1}{a^2\cos\phi}\left[\frac{\partial(aRJ_2^{\mathrm{imp}})}{\partial\lambda}+\frac{\partial(a\cos\phi RJ_1^{\mathrm{imp}})}{\partial\phi}\right]&\end{aligned}\tag{G.1}$$

where $R=1/\Sigma$ is the resistivity. In both discretizations, the stream function and resistivity are discretized at S points (see Fig. 5.10).

G.1.1 Original discretization

The original discretization is based on L_Ψ written in the form,

$$L_\Psi=\frac{1}{a^2\cos^2\phi}\left(\frac{\partial R}{\partial\lambda}\frac{\partial\Psi}{\partial\lambda}+R\frac{\partial^2\Psi}{\partial\lambda^2}\right)+\frac{1}{a^2\cos\phi}\left(\frac{\partial\left(R\cos\phi\right)}{\partial\phi}\frac{\partial\Psi}{\partial\phi}+R\cos\phi\frac{\partial^2\Psi}{\partial\phi^2}\right).\tag{G.2}$$

The discrete form of L_Ψ is then

$$\begin{aligned}
L_\Psi = {} & \frac{\left(R_{i+1,j} - R_{i-1,j}\right)\left(\Psi_{i+1,j} - \Psi_{i-1,j}\right) + 4R_{i,j}\left(\Psi_{i+1,j} - 2\Psi_{i,j} + \Psi_{i-1,j}\right)}{4a^2\cos^2\phi_j(\Delta\lambda)^2} \\
& + \frac{\left(R_{i,j+1}\cos\phi_{j+1} - R_{i,j-1}\cos\phi_{j-1}\right)\left(\Psi_{i,j+1} - \Psi_{i,j-1}\right)}{4a^2\cos\phi_j(\Delta\phi)^2} \\
& + \frac{4R_{i,j}\cos\phi_j\left(\Psi_{i,j+1} - 2\Psi_{i,j} + \Psi_{i,j-1}\right)}{4a^2\cos\phi_j(\Delta\phi)^2} \\
& = (-Y_1 + Y_2)\Psi_{i,j-1} + (-X_1 + X_2)\Psi_{i-1,j} - 2(X_2 + Y_2)\Psi_{i,j} \\
& + (X_1 + X_2)\Psi_{i+1,j} + (Y_1 + Y_2)\Psi_{i,j+1}, \qquad \text{(G.3)}
\end{aligned}$$

where

$$\begin{aligned}
X_1 &= \frac{R_{i+1,j} - R_{i-1,j}}{4(\Delta X_j)^2}, & X_2 &= \frac{R_{i,j}}{(\Delta X_j)^2}, \\
Y_1 &= \frac{R_{i,j+1}\Delta X_{j+1} - R_{i,j-1}\Delta X_{j-1}}{4\Delta X_j(\Delta y)^2}, & Y_2 &= \frac{R_{i,j}}{(\Delta y)^2}, \qquad \text{(G.4)}
\end{aligned}$$

where Δx and Δy denote the zonal and meridional grid spacings in the geographic coordinates, respectively.

G.1.2 New discretization

The new discretization is based on L_Ψ as it is written in Eq. (G.1). The discrete form of L_Ψ is then

$$\begin{aligned}
L_\Psi = {} & \frac{R_{i+1/2,j}\left(\Psi_{i+1,j} - \Psi_{i,j}\right) - R_{i-1/2,j}\left(\Psi_{i,j} - \Psi_{i-1,j}\right)}{a^2\cos^2\phi_j(\Delta\lambda)^2} \\
& + \frac{R_{i,j+1/2}\cos\phi_{j+1/2}\left(\Psi_{i,j+1} - \Psi_{i,j}\right) - R_{i,j-1/2}\cos\phi_{j-1/2}\left(\Psi_{i,j} - \Psi_{i,j-1}\right)}{a^2\cos\phi_j(\Delta\phi)^2} \\
& = Y_2\Psi_{i,j-1} + X_2\Psi_{i-1,j} - (X_1 + X_2 + Y_1 + Y_2)\Psi_{i,j} + X_1\Psi_{i+1,j} + Y_1\Psi_{i,j+1}, \\
& \qquad \text{(G.5)}
\end{aligned}$$

where

$$\begin{aligned}
X_1 &= \frac{R_{i+1/2,j}}{(\Delta x_j)^2}, & X_2 &= \frac{R_{i-1/2,j}}{(\Delta x_j)^2}, \\
Y_1 &= \frac{R_{i,j+1/2}\Delta x_{j+1/2}}{\Delta x_j(\Delta y)^2}, & Y_2 &= \frac{R_{i,j-1/2}\Delta x_{j-1/2}}{\Delta x_j(\Delta y)^2}. \qquad \text{(G.6)}
\end{aligned}$$

G.2 Simple numerical test with analytic solution

We designed a simple numerical test to check out that the UTSM solver has been coded correctly. Consider a global ocean in which the flow is given by

$$U = U_0\cos(2\phi)\cos\lambda, \qquad \text{(G.7)}$$

$$V = U_0\sin\phi\sin\lambda, \qquad \text{(G.8)}$$

the main magnetic field in the form of a dipole with the radial component B_{Mr},

$$B_{Mr} = B_{M0r} \sin\phi \tag{G.9}$$

and constant conductivity σ everywhere in the crustal layer, $\sigma = \sigma_{\text{ocean}} = \sigma_{\text{crust}}$. The vertically integrated imposed electric current density is equal to

$$\begin{aligned} \mathbf{J}^{\text{imp}} &= \sigma \mathbf{U} \times \mathbf{B}_M = (\sigma V B_{Mr})\, \mathbf{e}_\lambda - (\sigma U B_{Mr})\, \mathbf{e}_\phi \\ &= \sigma B_{M0r} U_0 \left[\left(\sin^2\phi \sin\lambda \right) \mathbf{e}_\lambda - (\cos(2\phi) \sin\phi \cos\lambda)\, \mathbf{e}_\phi \right]. \end{aligned} \tag{G.10}$$

If we insert $\mathbf{J}^{\text{imp}}$ into Eq. (G.1), we obtain the equation for the stream function in the form

$$\frac{1}{\cos\phi} \frac{\partial^2 \Psi}{\partial \lambda^2} + \frac{\partial}{\partial \phi} \left(\cos\phi \frac{\partial \Psi}{\partial \phi} \right) = a \sigma B_{M0r} U_0 \sin\phi \cos^2\phi \sin\lambda. \tag{G.11}$$

It can be proved that the solution of Eq. (G.11) is

$$\Psi = -\Psi_0 \sin(2\phi) \sin\lambda \tag{G.12}$$

with the amplitude

$$\Psi_0 = \frac{a \sigma B_{M0r} U_0}{12}. \tag{G.13}$$

The radial component of the OIMF is computed from the stream function according to Eq. (2) in Irrgang et al. [2016a],

$$B_r(\lambda, \phi, r) = -\sum_{l=0}^{\infty} \sum_{m=-l}^{l} \frac{\mu_0}{2r} \Psi_{lm} \left(\frac{a}{r} \right)^{l+1} (l+1) Y_{lm}(\lambda, \phi), \tag{G.14}$$

where $Y_{lm}(\lambda, \phi)$ is the spherical harmonic function of degree l and order m. The stream function (G.12) corresponds to the Y_2^1 (up to the normalization coefficient) and thus we have

$$B_r(\lambda, \phi, r) = \frac{3\mu_0}{2r} \left(\frac{a}{r} \right)^3 \Psi. \tag{G.15}$$

And the radial component of the OIMF at the Earth's surface is

$$B_r(\lambda, \phi, a) = -\frac{3\mu_0}{2a} \Psi = B_{0r} \sin(2\phi) \sin\lambda \tag{G.16}$$

with the amplitude

$$B_{0r} = \frac{\mu_0 \sigma B_{M0r} U_0}{8}. \tag{G.17}$$

If we choose

$$a = 6.371 \cdot 10^6 \text{ m}, \tag{G.18}$$

$$\sigma = 3.2 \text{ S/m}, \tag{G.19}$$

$$B_{M0r} = 3 \cdot 10^4 \text{ nT}, \tag{G.20}$$

$$U_0 = 4 \cdot 10^3 \text{ m}^2/\text{s}, \tag{G.21}$$

the amplitudes of the stream function and the OIMF are equal to

$$\Psi_0 \approx 2.04 \cdot 10^5 \text{ A}, \tag{G.22}$$

$$B_{0r} \approx 60.32 \text{ nT}. \tag{G.23}$$

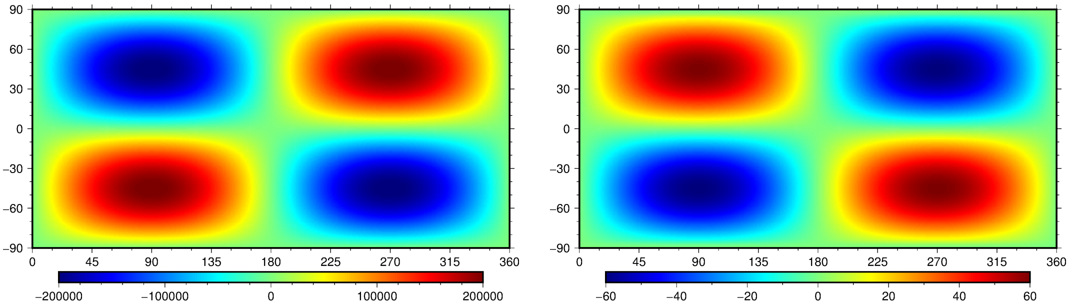

Figure G.1: Stream function [A] (left panel) and radial component of the induced magnetic field at the surface [nT] (right panel) computed using the UTSM solver in the simple numerical test.

Fig. G.1 shows the stream function and the radial component of the OIMF calculated using the UTSM solver. Both fields are modelled correctly in terms of shape and amplitude.

The performance of the UTSM solver in a realistic setup is studied in Chapter 8.

List of Figures

List of Tables

List of Abbreviations

Abbreviation	Meaning
AB3	third-order Adams-Bashforth (method)
ACC	Antarctic-Circumpolar Current
AM4	fourth-order Adams-Moulton (method)
BBL	bottom boundary layer
BRU	Brunnabend [2010]
CIE	contracting integral equation
CFL	Courant–Friedrichs–Lewy (criterion)
CNmod	modified Crank-Nicolson (scheme)
DFP	dual-step five-point-involved (smoother)
DST3	third order direct space time (scheme)
EM	electromagnetic
EMIC	Earth system models of intermediate complexity
EOS	equation of state
EOS-80	EOS approved in 1980 [UNESCO, 1981]
FB	forward-backward (scheme)
FBgen	generalized forward-backward (scheme)
GC	generalized horizontal coordinates
IDW	inverse-distance-weighting (interpolation)
IE	integral equation
OIMF	ocean-induced magnetic field
IMP	Euler implicit (scheme)
IWD	internal wave drag
KRH	Kara et al. [2002]
KON	Kondo [1975]
LA	latent (heat flux)
LSG	Large-Scale Geostrophic (ocean model)
LSOMG	Libor Sachl Ocean Model for Geophysics
LSOMG-BT	barotropic version of LSOMG
LW	Lax-Wendroff (scheme)
LW	longwave (heat flux)
LY	Large and Yeager [2004], Large [2006]
OGCM	ocean general circulation model
PC	predictor-corrector (scheme)
PSU	practical salinity unit
RSC	reduced spherical coordinate (grid)
RMS	root-mean-square

Table G.1: Abbreviations introduced in the thesis and their meaning. Part 1 (a-r)

Abbreviation	Meaning
SAL	self attraction and loading
SGS	subgrid scale
SSH	sea surface height
SC	spherical coordinates
SN	sensible (heat flux)
SW	shortwave (heat flux)
SWE	shallow-water equations
S5p	standard five-point-involved (smoother)
TSU, TIDa, TIDb	simple numerical tests in Sec. 6.1
TSU0, TID0, mTIDa	simple numerical tests in Sec. 6.2
TVD	total-variation diminishing
WOA	World Ocean Atlas
YY	Yin-Yang (grid)

Table G.2: Abbreviations introduced in the thesis and their meaning. Part 2 (s-z)

List of Symbols

Symbol	Meaning
a	Earth's radius
A	ocean surface
$\mathbf{A}$	viscosity tensor
A_d	damping coefficient in the divergence damping method
A_H	horizontal viscosity
A_s	smoothing diffusivity in Eq. (4.51)
A_V	vertical viscosity
α	right ascension of a celestial body
α_T	thermal expansion coefficient
α_{SW}	shortwave albedo
B_r	radial component of OIMF
$\mathbf{B}$	ocean-induced magnetic field (OIMF)
$\mathbf{B}_M$	main geomagnetic field
β	meridional gradient of planetary vorticity
β_s	coefficient in the scalar approximation of SAL
β_S	saline contraction coefficient
c	Courant number
c_{pa}	specific heat of air
c_w	specific heat capacity of water
C	tracer (temperature or salinity)
C	Coriolis matrix, Eq. (D.10)
C_b	bottom-friction coefficient
C^{data}	data prescribed tracer concentration
C_D	drag coefficient in the wind-stress formula (4.24)
C_E, C_H	bulk transfer coefficients, Eqs. (5.213), (5.214)
C_{iwd}	scalar approximation of the internal wave drag tensor
C_m	constant in the CFL criterion (4.15)
C_w	tracer concentration in the fresh water
C_{z_0}	tracer concentration in the atmosphere
$\mathbf{C}_{iwd}$	internal wave drag tensor
d	horizontal grid spacing
D	deformation rate used in the Smagorinsky viscosity
D_e	thickness of the Ekman layer
D_S	horizontal shearing strain
$\widehat{D_S}$	barotropic horizontal shearing strain
D_T	horizontal tension
$\widehat{D_T}$	barotropic horizontal tension
δ	declination of a celestial body
Δ_h	horizontal Laplacian
Δt	baroclinic time step
$\Delta \tau$	barotropic time step
Δx, Δy	zonal and meridional grid spacings in the geographic coordinates
$\mathscr{D}$	divergence of horizontal velocity

Table G.3: Symbols used in the thesis and their meaning. Part 1 (a-d).

Symbol	Meaning
e_a	water vapor pressure at the sea surface
e_s	saturated water vapor pressure
E	total mechanic energy
E^g	energy invariant
E_k	kinetic energy
E_p	potential energy
E^s	contribution from the external force in Eq. (6.9)
$\mathbf{e}$	deformation or strain tensor
$\widehat{\mathbf{e}}$	barotropic strain tensor
$\mathbf{e}_k$	k-th base vector
$\overline{\mathbf{e}}_k$	k-th base vector of the neutral frame
$\mathbf{e}_x$, $\mathbf{e}_y$, $\mathbf{e}_z$	base vectors of the Cartesian coordinate system
$\mathbf{e}_\lambda$, $\mathbf{e}_\phi$	base vectors of SC in the zonal and meridional directions
$\mathbf{E}$	electric field
$\mathbf{E}^{\text{imp}}$	imposed electric field
ϵ	ratio of dianeutral to epineutral diffusivities
η	sea surface height (SSH)
η^b	SSH before it is passed to the baroclinic system
f	Coriolis parameter
f_l^m	spherical-harmonic coefficient of degree l and order m
F	1-D tracer flux
F_C	tracer flux which cross the ocean surface (from the ocean side)
F_s	additional term that suppresses noise on Arakawa grids B and E
F^z	vertical turbulent tracer flux
$\mathbf{F}$	turbulent tracer flux
$\mathbf{F}$	forcing on the right-hand side of SWE
$\mathbf{F}_c$	vector containing components of the Coriolis force
$\mathbf{F}_d$	small slope diffusive flux
$\mathbf{F}_e^a$	advective GM flux
$\mathbf{F}_e^s$	skew GM flux
$\mathbf{F}^h$	horizontal turbulent tracer flux
$\mathbf{F}_{tid}$	tidal force
$\mathbf{F}^{(\mathbf{u})}$	friction force
$\mathbf{F}_H^{(\mathbf{u})}$	horizontal friction force
$\mathbf{F}_V^{(\mathbf{u})}$	vertical friction force
$\mathbf{F}_{z_0}^z$	vertical flux of horizontal momentum at the surface
g	gravitational acceleration
G	gravitational constant
G	Gibbs function
$\mathbf{G}$	baroclinic forcing
γ	slope ratio
γ_C	inverse restoring time for tracers
γ_T	diminishing factor
$\boldsymbol{\gamma}$	vector stream function
$\boldsymbol{\gamma}_{gm}$	GM vector stream function

Table G.4: Symbols used in the thesis and their meaning. Part 2 (e-g).

Symbol	Meaning
h	water-column height
h_e	enthalpy
h_k	k-th metric coefficient
h_p	potential enthalpy
H	depth of ocean bottom
$\hat{H}$	bottom roughness
H_E	Ekman depth
H_{max}	maximum depth in the ocean model
I	number of grid on the model "parallel"
I	index used in 1-D advection schemes, Eq. (2.13)
J	number of grid on the model "meridian"
$j_{\max}$	spherical harmonic truncation degree
$\mathbf{j}$	electric current density
$\mathbf{j}^{\mathrm{imp}}$	imposed electric current density
$\mathbf{J}$	second order tracer transport tensor
$\mathbf{J}^{\mathrm{imp}}$	vertically integrated imposed electric current density
K	secant bulk modulus in EOS-80
k_H	parameter in the Smagorinsky viscosity, see Eq. 5.73
k_T, h_T	Love numbers
K_H	epineutral diffusivity
K_V	dianeutral diffusivity
$\mathbf{K}$	diffusion tensor (symmetric part of tensor $\mathbf{J}$)
$\overline{\mathbf{K}}$	diffusion tensor in the neutral frame
$\mathbf{K}_{ssa}$	small slope approximation of $\mathbf{K}$
κ	Gent-McWilliams stirring diffusivity
$\mathbf{k}$	unit vector parallel to the local vertical direction
l	geocentric distance between the Earth and celestial body
l_f	latent heat of freezing or melting
L	coefficient in the scheme of Jayne and St. Laurent [2001]
L_e	latent heat of vaporization
L_M	width of the Munk boundary layer
L_ψ	left-hand side of the TSA stream-function equation
λ	longitude
$\mathbf{\Lambda}$	transformation matrix from z-frame to neutral frame
m	total mass in the global ocean
M	advective metric frequency
M	mass of the celestial body, Eq. (4.33)
μ_0	permeability of vacuum
$\mathbf{N}$	vector perpendicular to the ocean surface
N	number of barotropic subcycles per baroclinic time step
N	buoyancy frequency
N_b	buoyancy frequency at the sea bed
∇	3-D gradient operator
∇_h	2-D horizontal gradient operator
ν	global tracer variance
ν_{tot}	total variation of a tracer

Table G.5: Symbols used in the thesis and their meaning. Part 3 (h-n).

Symbol	Meaning
Ω	angular frequency
p	pressure
p_a	atmospheric pressure
p_r	reference pressure
P_j	spectral power on degree j
P_l^m	associated Legendre function of degree l and order m
ϕ	latitude
ϕ_{max}	maximum latitude in the simulation
ϕ_{JN}	join latitude used in dipolar and tripolar grids
ψ	limiter function
ψ_b	barotropic stream function
$\boldsymbol{\Psi}$	stream function in the unimodal thin-sheet approximation
q	potential vorticity
q_a	surface air specific humidity
q_s	saturated specific humidity
q_w	surface water flux
Q	total heat flux
Q_n, Q_n^g	n-th vorticity invariant and its generalized form
Q_{mom}	momentum flux
Q_C	tracer flux which crosses the ocean surface (from outside)
Q_C^{turb}	turbulent tracer flux
$Q_C^{turb,0}$	turbulent tracer flux from data or another model
Q_{LA}	latent heat flux
Q_{LW}	longwave heat flux
Q_{SN}	sensible heat flux
Q_{SW}	shortwave heat flux
r	length of the radius vector
r	parameter in the linear friction
Ri	Richardson number
R_r	Rossby radius of deformation
$\mathbf{r}$	radius vector
$\mathbf{R}$	antisymmetric part of $\mathbf{J}$
ρ	density of water
ρ_0	constant reference density
ρ_a	air density
ρ^*	density of adiabatically displaced water parcel
s	coefficient in the DFP smoother, Eqs. (5.127), (5.128)
S	salinity
S^C	volume source of tracer C
$\mathbf{s}$	neutral direction slope with respect to the horizontal
$\boldsymbol{\sigma}$	stress tensor
σ	vertical coordinate described in Sec. 2.3.2
σ	electric conductivity
σ_e	specific entropy
Σ	vertically integrated conductivity

Table G.6: Symbols used in the thesis and their meaning. Part 4 (o-s).

Symbol	Meaning
t	time
t_{fr}	freezing temperature
T	in-situ temperature
τ	local hour angle
τ_{dec}	decay time
$\boldsymbol{\tau}_b$	bottom friction
$\boldsymbol{\tau}_w$	surface wind stress
$\boldsymbol{\tau}_{sal}$	self-attraction and loading (SAL)
$\boldsymbol{\tau}_{iwd}$	internal wave drag
θ	potential temperature
θ_a	air temperature
θ_a	dew point temperature
θ_s	sea surface temperature
θ	conservative temperature
u	velocity component in the direction of the 1st coordinate axis
u_w	fresh water velocity
U	1st component of the vertically integrated horizontal velocity
U_R	velocity for the Reynolds-number constraint, see Eq. 5.79
$\mathbf{u}$	2-D horizontal velocity
$\mathbf{u}'$	baroclinic velocity
$\mathbf{u}_w$	wind speed
$\lvert\mathbf{u}_{tid}\rvert$	typical tidal velocity
$\bar{\mathbf{u}}$	vertically averaged horizontal velocity = barotropic velocity
$\bar{\mathbf{u}}^b$	barotropic velocity before it is passed to the baroclinic system
$\mathbf{u}_p$	2-D provisional horizontal velocity
$\mathbf{U}$	vertically integrated horizontal velocity
v	velocity component in the direction of the 2nd coordinate axis
V	2nd component of the vertically integrated horizontal velocity
V_0	total volume of ocean water above the reference level $\eta = 0$
V_2	2nd degree tidal potential
V_{piston}	piston velocity
$\mathbf{v}$	3-D velocity
$\mathbf{v}^\rho$	3-D velocity defined by the the linear momentum density
$\mathbf{v}^*$	eddy-induced velocity
ϑ	colatitude
w	vertical velocity
w_i	inverse distance from the i-th neighbouring data point
W	ocean-land mask
X	meridional component of the OIMF
ξ_k	k-th generalized orthogonal curvilinear coordinate
Y	zonal component of the OIMF
Y_l^m	spherical harmonic of degree l and order m
z	vertical geopotential coordinate
Z	vertical component of OIMF in the direction of $-\mathbf{e}_r$
ζ	relative vorticity

Table G.7: Symbols used in the thesis and their meaning. Part 5 (t-z).

List of publications

Related to the thesis topic

L. Šachl, D. Einšpigel, Z. Martinec. Simple numerical tests for ocean tidal models. *Accepted to Stud. Geophys. Geod.*.

L. Šachl, Z. Martinec, J. Velímský, C. Irrgang, J. Petereit, J. Saynisch, D. Einšpigel, and N. R. Schnepf. Modelling of electromagnetic signatures of global ocean circulation: physical approximations and numerical issues. *Earth Planets Space*, 71(1):58, 2019.

J. Velímský, **L. Šachl**, and Z. Martinec. The global toroidal magnetic field generated in the Earth's oceans. *Earth Planet. Sc. Lett.*, 509:47–54, 2019.

J. Velímský, A. Grayver, A. Kuvshinov, and **L. Šachl**. On the modelling of M_2 tidal magnetic signatures: Effects of physical approximations and numerical resolution. *Earth Planets Space*, 70(1):70–192, 2018.

Non-related to the thesis topic

L. Šachl. Validation of 3-D synthetic seismograms based on the ray-Born approximation. *Stud. Geophys. Geod.*, 57(1): 84-102, 2013.

Z. Martinec, J. Velímský, R. Haagmans, and **L. Šachl**. A two-step along-track spectral analysis for estimating the magnetic signals of magnetospheric ring current from Swarm data. *Geophys. J. Int.*, 212(2):1201–1217, 2017.

S. Sajjadi, Z. Martinec, P. Prendergast, J. Hagedoorn, **L. Šachl**, P. Readman, E. Robin, B. O'Reilly and C. Horan. The unification of gravity data for Ireland-Northern Ireland. *Lead. Edge*, 39(2):135-143, 2020.

A. Attachments

Earth and Planetary Science Letters 509 (2019) 47–54

Contents lists available at ScienceDirect

Earth and Planetary Science Letters

www.elsevier.com/locate/epsl

The global toroidal magnetic field generated in the Earth's oceans

Jakub Velímský [a,*], Libor Šachl [a], Zdeněk Martinec [a,b]

[a] Charles University, Faculty of Mathematics and Physics, Department of Geophysics, Prague, Czech Republic
[b] Dublin Institute for Advanced Studies, School of Cosmic Physics, Geophysics Section, Dublin, Ireland

ARTICLE INFO

Article history:
Received 2 May 2018
Received in revised form 18 October 2018
Accepted 23 December 2018
Available online xxxx
Editor: B. Buffett

Keywords:
ocean-induced magnetic field
toroidal magnetic field

ABSTRACT

The magnetic field induced in the Earth's ocean by the large-scale global circulation consists of the toroidal and poloidal modes. Lateral variations of the ocean electrical conductivity allow for the energy exchange between both regimes. In this paper, we predict that the eastward component of the toroidal magnetic field in the area of the Antarctic Circumpolar Current can reach amplitudes of 15 nT at the depth of about 1800 m. Moreover, even though the toroidal field is invisible on the ocean surface, it can significantly influence the observable poloidal field, both in terms of its amplitude, and seasonal variations.

1. Introduction

It is well known that the movement of the oceans through the Earth's main magnetic field generates the secondary, motionally induced magnetic field (Sanford, 1971). On a global scale, the ocean flows and their corresponding induced magnetic signatures can be divided in two distinct classes (Kuvshinov, 2008). The tidal flows are driven by the gravitational attraction of the Sun and the Moon. The individual tidal constituents are manifested at discrete frequencies related to the movements of the celestial bodies, although compound tides spurred by non-linear ocean dynamics are also present (Einšpigel and Martinec, 2017). Due to the volume character of the external gravitational force, the tidal flows have little vertical stratification, and therefore are often modelled in the barotropic approximation. A number of studies have been dedicated to the tidally induced magnetic fields, including their observation on ground observatories (Maus and Kuvshinov, 2004), by low-orbit satellite missions CHAMP (Tyler et al., 2003) and Swarm (Sabaka et al., 2016), and in sea surface measurements (Lilley et al., 2004). Recently, Grayver et al. (2016, 2017) have used the M_2 tidal signals to constrain the electrical conductivity at the lithosphere–asthenosphere boundary. The toroidal magnetic field generated by tidal signals has been modelled by Dostal et al. (2012) in the case of spherically symmetric Earth.

The global ocean circulation, on the other hand, has very different spatio-temporal characteristics. Driven by wind stresses and heat fluxes on the ocean surface, the horizontal components of the flows possess a significant vertical gradient and the vertical flows are non-negligible. Their time variations are manifested on seasonal and longer time scales, and the numerical modelling is often based on the three-dimensional (3-D) baroclinic approach (Stewart, 2008). Such flows are capable of generating both the poloidal and toroidal magnetic fields. In addition, the lateral conductivity variations can lead to the energy exchange between the magnetic modes. The toroidal field vanishes above the ocean surface, where its presence can be detected only indirectly according to how it affects the observable poloidal field. However, it is expected to reach local values of up to 100 nT in the ocean, cf. the equation E.1 in Tyler et al. (2017) for analytical derivation, or the measurements of the magnetic field vertical gradient by Lilley et al. (2001). The observable ocean-induced poloidal magnetic field on the ocean surface can reach amplitudes of several nT, with largest values present in the area of the wind-driven Antarctic Circumpolar Current (ACC) (Kuvshinov, 2008; Irrgang et al., 2016).

The observations of the magnetic field induced by the global ocean circulation have the potential to be used as a constraint when examining the spatio-temporal dynamics of the oceans (Tyler et al., 1997b; Vivier et al., 2004). A number of studies have, therefore, been concerned with the forward modelling of the ocean-induced magnetic field (e.g., Sanford, 1971; Chave and Luther, 1990; Larsen, 1992; Tyler et al., 1997; Manoj et al., 2006). However, none of the studies used a complete 3-D description of both the electrical conductivity distribution and the velocity flows. Typically, one-dimensional integration from the seabottom to the ocean surface is applied, yielding a simplified, quasi two-dimensional problem, and smearing the effect of vertical stratification of the horizontal flows. As we will demonstrate here, this can have important consequences for the modelling of the toroidal component of the magnetic field in the ocean (Lilley et al., 1993, 2001).

---

[*] Corresponding author.
E-mail address: velimsky@karel.troja.mff.cuni.cz (J. Velímský).

https://doi.org/10.1016/j.epsl.2018.12.026

Direct observations of the ocean-induced magnetic field are now also available from sea-bottom geomagnetic stations, e.g. in the northwestern Pacific (Toh et al., 2006; Toh and Hamano, 2015). While the static part of ocean circulation signatures is difficult to distinguish from the crustal field, the seasonal variations should be in principle detectable at suitable locations. For satellite data, the challenge is considerably higher due to the lower amplitudes of the surface field, and the geometric filtering of small-scale field structures. However, accurate modelling predictions could provide data corrections to improve the satellite-based crustal field models (Kuvshinov, 2008). To our knowledge, a thorough study of the toroidal magnetic field induced by large-scale three-dimensional flows in laterally and radially electrically heterogeneous oceans has not yet been performed.

In this paper, we concentrate on the calculation of the global toroidal magnetic field in the ocean interior, and the phenomenon of mutual interaction of the poloidal and toroidal modes through lateral conductivity variations. The paper is set up as follows. The electromagnetic induction (EMI) equation for arbitrary 3-D distribution of electrical conductivity and ocean flows is discussed in Section 2. Following the introduction of our large-scale ocean model and the EMI solver in Section 3, we demonstrate in Section 4 the influence of the toroidal magnetic field on the observable poloidal component by the direct comparison of numerical simulations where these effects are respectively included and excluded.

2. Poloidal–toroidal separation of the induced magnetic field

The magnetic field $\boldsymbol{B}(\boldsymbol{r};t)$ induced by the flow of conductive ocean water in the presence of the Earth's main magnetic field $\boldsymbol{B}_0(\boldsymbol{r};t)$ is described by the EMI equation,

$$\mu_0 \frac{\partial \boldsymbol{B}(\boldsymbol{r};t)}{\partial t} + \mathrm{curl}\left[\frac{1}{\sigma(\boldsymbol{r};t)}\mathrm{curl}\boldsymbol{B}(\boldsymbol{r};t)\right] = \mu_0\,\mathrm{curl}\left[\boldsymbol{v}(\boldsymbol{r};t)\times\boldsymbol{B}_0(\boldsymbol{r};t)\right]. \tag{1}$$

Here $\boldsymbol{r}=(r,\vartheta,\varphi)$ is the position vector expressed in spherical coordinates of radius, colatitude, and longitude, t is time, μ_0 is the magnetic permeability of vacuum, $\sigma(\boldsymbol{r};t)$ is the electrical conductivity, and $\boldsymbol{v}(\boldsymbol{r};t)$ stands for the flow velocity. The EMI equation is derived from the quasi-stationary Maxwell equations under the assumption that the main magnetic field is much larger than the induced field, yet it varies on a much longer time scale, and can be described by a scalar magnetic potential $U_0(\boldsymbol{r};t)$,

$$|\boldsymbol{B}_0| \gg |\boldsymbol{B}|, \tag{2}$$

$$\left|\frac{\partial \boldsymbol{B}_0}{\partial t}\right| \ll \left|\frac{\partial \boldsymbol{B}}{\partial t}\right|, \tag{3}$$

$$\boldsymbol{B}_0(\boldsymbol{r};t) = -\mathrm{grad}U_0(\boldsymbol{r};t). \tag{4}$$

The equation (1) holds in the oceans as well as in the underlying lithosphere and mantle, where the flow of the conductive material occurs on geological scales, and for our purposes $\boldsymbol{v}=\boldsymbol{0}$. In the insulating atmosphere surrounding the Earth, the induced magnetic field is also described by a scalar magnetic potential $U(\boldsymbol{r};t)$, with the continuity of all three field components imposed across the Earth's surface $r=a$,

$$\boldsymbol{B}(a,\vartheta,\varphi) = -\mathrm{grad}U(r,\vartheta,\varphi)|_{r=a}\,. \tag{5}$$

The scalar magnetic potential U satisfies the Laplace equation,

$$\Delta U(\boldsymbol{r};t) = 0 \quad \text{for } r \geq a, \tag{6}$$

and, in the absence of external sources, it must vanish for $r\to\infty$. We do not consider here the induction caused by external sources, i.e., the time variations of magnetospheric and ionospheric currents. Their induced fields also satisfy condition (2), and therefore represent an independent solution of the homogeneous form of equation (1), which combines linearly with the ocean-induced field.

The EMI equation (1) satisfies implicitly the divergence-free constraint on the induced magnetic field, when provided with a divergence-free initial condition. Therefore, the magnetic field vector can be decomposed into its poloidal and toroidal parts,

$$\boldsymbol{B}(\boldsymbol{r};t) = \boldsymbol{B}_\mathrm{P}(\boldsymbol{r};t) + \boldsymbol{B}_\mathrm{T}(\boldsymbol{r};t), \tag{7}$$

$$\boldsymbol{e}_\mathrm{r}\cdot\boldsymbol{B}_\mathrm{T} = 0, \tag{8}$$

$$\mathrm{div}\boldsymbol{B}_\mathrm{T} = 0, \tag{9}$$

$$\boldsymbol{e}_\mathrm{r}\cdot\mathrm{curl}\boldsymbol{B}_\mathrm{P} = 0, \tag{10}$$

$$\mathrm{div}\boldsymbol{B}_\mathrm{P} = 0, \tag{11}$$

where $\boldsymbol{e}_\mathrm{r}$ denotes the radial unit vector. The boundary condition (5) then implies that the toroidal field is zero at the surface, while the poloidal field contains only the contribution of the internal electric currents,

$$\boldsymbol{B}_\mathrm{T}(a;t) = \boldsymbol{0}, \tag{12}$$

$$\boldsymbol{B}_\mathrm{P}^{(\mathrm{ext})}(a;t) = \boldsymbol{0}, \tag{13}$$

where the external–internal field separation is achieved by expanding the scalar potential U into spherical harmonic series (Velímský and Martinec, 2005).

Since the curl operator converts the poloidal field into toroidal, and vice versa (Varshalovich et al., 1989), we can split the EMI equation into its toroidal and poloidal parts,

$$\mu_0\frac{\partial \boldsymbol{B}_\mathrm{T}}{\partial t} + \left[\mathrm{curl}\left(\frac{1}{\sigma}\mathrm{curl}\boldsymbol{B}_\mathrm{T}\right)\right]_\mathrm{T} = \mu_0\left[\mathrm{curl}\,(\boldsymbol{v}\times\boldsymbol{B}_0)\right]_\mathrm{T} - \left[\mathrm{curl}\left(\frac{1}{\sigma}\mathrm{curl}\boldsymbol{B}_\mathrm{P}\right)\right]_\mathrm{T}, \tag{14}$$

$$\mu_0\frac{\partial \boldsymbol{B}_\mathrm{P}}{\partial t} + \left[\mathrm{curl}\left(\frac{1}{\sigma}\mathrm{curl}\boldsymbol{B}_\mathrm{P}\right)\right]_\mathrm{P} = \mu_0\left[\mathrm{curl}\,(\boldsymbol{v}\times\boldsymbol{B}_0))\right]_\mathrm{P} - \left[\mathrm{curl}\left(\frac{1}{\sigma}\mathrm{curl}\boldsymbol{B}_\mathrm{T}\right)\right]_\mathrm{P}. \tag{15}$$

The equation (14) contains the diffusion terms for toroidal field on the left-hand side. In the absence of sources, its solution is zero everywhere due to the boundary condition (12). The first term on the right-hand side involves the poloidal part of the Lorentz force $\boldsymbol{v}\times\boldsymbol{B}_0$ acting on a unit charge, or the toroidal part of its rotation. The second term describes the conversion from the poloidal induced field through the lateral variations of electrical conductivity. It is identically equal to zero if σ is only a function of radius r. Note that even in the presence of sources, the boundary condition (12) still holds, and the toroidal field is not directly observable at the Earth's surface. However, it can be measured inside the ocean, or at the seabottom.

A similar analysis applies to the equation (15) describing the diffusion of the poloidal field. Without any internal sources on the right-hand side, and without the external sources in the boundary condition (13), the poloidal field is zero. The right-hand side contains two terms responsible for poloidal field generation: the toroidal component of the Lorentz force converted into the poloidal component of its rotation, and the contribution from the induced toroidal field conveyed by means of laterally heterogeneous conductivity.

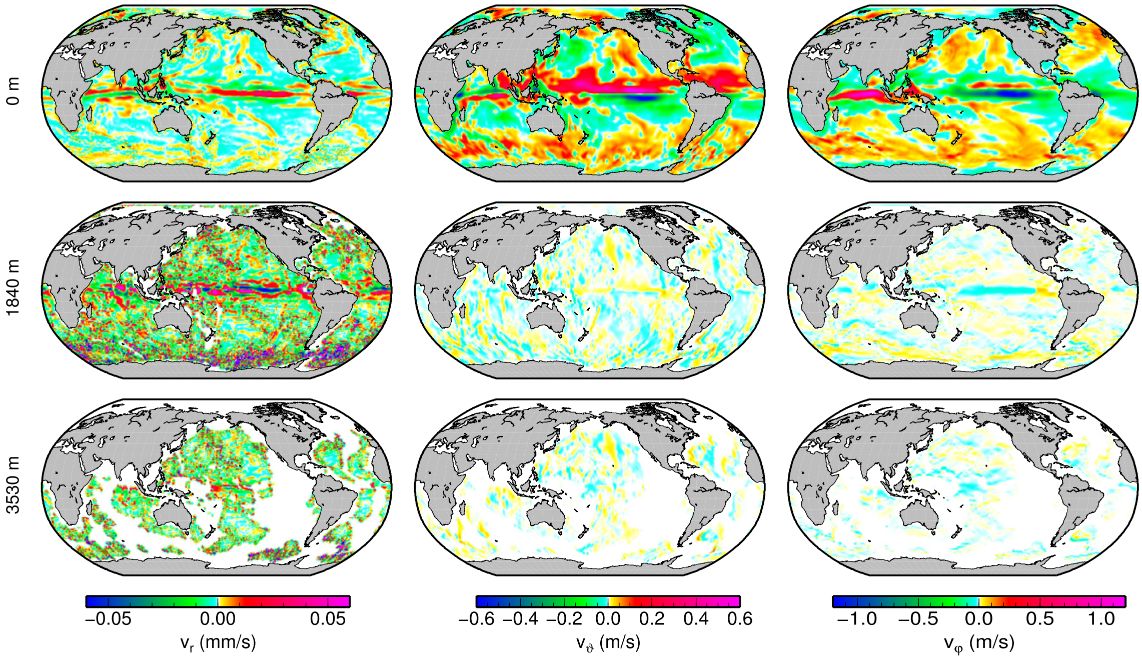

Fig. 1. Snapshots of ocean flow velocities on December 31, 2014. The individual rows correspond to different depths, while the radial, meridional and zonal components are shown in the columns from left to right. (For interpretation of the colours in the figure(s), the reader is referred to the web version of this article.)

How large is the poloidal and toroidal source stemming from the Lorentz force? Under the assumption of incompressible ocean flow, we can write

$$\operatorname{curl}(\boldsymbol{v} \times \boldsymbol{B}_0) = \boldsymbol{B}_0 \cdot \operatorname{grad}\boldsymbol{v} - \boldsymbol{v} \cdot \operatorname{grad}\boldsymbol{B}_0. \tag{16}$$

Let us further assume as a first-order approximation that the main field is represented by an axial dipole with magnetic momentum $4\pi\gamma/\mu_0$,

$$\boldsymbol{B}_0 = \gamma \left(\frac{2\cos\vartheta}{r^3}\boldsymbol{e}_\mathrm{r} + \frac{\sin\vartheta}{r^3}\boldsymbol{e}_\vartheta \right), \tag{17}$$

and the velocity field is dominated by the zonal toroidal component,

$$\boldsymbol{v} = v_\varphi \boldsymbol{e}_\varphi, \quad \frac{\partial v_\varphi}{\partial\varphi} = 0, \tag{18}$$

where $\boldsymbol{e}_\vartheta$ and $\boldsymbol{e}_\varphi$ are respectively the meridional and zonal unit vectors. Then the rotation of the Lorentz force,

$$\operatorname{curl}(\boldsymbol{v} \times \boldsymbol{B}_0) = \frac{\gamma}{r^3}\left(2\cos\vartheta \frac{\partial v_\varphi}{\partial r} + \frac{\sin\vartheta}{r}\frac{\partial v_\varphi}{\partial\vartheta} - \frac{3\cos\vartheta}{r} v_\varphi \right)\boldsymbol{e}_\varphi \tag{19}$$

is also a zonal toroidal field. In the polar areas, it is dominated by the first term which depends on the radial derivative of the zonal flow. The meridional derivative of the zonal flow is important in the equatorial area, however, it is downscaled by $1/r \approx 1/a$ factor, as is the last term depending on v_φ. Obviously, the spatial structure of the Lorentz forcing will become much richer by incorporating also the meridional and vertical flows, and using a more detailed description of the main magnetic field. Nevertheless, in the presence of vertical stratification of zonal flows, there will always be a substantial forcing contributing to the generation of the toroidal induced magnetic field. This is basically the ω-effect, well known in the classical dynamo theory (Roberts, 1992).

How does the toroidal field influence the generation of the observable poloidal field? We can carry out a similar first-order analysis by assuming that

$$\boldsymbol{B}_\mathrm{T} = B_\varphi \boldsymbol{e}_\varphi, \quad \frac{\partial B_\varphi}{\partial\varphi} = 0. \tag{20}$$

The radial component of the second term on the right-hand side of equation (15) then becomes,

$$\left[\operatorname{curl}\left(\frac{1}{\sigma}\operatorname{curl}\boldsymbol{B}_\mathrm{T}\right)\right]_r = \frac{1}{r^3\sin\vartheta}\frac{\partial}{\partial\varphi}\left(\frac{1}{\sigma}\right)\frac{\partial\left(rB_\varphi\right)}{\partial r}. \tag{21}$$

Similar formula can be derived for the meridional part, depending on the meridional gradient of the zonal magnetic field. We see that the conversion of the toroidal to poloidal field is intensified in the polar areas through the $1/\sin\vartheta$ factor, and it is pronounced in the areas where the vertical stratification of zonal magnetic field couples with a significant zonal gradient of electrical conductivity.

3. Modelling setup

We use the recently developed 3-D z-coordinate baroclinic ocean model LSOMG to calculate the ocean flows forced by the wind stresses and heat fluxes derived from ERA-Interim data (Dee et al., 2011). A more detailed description of the model is provided in the Supplementary material. We run the model with 1° horizontal resolution and for 11 vertical layers. The model reaches a quasi equilibrium after the spin-up period of 20 yr. In this paper, we use the predictions of the ocean flows for year 2014.

Fig. 1 shows the cross-sections of the velocity field at three different depths as predicted by our model on December 31, 2014. The horizontal velocities in the LSOMG model are several orders of magnitude larger than the vertical velocities. The maximum horizontal velocities measured in the real ocean are up to 1–2 m/s, with common values of one or two orders of magnitude smaller. The measured vertical velocities reach 10^{-3} m/s in the restricted regions of deep water formation and 10^{-4} m/s in the regions of Equatorial upwelling, the common values are smaller though (Liang et al., 2017). The magnitudes of measured ocean velocities and velocities computed by the LSOMG model are thus in a good agreement. Since the ocean forcing is applied to the ocean surface, the surface (horizontal) velocities are the largest and the velocities in deep waters are significantly smaller. The upper and lower

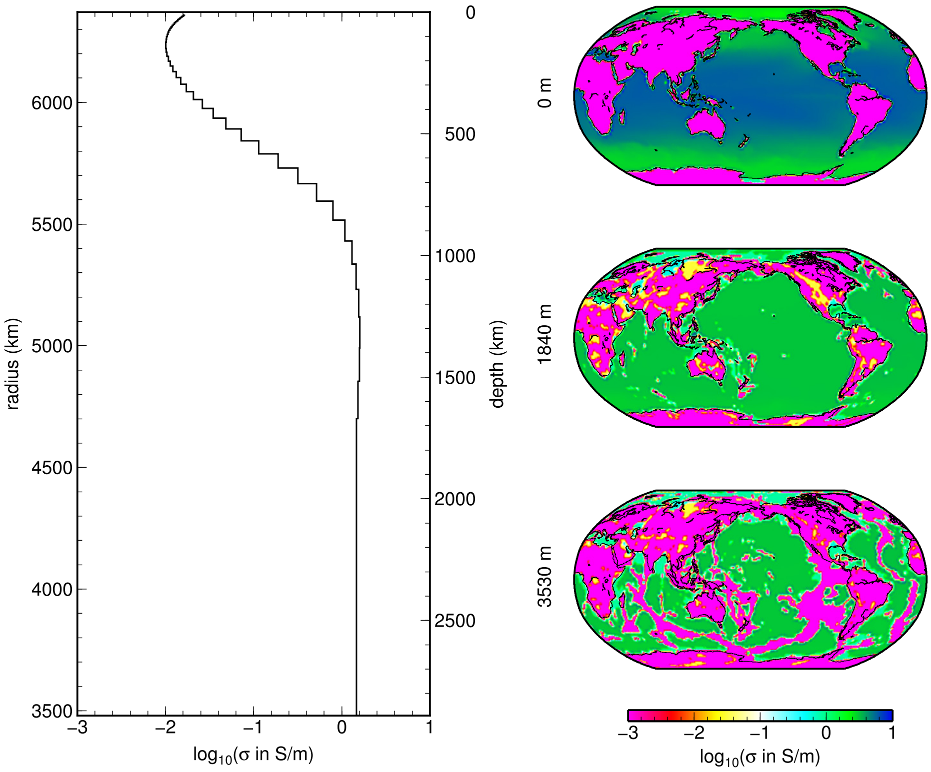

Fig. 2. Electrical conductivity model used in our study. The 1-D profile of the mantle conductivity (Püthe et al., 2015) is shown on the left. The right-hand panel shows three cross-sections of the ocean and continental conductivities at the depths of 0, 1840 and 3530 m.

parts of the ocean are linked together via the advection, diffusion and friction processes. The surface velocities are dominated by the Equatorial and boundary currents, and the Antarctic Circumpolar Current (ACC).

In order to calculate the magnetic field induced by the ocean flow model LSOMG, we employ the time-domain, spherical harmonic-finite element approach to the EM induction equation with 3-D distribution of electrical conductivity (Velímský and Martinec, 2005) that has been recently modified to include the internal sources described in equation (1). The use of the vector spherical harmonic base (Varshalovich et al., 1989) to represent the magnetic field vector $\boldsymbol{B}$ implicitly comprises the separation of the poloidal and toroidal components. Our model uses the same 11 ocean layers as the LSOMG model, the lateral resolution is truncated at spherical harmonic degree 60. The 3-D electrical conductivity of the oceans is assembled from the temperatures and salinities provided by the World Ocean Atlas 2013 (Locarnini et al., 2013; Zweng et al., 2013), using an empirical formula (Apel, 1987). The seasonal variations of the ocean electrical conductivity are neglected. We have not yet implemented the recent improved conductivity map by Tyler et al. (2017), however, we believe that the differences in the large-scale induced fields would be negligible. For continental conductivity, we have followed the approach by Everett et al. (2003), combining the thicknesses of continental and oceanic sediments, and igneous rocks, with a-priori fixed conductivity values. Three cross-sections of oceanic and continental conductivity at different depths are shown in the right-hand panels of Fig. 2. In the Earth's mantle, we have used a global 1-D conductivity model derived from satellite measurements (Püthe et al., 2015), which is shown in the left-hand panel of Fig. 2. Our modelling domain also includes the Earth's core with conductivity of 10^5 S/m. The time evolution of magnetic field is started from a stationary solution of equation (1) using a three-year spin-up interval.

4. Results

This paper aims to answer two questions concerning the global toroidal magnetic field induced in the Earth's oceans. First, what is its amplitude and spatial distribution, and second, how it is pronounced in the directly observable poloidal field at the Earth's surface.

The answer to the first question is presented in Fig. 3, which shows a snapshot of magnetic field components from December 31, 2014 at the Earth's surface, at the depth of 1840 m, where the amplitude of toroidal field is at its peak, and at the depth of 3530 m, corresponding to the average ocean depth. The horizontal components of the toroidal and poloidal fields are plotted separately. At the Earth's surface, the toroidal field vanishes, as required by the boundary condition (12). However, in the deep ocean, the amplitude of the toroidal field, especially its zonal component, as shown in the rightmost column, is almost one order of magnitude larger, than that of the poloidal field. The most pronounced feature, as anticipated by the zonal flow structure in Fig. 1 and the equation (19) is the eastward ACC signature. Significant zonal toroidal fields, comparable in amplitude with the poloidal component, are also present throughout the Pacific, Atlantic and Indian oceans with eastward direction prevailing just north of the equator, and westward direction prominent south of the equator and again in the mid-latitude region of the northern hemisphere. The toroidal meridional component (second column from the right) points mostly to the north in the Atlantic and Pacific oceans. In the Southern Ocean, its spatial variations are influenced by the small-scale variations of the zonal field through the divergence-free condition. The radial magnetic field shown in the left column is almost invariable with depth. It is dominated by the ACC signature, with largest signals present in the Southern Ocean, Southern Pacific, and Southern Indian Oceans. Its spatial structure and amplitude agree well with the predictions of OCCAM and ECCO circulation models obtained by Manoj et al. (2006)

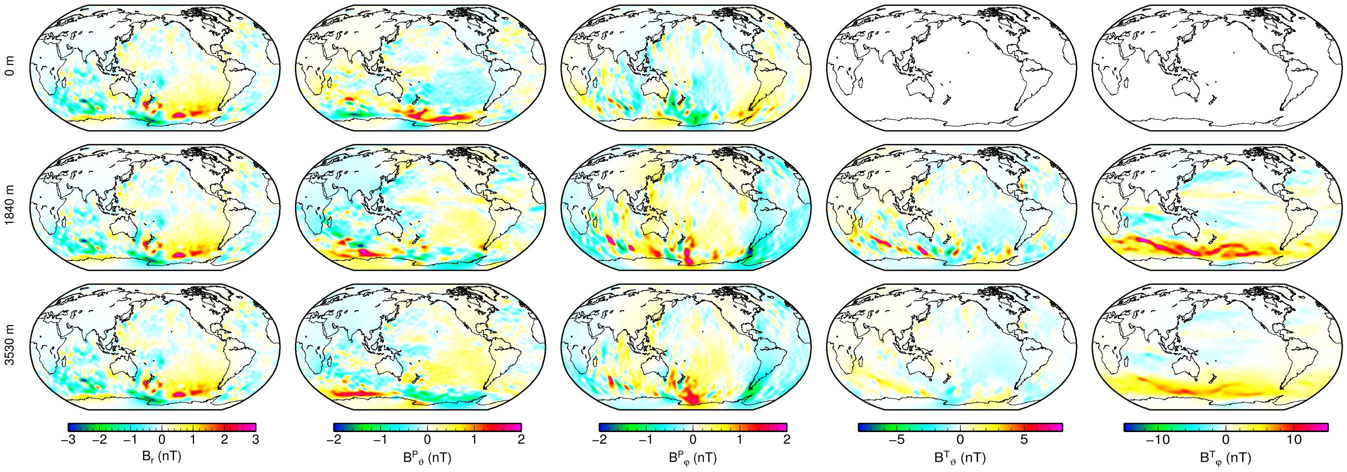

Fig. 3. Snapshots of the induced magnetic field on December 31, 2014 for the full solution. Each row corresponds to a different depth. The poloidal and toroidal parts of the field are shown separately, the individual columns from left to right display respectively the radial, poloidal meridional, poloidal zonal, toroidal meridional, and toroidal zonal components.

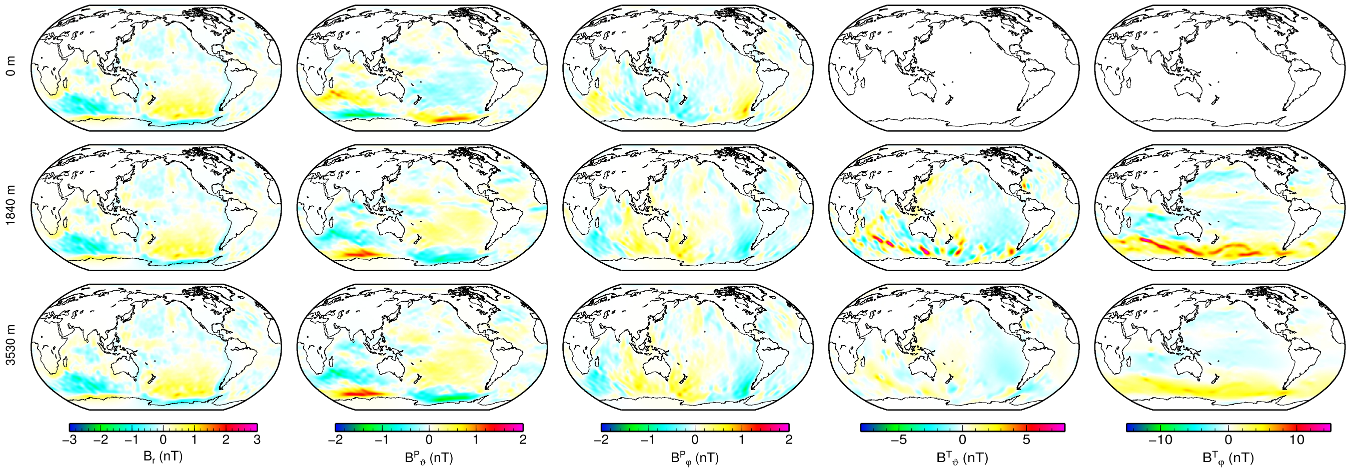

Fig. 4. Snapshots of the induced magnetic field on December 31, 2014 for the decoupled solution. Ordering of the layers by rows and components by columns follows Fig. 3. Note that the colour scales in both figures are the same.

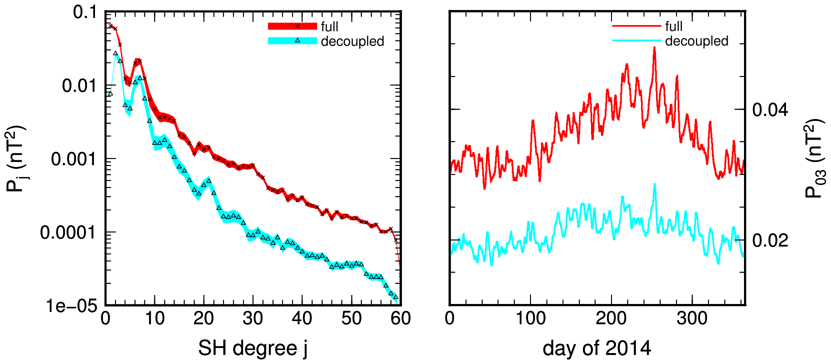

Fig. 5. The power spectra of the induced magnetic field at the surface. In the left-hand panel, the annual geometric means for the full and decoupled runs are shown respectively by crosses and triangles. The geometric standard deviation intervals are marked by the red and blue bands. In the right-hand panel, the time evolution of degree 3 power for both models in 2014 is shown.

(as shown in Fig. 36 in Kuvshinov, 2008). On the other hand, the poloidal horizontal field, shown in the second and third columns of Fig. 3 reverses its sign between the surface and the 1840 m depth. This is a direct consequence of the concentration of horizontal fluxes and corresponding horizontal electric currents in the shallower parts of the ocean.

In order to answer the second question, we have performed an alternate calculation, that we refer to as *decoupled*, to distinguish it from the *full* solution discussed above. In the equations (14) and (15), the terms on the right-hand sides responsible for the energy exchange between the toroidal and poloidal modes through lateral conductivity variations are removed. Therefore, the toroidal and poloidal fields are independent solutions of their corresponding governing equations, powered solely through the poloidal and toroidal components of the Lorentz force, respectively. The results of the decoupled model are shown in Fig. 4. The comparison with Fig. 3 gives us a direct insight into the effect of the poloidal–toroidal field conversion. In the decoupled model, both the toroidal and poloidal fields are significantly reduced in amplitude. The large-scale spatial features of the fields are preserved, including the overturn of the horizontal poloidal field direction in the deep ocean. However, many small-scale patterns are lost in both the poloidal and toroidal fields.

Another comparison of the full and decoupled models is provided by means of power spectra in Fig. 5. Here we show the average energy of the observable poloidal magnetic field at the Earth's surface as a function of spherical harmonic degree. The annual geometric means from 2014 are shown together with the geometric standard deviations corresponding to the temporal variations within year 2014. The full solution has approximately three times larger total energy of the observable field at the Earth's surface than the decoupled solution. While the relative time variations of the power spectra look similar on the log scale, in absolute terms the time variations of the full model are more pronounced, as shown in the right-hand panel of Fig. 5 for degree 3.

5. Conclusions

We have calculated one year of magnetic signatures of global Earth's ocean by solving the 3-D EMI equation with realistic conductivity distribution of the Earth's oceans, lithosphere, and underlying mantle, and using vertically stratified 3-D ocean flows predicted by a state-of-the-art baroclinic ocean model LSOMG. In particular, we have demonstrated that the global toroidal field induced by differential zonal velocities reaches the values of up to 15 nT at the depth of 1800 m and in the vicinity of the ACC. This is almost one order of magnitude larger than the poloidal field. The direct observability of toroidal magnetic field at sea-bottom observatories remains an open question. We predict the seasonal variations of toroidal field in the order of units of nT, a value possibly detectable by the modern sea-bottom equipment. However, to our knowledge, no such observatory has been yet deployed in the area of ACC, where maximum amplitudes can be expected.

We have also quantified the effect of the energy exchange between the toroidal and poloidal fields through lateral conductivity variations. The toroidal field, while invisible on the Earth's surface, has a substantial effect on the observable poloidal component. When the toroidal field is omitted, the power of the poloidal field is about three times smaller with reduced spatial and temporal variability.

In general, in the case of global ocean circulation the 3-D models incorporating the full physics of the EMI equation should be used for the accurate prediction of the motionally induced magnetic field within the oceans.

Acknowledgements

This research was supported by the Grant Agency of the Czech Republic, project No. SVV P210/17-03689S, the European Space Agency, contract No. 4000109562/14/NL/CBi Swarm+Oceans, and the Charles University grant 115-09/260447. The computational resources were provided by The Ministry of Education, Youth and Sports from the Large Infrastructures for Research, Experimental Development and Innovations project "IT4Innovations National Supercomputing Center — LM2015070", project ID OPEN-10-13.

Appendix A. Supplementary material

Supplementary material related to this article can be found online at https://doi.org/10.1016/j.epsl.2018.12.026.

References

Apel, J.R., 1987. Principles of Ocean Physics. Academic Press, London.
Chave, A.D., Luther, D.S., 1990. Low frequency, motionally induced electromagnetic fields in the ocean, 1: theory. J. Geophys. Res. 95, 7185–7200.
Dee, D.P., Uppala, S., Simmons, A., Berrisford, P., Poli, P., Kobayashi, S., Andrae, U., Balmaseda, M., Balsamo, G., Bauer, P., et al., 2011. The ERA-Interim reanalysis: configuration and performance of the data assimilation system. Q. J. R. Meteorol. Soc. 137 (656), 553–597.
Dostal, J., Martinec, Z., Thomas, M., 2012. The modelling of the toroidal magnetic field induced by tidal ocean circulation. Geophys. J. Int. 189, 782–798.
Einšpigel, D., Martinec, Z., 2017. Time-domain modelling of global ocean tides generated by the full lunisolar potential. Ocean Dyn. 67, 165–189.
Everett, M.E., Constable, S., Constable, C., 2003. Effects of near-surface conductance on global satellite induction responses. Geophys. J. Int. 153, 277–286.
Grayver, A.V., Munch, F.D., Kuvshinov, A.V., Khan, A., Sabaka, T.J., Tøffner-Clausen, L., 2017. Joint inversion of satellite-detected tidal and magnetospheric signals constrains electrical conductivity and water content of the upper mantle and transition zone. Geophys. Res. Lett. 44, 6074–6081.

Grayver, A.V., Schnepf, N.R., Kuvshinov, A.V., Sabaka, T.J., Manoj, C., Olsen, N., 2016. Satellite tidal magnetic signals constrain oceanic lithosphere–asthenosphere boundary. Sci. Adv. 2, e1600798.

Irrgang, C., Saynisch, J., Thomas, M., 2016. Impact of variable seawater conductivity on motional induction simulated with an ocean general circulation model. Ocean Sci. 12 (4), 129–136.

Kuvshinov, A.V., 2008. 3-D global induction in the oceans and solid Earth: recent progress in modeling magnetic and electric fields from sources of magnetospheric, ionospheric and oceanic origin. Surv. Geophys. 29 (2), 139–186.

Larsen, J.C., 1992. Transport and heat flux of the Florida Current at 27°N derived from cross-stream voltages and profiling data: theory and observations. Philos. Trans. R. Soc. Lond. A 338, 169–236.

Liang, X., Spall, M., Wunsch, C., 2017. Global ocean vertical velocity from a dynamically consistent ocean state estimate. J. Geophys. Res., Oceans 122 (10), 8208–8224.

Lilley, F.E.M., Filloux, J.H., Mulhearn, P.J., Ferguson, I.J., 1993. Magnetic signals from an ocean eddy. J. Geomagn. Geoelectr. 45, 403–422.

Lilley, F., White, A., Heinson, G., 2001. Earth's magnetic field: ocean current contributions to vertical profiles in deep oceans. Geophys. J. Int. 147, 163–175.

Lilley, F., Hitchman, A., Milligan, P.R., Pedersen, T., 2004. Sea-surface observations of the magnetic signals of ocean swells. Geophys. J. Int. 159, 565–572.

Locarnini, R.A., Mishonov, A.V., Antonov, J.I., Boyer, T.P., Garcia, H.E., Baranova, O.K., Zweng, M.M., Paver, C.R., Reagan, J.R., Johnson, D.R., Hamilton, M., Seidov, D., 2013. In: Levitus, S. (Ed.), World Ocean Atlas 2013, vol. 1. Temperature: NOAA Atlas NESDIS 73, p. 40.

Manoj, C., Kuvshinov, A., Maus, S., Lühr, H., 2006. Ocean circulation generated magnetic signals. Earth Planets Space 58, 429–437.

Maus, S., Kuvshinov, A., 2004. Ocean tidal signals in observatory and satellite magnetic measurements. Geophys. Res. Lett. 31, L15313.

Püthe, C., Kuvshinov, A., Khan, A., Olsen, N., 2015. A new model of Earth's radial conductivity structure derived from over 10 yr of satellite and observatory magnetic data. Geophys. J. Int. 203 (3), 1864–1872. https://doi.org/10.1093/gji/ggv407.

Roberts, P., 1992. Dynamo theory. In: Yuen, D.A. (Ed.), Chaotic Processes in the Geological Sciences. Springer-Verlag, New York, pp. 237–280.

Sabaka, T.J., Tyler, R.H., Olsen, N., 2016. Extracting ocean-generated tidal magnetic signals from Swarm data through satellite gradiometry. Geophys. Res. Lett. 43, 3237–3245.

Sanford, T.B., 1971. Motionally induced electric and magnetic fields in the sea. J. Geophys. Res. 76, 3476–3492.

Stewart, R.H., 2008. Introduction to Physical Oceanography. Texas A & M University.

Toh, H., Hamano, Y., 2015. The two seafloor geomagnetic observatories operating in the Western Pacific. In: Favali, P., De Santis, A., Beranzoli, L. (Eds.), Seafloor Observatories — A New Vision of the Earth from the Abyss. Springer, pp. 307–323.

Toh, H., Hamano, Y., Ichiki, M., 2006. Long-term seafloor geomagnetic station in the Northwest Pacific: a possible candidate for a seafloor geomagnetic observatory. Earth Planets Space 58, 697–705.

Tyler, R.H., Boyer, T.P., Minami, T., Zweng, M.M., Reagan, J.R., 2017. Electrical conductivity of the global ocean. Earth Planets Space 69, 156.

Tyler, R.H., Maus, S., Lühr, H., 2003. Satellite observations of magnetic fields due to ocean tidal flow. Science 299, 239–241.

Tyler, R.H., Mysak, L.A., Oberhuber, J.M., 1997. Electromagnetic fields generated by a three dimensional global ocean circulation. J. Geophys. Res., Oceans 102 (C3), 5531–5551.

Tyler, R.H., Sanford, T.B., Oberhuber, J.M., 1997b. Geophysical challenges in using large-scale ocean-generated EM fields to determine the ocean flow. J. Geomagn. Geoelectr. 49, 1351–1372.

Varshalovich, D.A., Moskalev, A.N., Khersonskii, V.K., 1989. Quantum Theory of Angular Momentum. World Scientific, Singapore.

Velímský, J., Martinec, Z., 2005. Time-domain, spherical harmonic-finite element approach to transient three-dimensional geomagnetic induction in a spherical heterogeneous Earth. Geophys. J. Int. 160, 81–101.

Vivier, F., Maier-Reimer, E., Tyler, R.H., 2004. Simulations of magnetic fields generated by the Antarctic Circumpolar Current at satellite altitude: can geomagnetic measurements be used to monitor the flow? Geophys. Res. Lett. 31 (10).

Zweng, M., Reagan, J., Antonov, J., Locarnini, R., Mishonov, A., Boyer, T., Garcia, H., Baranova, O., Johnson, D., Seidov, D., Biddle, M., 2013. In: Levitus, S. (Ed.), World Ocean Atlas 2013, vol. 2, Salinity: NOAA Atlas NESDIS 74, p. 39.